

AD-A119 099 AIR FORCE INST OF TECH WRIGHT-PATTERSON AFB OH
MICROMECHANISMS OF CRACK EXTENSION IN ALLOYS. (U)
1982 J A BLIND
UNCLASSIFIED AFIT/CI/NR/82-250

F/G 11/6

NL

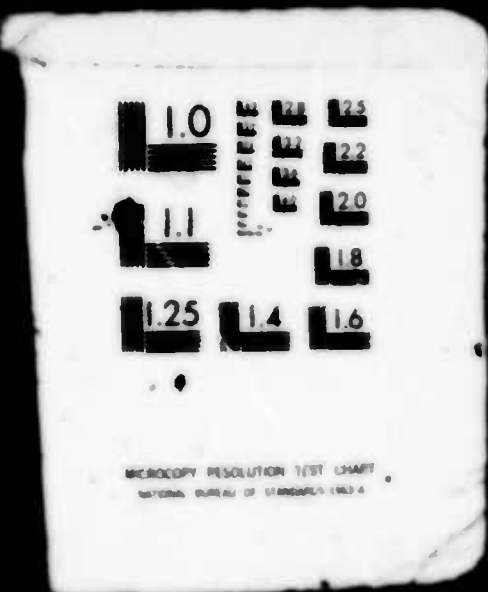
104
AD-A
119099



1 OF 4

AD A

119099



SEC:

AD A119099

READ INSTRUCTIONS BEFORE COMPLETING FORM		
1. REPORT NUMBER AFIT/CI/NR/82-250	2. GOVT ACCESSION NO. Q AC-A119099	3. RECIPIENT'S CATALOG NUMBER
4. TITLE (and subtitle) Micromechanisms of Crack Extension in Alloys	5. TYPE OF REPORT & PERIOD COVERED THESIS/DISSERTATION	
7. AUTHOR(S) John A. Blind	6. PERFORMING ORG. REPORT NUMBER	
9. PERFORMING ORGANIZATION NAME AND ADDRESS AFIT STUDENT AT: Merton College University of Oxford England	10. PROGRAM ELEMENT, PROJECT, TASK AREA & WORK UNIT NUMBERS	
11. CONTROLLING OFFICE NAME AND ADDRESS AFIT/NR WPAFB OH 45433	12. REPORT DATE 1982	
14. MONITORING AGENCY NAME & ADDRESS (if different from Controlling Office)	13. NUMBER OF PAGES 135	
	15. SECURITY CLASS. (if info report) UNCLASS	
	16. DECLASSIFICATION/DOWNGRADING SCHEDULE	

17. DISTRIBUTION STATEMENT (in this Report)

APPROVED FOR PUBLIC RELEASE; DISTRIBUTION UNLIMITED

DTIC
ELECTED
SEP 9 1982

17. DISTRIBUTION STATEMENT (in the abstract entered in Block 20, if different from Report)

18. SUPPLEMENTARY NOTES

APPROVED FOR PUBLIC RELEASE: IAW AFR 190-17

30 AUG 1982

Lynn E. WOLVER
Dean for Research and
Professional Development
AFIT, Wright-Patterson AFB, OH

BY WORDS (Continue on reverse side if necessary and identify by block number)

ABSTRACT (Continue on reverse side if necessary and identify by block number)

ACHED

YCS

1473

EDITION OF 1 NOV 88 IS OBSOLETE

UNCLASS

82 09 07

SECURE

DISTRIBUTION OF THIS PAGE IS UNCLASSIFIED

John A. Blind
Merton College

P-1
D.Phil. Thesis
Hilary Term, 1982

Micromechanisms of Crack Extension in Alloys

Abstract

This work describes an investigation of the effect of manganese-bearing dispersoid particles on the fracture characteristics of peak aged Al-Mg-Si alloys.

Current elastic and elastic-plastic fracture toughness parameters are reviewed. The applicability of these parameters as criteria for the onset of crack extension and their variation with alloy microstructure are examined based on experimental results for a series of alloys containing differing volume fractions of dispersoid. High purity alloys were used to isolate the effect of dispersoids from that of coarse constituent particles. Also, for comparison, one alloy of commercial purity containing both dispersoids and coarse iron-bearing inclusions was studied.

The ductile fracture toughness, J_{IC} , and the resistance to instability as measured by the tearing modulus, T , were found to increase with dispersoid content. The values of these parameters were lower in the commercial purity alloy than for the equivalent high purity alloy.

The effect of an increasingly triaxial stress state on fracture strain was measured using a series of notched tensile specimens. The alloy ductility was found to increase with dispersoid content and to decrease with increased stress triaxiality.

Crack tip plastic zone sizes on the midplane of compact tension specimens were measured using the SEM electron channelling pattern technique. Zone size was found to correlate with the square of the applied stress intensity factor. The constant of proportionality decreased with increasing dispersoid content. The calculated work per unit area of new crack surface was found to correspond to the ductile fracture toughness measured for each alloy.

These results are explained in terms of the effect of slip distribution on the dominant micromechanisms of crack extension. The stress and strain distributions in the plastic zone are then related to the micromechanisms of crack extension using a semi-cohesive zone model of the crack tip region.



Accession For	
NTIS Grid	
DTIC TAB	
Unannounced	
Justification	
By	
Distribution/	
Availability Codes	
Dist	Avail and/or Special
A	

AFIT RESEARCH ASSESSMENT

The purpose of this questionnaire is to ascertain the value and/or contribution of research accomplished by students or faculty of the Air Force Institute of Technology (ATC). It would be greatly appreciated if you would complete the following questionnaire and return it to:

AFIT/NR
Wright-Patterson AFB OH 45433

RESEARCH TITLE: Micromechanisms of Crack Extension in Alloys

AUTHOR: John A. Blind

RESEARCH ASSESSMENT QUESTIONS:

NAME _____ GRADE _____ POSITION _____
CITY _____ STATE _____ ZIP CODE _____

STATEMENT(s):

82-250

MICROMECHANISMS OF CRACK EXTENSION IN ALLOYS

An investigation of the effect of manganese-bearing dispersoids on the
fracture characteristics of Al-Mg-Si alloys.

John A. Blind

Merton College

Oxford

A thesis submitted for the degree of Doctor of Philosophy at the
University of Oxford, Hilary Term, 1982.

He that has a "spirit of detail" will do better in life than many who figured beyond him in the university. Such an one is minute and particular. He adjusts trifles; and these trifles compose most of the business and happiness of life. Great events happen seldom, and affect few; trifles happen every moment to everybody; and though one occurrence of them adds little to the happiness or misery of life, yet the sum total of their continual repetition is of the highest consequence.

- Daniel Webster

Table of Contents

Abstract

Acknowledgements

Preface

**Chapter 1 : FRACTURE MECHANICS AND FRACTURE MICROMECHANISMS IN
ALUMINIUM ALLOYS**

1.1	Introduction	1
1.2	Fracture Mechanics	2
1.2.1	Formulation of Crack Tip Equations	3
1.2.2	Plasticity Corrections to LEFM	7
1.3	Fracture Criteria	14
1.3.1	Energy Release Rate	14
1.3.2	Stress Intensity Factor	19
1.3.3	Crack Opening Displacement	20
1.3.4	The J-Integral	22
1.4	Microstructural Effects on Fracture Mechanics	26
1.4.1	Crack Propagation Mechanisms	26
1.4.2	Effect of Particles	28
1.4.3	Effect of Sliy Distribution	30
1.4.4	Effect of Grain Size	34
1.5	Crack Tip Plastic Zone	35
1.5.1	Stresses in the Plastic Zone	36
1.5.2	Strains in the Plastic Zone	39
1.5.3	Experimental Determination of Plastic Zone Size	42

1.6 The Present Work	46
1.6.1 The Aluminium-Magnesium-Silicon System	47
1.6.2 Fracture Mechanisms in Al-Mg-Si Alloys	49
1.6.3 Object of the Present Work	53
 Chapter 2 : MATERIALS AND EXPERIMENTAL PROCEDURES	 54
2.1 Materials	54
2.1.1 Casting	54
2.1.2 Thermomechanical Treatment	55
2.2 Tensile Tests	58
2.2.1 Unnotched Tensile Tests	59
2.2.2 Notched Tensile Tests	60
2.3 Fracture Toughness Tests	61
2.3.1 K _{IC} Testing	62
2.3.2 J _{IC} Testing	64
2.4 Plastic Zone Size Measurement	66
2.4.1 Electron Channelling Patterns (ECP)	66
2.4.2 Experimental Technique	68
2.4.3 Sensitivity, Reproducibility and Accuracy	71
2.5 Metallography	73
2.6 Fractography	74
 Chapter 3 : EXPERIMENTAL RESULTS	 76
3.1 Tensile Tests	76
3.1.1 Unnotched Tensile Tests	76
3.1.2 Notched Tensile Tests	78

3.2 Fracture Toughness Tests	80
3.2.1 Plane Strain Fracture Toughness (K _{IC})	80
3.2.2 Ductile Fracture Toughness (J _{IC})	82
3.3 Plastic Zone Size Measurement	84
3.4 Metallography	88
3.5 Fractography	89
3.5.1 Alloy MT	89
3.5.2 Alloy ML	90
3.5.3 Alloy MM	91
3.5.4 Alloy MH	92
3.5.5 Alloy MC	92
3.5.6 Summary of Fractography	93
 Chapter 4 : DISCUSSION	 95
4.1 Microstructural Features	95
4.2 Unnotched Tensile Tests	96
4.2.1 Yield Strength	96
4.2.2 Work Hardening Rates	97
4.2.3 Fracture Strains	99
4.3 Notched Tensile Specimens	100
4.4 Fracture Toughness Parameters	103
4.4.1 Ductile Fracture Toughness - J _{IC}	103
4.4.2 Comparison of J with K	104
4.4.3 Comparison of J with G	106
4.4.4 Detecting the Onset of Crack Extension	108
4.4.5 Tearing Modulus - T	112

4.4.6	Summary of Fracture Toughness Parameters	113
4.5	Crack Tip Plastic Zone Size	114
4.5.1	Correlation with K	114
4.5.2	Values at Onset of Crack Extension	116
4.5.3	Correlation with dW/dA	117
4.5.4	Stress and Strain Distributions	120
4.6	Micromechanisms of Crack Extension	125
Chapter 5 : CLOSURE		132
5.1	Conclusions	132
5.2	Implications for Alloy Design	134
5.3	Suggestions for Further Work	134

List of References

Acknowledgements

There are a great many people to whom I would like to express my gratitude for their assistance in the course of this research project. Although I cannot hope to list them all, I would particularly like to thank the following:

Professor Sir Peter Hirsch F.R.S. for provision of the laboratory facilities and the United States Air Force for financial support.

General Philip J. Erdle and Colonel Wallace E. Fluhr, USAF, for giving me the opportunity to study at Oxford.

Dr. J.W. Martin, my supervisor, for his advice and encouragement throughout the project.

Alcan Laboratories Ltd. for providing the alloys, and Mr. A.T. Thomas and Mr. B.J. Dunwoody for many helpful discussions.

Mr. J. Short and other members of the laboratory workshops for their cheerful assistance and valuable advice.

Dr. Lyndon Edwards for innumerable impromptu tutorials and for his consistent willingness to give advice on anything.

All members of the JWM group, especially Jeff Crompton and Ian Baker, for their friendship, assistance and patient acceptance of numerous cultural idiosyncrasies.

Glynis Edwards for the careful typing of the manuscript and George K. Williams for exhaustive proofreading of the text.

Sandy Roest for professional preparation of the figures.

Lastly, I would like to thank my wife, Janie, for her constant support and understanding and without whom the work could not have been done.

John A. Blind

Preface

This thesis is an account of research carried out in the Department of Metallurgy and Science of Materials at the University of Oxford between October 1979 and March 1982. The work reported is original and is not substantially the same as any thesis submitted in this or any other university. The work of other authors, when included in the text, has been acknowledged and its source given in an alphabetical list of references at the end of the thesis.

Chapter 1

FRACTURE MECHANICS AND FRACTURE MICROMECHANISMS IN ALUMINIUM ALLOYS

1.1 Introduction

"It should be noted that there are two extreme approaches to the fracture problem. The first seeks to avoid as far as possible any discussion of the physical processes occurring at the crack tip and looks for one or more characterizing parameters whose critical value, measured in the testing laboratory, can be used to assess the safety of the structure. The second approach puts more emphasis on improving our natural knowledge of fracture, in the belief that this will ultimately lead to a greater control of it. Clearly, despite the pressing demands on the engineer for immediate decisions, both approaches must be pursued, not least because changes in the physical processes of fracture can alter the characterizing parameters considerably.

However, there are some half-way houses between these two extremes. One is to make a very simple theory and to try to back up the predictions with empirical results."

B.A. Bilby (1981)

Professor Bilby's statement clearly expresses the dual strategies of the present work: to consider the fracture process from both the macroscopic and microscopic points of view. The macroscopic approach seeks to determine the large scale parameters that control crack extension, while the micromechanistic approach seeks to clarify the effect of microstructure on fracture. To obtain a better understanding of the ways the microstructure of alloys can be altered to improve their resistance to fracture is the objective of both approaches.

Chapter One of this thesis first examines the macroscopic approach to the characterization of crack extension; crack extension criteria that have evolved from the field of fracture mechanics are

briefly reviewed. Next, the effect of material microstructure on micromechanisms of crack extension, slip distribution and crack tip plastic zone processes is considered. Finally, the specific research undertaken to clarify the relationship between microscopic crack tip deformation and macroscopic material characterizing parameters is presented.

1.2 Fracture Mechanics

Fracture implies the separation of a component into two or more pieces, regardless of whether or not that component contains initial flaws or cracks. If the component contains an initial crack, then crack extension becomes the first stage of the process ultimately leading to fracture. In brittle material, the crack may propagate rapidly once it has begun to extend so that the component fractures catastrophically, i.e. by unstable crack propagation. However, if the material is relatively ductile, its greater resistance to initial crack extension may permit the crack to propagate in a slow, stable manner. Such resistances to both initial crack extension and subsequent crack propagation are important considerations when selecting a material for many design applications.

Fracture mechanics, developed as a method to analyze structures containing cracks, is something of a misnomer since the crack does not necessarily lead to fracture. Nevertheless, fracture mechanics has contributed greatly to the effective design of structural components, particularly in knowledge of the stresses in a body near a crack tip.

1.2.1 Formulation of Crack Tip Equations

Linear elastic fracture mechanics (LEFM) is based on an ideal, elastic solid (i.e., one that is homogeneous, isotropic and obeys Hooke's Law) conforming to the continuum mechanics relation for stresses and strains. Thus LEFM relations for the stresses and strains in a body containing a crack must satisfy the requirements for equilibrium of stresses, compatibility of strains and the boundary conditions of the crack geometry. Because several authors have adequately presented the development of these equations, including Broek (1978), Knott (1973) and Perker (1981), the subject will only be briefly reviewed here.

The objective of the LEFM analysis is to obtain expressions, satisfying the conditions mentioned above, for the stresses in a body containing a crack in terms of the loads and the geometry. For the axis system shown in fig. 1.1, these expressions can be obtained by considering only stresses in the X-Y plane, and then extending this initial result into three dimensions. Airy (1862) was the first to demonstrate that a stress function ϕ can exist which gives the stresses as follows:

$$\begin{aligned}\sigma_{xx} &= \frac{\partial^2 \phi}{\partial y^2} \\ \sigma_{yy} &= -\frac{\partial^2 \phi}{\partial x^2} \\ \tau_{xy} &= -\frac{\partial^2 \phi}{\partial x \partial y}\end{aligned}\tag{1.1}$$

It can be shown (e.g., Broek, 1978) that the Airy stress function ϕ satisfies the equilibrium and continuity requirements. However, the problem then becomes one of deriving a function ϕ that also satisfies the boundary conditions. Westergaard (1939) proposed a solution, in terms of a complex function ψ , applicable to a body containing a sharp crack and subjected to mode I loading (see fig. 1.2). To simplify the boundary conditions, Westergaard applied the complex function to the specific case of an infinite sheet under biaxial loading σ , containing a crack of length $2a$ (as shown in fig. 1.3). Thus by judicious choice of the complex function, the crack tip stresses are given in polar coordinates as:

$$\sigma_{xx} = \frac{\sigma\sqrt{\pi a}}{\sqrt{2\pi}} \frac{\cos\theta}{2} \frac{1}{2} \frac{\sin\theta}{2} \frac{\sin 3\theta}{2} + \text{additional terms}$$

$$\sigma_{yy} = \frac{\sigma\sqrt{\pi a}}{\sqrt{2\pi}} \frac{\cos\theta}{2} \frac{1}{2} \frac{\sin\theta}{2} \frac{\sin 3\theta}{2} + \text{additional terms} \quad (1.2)$$

$$\tau_{xy} = \frac{\sigma\sqrt{\pi a}}{\sqrt{2\pi}} \frac{\sin\theta}{2} \frac{\cos\theta}{2} \frac{\cos 3\theta}{2} + \text{additional terms}$$

If the point (r, θ) is sufficiently close to the crack tip, the additional terms referred to in eq. (1.2) are negligible compared to the first term. This elastic solution predicts infinite stresses at the crack tip ($r=0$); these are not infinite in practice since plastic flow occurs in the highly stressed region near the tip. However, if this region of plastic flow is small compared to the region over which the $r^{-1/2}$ term dominates the stress field (small scale yielding), it may be assumed that the first terms in eq. (1.2) determine the

behaviour of the crack. This assumption forms the basis of LEFM.

However, the Westergaard solution was derived for the specific case of balanced biaxial tension. Sih (1966) and Eftis and Liebowitz (1972) demonstrated that the Westergaard solution is not completely correct. Also, for the more common case of uniaxial tension, the result must be modified by superimposing a pressure of $(-\sigma)$ in the X direction (fig. 1.3), making $\sigma_{xx} = 0$ at large values of r . However, these corrections do not affect the value of the stresses near the crack tip.

Irvin (1958), recognizing the group of terms σ/\sqrt{r} in eq. (1.2) as a fundamental quantity, labelled them the stress intensity factor K . For an infinitely sharp crack in an infinitely wide elastic plate, the stress intensity factor can now be defined as:

$$K_I = \sigma/\sqrt{r} \quad (1.3)$$

The subscript on K represents mode I opening. Similarly, K_{II} and K_{III} represent the stress intensity factors for mode II and mode III opening (see fig. 1.2). For a body with finite dimensions, eq. (1.3) becomes:

$$K_I = Y\sigma/\sqrt{r} \quad (1.4)$$

where Y is a size correction factor. K has become an important parameter in the field of fracture mechanics because it characterizes the stress field around the crack tip. Thus, if K can be determined for a specific geometry and loading situation, the severity of the crack tip stress singularity can be compared to that of other alternative geometries and loading situations where K is known. This capability is a valuable tool in structural design.

Rewriting eq. (1.2) in terms of the stress intensity factor gives:

$$\sigma_{xx} = \frac{K_I}{\sqrt{2\pi r}} \frac{\cos\theta}{2} \frac{1 - \sin\theta \sin 3\theta}{2}$$

$$\sigma_{yy} = \frac{K_I}{\sqrt{2\pi r}} \frac{\cos\theta}{2} \frac{1 + \sin\theta \sin 3\theta}{2} \quad (1.5)$$

$$\tau_{xy} = \frac{K_I}{\sqrt{2\pi r}} \frac{\cos\theta}{2} \frac{\sin\theta \sin 3\theta}{2}$$

$$\sigma_{zz} = 0 \quad \text{for plane stress}$$

$$\sigma_{zz} = v(\sigma_{xx} + \sigma_{yy}) \quad \text{for plane strain}$$

At this point, one other geometric factor, indicated in the latter two expressions of eq. (1.5), must be noted. Plane stress and plane strain refer to the idealized situations of either a totally two dimensional stress field or two dimensional deformation. For example, plane stress conditions are approximated in a thin sheet. Because its free surfaces cannot transmit a load in the direction perpendicular to the sheet, σ_{zz} is zero at the surface and remains small across the thickness. Plane strain conditions are approximated on the mid-plane of a thick plate because of constraint from the surrounding elastic material. In this case, the Poisson's strain is prevented ($\epsilon_{zz}=0$) and $\sigma_{zz}=v(\sigma_{xx} + \sigma_{yy})$. As Lake (1976) and Boyd (1972) have pointed out, caution should be used when applying the concept of plane stress and plane strain to actual fractured materials since plane stress and plane strain are idealized extremes. Their use simplifies calculations, but most practical situations lie somewhere between the

two extremes.

1.2.2 Plasticity Corrections to LEFM

The equations for crack tip stresses derived from linear elasticity predict a stress singularity at the crack tip ($\sigma \rightarrow \infty$ as $r \rightarrow 0$) with the stress intensity factor K controlling the severity of the singularity. Since the stresses within the material cannot become infinite, either its fracture stress σ_y will be exceeded and fracture will occur or the yield strength σ_y will be exceeded and the material will plastically deform. The great majority of engineering materials will show some plasticity at the crack tip. Since the degree of this plasticity — reflected by the crack tip plastic zone size — will obviously affect the crack tip stresses, it is important to be able to calculate the plastic zone size.

Lankford et al. (1977) provide an excellent review of the various methods of plastic zone size calculations; their notation is used here. Let r_p represent the actual plastic zone size and r_1 through r_6 represent the various estimates of plastic zone size.

The first estimate of plastic zone size uses eq. (1.5) for the y -direction stress at the tip of a sharp crack in an infinite plate (see fig. 1.4) with θ set equal to 0° , giving

$$\sigma_{yy} = \frac{K_1}{\sqrt{2\pi r}} \quad (1.6)$$

Substituting the yield stress σ_y for σ_{yy} and solving for r gives

$$r_1 = \frac{1}{2\pi} \frac{K_1^2}{\sigma_y^2} \quad (1.7)$$

The actual plastic zone will be larger than r_1 , however, because the load represented by the shaded region in fig. 1.4 will be supported by the material immediately ahead of the r_1 plastic zone. This added load causes more material to yield so that the plastic zone becomes r_2 (fig. 1.5). Rice (1967) suggested $r_2 = 2r_1$, where:

$$r_2 = \frac{1 K^2}{2 \sigma_y^2} \quad (1.8)$$

Irwin (1960) maintained that it is not necessary to know the exact size and shape of the plastic zone. Since plasticity at the crack tip creates larger displacements and the material has lower stiffness than when totally elastic, the plasticity makes the crack behave as if it were longer than its actual size. Consequently, Irwin proposed a plastic zone correction factor r_p^* such that, in the equation for stress intensity, the crack length a is replaced by $(a+r_p^*)$.

$$\text{e.g. } K = \sigma \sqrt{a(a+r_p^*)} \quad (1.9)$$

Irwin chose

$$r_p^* = r_1 = \frac{1}{2} \frac{K^2}{\sigma_y^2} = \frac{1}{6} \frac{K^2}{\sigma_y^2} \quad (1.10)$$

Equations (1.9) and (1.10), in which K is given in terms of r_p^* and r_p^* is given in terms of K , imply that K must be determined by an iterative process. Although a plastic zone correction factor allows a more exact calculation of K , Irwin's r_p^* was not meant to be an estimate of the true plastic zone size, although it is frequently used as such.

Dugdale (1960) proposed a different approach, postulating a model which assumes that yielding occurs in a narrow strip ahead of the crack (fig. 1.6). Essentially, the crack of length $2a$, with yield zones at the crack tip, is replaced by a totally elastic crack of length $2(a+r_3)$ plus a crack of length $2(r_3)$ which is prevented from opening over the region r_3 by restraining stresses equal to the yield stress σ_y . Then r_3 is determined such that the stress at the crack tip $2(r_3)$ is finite. This means that the K due to the two superimposed cracks is zero. In other words, the stress intensity factors for the cracks of length $2(r_3)$ are equal in magnitude but opposite in sign. Since expressions for the elastic K can be determined in each case in terms of $(a+r_3)$, r_3 can be found:

$$r_3 = \frac{K^2}{8\sigma_y^2} \quad (1.11)$$

Although useful as a means of calculating plastic zone size, the Dugdale model loses some physical significance by requiring a zero stress intensity factor at $(a+r_3)$, in effect implying that a Dugdale crack has no driving force for crack extension. (The concept of a crack driving force will be considered in some detail later.) A similar model was propounded by Barenblatt (1962) using molecular cohesive forces to eliminate the crack tip stress singularity. Also, Bilby, Cottrell and Swinden (1963) developed their BCS model, which employs a continuously distributed array of dislocations. Overall, the Dugdale, Barenblatt and BCS models yield similar predictions for plastic zone size.

However, their estimates only consider one dimension of the three dimensional plastic zone. More precise predictions of plastic zone

size consider the state of stress (plane stress or plane strain referred to earlier) and the yield condition. For example, the Tresca yield condition states that yielding will occur when the maximum applied shear stress exceeds a critical value τ_y , i.e:

$$\tau_{\max} = \frac{\sigma_1 - \sigma_3}{2} \geq \tau_y \quad (1.12)$$

where σ_1 and σ_3 are the maximum and minimum principal stresses, respectively. In uniaxial tension the maximum applied normal stress is twice the maximum applied shear stress ($\sigma_3=0$), and eq. (1.12) reduces to

$$\sigma_1 > \sigma_y \quad (1.13)$$

Alternatively, the von Mises yield criterion is based on a maximum in strain energy density and is given by (Broek, 1978, pg.96)

$$\sigma_y < \frac{\sqrt{2}}{2} \sqrt{(\sigma_1 - \sigma_2)^2 + (\sigma_2 - \sigma_3)^2 + (\sigma_3 - \sigma_1)^2} \quad (1.14)$$

The von Mises criterion has been found to closely predict the experimental results for the onset of yielding in ductile metals.

If the crack tip stress field equations (1.5) are rewritten in terms of principal stresses, the following equations result:

$$\sigma_1 = \frac{K}{\sqrt{2\pi r}} \frac{\cos\theta}{2} \frac{(1+\sin\theta)}{2}$$

$$\sigma_2 = \frac{K}{\sqrt{2\pi r}} \frac{\cos\theta}{2} \frac{(1-\sin\theta)}{2} \quad (1.15)$$

$$\sigma_3 = 0 \text{ for plane stress}$$

$$\sigma_3 = \nu(\sigma_1 + \sigma_2) = \frac{2\nu}{\sqrt{2\pi r}} \frac{K \cos\theta}{2} \text{ for plane strain}$$

Substituting equations (1.15) into the von Mises yield condition allows solution for the boundary of the plastic zone as a function of θ as

$$r_p(\theta) = \frac{K^2}{4\pi\sigma_y^2} \left[\frac{3\sin^2\theta + (1-2\nu)^2(1+\cos\theta)}{2} \right] \quad (1.16)$$

for plane strain

$$r_p(\theta) = \frac{K^2}{4\pi\sigma_y^2} \left[\frac{1+3\sin^2\theta+\cos\theta}{2} \right] \quad (1.16)$$

for plane stress

This is equivalent to the first estimate of plastic zone size r_1 . In fact, substituting $\theta=0$ in the plane stress equation for $r_p(\theta)$ gives the same result as eq. (1.7)

$$r_p(\theta=0) = \frac{1}{2} \frac{K^2}{\pi\sigma_y^2} \approx r_1 \quad (1.17)$$

However, the plane strain equation gives

$$r_p(\theta=0) = \frac{(1-2\nu)^2}{2\pi} \frac{K^2}{a_y^2} \quad (1.18)$$

Therefore, the plane stress value for r_p at $\theta=0^\circ$ is approximately nine times greater than the plane strain r_p . Thus, the plastic zone size estimate r_1 applies accurately to the plane stress situation but greatly overestimates the plane strain plastic zone.

When equations (1.16) are plotted on normalized axes as in fig. 1.7, the relative sizes as a function of θ of calculated plane stress and plane strain plastic zones emerge. Due to these differences in size and shape, any plate that is thick enough to approximate plane strain constraint on its mid-plane would develop a three-dimensional plastic zone through the thickness as shown in fig. 1.8. However, McClintock and Irwin (1965) felt it unlikely that sufficient constraint would be generated to produce a plane strain plastic zone that is nine times smaller than the plane stress plastic zone. Their estimate of this constraint reduces the plane strain plastic zone to about one-third the plane stress zone. Therefore, two additional estimates of the plane strain plastic zone size can be made based on r_1 and r_2 (Lankford et al., 1977) as

$$r_3 = r_1 = \frac{1}{3} \frac{K^2}{6\pi a_y^2} \quad (1.19)$$

$$r_4 = r_2 = \frac{1}{3} \frac{K^2}{3\pi a_y^2} \quad (1.20)$$

More accurate estimates use finite element methods which take into account material hardening characteristics (e.g. Rice and Tracey, 1973 and Tracey, 1971 and 1976). These studies show that the plane

strain plastic zone is not symmetric about the y-axis (the vertical axis in figs. 1.7 and 1.8). Instead, the lobes are rotated forward toward the horizontal axis so that the maximum plastic zone dimension occurs at $\theta = 70^\circ$.

According to Rice and Rosengren (1968), the plastic zone size is slightly affected by the work hardening rate for a power law hardening material whose true stress-true strain curve is described by

$$\sigma = k\epsilon^N \quad (1.21)$$

where k is a constant and N is the work hardening exponent. They showed that the maximum distance from the crack tip to the elastic-plastic boundary was at $\theta=100^\circ$. Also, they found that for $N=0.05$, r_p is given by

$$r(\theta=0) = 0.007 \frac{k^2}{\sigma_y^2} \quad (1.22)$$

Thus a great many theoretical estimates of plastic zone size have been postulated, based on various assumptions and using different models for their calculations. It is perhaps noteworthy that the only metallurgical variables involved in these estimates are yield strength and strain hardening rate. The amount of effort expended to calculate plastic zone size goes far beyond its value as a correction factor to LEFM stress intensity factors; the interest in the crack tip plastic zone reflects its importance in the metallurgical view of crack extension and, ultimately, fracture. Since it is widely felt that the energy required for fracture is expended in this crack tip zone, valid fracture criteria must relate to the deformation processes occurring in the crack tip plastic zone.

1.3 Fracture Criteria

Prior to considering the micro-mechanistic aspects of crack extension, the major macroscopic parameters in current use as fracture criteria will be reviewed. These criteria include the energy release rate G , stress intensity factor K , crack tip opening displacement δ , and the J -integral. Underlying each of these theories is the assumption that fracture will occur once a critical value of the applicable parameter is achieved. The symbol for this parameter is given a subscript c to represent the critical value. Of the theories mentioned, the energy release rate was the first to be developed, based on the early work of Griffith.

1.3.1 Energy Release Rate

Griffith (1920) reasoned that crack extension of a small increment da would occur at the tip of a crack of length $2a$ when the total energy E of the cracked body is decreased by the extension, i.e.

$$\frac{dE}{da} < 0 \quad (1.23)$$

Considering the case of a cracked plate of thickness B under a load P , the total energy E of the system is composed of the elastic energy U contained in the plate, the work P performed by the external force and the energy W for crack formation. The Griffith condition of equation (1.23) can be written as the condition for neutral

equilibrium:

$$\frac{d(U-P+W)}{da} = 0 \quad (1.24)$$

or $\frac{d(F-U)}{da} = \frac{dW}{da}$

The left side of the second equation (1.24) represents the energy tending to extend the crack and, since it has dimensions of force per unit length, is often called the crack extension force. The right side of equation (1.24) reflects the energy opposing crack extension -- the crack resistance force.

Boyd (1972) provides an excellent review of Griffith's evaluation of the terms in equation (1.24). Griffith considered the particular problem of the fracture of glass. He assumed that glass fractured so quickly that there was no time for external energy to be applied, so that $dP/da=0$. Since glass is a very brittle substance which he considered unable to deform plastically, he set the energy for crack formation, dW/da , equal to twice the surface energy γ (since two new surfaces are formed when the crack extends) such that $dW/da=2\gamma$.

The term dW/da is the elastic strain energy released by unit extension of the crack. For example, the area under the elastic portion of a stress-strain curve gives the elastic strain energy per unit volume for a given amount of strain. This area is proportional to σ^2/E where σ is the applied stress and E is the elastic modulus.

Therefore, one would expect

$$\frac{dU}{da} = \frac{\sigma^2}{2} \quad (1.25)$$

Griffith used a solution derived by Inglis for the stress field in the vicinity of an elliptical hole in an infinite, thin lamina. The result was

$$\frac{dU}{da} = \frac{-2\pi\sigma^2e}{z} \quad (1.26)$$

Returning to equation (1.24) and substituting for each term gives

$$\frac{2\pi\sigma^2e}{z} = 4\gamma \quad (1.27)$$

This equation represents a crack that is on the threshold of instability. Griffith then solved this equation for the critical value of stress σ_c remote from the crack for which the crack would extend, giving

$$\sigma_c = \left[\frac{2E\gamma}{\pi a} \right]^{1/2} \quad (1.28)$$

This equation gave Griffith satisfactory predictions for the fracture stress of brittle glass but involved quite a few assumptions. A major one is that the energy for crack formation term dW/da is just the surface energy of the new crack faces. Irwin (1948) recognized the importance of Griffith's equation but realized that in a metal, crack extension requires energy for new surfaces plus energy for plastic

deformation as the crack tip plastic zone advances. Therefore, the Griffith equation (1.28) becomes

$$\sigma_c = \left[\frac{2E(\gamma + \gamma_p)}{\gamma a} \right]^{1/2} \quad (1.29)$$

The plastic work energy γ_p is considered to be much larger than the surface energy term γ and so the latter is normally neglected for metals. Irwin then denoted by G the total work per unit area of crack extension $dW/da=G$ which includes the theoretical surface energy and the work absorbed in causing plastic flow during fracture. Equation (1.29) can be rewritten

$$\sigma_c = \left[\frac{2Gc}{\gamma a} \right]^{1/2} \quad (1.30)$$

Strictly speaking, this equation is only correct precisely at the moment of crack extension where

$$G_c = \frac{dW}{da} = \frac{-dU}{da} \quad (1.31)$$

However, G has come to represent the energy release rate (or energy absorption rate) in general so that for a plate of thickness B

$$G = -\frac{1}{B} \frac{dU}{da} \quad (1.32)$$

The use of G as a fracture criterion is depicted in fig. 1.9. By assuming that the crack growth resistance R is independent of crack size, rearranging equation (1.30) for the general case of plane strain gives

$$G = \frac{(1-v^2)\sigma^2 a}{2} \quad (1.33)$$

Thus for a given crack length fracture will occur when $G > G_c = R$. The two G lines shown represent two crack lengths where $a_2 > a_1$. The slope of the G line for crack length a_2 is smaller than for a_1 indicating a smaller critical stress required for the longer crack. Thus G_c can be regarded as a material property. In order to use G in design, it is necessary to calculate G for a particular configuration. Broek (1978) shows that for a plate of thickness B under a load P , the energy release rate is given by

$$G = \frac{P^2 \Delta C}{2B \Delta a} \quad (1.34)$$

where $\Delta C/\Delta a$ represents the change in compliance of the plate per unit crack extension. The critical value of G in plane strain (labelled G_{lc}) can be found experimentally for a particular material in such a configuration, and the value of G calculated from any other configuration can be compared to this material parameter G_{lc} . The energy release rate G has the units of work per unit area of new crack surface, equivalent dimensionally to force per unit length of crack front giving rise to the term crack extension force.

Thus, although many assumptions are involved, the energy approach produces a fracture criterion in the form of a critical energy release rate. This result leads directly to the critical stress intensity criterion.

1.3.2 Stress Intensity Factor

The stress intensity factor K as given in equations (1.3) and (1.4) is the most commonly used macroscopic fracture parameter. Substituting equation (1.3) into equation (1.33) gives

$$G = \frac{(1-v^2)K^2}{E} \quad \text{plane strain} \quad (1.35)$$

$$G = \frac{K^2}{E} \quad \text{plane stress}$$

If there is a critical plane strain energy release rate G_{Ic} , there is also a corresponding critical plane strain stress intensity factor. K_{Ic} is defined for plane strain rather than plane stress because the critical stress intensity for crack extension K_c varies with thickness as shown in fig. 1.10. After an initial sharp increase with thickness for very thin sheets (3<2mm for 7075-T6 Al), the K_c decreases with thickness to a limiting value, K_{Ic} . This is due to the increase in constraint referred to in Section 1.2.1. When defined in this way, K_{Ic} represents the worst case condition for a particular material and so can be taken as a material parameter. Thus, K_{Ic} is defined as the plane strain fracture toughness. Unfortunately, this is somewhat of a misnomer since K_{Ic} is based on G which is defined as the elastic energy release rate. However, K_{Ic} is still considered a valid material parameter and fracture criterion as long as the plastic zone at the crack tip is small in relation to the crack length and dimensions of the test piece. Specific limitations on this small scale yielding requirement will be considered in Chapter 2.

The fracture criteria discussed so far are based on linear elastic fracture mechanics and can be applied only when the small scale yielding conditions apply. Thus G_{Ic} and K_{Ic} give satisfactory results for the fracture toughness of inherently brittle materials and ones with high yield strengths. However, structural steels and aluminium alloys often have low strength and high toughness which imply plasticity before fracture. In these materials LEFM assumptions no longer apply, and the goal is to develop suitable elastic-plastic fracture criteria.

1.3.3 Crack Opening Displacement

The need for a fracture parameter that would allow for large amounts of plasticity and yet would be related to the energy and stress intensity concepts resulted in the crack opening displacement (COD) approach. This approach assumes that fracture will occur when the local stress-strain conditions in the region close to the crack tip exceed some critical value that is a function of the material properties. Wells (1962) proposed that the crack opening displacement is a measure of the work done in extending the crack. He also pointed out that the COD could be related directly to G and K when LEFM conditions apply. This follows from the Dugdale model mentioned previously (Dugdale, 1960) and is shown in fig. 1.6. Burdekin and Stone (1966) point out that the separation of the crack faces at the tip of a Dugdale crack is given by

$$\text{COD} = \delta = \frac{8\sigma_y a}{\pi E} \ln \frac{r_0}{2\sigma_y} \quad (1.36)$$

where σ is the remotely applied tensile stress. When σ is small compared to σ_y , the COD can be approximated (using equation (1.33)) by

$$\frac{\delta}{\delta \sigma_y} = \frac{\sigma^2}{E \sigma_y} = \frac{G_1}{\sigma_y} \quad (1.37)$$

Therefore,

$$G = \delta \sigma_y = \frac{\sigma^2 (1 - \nu^2)}{E} \quad (1.38)$$

Thus when LEFM conditions apply, the critical COD is equivalent to a critical G or K . However, COD was developed as a candidate for a fracture parameter to be applied when there is considerable plasticity; its validity as such depends on the critical COD being a unique characterization of the fracture resistance of any particular ductile material. Unfortunately, experimental determination of COD is extremely difficult both to perform and to standardize. For example, there is no widely accepted precise definition for the position within the crack where the COD should be measured. Much of the literature now refers to CTOD, for crack tip opening displacement, presumably to distinguish the tip displacement from displacement elsewhere along the crack, e.g. the load line. For tough materials, there is also the problem of slow stable crack growth making definition of the precise moment of crack extension difficult. Also, application of a critical CTOD for a particular design structure causes problems because a fracture stress or a critical crack size cannot be calculated directly. It seems that the major utility of a critical CTOD is as an empirical value which provides a relative measure of toughness.

Since the COD approach does not generally qualify as an

elastic-plastic fracture criterion, much attention has been given to the J-integral.

1.3.4 The J-integral

The G_{lc} and K_{lc} fracture criteria are strictly valid only for LEFM, but they are useful also when strict requirements are placed on the amount of plasticity (small scale yielding). For many structural metals, dimensions of test specimens must be prohibitively large to obtain a valid K_{lc} . The J-integral as defined by Rice (1968) has been regarded as an elastic-plastic fracture parameter that will accommodate larger plasticity and thus allow determination of J_{lc} from relatively small specimens.

Rice (1968) defined a two dimensional energy line integral as follows (fig. 1.11)

$$J = \int_{\Gamma} \left(W dy - T \frac{\partial u}{\partial x} ds \right) \quad (1.39)$$

where W = strain energy density = $\int \sigma_{ij} \epsilon_{ij} dV$

T = traction vector perpendicular to the line

u = displacement in the X direction

ds = an element of the line

Γ = the closed contour followed counterclockwise

Rice (1968) showed that the line integral is path independent on a contour around a crack tip and that under LEFM conditions

$$J = G = -\frac{1}{B} \frac{\partial U}{\partial a} \quad (1.40)$$

Although J was originally developed for non-linear elastic materials, the concept has been extended to elastic-plastic materials and demonstrated to be valid where deformation theory of plasticity is valid (Rice, 1968b). Dowling and Begley (1976) point out that in the energy definition of J (equation 1.40) for elastic-plastic materials the quantity U is no longer the potential energy but rather the elastic-plastic work necessary to deflect the specimen. Thus, J can not be interpreted as the potential energy available for crack extension. However, J does have physical significance because it is a measure of the characteristic crack tip stress field (Begley and Landes, 1972) and is thus usable as a geometry-independent static fracture toughness criterion.

Before considering the experimental measurement of J , the relationship between J and the previously discussed fracture criteria will be presented. From equations (1.40) and (1.38)

$$J = G = \frac{\sigma_y \delta}{\frac{1-v^2}{E}} \quad (1.41)$$

These equations strictly apply only under LEFM conditions and at the critical value of each parameter at the onset of crack extension.

The experimental determination of J is based not on the line integral definition but on the energy rate definition. Clarke et al. (1979) have developed a procedure for determining ductile fracture toughness using the J -integral. Their procedure is based on an analysis by Rice, Paris and Merkle (1973) which showed that J can be estimated for a deeply cracked bend specimen from the load-displacement record by

$$\frac{J = 2A}{Bb}$$

(1.42)

where A is the area under the load versus load point displacement curve and b is the uncracked ligament length (B is the thickness). Clarke and Landes (1979) have extended this formula to include compact tension specimens, and this technique will be covered in detail in Chapter 2. However, the result is a plot of experimental points for J against crack extension da as shown in fig. 1.12. J_{lc} is determined from the intersection of the best fit line and the crack blunting line given by $J=2\sigma_y da$. The slope of the J - da line is a measure of the resistance of the material to continued crack extension. The slope dJ/da has been used to formulate the tearing modulus T defined by Paris et al. (1977) as

$$T = E \frac{dJ}{\sigma_y^2 da} \quad (1.43)$$

A surge of recent work has attempted to characterize different materials using J and T ; a major concern therefore is whether or not J_{lc} and T are in fact material parameters. One approach has been to measure J_{lc} on small specimens for comparison with K_{lc} as determined on thicker specimens using equation (1.41). Logsdon (1976) did this for four rotor forging steels and one cast steel and obtained good agreement. Another approach is to vary specimen geometry, e.g. crack length a , remaining ligament b , thickness B , and to determine if J_{lc} and T in fact remain independent of these variations. Gudas, Joyce and Davis (1979) did this using HY-130 steel. They found that J_{lc} was independent of specimen geometry but that T increased with a/B (where

(
W is specimen width). They felt that the tearing modulus is sensitive to crack tunnelling, which can be decreased by face grooving the specimen. Druce (1981) performed similar tests on C-Mn steel and found that the initiation of ductile cracking and the slope of the J resistance curve are geometry dependant. However, he felt that if the remaining ligament b and the specimen thickness B were large enough ($b > 60J/\sigma_y$ and $B > 90J/\sigma_y$), then a material characterizing value of these parameters could be obtained.

(
Despite some mixed results on their validity as material parameters, J_{Ic} and to a lesser extent T have gained widespread acceptance for the characterization of ductile fracture for aleastic-plastic materials. Since J was developed initially for non-linear elastic conditions and then extended using the deformation theory of plasticity which does not allow for any unloading, J should only be used for crack initiation and small amounts of crack extension. The assumptions in the derivation of J have been subjected to considerable abuse by some investigators who use J to characterize quite large amounts of crack extension (Abou-Sayed et al., 1981). However, their investigations are partially defensible on the grounds that these empirical results correlate well with anticipated behaviour.

(
Many other quantities have been proposed as fracture criteria such as strain energy density (Gerberich, 1964), stretch zone width (Kobayashi et al., 1979) and work to fracture (Stuve, 1980). Since many of the proposed models seek to determine critical parameters and their interaction with specific microstructural features, e.g. second phase particles, grain size, voids, slip distribution etc., the next section will address some major effects of microstructure on the

fracture process.

1.4 Microstructural Effects on Fracture Mechanics

At present no systematic, generally accepted method exists for determining the effect of microstructure on crack propagation and fracture, due mainly to the great variety of microstructures in metallic materials. Thus, it is not always possible to describe the microstructure accurately. However, a great number of empirical results have been formulated concerning the effect of microstructure on crack propagation properties. Schwalbe (1977) provides an excellent survey of some of these results. Before considering the effects of particular microstructural features, common crack propagation mechanisms will be examined.

1.4.1 Crack Propagation Mechanisms

As a means of reviewing results on microstructural effects, Schwalbe (1977) introduced the commonly encountered microstructures of polycrystalline metallic materials, shown in figure 1.13. The five major types of microstructure are (a) single phase, polycrystalline metallic material; (b) two phase material, β in α ; (c) two phase material, β in α with approximately equal volume content; (d) second phase particles along the grain boundaries of the first phase; and (e) continuous network of the second phase along the grain boundaries of the first phase. For these types of microstructure, Schwalbe listed ten potential crack propagation mechanisms, shown in figure 1.14 as:

- a) cleavage crack propagation

- b) dimple fracture due to coarse particles
- c) dimple fracture due to fine particles
- d) dimple fracture due to coarse and fine particles
- e) intergranular crack propagation due to grain boundary precipitates
- f) intergranular crack propagation due to a hard phase grain boundary film
- g) intergranular crack propagation due to a soft phase grain boundary film
- h) crack propagation by slip plane/slip plane interaction
- i) crack propagation by slip plane/grain boundary interaction
- j) crack propagation solely by plastic blunting

Such a relatively large number of potential mechanisms highlights the problem of modelling crack propagation since each mechanism may in turn depend on a different local parameter for operation. Also, the model is further complicated by metals in which cracks propagate due to several of the above mechanisms in competition. Despite the difficulties some general comments can be made. Low temperature, high deformation rate and a triaxial stress state can cause low and medium strength steels to fracture by the low energy cleavage mechanism (figure 1.14(a)). A cleavage crack is considered to initiate at dislocation pile-ups (Tetelman and McEvily, 1967) when several dislocations at the head of the pile-up coalesce. This cleavage crack then propagates due to the stress concentration at the pile-up whenever the tensile stress on a plane normal to the slip plane reaches the ideal fracture stress (Honeycombe, 1968, pg.430). Thus the extent of dislocation movement prior to propagation of the crack can

be fairly small; this mechanism represents the lowest fracture toughness.

1.4.2 Effect of Particles

Mechanisms (b), (c) and (d) in figure 1.14 illustrate ductile crack propagation due to rupture around second phase particles. The large second phase particles in (b) and (d), usually called inclusions, are caused by impurities. Such inclusions do not contribute significantly to the material's strength. The fine particles in mechanisms (c) and (d) can be either large precipitates or dispersoids. The resultant dimple formation mechanism around such second phase particles is illustrated schematically in figure 1.15. As the component is loaded, the crack tip blunts. Large plastic strains at the tip cause second phase particles either to crack or to decohere at the particle-matrix interface, depending upon the strength, size, and shape of the particles and the interface strength. The voids thus formed then grow until they coalesce either with each other or with the crack tip. If each particle in the crack plane either cracks or voids, then the dimple size would correspond to the particle spacing. Broek (1972), after examining the fracture surfaces and microstructure of 13 aluminium alloys, found that ductile rupture was initiated at small inclusions and that the average dimple spacing was equal to the average inclusion distance. He concluded that void initiation is followed immediately by spontaneous growth and coalescence. Therefore void initiation is the critical event in ductile fracture. His conclusion implies that more particles will yield more void nucleation sites and thus reduce toughness. This reduction in fracture toughness

with inclusion content (shown in figure 1.16) is also suggested by other investigators. Hahn and Rosenfield (1973) found that K_{Ic} varied with $f_c^{-1/6}$ where f_c is the volume fraction of cracked particles. They proposed an equation for K_{Ic} as

$$K_{Ic} = \left[2\sigma_y E \left(\frac{\pi}{6} \right)^{1/3} D \right]^{1/2} f_c^{-1/6} \quad (1.44)$$

where D is the particle diameter. This expression is based on previous work by Rice and Johnson (1970), whose proposed model for hole growth at a blunting crack tip assumes that crack growth occurs by coalescence of the void with the crack tip. Later, Van de Kastele and Broek (1977) investigated the failure of large second phase particles in 7075-T651 aluminium alloy, using this model. However, they subsequently modified it because they found that the ligament between large particles failed by the initiation and growth of voids at much smaller particles. Thus, they observed the ductile fracture mechanism in figure 1.14(d) and obtained

$$K_{Ic} = f^{-1/4} \quad (1.45)$$

Van de Kastele and Broek eventually concluded that both spacing and volume fraction of large particles are important to toughness and that the failure of particles is dictated by the maximum principal stress.

Referring again to figure 1.14(b), (c) and (d), Schwalbe (1977) compared these three propagation mechanisms according to the size of particles active in dimple formation and relative toughness as follows: mechanism (b) — large particles active, low toughness; mechanism (c) — small particles active, high toughness; mechanism (d)

-- Both types of particles active, even lower toughness than for mechanism (b) since the small particles reduce the ductility of the ligaments between the large particles.

Although the majority of experimental evidence shows that toughness decreases with increase in volume fraction of particles, Dunwoody, Moore and Thomas (1973) achieved an increase in toughness by adding particles to an Al-Mg-Si alloy. One possible explanation for this increase is the effect of small incoherent particles on slip distribution.

1.4.3 Effect of Slip Distribution

Hornbogen and Zum Gahr (1975) examined the distribution of plastic strain in alloys containing small particles. Their model of a given amount of plastic strain which can be distributed either homogeneously or heterogeneously within a crystal volume is shown in figure 1.17. Fig. 1.17(a) defines the macroscopic shear strain ϕ , and figs. 1.17(b), (c) and (d) illustrate three ways in which different slip distributions can provide ϕ . Figs. 1.17(b) and (c) depict the extreme examples of heterogeneous and homogeneous slip distributions, respectively. In fig. 1.17(d) the shear strain is provided by localized slip in a band of width B with the slip band spacing being A . This distribution corresponds to a situation intermediate between figures 1.17(b) and (c) in terms of slip heterogeneity.

Hornbogen and Zum Gahr (1975) list several micro-structural features that are expected to effect strain distribution. Coarse slip is favoured by:

1 low stacking fault energy

- 2 sheared precipitate particles
- 3 short range order
- 4 radiation damage and holes
- 5 few slip systems operating
- 6 emisary dislocations
- 7 large grain size

Fine slip is favoured by:

- 1 high stacking fault energy
- 2 by-passed particles
- 3 dislocation forest
- 4 dislocation climb
- 5 many slip systems operating
- 6 small grain size

Martin and Edwards (1980) discussed slip distribution in particle hardened alloys. Above a certain critical particle diameter d_c , dislocation-particle interactions will form Orowan loops. On further straining dislocation debris accumulates around the particle, the slip plane work hardens, and other slip planes become active, thus causing more homogeneous slip. When the average particle diameter is less than d_c the particles are sheared. The first dislocation cutting such a particle causes it to shear by an amount equal to the Burgers vector so that the effective cross-section of the particle is reduced. Subsequent dislocations from the same source will encounter an effectively softer particle, which is again sheared; the slip plane is thus progressively softened. Slip distribution in this type of crystal tends to be heterogeneous because there is less tendency to activate

additional slip planes.

The shear yield stress, τ_y , of a crystal containing a volume fraction f of particles of diameter d which are sheared by the dislocations at yield is usually given (Martin, 1980) by an equation of the form

$$\tau_y = Cf^{1/2}d^{1/2} \quad (1.46)$$

where C is a constant whose value depends upon the hardening mechanism being considered. If a dislocations of Burgers vector b shear a given particle, assuming for simplicity that the particles are sheared across a diameter, then the stress for further shear becomes

$$\begin{aligned} \tau_y &= Cf^{1/2}(d-nb)^{1/2} \\ &= Cf^{1/2}d^{1/2}(1-nb/d)^{1/2} \end{aligned} \quad (1.47)$$

The tendency to produce heterogeneous slip will be more pronounced the more τ decreases by the passage of one dislocation, i.e.

$$\frac{d\tau}{dn} = \frac{-bCf^{1/2}}{2d^{1/2}(1-nb/d)^{3/2}} \quad (1.48)$$

This expression indicates that the tendency for coarse slip is more pronounced the higher the volume fraction of particles, the higher the value of C and the smaller the diameter of the particles.

Several ways to obtain a more homogeneous slip distribution based on the above results are feasible: Overageing an age hardenable alloy causes the precipitate particles to become large and incoherent. When a highly overaged specimen with a polished surface is deformed, the surface then contains a large number of small slip steps that are

homogeneously distributed. A disadvantage of this method of slip homogenization is the corresponding decrease in yield strength associated with overageing. A preferable method of slip homogenization uses a duplex ageing heat treatment to form a bimodal precipitate distribution consisting of a finely dispersed coherent phase plus a distribution of incoherent particles. The finely dispersed coherent phase provides a high yield stress while the incoherent particles homogenize the slip distribution. Although this duplex ageing heat treatment technique is not widely used, it does suggest yet another method which is widely encountered in industrial age-hardenable alloys, that of dispersoid addition.

There are three types of particles present in aged commercial heat-treatable aluminium alloys:

- 1 Fine coherent or semi-coherent precipitate particles which are the source of strengthening.
- 2 Coarse particles ($D > 1\mu\text{m}$) called inclusions that originate during casting and are linked to the iron impurity content of the alloy.
- 3 Fine incoherent particles ($D = 0.1\mu\text{m}$) called dispersoids which are intermetallic phases arising from the addition of transition elements.

Dispersoids are empirically added to these commercial aluminium alloys to inhibit grain growth during heat treatment. Dowling and Martin (1973) showed that these dispersoids promote the homogenization of slip.

Lutjering (1976) did extensive work on the slip distribution and mechanical properties of metallic materials. In general, he found that

the mechanical properties of materials with inhomogeneous slip are substantially inferior to those of corresponding materials with a homogeneous slip distribution. In considering the mechanisms of crack nucleation and propagation as a function of slip distribution, Lutjering observed that in a material with a homogeneous slip distribution the fracture mechanism is determined by the presence and distribution of hard incoherent particles. However, when slip is inhomogeneously distributed, crack nucleation is determined by the reaction of slip bands with the test piece surface, with other slip bands, and with the grain boundaries. Depending on the degree of inhomogeneity of the slip distribution, cracks may propagate through the matrix, along the grain boundaries, or along the slip bands.

Following this review of slip distribution, another factor which effects fracture mechanisms will be considered -- the grain size.

1.4.4 Effect of Grain Size

A major problem in experimentally assessing the effect of grain size on fracture is that it is very difficult to vary grain size without effecting other potentially significant parameters such as yield strength, width or total amount of grain boundary precipitate free zones, amount of grain boundary precipitate, and so on. It seems probable that the grain size would effect all the intergranular crack propagation mechanisms shown in figure 1.14 (i.e. (e), (f), (g) and (i)). Hornbogen (1975) developed a model for the grain size dependence of fracture toughness of precipitate hardened alloys for instances where plastic deformation is confined to small planar portions (such as the precipitate free zone or planar slip bands). By assuming a

local critical strain for crack propagation, Hornbogen arrived at the relation

$$K_{Ic} = \text{ad}^{-1/2} \quad (1.49)$$

where a is a constant and d is the grain size. This reciprocal square root relationship was found to be reasonably well observed for a precipitation hardened 7075 aluminium alloy.

Since ductility measured in a tensile test and fracture toughness often show the same trends, and since tensile ductility exhibits a $1/d$ dependence, K_{Ic} should increase with decreasing grain size (Schwalbe, 1977). Thompson and Zinkham (1975) found this effect on plane stress fracture toughness data on overaged 7000 series aluminium alloys with various grain sizes (see figure 1.18). For intergranular fracture along a precipitate free zone (PFZ), the grain size effect can be explained by the increase in volume fraction of PFZ with decreasing grain size, thus decreasing the average local strain in the PFZ. In the case of slip plane decohesion (figure 1.14(h)), the grain size controls the number of dislocations on the slip plane; here a smaller grain size means a less severe slip plane/slip plane interaction.

Although other microstructural features can affect fracture mechanisms, we will now focus on the region where these microstructural features are important - the crack tip plastic zone.

1.5 Crack Tip Plastic Zone

Considerable research has been directed at determining the size and shape of the crack tip plastic zone. Much of the interest in this crack tip region has been due to its perceived importance in

correlating microstructural features to macroscopic fracture toughness parameters. This region has become the focus of microstructural models which seek to define critical local fracture criteria, such as stress or strain, in terms of the overall fracture process. Before considering experimental methods of determining the crack tip plastic zone size and shape, important aspects of stress and strain variation within the plastic zone warrant a review.

1.5.1 Stresses in the Plastic Zone

For the theoretical crack tip stress field under LEFM assumptions, presented in Section 1.2.1, the $r^{-1/2}$ dependence of near tip stresses predicts infinite stresses at $r=0$. In engineering materials, however, these stresses do not become infinite because plasticity causes stress redistribution.

Boyd (1972) described the three dimensional stress system for the case of an edge-notched, semi-infinite plate of finite thickness subjected to Mode I loading. His presentation was based on three dimensional photoelastic experiments by Dixon (1966). The variations in σ_{xx} , σ_{yy} and σ_{zz} (shown in figure 1.19) follow:

σ_{yy} -The stress parallel to the applied loading (fig. 1.19a) is a maximum slightly ahead of the notch root, diminishing rapidly until it is equal to the applied stress remote from the notch. This stress is larger on the midplane of the plate than at the surface and is limited at the notch root by yielding of the material.

σ_{xx} -The stress perpendicular to and in the plane of the notch (figure 1.19b) is zero at the notch root but increases rapidly to a maximum near σ_{yy} . It then decreases rapidly, becoming approximately

$1/3 \sigma_{yy}$ at large distances from the notch root. This stress is also largest on the midplane.

σ_{zz} -The stress in the thickness direction (figure 1.19c and d) is zero at the plate surfaces but increases rapidly toward the midplane, where it is equal to $v(\sigma_{xx} + \sigma_{yy})$ in thick plate but less in thin plate (where v is Poisson's ratio).

The octahedral shear stress is given by

$$\sigma_{oct} = \frac{1}{3} \sqrt{(\sigma_{xx} - \sigma_{yy})^2 + (\sigma_{yy} - \sigma_{zz})^2 + (\sigma_{zz} - \sigma_{xx})^2} \quad (1.50)$$

This octahedral shear stress is highest at the plate surfaces and at the immediate notch root where either σ_{xx} or σ_{zz} (or both) are zero. This suggests that fracture mechanisms controlled by a critical maximum shear stress will occur first at these locations.

The mean stress is given by

$$\sigma_m = \frac{1}{3}(\sigma_1 + \sigma_2 + \sigma_3) \quad (1.51)$$

where σ_1 , σ_2 and σ_3 are principal stresses.

Taking the x, y, and z axes as the principal directions, it can be seen from figure 1.19 that σ_{xx} , σ_{yy} and σ_{zz} all have their maxima at the midplane and that the maximum σ_m will occur at some small distance ahead of the notch on the midplane. Boyd (1972) suggests that fracture mechanisms which are controlled by a maximum normal tensile stress will occur at a critical volume dilatation given by

$$\delta V_c = \frac{1-2v}{E} (\sigma_{xx} + \sigma_{yy} + \sigma_{zz}) \quad (1.52)$$

Thus in a region at the midplane a short distance from the notch root the volume dilatation is a maximum and the octahedral shear stress a minimum. Boyd calls this region a decohesion enclave where fracture mechanisms that favour a critical normal stress will operate. One might thus expect differences in crack initiation stress and position for different crack extension mechanisms.

This emphasis on stress state resembles that of Mackenzie, Hancock and Brown (1977) who investigated the effect of stress state on the effective plastic strain necessary to initiate ductile fracture in high strength steels. They used a nondimensional parameter $\sigma_n/\bar{\sigma}$ for stress triaxiality, where σ_n is defined by equation (1.51) and $\bar{\sigma}$, the effective stress, is defined by

$$\bar{\sigma} = \sqrt{2} \sqrt{\frac{(\sigma_1 - \sigma_2)^2 + (\sigma_2 - \sigma_3)^2 + (\sigma_3 - \sigma_1)^2}{2}} \quad (1.53)$$

Using results from Bridgman (1952) for stress and strain states in necked tensile specimens, Mackenzie et al. determined the failure initiation strain as a function of stress triaxiality for their materials. Next they used an analysis by Rice and Johnson (1970) for the stress and strain distributions in the region of a blunting crack tip; they could then infer that there is a critical material size parameter or characteristic length over which a critical strain must act for fracture initiation. Although a great many assumptions and approximations vitiate this analysis, the result is particularly attractive from the view of explaining ductile fracture toughness values in terms of a microstructurally determined critical length at the crack tip. Ritchie, Server and Muller (1979) extended the results of Mackenzie et al. (1977) to apply them to the upper shelf

toughness of two nuclear pressure vessel steels. Ritchie et al. also depict ductile fracture as being strain induced due to crack growth by linking of voids when some critical strain is exceeded ahead of the crack tip. However, this critical strain must be exceeded over a minimum volume which is characteristic of the scale of physical events involved in the material. This they call the stress modified strain model where l_0^* is the microstructurally significant characteristic distance. While pointing out that l_0^* is an empirical quantity, presumably related to microstructural aspects of fracture initiation, Ritchie et al. nevertheless regard the characteristic distance for ductile fracture as reflecting the spacing between particles nucleating major voids as well as the critical number of voids which coalesce with the main crack at the initiation of crack growth.

1.3.2 Strains in the Plastic Zone

There have been various attempts to derive the manner in which strain varies with distance r ahead of the crack tip. The LEFM analysis for displacements in front of the crack gives analogous results to the stresses discussed in Section 1.2.1 in that the strain in the y -direction ϵ_y is proportional to $r^{-1/2}$. Hutchinson (1968) developed a relationship between the plastic strain ϵ_p , the distance r and the work hardening exponent N as

$$\epsilon_p = \frac{1}{r^{\frac{N}{N+1}}} \quad (1.34)$$

However, Rice and Rosengren (1968) used the slightly different form

$$c_p = \frac{1}{\frac{1}{N+1} - \frac{1}{r}} \quad (1.55)$$

Both of these forms reduce to the LEFM result when N equals unity.

Perhaps a more realistic analysis was made by Rice and Johnson (1970) in their widely referenced work on the stress and deformation fields near a crack tip undergoing large geometry changes in elastic-plastic materials. They applied slip line field theory to a progressively blunting crack tip using a numerical analysis to obtain a plot of the true strain distribution as a function of (X/δ_t) . Here X represents the distance of a material point in front of the crack tip before deformation, and δ_t is the crack tip opening displacement for both small scale yielding and fully plastic conditions (see fig. 1.21). Although Rice and Johnson do not offer the equation for these curves, Schwalbe (1977) states that this strain distribution can be approximated by

$$\epsilon_y = 0.44 \frac{\delta_t}{X} - 0.23 \quad (1.56)$$

Rice and Johnson use this derived plastic strain distribution to develop a model for fracture by ductile void growth at a crack tip where X_0 is the distance over which some critical fracture strain must be achieved. They suggest that X_0 might be identified with a grain size or a mean spacing of large second-phase inclusions responsible for ductile fracture.

Prince (1977) studied crack propagation in Al-Mg-Si alloys and

found that they failed in a predominantly intergranular manner along the grain boundary PFZ . Prince and Martin (1979) presented a model for this intergranular crack propagation in terms of the slip distribution and a critical local fracture strain ϵ_{lf} at the grain boundary. A schematic diagram of the proposed local plastic strain and the macroscopic plastic strain ahead of the crack is shown in figure 1.20. The macroscopic strain, the strain averaged over distances larger than the slip band spacing, is shown to decrease linearly with distance ahead of the crack. The actual rate of decrease will be determined by the stress field ahead of the crack and by the work hardening characteristics of the material. The local strain ϵ_l is shown to fluctuate around the macroscopic strain ϵ_m by an amount proportional to the slip band spacing and the macroscopic strain such that

$$\epsilon_l = k_1 d \Delta b \epsilon_m \quad (1.57)$$

where k_1 is a constant, d is the grain size and Δb is the mean planar spacing of dispersoids, a spacing proportional to the slip band spacing. If the critical local fracture strain ϵ_{lf} is constant, eq. (1.57) can be used to show that as Δb is reduced by increasing the volume fraction of dispersoids the macroscopic strain ϵ_m must necessarily increase to attain the critical local plastic strain. In other words, the dispersoids homogenize the slip distribution so that a higher strain must be applied to achieve a given local strain.

The models that seek to relate microstructure to fracture toughness rely on the analytical results for stresses, strains and plastic zone dimensions previously discussed; therefore much experimental work has been done in attempts to verify the analytical results.

1.5.3 Experimental Determination of Plastic Zone Size

It is difficult to compare experimental determinations of crack tip plastic zone size because of the wide range of techniques used and the many experimental variables involved. A list of references including technique, material and type zone measured (plane stress or plane strain) is given in Table 1.1.

Many techniques, such as stereo-imaging, photoelectron microscopy, grids, brittle lacquer, etc., must be employed on a free surface. Although potentially useful when comparing plastic zones in plane stress conditions, these techniques are not applicable to plane strain, an area of considerably more interest with regard to fracture criteria. Further, the few techniques that are applicable to plane strain conditions are usually severely limited in some way.

To measure plane strain plastic zones, it is necessary to test a specimen thick enough to obtain plane strain constraint on the midplane and then to section the specimen to expose the plane perpendicular to the crack. Hahn, Hoagland and Rosenfield (1972) used Pry's reagent to etch the plastic zone in low carbon steel, but this technique is only applicable to this type of material. Recrystallization (Shoji, 1976) and precipitation on dislocations (Clavel et al., 1975) are also limited to a small range of materials. Transmission electron microscopy can be used to measure dislocation density at precise points around a crack tip, but this method is very time consuming and requires destruction of the specimen. X-ray microbeam techniques have limited sensitivity due to a several hundred micron thickness probe size. Microhardness tests also have limited sensitivity and are suitable only for materials that strongly work

harden or work soften.

Prince (1977) effectively used electron channelling patterns (ECPs) described by Stickler and Booker (1971), a technique also successfully employed by other investigators (Davidson and Lyle, 1975; Davidson and Lankford, 1976; Lankford and Davidson, 1976; Davidson et al., 1976). The theory of the resulting ECP has been given elsewhere (Spencer, 1974). The method will be covered in more detail in Chapter 2. However, briefly, the procedure involves rocking the collimated electron beam in the scanning electron microscope (SEM) about a point (~ 10 μ m diameter) on the specimen surface. The ECP is a pattern of lines that results from the interaction of the collimated beam and the crystal structure. Since the quality of the ECP depends on the perfection of the crystal lattice, deformation causes systematic degradation in the resulting ECP. The crack tip plastic zone size is determined by examining numerous small volumes of material with the electron beam. The strain in each resulting ECP can then be derived by comparison with ECPs from a calibration specimen. Some advantages of the ECP method of plastic zone measurement are:

- 1 Information comes from a small interaction volume of material which depends on the area of the electron beam on the specimen surface and the accelerating voltage. This area can be kept quite small, as shown by Joy and Newbury (1972) who obtained a selected area of 1 μ m diameter.
- 2 The specimen is not destroyed. Therefore, repeat measurements can be made to verify results.
- 3 Sensitivity is fairly good since relatively small strains cause detectable deterioration of the ECP. In theory, ECP line widths can be compared to those from tensile specimens at known

strains. Stickler and Booker (1971) obtained a good correlation between line width and strain over the range 0.03 to 0.20 tensile strain.

The method is applicable to plane strain plastic zone measurements and can be used on any crystalline material that will give good quality channelling patterns, e.g. nickel, aluminium, copper, lead, silicon and low carbon and stainless steel.

There are also some limitations on the method: The dislocation density in the undeformed material around the plastic zone must be low enough for a good quality ECP. Further, the grain size should be larger than the selected area size so the entire ECP can be obtained from a single grain. Finally, the material must be receptive to electropolishing. Despite these restrictions, the ECP method of plastic zone measurement has proved effective and has been shown (Davidson et al., 1976) to correlate well with other techniques.

The crack tip plastic zone has been the focus of much of the preceding discussion because it promises to provide a measurable link between macroscopic fracture mechanics parameters and microstructural models. With this discussion as background, the approach taken to relate these can now be outlined.

Table 1.1

Some Experimental Plastic Zone Size References

Reference	Measurement Technique	State of Stress	Material
Bethais (1977)	microhardness	Pe	316 stainless
Bethais & Pelloux (1973)	microhardness	Pe	16-13 stainless
Baxter & Rouze (1976)	photostimulated electron emission	Pe	1018 steel 1065 steel
Chanani (1977)	optical interference	Pe	2024-T3 Al 2024-T8 Al 7075-T6 Al
Clavel et al. (1975)	etching	Pa, Pe	INCO 718
Davidson & Lenkford (1976)	ECP, replication	Pe	6061-T6 Al Pe-351 304 stainless
Davidson et al. (1976)	ECP	Pe	low carbon steel
Hahn et al. (1972)	etching	Pa, Pe,	Pe-351
Inoue (1976)	recrystallization	Pe	304 stainless
Izumi & Fine (1979)	foil strain gauges	Pe	Al-6.3%Cu 7075-T76 Al 7050-T4 Al 2024-T4 Al 2219-T861 Al 2219-0A Al
Krum & Fine (1980)	foil strain gauges	Pe	HA87 (Al)
Listiere (1976)	XRD	Pe	AU2GN, ACS (Al)
Liu & Ino (1969)	grid	Pe	2024-T3 Al
Petit et al. (1977)	microhardness, slip lines	Pe Pe	AU4 (Al) AU4 (Al)
Petit & Hoepfner (1973)	image distortion	Pe	7075-T6 Al
Pineau & Pelloux (1974)	microhardness	Pe	Pe-34Ni

Purcell & Weertman (1974)	microhardness	Pc	copper
Saxena & Antolovich (1975)	microhardness	Pc	copper Cu-2.2Al Cu-4.2Al Cu-6.3Al
Tschegg et al. (1980)	DB recrystallization	Po	mild steel mild steel
Wilkins & Smith (1970)	TEM	Pc	Al-1/2Mg
Yokobori et al. (1973)	DB, sliplines	Po	low carbon steel

1.6 The Present Work

As previous sections have pointed out, a great deal of uncertainty exists as to the precise manner in which microstructural variables affect macroscopic fracture parameters. In particular, the crack tip plastic processes and their role in determining toughness are unclear. Although large particles or inclusions may seem to be generally detrimental to fracture toughness (Hahn and Rosenfield, 1973), dispersoids were shown to increase toughness in Al-Mg-Si alloys (Dunwoody et al., 1973) and to change the fracture mode from mainly intergranular to at least partly transgranular.

Previous work at Oxford University (Dowling, 1975; Prince, 1977 and Edwards, 1981) investigated the influence of Mn-bearing dispersoid particles on the behaviour of Al-Mg-Si alloys. Published work includes Dowling and Martin (1976) on slip distribution, Dowling and Martin (1977) on tensile fracture processes, Prince and Martin (1977, 1979) on monotonic crack propagation, and Edwards and Martin (1981) on fatigue crack propagation. The present work is proposed to extend

these previous studies and to establish quantitatively and unambiguously the role of microstructure in determining fracture toughness of these alloys.

1.6.1 The Aluminium-Magnesium-Silicon System

The alloy used in the present work has the basic composition Al-0.62Mg-1.02Si. This is a commercial alloy with a good combination of strength, corrosion resistance, extrudability and weldability. Edwards (1981) gave an excellent review of work done on this system which is summarised here. The composition of this alloy was arrived at empirically (Allais and Mercher, 1972) and differs from pseudo-binary Al-Mg₂Si in that it contains an excess of silicon. This excess silicon goes into solution and has the effect of raising the solution temperature of the Mg₂Si phase. As the silicon content is increased the alloy has a higher solute supersaturation after quenching. Thus the volume fraction of the ageing precipitate is increased leading to a finer ageing structure. Some of the excess silicon is also taken up in the intermetallic manganese-bearing phase.

The alloy ageing characteristics were discussed by Dowling (1975). Briefly, the alloy is homogenized, quenched and aged to produce a marked increase in yield strength. GP zones cause the hardening when the ageing is at low temperatures while needle-shaped Mg₂Si precipitates form at higher temperatures. The ageing process is sensitive to the time of holding at room temperature after quenching. Vacancy clusters are formed rapidly at room temperature after quenching, and since these clusters provide nuclei for precipitation at higher temperatures it is necessary to control carefully the hold

time between quenching and ageing.

As discussed by Dowling (1975) some controversy exists over the exact structure of the GP zone hardening phase (β''). Thomas (1961) suggests that it is a FCC superlattice while Jacobs (1972) and Wahl and Von Heimendahl (1974) suggest hexagonal and monoclinic structures respectively.

Like most age hardening systems, the present alloy displays precipitate free zones (PFZ) at the grain boundaries and grain boundary precipitates in the aged condition. Their sizes depend upon homogenizing temperature, quenching conditions and ageing time and temperature. The grain boundary precipitates are believed to be silicon (Thomas, 1961).

In commercial aluminium alloys, manganese is added as a grain refiner and to reduce the susceptibility to intergranular embrittlement (Harris and Varley, 1953; Allais and Mercher, 1972). Iron is also present as an impurity. Iron forms coarse second phase particles which are generally regarded as harmful (Hahn and Rosenfield, 1975). However, it is usually uneconomic to reduce the iron level below about 0.1-0.3wt%. Manganese has the added advantage of changing the morphology of the iron bearing phase from the relatively harmful plates of α -(FeSi)Al to the less harmful script morphology (Chadwick et al., 1953).

Upon casting and rapid solidification of an Al-Mg-Si-Mn alloy, most of the Mg, Si and Mn is retained in supersaturated solid solution. In industrial practice, the alloy is then homogenized. During the homogenization heat treatment, the magnesium and silicon are homogeneously redistributed, but the manganese is precipitated out of solution to form the rod-shaped intermetallic α -Al₁₂Mn₃Si phase

(dispersoids). These dispersoids precipitate quickly but coarsen slowly so that their final size of about 0.1μm is reasonably constant regardless of subsequent heat treatment. The dispersoids cannot be redissolved because of the low solidus (Dowling, 1975). Since the alloy must be homogenized to remove the cast structure, the dispersoids inevitably form then. Toward the end of homogenization, the dispersoids undergo Ostwald ripening, and their size varies as the cube root of time (Dowling, 1975). Thus significant growth would require very long homogenization times.

1.6.2 Fracture Mechanisms in Al-Mg-Si Alloys

Details of the fracture mechanisms in Al-Mg-Si alloys have been under study for a number of years. Chadwick et al. (1953) looked at the addition of Fe, Mn and Cr to the basic alloy and found that all three increased the strength of the alloy. They found that the alloys without Mn and Cr were brittle and fractured intergranularly while ones with Mn and Cr were stronger, more ductile and fractured transgranularly. The rather tentative conclusion was that the intergranular fracture was caused by the low strength of the grain boundary precipitates. The implication was that Mn and Cr reduced the amount of precipitation at the grain boundary and thus suppressed the tendency for intergranular fracture. At the same time Harris and Varley (1953) were varying the Mg and Si contents of the alloy which also contained about 0.2%P. They concluded that excess silicon was necessary for brittleness and that the low energy intergranular fracture path was due to the preferential grain boundary precipitation of either free silicon or Mg_2Si to form a continuous grain boundary

film. Beneficial effects of manganese and chromium were attributed to their inhibiting preferential grain boundary precipitation although the precise mechanism of this inhibition is unclear.

Dunwoody, Moore and Thomas (1973) also found that the basic alloy Al-0.6%Mg-1.0%Si had very low toughness and failed intergranularly. By adding Mn or Fe they increased the toughness by a large amount (Mn only) or by a small amount (Fe only). Adding Mn and Fe together gave toughness lower than for Mn only but better than the basic alloy or for Fe only. They concluded that the resistance to crack propagation of Al-Mg-Si is increased by incoherent particles due to Fe and Mn. The toughness increase was accompanied by a change in fracture mode from mainly intergranular to at least partly transgranular. The most effective particles were the fine ones of 0.05 to 0.25μm diameter (dispersoids) formed during homogenization and hot working of the cast ingot. Inclusions (> 1.0μm) were considered detrimental to toughness but only when fine particles were present.

Dowling and Martin (1976) and (1977) investigated the effect of Mn-bearing dispersoids on slip distribution and tensile fracture processes. As regards slip distribution, Dowling and Martin (1976) found that Mn dispersoids caused lateral spreading of the slip bands and thus gave smaller stress concentrations at the head of the slip band. The stress concentrations were also reduced by the smaller grain size of dispersoid containing alloys. These two effects then suppress intergranular fracture at low strains because the stress concentrations are too small to cause decohesion at the grain boundary precipitates. As regards tensile processes, Dowling and Martin (1977) studied the basic alloy (Al-0.6%Mg-1.0%Si) containing approximately 0.1, 0.25, and 0.62Mn. These will be referred to as alloys 1, 2 and 4

consistent with the nomenclature of Prince (1977). Dowling and Martin found that alloy 1 failed intergranularly but the intergranular fracture surfaces were covered with fine dimples of 0.5 - 1.0µm diameter. This corresponds to the average spacing of the grain boundary precipitates, suggesting these as nucleation sites for the grain boundary voids. Schwellinger (1980) has suggested, however, that failure by microvoid coalescence along the PFZ in Al-Mg-Si alloys may nucleate homogeneously by void formation in the dislocation substructure.

Dowling (1975) found that alloys 2 and 4 fractured in a ductile manner in tensile tests with voids forming at coarse particles in the matrix. In alloy 2 these voids grew in directions 45° to the tensile axis, and catastrophic failure occurred leaving 45° shear fracture surfaces. In alloy 4, the higher volume fraction of dispersoids suppressed the 45° propagation, and the stress increased until voids formed at the dispersoids. Failure then occurred by the coalescence of these small voids.

Prince (1977) took a slightly different view. He felt that all three alloys failed in a predominantly intergranular manner. He found that voids did open up at coarse particles ahead of a crack tip, but these were on or very near grain boundaries and thus crack propagation occurred along the grain boundary. Prince measured the size of crack tip plastic zones after crack propagation, using selected area channelling patterns. The results showed that increasing volume fractions of dispersoids increased the propagated crack plastic zone size and also increased toughness. Prince proposed a model for fracture based on a critical local strain that must be achieved at the head of a slip band to cause an increment of crack propagation.

According to the Prince model (reviewed in Sect. 1.5.2) dispersoids homogenize the slip distribution so that a higher macroscopic strain must be applied to achieve a given local strain. Lohne and Maess (1979) agree with some aspects of this model, e.g. fracture initiation due to a critical strain in the PFZ. However, they feel that grain size is the dominant factor and that the effect of dispersoids is primarily to produce finer grains.

Edwards (1981) examined fatigue life and fatigue crack propagation rates of these alloys. The fatigue life was found to increase with the volume fraction of dispersoid. Also, fatigue crack growth rate decreased as the volume fraction of dispersoid increased for low and intermediate values of ΔK , the cyclic stress intensity factor. However, at high ΔK and high amounts of dispersoid, void formation at coarse particles tended to outweigh the beneficial effect of dispersoids. The intergranular fracture mode was dependent on the maximum stress intensity in the fatigue cycle with the micromechanisms identified as microvoid coalescence along the grain boundary PFZ. Edwards extended a semi-cohesive zone model originally used by Moody and Gerberich (1980) to explain the micromechanisms of fatigue crack propagation. The Edwards model predicts that fatigue crack growth rates at intermediate ΔK are controlled by K_{max} . The corresponding lowering of fatigue crack growth rates by dispersoids reflects a decrease in the degree of intergranular fracture due to homogenization of slip by the dispersoid particles.

1.6.3 Object of the Present Work

The overall objective of this investigation is to elucidate the role of microstructure on fracture toughness and the micromechanisms of crack extension in Al-Mg-Si alloys. The specific aim is to determine the effect of varying the volume fraction of Mn-bearing dispersoids on ductile fracture toughness criteria, response to triaxial stress states and crack tip plastic zone sizes up to the instant of crack extension. Ultimately, the aim is to incorporate the effects of these variables on the crack extension mechanisms into a model which explains the role of dispersoids in determining the fracture toughness of these alloys.

Figure 1.1

Coordinate system for equilibrium and compatibility
equations.

Figure 1.2

Modes of crack loading.

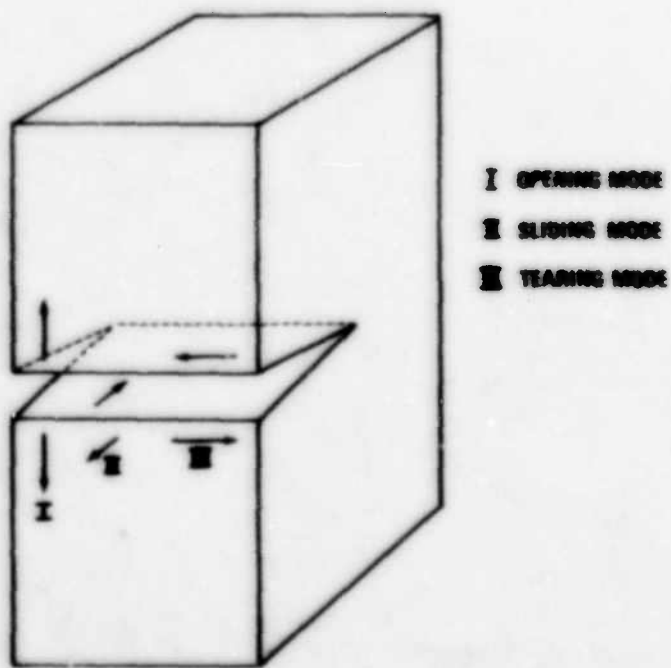
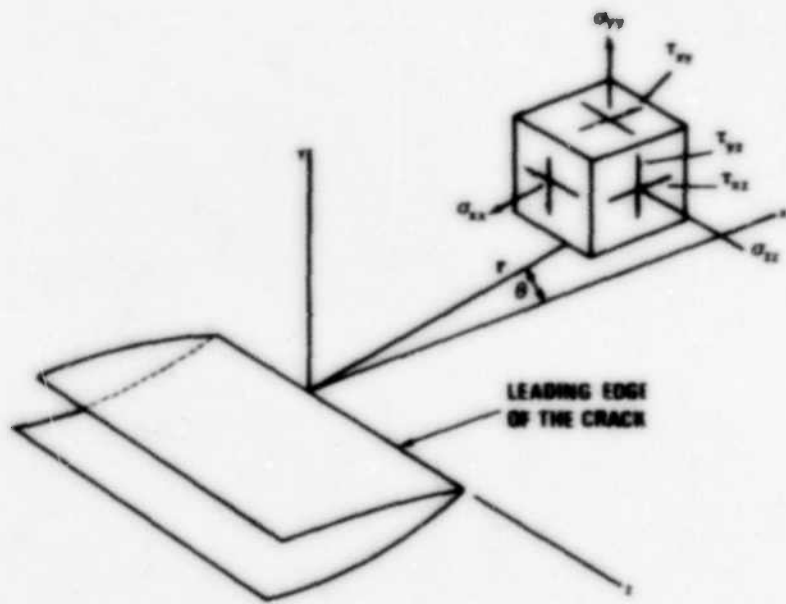


Figure 1.3

Mode I crack under biaxial stress.

Figure 1.4

First estimate of crack tip plastic zone size.

Figure 1.5

Second estimate of crack tip plastic zone size.

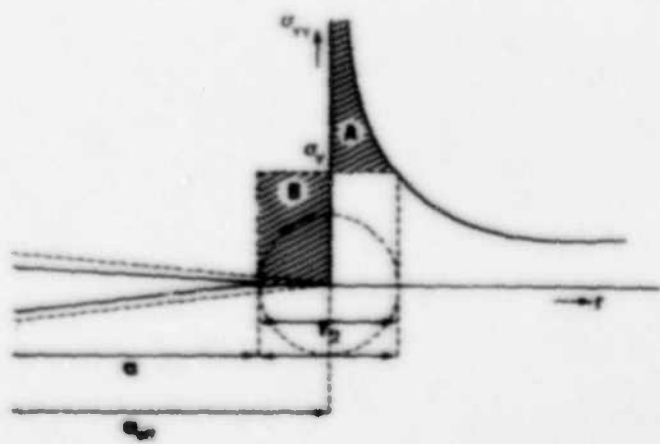
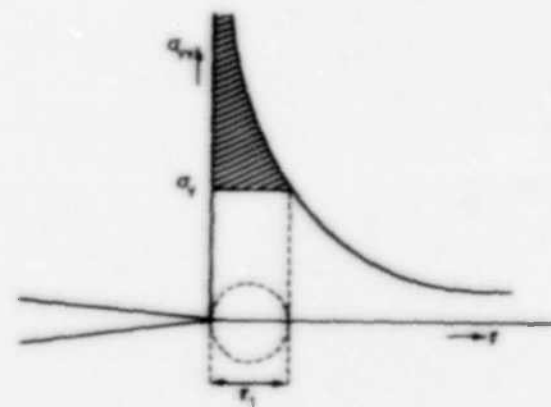
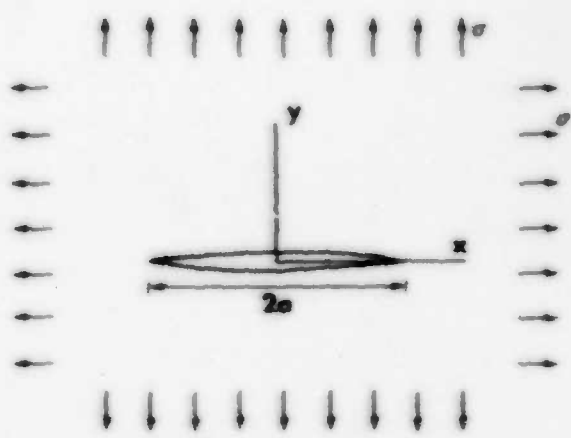


Figure 1.6

Dugdale model for crack tip plastic zone size.

Figure 1.7

Relationship between plane stress and plane strain plastic zones using von Mises yield criterion (after Broek, 1978).

Figure 1.8

Effect of specimen thickness on plastic zone shape.

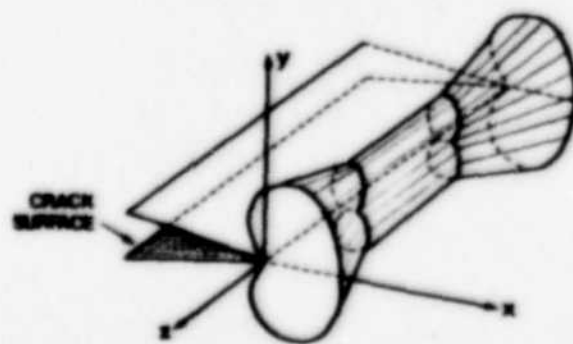
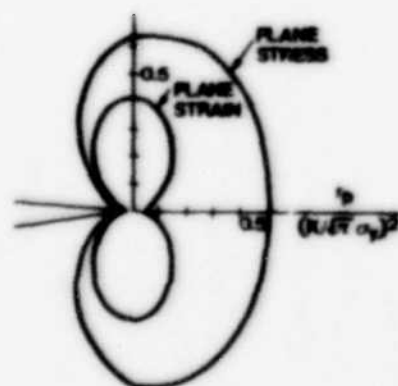
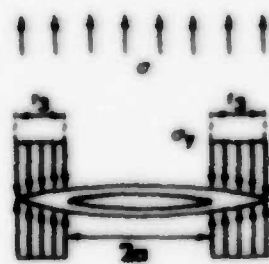


Figure 1.9

Graphical representation of the energy criterion.

Figure 1.10

Variation of toughness with specimen thickness.

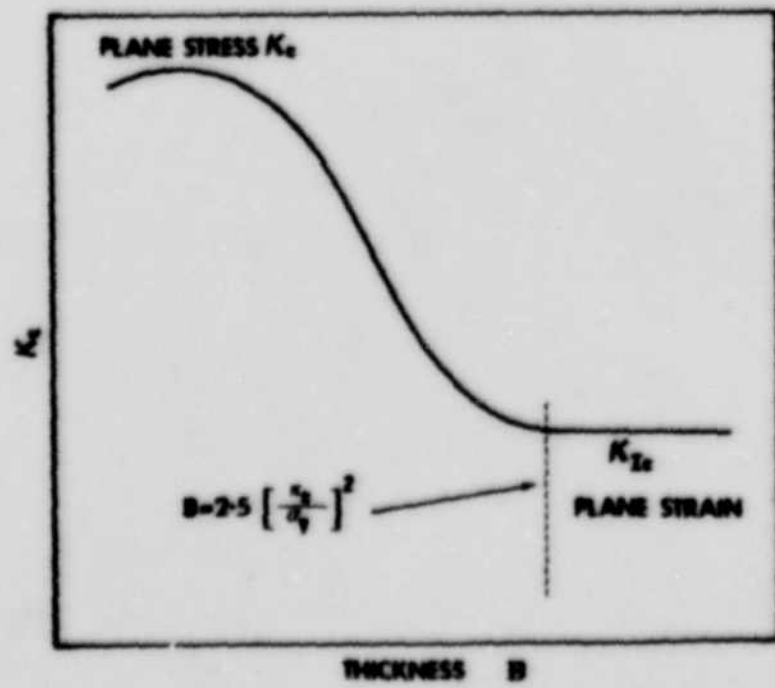
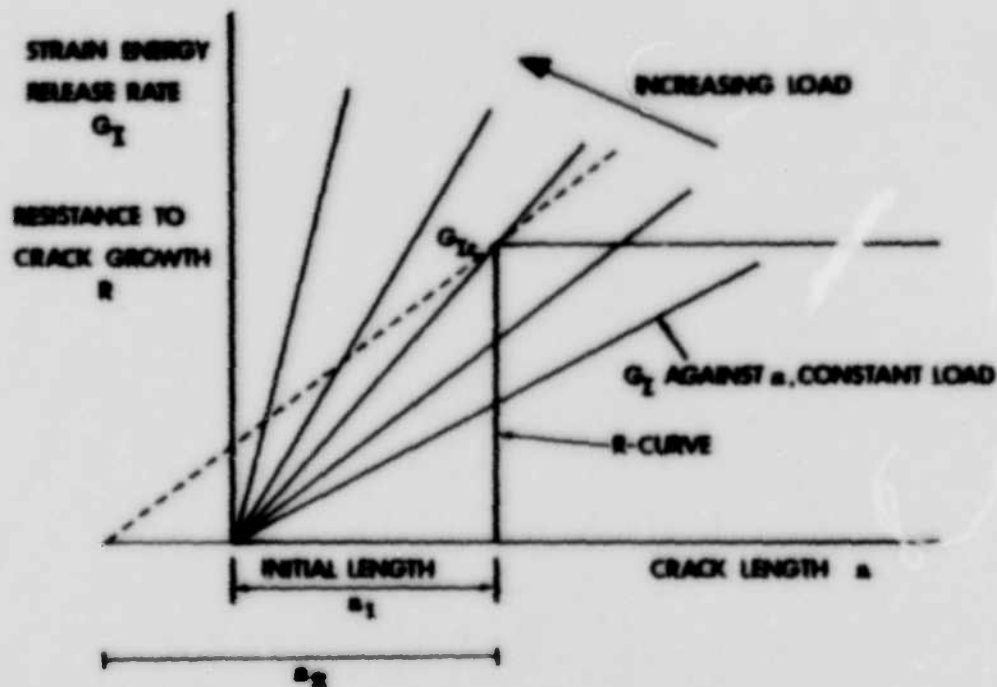


Figure 1.11

Definition of J-integral.

W = strain energy density = $\int \sigma \, d\varepsilon$

T = traction vector perpendicular to the line

u = displacement in the X direction

ds = an element of the line

Γ = the closed contour followed counterclockwise

Figure 1.12

Schematic of J versus Δs resistance line.

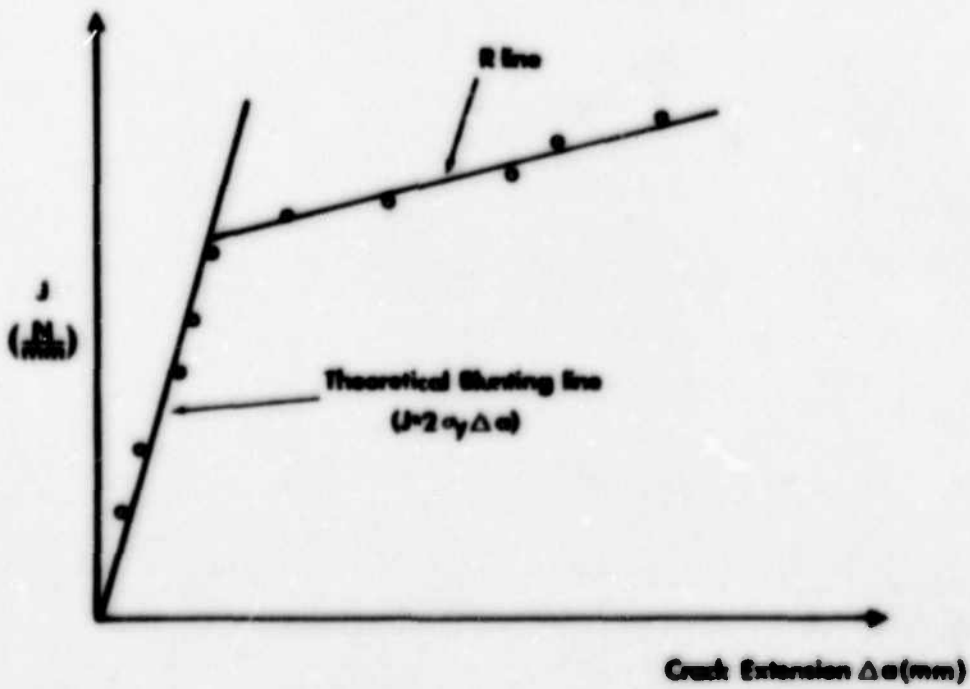
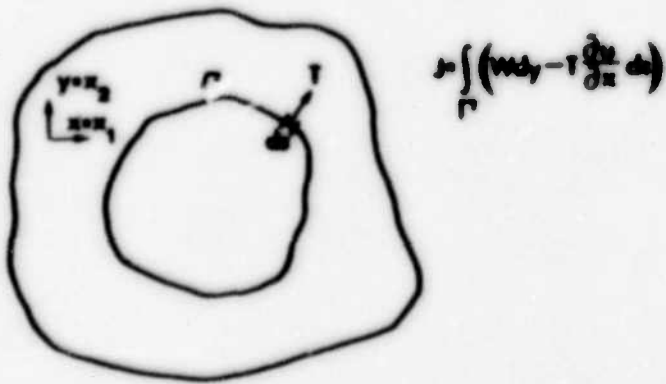
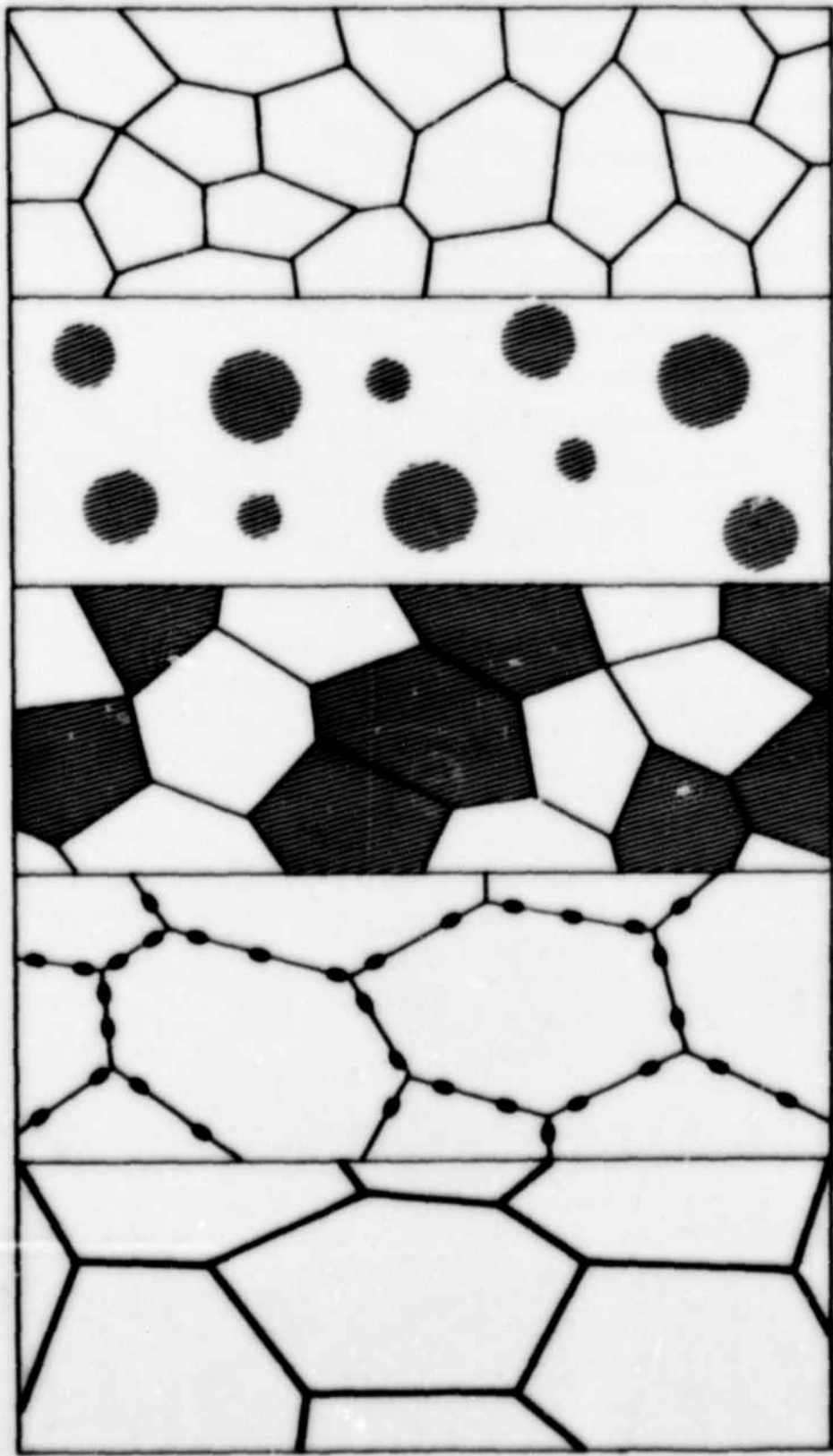


Figure 1.13

Some types of microstructure of metallic materials (after Schwalbe, 1977).

- a) Single phase, polycrystalline material.
- b) Two phase material, β in α .
- c) Two phase material, β in α with approximately equal volume content.
- d) Second phase particles along the grain boundaries of the first phase.
- e) Continuous network of the second phase along the grain boundaries of the first phase.



a)

b)

c)

d)

e)

Figure 1.14

Crack propagation mechanisms (after Schwalbe, 1977).

- a) Cleavage crack propagation.
- b) Dimple fracture due to coarse particles.
- c) Dimple fracture due to fine particles.
- d) Dimple fracture due to coarse and fine particles.
- e) Intergranular crack propagation due to grain boundary precipitates.
- f) Intergranular crack propagation due to a hard phase grain boundary film.
- g) Intergranular crack propagation due to a soft grain boundary film.
- h) Crack propagation by slip plane/slip plane interaction.
- i) Crack propagation by slip plane/grain boundary interaction.
- j) Crack propagation solely by plastic blunting.

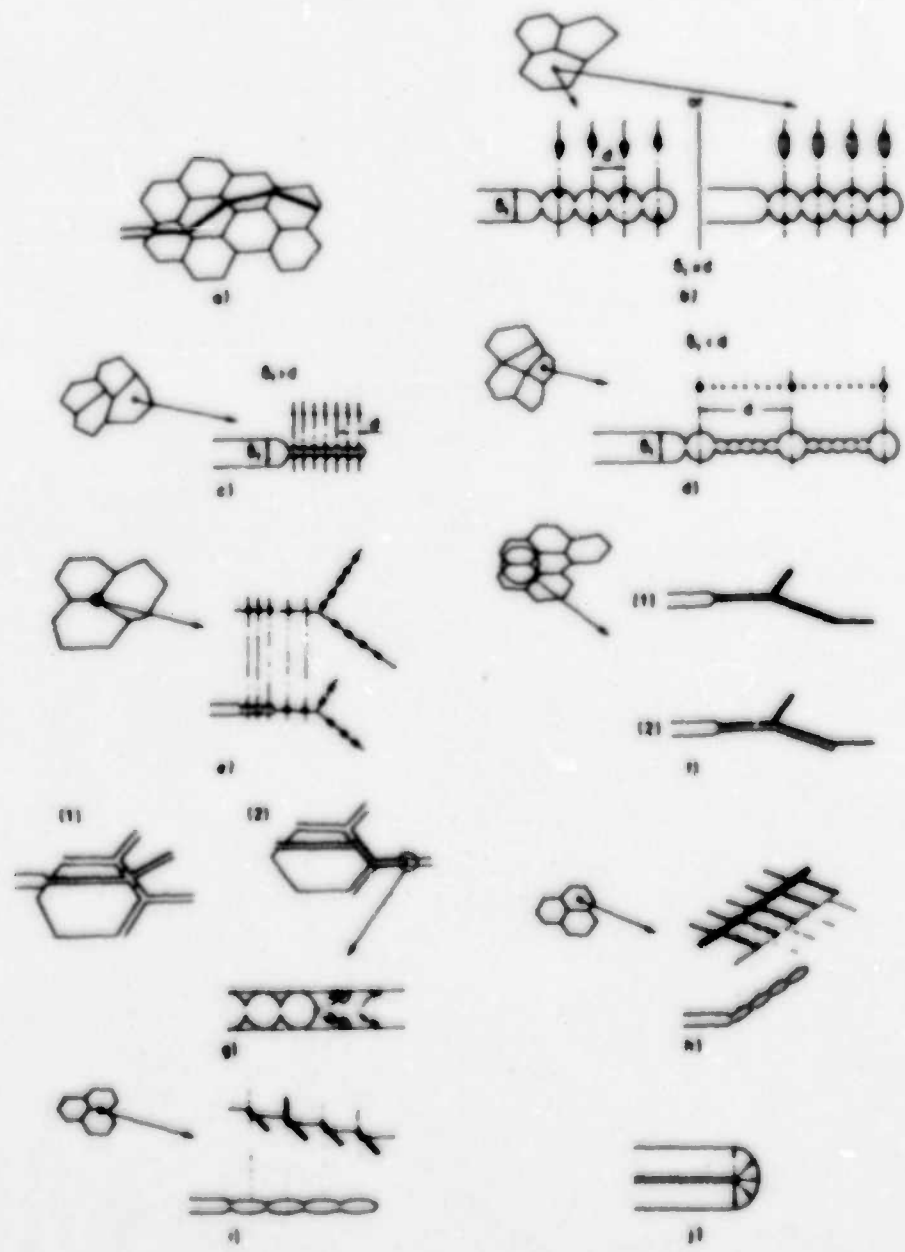


Figure 1.15

Ductile crack propagation by dimple formation (after Schwalbe, 1977).

Figure 1.16

Fracture toughness of some aluminium alloys versus volume fraction of inclusions (after Schwalbe, 1977).

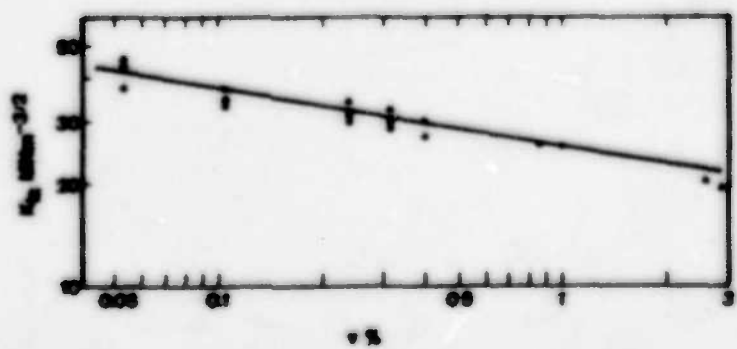
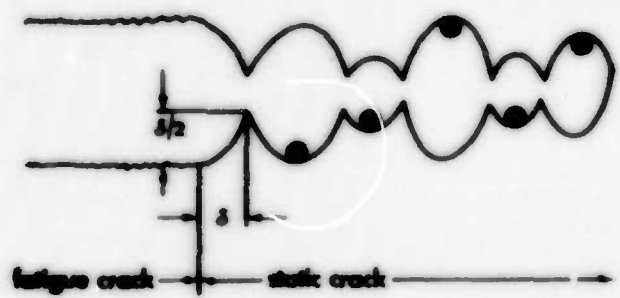


Figure 1.17

Geometric possibilities for plastic deformation in one slip system. A = spacing between slip steps; H = height of slip steps; α = angle between slip plane and crystal surface; B = thickness of a slip band (after Hornbogen and Zum Gahr, 1975).

Figure 1.18

Effect of thickness on K_c of overaged 7000 series alloys with various grain sizes (after Thompson and Zinkham, 1975).

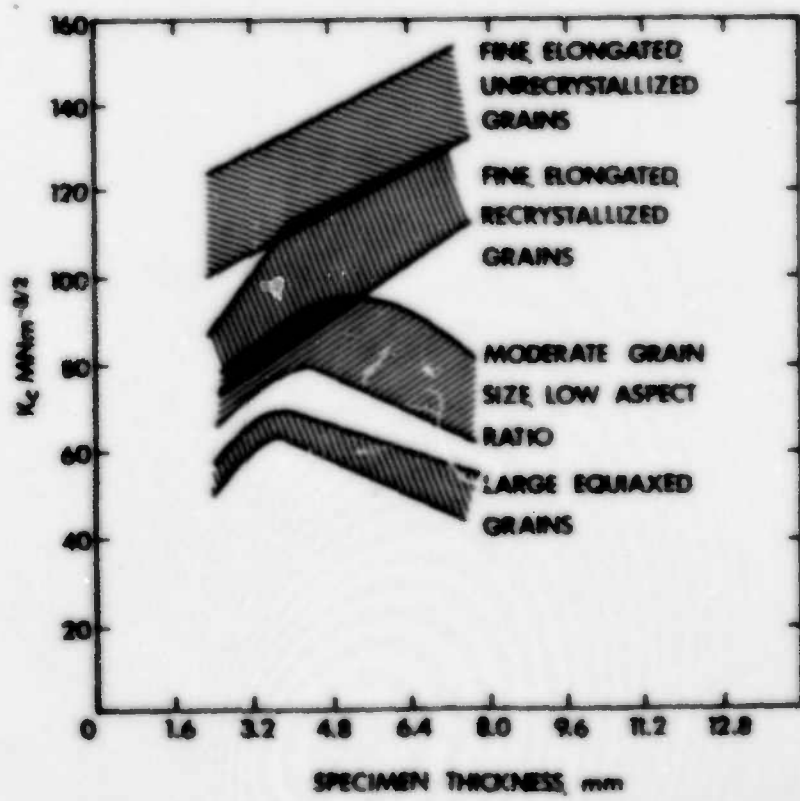
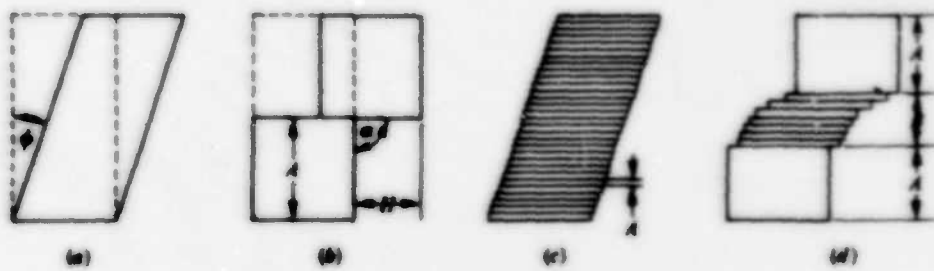


Figure 1.19

Schematic of variation in crack tip stresses with position
(after Boyd, 1972).

- a) σ_{yy}
- b) σ_{xx}
- c) σ_{zz}
- d) σ_{zz} versus thickness for thin and thick plate.

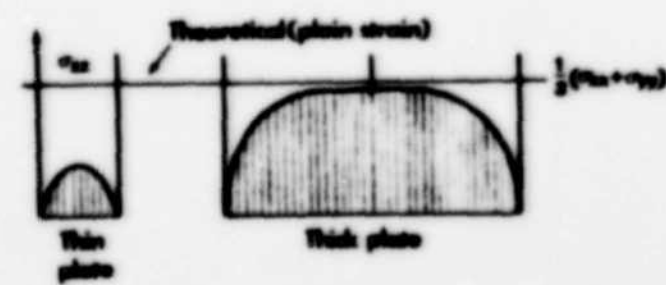
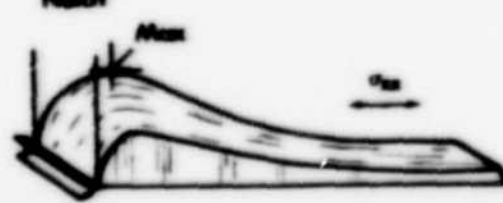
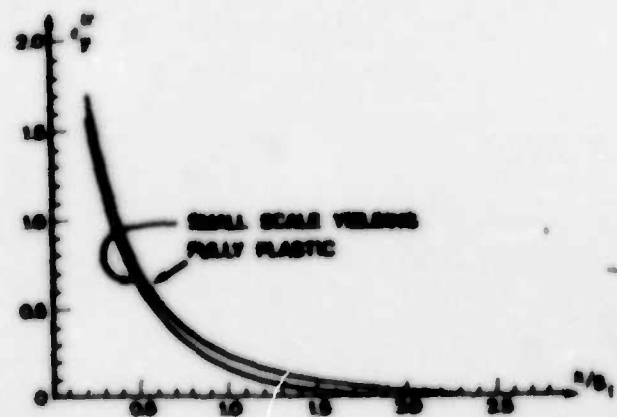
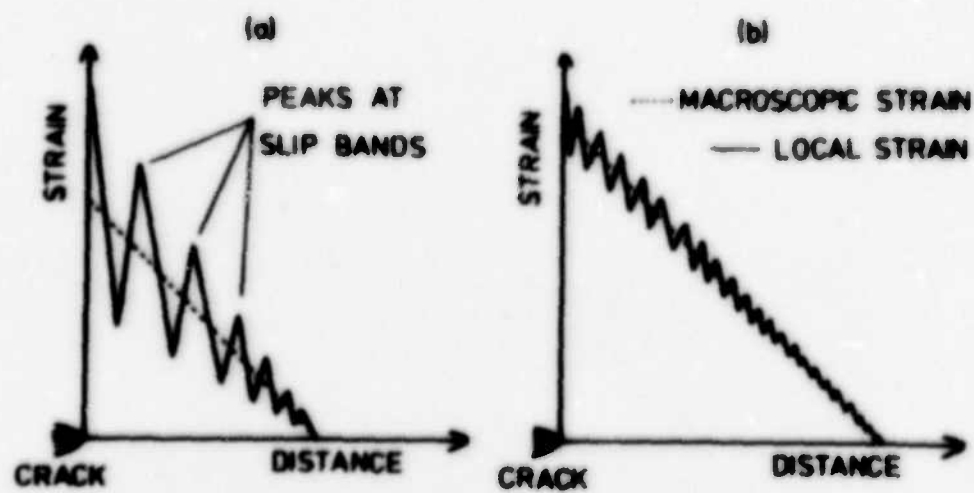


Figure 1.20

Prince model for the variation of macroscopic and local strain as a function of distance ahead of a crack tip for (a) an alloy containing few dispersoids and (b) an alloy containing many dispersoids. Both alloys achieve the same maximum local strain at the crack tip but with different degrees of macroscopic strain (from Prince and Martin, 1979).

Figure 1.21

True strain on the line ahead of a blunting crack tip as a function of distance X of a material point from the tip before deformation divided by the crack opening displacement δ (from Rice and Johnson, 1970).



Chapter 2

MATERIALS AND EXPERIMENTAL PROCEDURES

2.1 Materials

Materials and their compositional analysis were supplied by Meccor, Alcan International Ltd; compositions are given in Table 2.1. The alloys are based on the commercial alloy Al-0.62Mg-1.02Si-0.62Mn. Alloy MT, a high purity ternary alloy, has magnesium and silicon contents which are the same as the commercial alloy. The alloys ML, MM and MI are all quaternary alloys containing low (0.2wt%), medium (0.4wt%) and high (0.6wt%) manganese respectively. Since the primary objective depends upon a determination of the effects of dispersoid without the potentially obscuring effects of coarse constituent particles, all three of these alloys were made from a super-pure aluminium base in order to maintain very low iron contents (less than 0.01wt%). This low iron content was obtained in ML and MM, but the iron content in MI was slightly higher than desired (0.06wt%). To allow comparison of results with a commercial purity alloy, alloy MC with 0.27wt%Fe was also used.

2.1.1 Casting

As Table 2.1 indicates, alloys MT, ML and MM were made in two casts. In the backmould cast, the molten alloys were chill cast into copper moulds approximately 25mm (1") thick. In the direct chill

method, the alloys were semi-continuously cast into a water cooled mould whose bottom is connected to a hydraulic ram. As the metal solidifies, the ram withdraws it from the mould so that the solidification rate can be controlled by the flow rate of the cooling water and the speed of the ram. The casting was then scalped to remove the surface layers and to obtain the desired thickness prior to thermomechanical treatment.

2.1.2 Thermomechanical Treatment

With the exception of alloy MT, which will be discussed separately, all the alloys were homogenized at 530°C for 16 hours. The alloys were then rolled at 530°C to an intermediate thickness, allowed to cool to room temperature and then cold rolled to final thickness. Two final thicknesses were required: 19mm for tensile test specimens and 13mm for fracture toughness specimens. Three thicknesses are therefore given in Table 2.1: scalped thickness, thickness after hot rolling and final cold rolled thickness. After machining to the required specimen form, the alloys were then given a solution and recrystallisation treatment of 30 minutes at 560°C in a molten salt bath, quenched in water, held at room temperature for 3 minutes and then aged in silicone oil at 185°C to peak hardness. Single specimen ageing curves were developed to determine time to peak hardness; these ageing curves are shown in figures 2.1 to 2.3. Hardness values were determined using a Vickers diamond indenter with 10kg load. The error bars represent a standard deviation based upon at least five measurements. Ageing times to peak hardness, consistent with those given by Dowling (1973), Prince (1977) and Edwards (1981), were as

Table 2.1
Materials Processing and Compositions

Alloy Casting	Type *	Thicknesses (mm)			Compositions (wt%)					
		Scalped	Hot	Cold	Ng	Si	Mn	Fe	Ti	B (ppm)
			Bullied	Rolled						
MT	BM	25	-	13	0.58	0.98	0.001	0.01	0.016	16
	DC	76	48	19	0.61	0.99	0.001	0.01	0.014	13
ML	BM	25	18	13	0.63	0.97	0.22	0.01	0.013	13
	DC	76	36	19	0.59	0.98	0.25	0.02	0.015	16
MH	DC	76	36	19	0.61	1.02	0.64	0.06	0.012	17
			24	13						
MH	DC	28	18	13	0.61	1.03	0.60	0.01	0.010	15
	DC	76	36	19	0.61	0.99	0.37	0.04	0.013	24
MC	DC	76	36	19	0.66	1.11	0.62	0.27	0.012	15
			24	13						

* BM = Back Mould DC = Direct Chill

follows: MT, 4hrs; ML and MM, 2.5hrs; MH and MC, 2hrs.

Alloy MT received a somewhat different thermo-mechanical treatment due to its tendency toward a larger grain size. When processed as above, MT has equiaxed grains of about 400 μ m diameter, in contrast to the dispersoid containing alloys having an equiaxed grain size of approximately 100 μ m. In order to isolate dispersoid volume fraction as the experimental variable, it was desirable to keep the grain size constant. Dowling (1975) tried unsuccessfully to increase the grain size of the dispersoid containing alloys. However, in another approach Edwards (1981) significantly reduced the grain size of alloy MT by cutting the solution treatment time after cold work to one minute and adding a one hour solution treatment at 360°C before the cold rolling. Thus by modifying the solution treatment and applying 50% cold work, Edwards obtained an MT grain size of 125 μ m without affecting the ageing characteristics or otherwise altering the microstructure.

This small grain size treatment was attempted on the MT alloys in this study. The MT hooknose cast, however, did not lend itself to the treatment because the cast thickness of 25mm and the desired final thickness of 13mm permitted only 48% cold work to be applied with no prior hot working. The resultant grain size in this alloy was approximately 325 μ m. (The method for grain size measurement is described in section 2.3) However, the direct chill cast MT alloy was hot rolled and received 60% cold work to give a final grain size of about 200 μ m. This is still larger than the grain size obtained by Edwards; the difference may be due to the different final thickness in each case.

Grain sizes for all the alloys are given in Table 2.2. Measurements were made on three orthogonal planes, each defined by a line normal to the plane as follows: L, longitudinal direction, parallel to the rolling direction; T, transverse direction, perpendicular to the rolling direction and the rolling plane normal; and ST, short transverse direction, parallel to the rolling plane normal.

Table 2.2

Grain sizes (μm) on principal plane

Alloy	ST	T	L	AVG
WT	200	200	200	200
ML	116	106	75	99
MM	98	89	72	86
MM	90	83	63	79
MC	88	79	61	76

2.2 Tensile Tests

Tensile tests were performed on a MARD closed loop, servo-hydraulic testing machine fitted with a 50kN load cell under position control. Both notched and parallel sided tensile specimens were machined so that the length of the specimens lay in the longitudinal direction. Specimens were held in place and the load applied through standard Mounsfeld No. 18 specimen chucks. A constant actuator speed of 0.1mm/minute was obtained by using the MARD ramp generator set on 0.2volts/min. All mechanical tests were performed in

laboratory air (~ 55% relative humidity) at room temperature (~ 20°C). An X-Y recorder plotted load versus change in specimen diameter. An Instron strain gauge extensometer, modified as shown in fig. 2.6, was used to measure specimen diameter. That its output was linear over the range of interest can be seen from the calibration shown in fig. 2.7; it was extremely sensitive to change in specimen diameter. Accuracy was to the nearest 0.01mm. Initial specimen diameter was measured using a travelling microscope to an accuracy of 0.01mm. This instrumentation ensured that both engineering and true stress could be calculated for any point during the test. The true strain is given by (Mackenzie et al., 1977)

$$\dot{\epsilon} = 2 \frac{\ln \frac{c_0}{c}}{c} \quad (2.1)$$

where c_0 is the original radius and c is the instantaneous radius.

2.2.1 Unnotched Tensile Tests

Conventional tensile properties of the materials were determined using the unnotched tensile specimen geometry shown in fig. 2.8. Initial diameter in the gauge length was approximately 8mm and the gauge length was 10mm. Thus the actuator speed of 0.1mm/minute gave a strain rate of 0.01/minute. Machining scratches were removed from the gauge length by grinding with successively finer grades of silicon carbide abrasive paper followed by polishing with Brasso. The strain gauge extensometer was attached to the middle of the specimen gauge length, where necking and final fracture occurred.

2.2.2 Notched Tensile Tests

Response of the materials to varying degrees of triaxial stress state was measured on circumferentially notched tensile specimens. The specimen geometry and stress analysis were based on the work of Mackenzie, Hancock and Brown (1977). The effective plastic strain to failure initiation was measured for different values of stress triaxiality produced by varying the notch root radius of curvature. Specimen geometry and notch radii are shown in fig. 2.9.

Ductile failure in this geometry initiates at the centre line of the specimen at the notch where the stress state is most severe (Mackenzie et al., 1977). The stress and strain states in the notch can be estimated from the results of an analysis by Bridgman (1952):

$$\sigma_{zz} = \bar{\sigma} \left[1 + \ln \left(\frac{c^2 + 2cR - a^2}{2cR} \right) \right]$$

$$\sigma_R = \bar{\sigma} \frac{\ln \left(\frac{c^2 + 2cR - a^2}{2cR} \right)}{2cR} \quad (2.2)$$

$$\dot{\epsilon}_p = 2 \ln \frac{c_0}{c}$$

Figure 2.10 illustrates these, with σ_{zz} the longitudinal stress, σ_R the radial stress and $\dot{\epsilon}_p$ the effective plastic strain. Also, c is the specimen radius, R is the notch root radius of curvature and a is distance measured from the central line of the specimen. $\bar{\sigma}$ is the effective stress given by

$$\bar{\sigma} = \frac{\sqrt{2}(\sigma_1 - \sigma_2)^2 + (\sigma_2 - \sigma_3)^2 + (\sigma_3 - \sigma_1)^2}{2} \quad (2.3)$$

The stress triaxiality, defined as the ratio of the mean stress to the effective stress, for this geometry is given by

$$\frac{\sigma_m}{\sigma} = 1 + \ln \left\{ \frac{e+1}{\frac{2}{3}} \right\} \quad (2.4)$$

Thus when R is large, the triaxiality approaches the unnotched tensile value of 1/3.

Hancock and Mackenzie (1976) determined that failure initiation corresponds to the maximum in the plot of true stress against effective plastic strain. In some materials there may be a considerable amount of strain between this point of failure initiation and subsequent final fracture of the specimen. However, such was not the case in the present study; the failure strain was taken as the strain at fracture.

2.3 Fracture Toughness Tests

Fracture toughness testing was performed on a HAN'D closed loop, servo-hydraulic testing machine fitted with a 25kN load cell operating in load control. Compact tension (CT) specimens were machined in the LT orientation, i.e. crack plane normal in the longitudinal direction and the crack propagation in the transverse direction. The specimen geometry and dimensions are shown in fig. 2.11. A specimen thickness of approximately 11.5mm was selected as a compromise between that desired for full plane strain constraint on the midplane and the

limitations imposed by casting size and heat treatment facilities. Prior to heat treatment, a sharp starter notch was spark eroded 3mm beyond the machine notch using 36 gauge copper wire. This starter notch provided sufficient stress concentration for the fatigue pre-crack to initiate at its tip. The fatigue pre-crack was grown from the starter notch at a ΔK in the range 10-13MPa $\sqrt{\text{m}}$. The desired ΔK was maintained as the crack grew by a manual load shedding technique, and this ΔK was reduced as the crack length approached the desired value of a/W . Crack length was measured at frequent intervals using a travelling microscope focused on the specimen surface, which had been mechanically polished to a 6µm finish. This technique enabled surface crack length to be detected to an accuracy of 0.01mm. The fatigue load waveform was sinusoidal with $R(K_{\min}/K_{\max})$ of 0.1. All tests were performed in laboratory air and at room temperature.

2.3.1 K_{IC} Testing

Plane strain fracture toughness tests were performed in accordance with ASTM standard E399 (ASTM, 1978) except that the thickness dimension was slightly less than that recommended in the standard for alternative compact tension specimens (11.5mm versus 12.5mm for $W=30\text{mm}$). It was clear that this thickness would be insufficient for a valid K_{IC} determination. However, since K could be measured from the same test record as obtained for the J test (to be discussed in section 2.3.2) it was decided to measure K_J as a possible comparison of toughness between materials. The specimen strength ratio mentioned in the ASTM standard had been calculated for these alloys by Prince (1977) who found it unsuitable as a relative measure of

toughness.

After the fatigue pre-crack had grown to an a/W value of approximately 0.55, the specimen was removed from the grips and a modified Instron strain gauge fitted. The clip gauge was mounted between two razor blades held by epoxy resin to the specimen load line. The clip gauge then monitored load line displacement (δ_{LL}). The calibration curve for this clip gauge is shown in fig. 2.12. The gauge response was linear over the range of interest and accurate to the nearest 0.001mm. Actuator speed was controlled using the MAND ramp generator set at 0.6volts/min to produce an actuator speed of 0.3mm/minute. Load (P) and load line displacement (δ_{LL}) were recorded graphically on an X-Y plotter; a typical test record of load - load line displacement is shown in fig. 2.13. Once the desired load was obtained, the specimen was unloaded by reversing the direction of the ramp generator. The clip gauge was removed and the specimen was fatigue loaded again until the crack grew well past its previous position during the K test. Crack length for the K calculation was determined by examining the crack plane in the JSM 35X scanning electron microscope. The termination line of the pre-fatigue crack front was clearly evident as seen in fig. 2.16. This crack length was measured at 1mm intervals across the thickness using the JSM 35-X stage micrometers. The readings were averaged to give a fatigue crack length which was then added to the notch length to produce a total crack length to the nearest 0.01mm. K values were calculated using the ASTM standard E399 formula

$$K = \frac{P\delta(a/W)}{W^{1/2}} \quad (2.3)$$

AD-A119 099

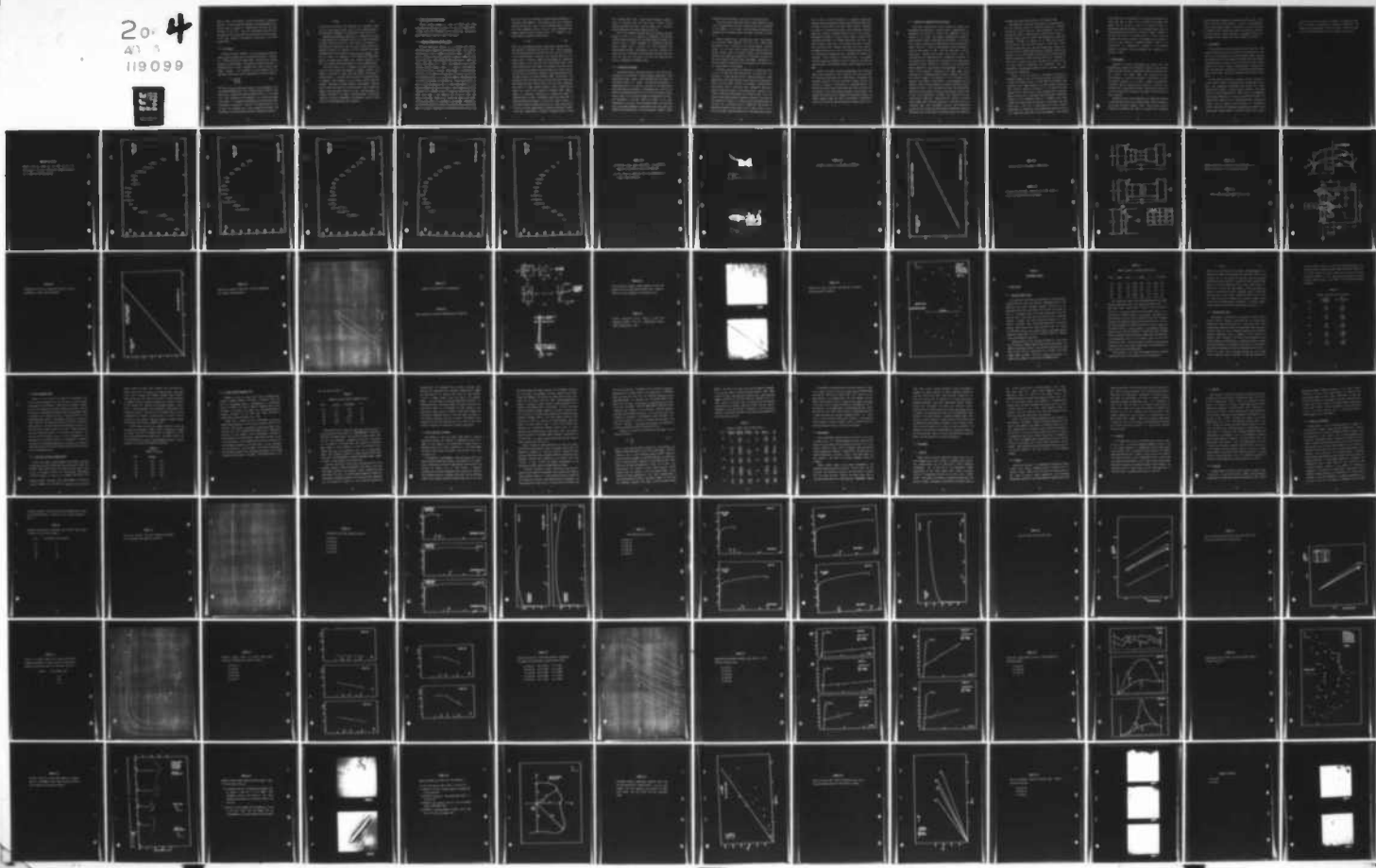
AIR FORCE INST OF TECH WRIGHT-PATTERSON AFB OH
MICROMECHANISMS OF CRACK EXTENSION IN ALLOYS. (U)

F/G 11/6

1982 J A BLINO
UNCLASSIFIED AFIT/CI/NA/82-250

NL

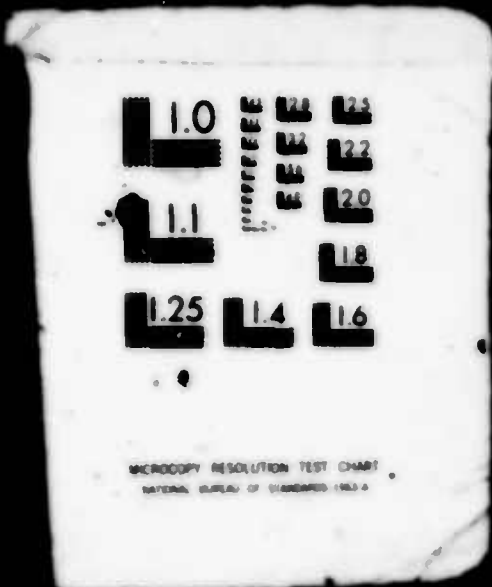
20-4
40-3
119099



20+

AD A

119099



where P is load, B is thickness, W is width and $f(a/W)$ is a polynomial function of a/W whose values are tabulated in the ASTM standard. K_Q is then the value of equation 2.5 obtained using the load P_Q at the intercept of the load - load line displacement trace and a line constructed on the trace having 95% of the slope of the linear portion of the trace. Details of the procedure are specified in the ASTM standard E399.

2.3.2 J_{IC} Testing

The ductile fracture toughness, J_{IC} , was determined with multiple compact tension specimens using the procedure developed by Clarke et al., (1979) and Clarke and Landes (1979). Although not yet adopted formally as an ASTM standard, this procedure has been widely used to determine the value of the J integral at the onset of stable crack growth. Briefly, J is calculated for each specimen from an experimental load versus load line displacement curve by the formula

$$J = \frac{1+a}{1+a^2} \frac{2A_T}{Bb} \quad (2.6)$$

where A_T is the total area under the curve, B is the thickness, b is the remaining ligament ($W-a$), and $(1+a)/(1+a^2)$ is a function of a/W whose value is tabulated by Clarke and Landes (1979) for the a/W range 0.45 - 0.80. The amount of crack extension, da , and the pre-fatigue crack length, a , are measured by examining the fracture surface after the specimen is pulled apart. Values of J are plotted against da for at least four specimens and a least squares line is drawn. The intersection of the least squares line and a blunting line given by

$$J = 20 \text{ yds}$$

(2.7)

is then taken as the value of J_Q . The value J_Q is considered a valid J_{lc} if it meets certain criteria that limit the allowable amount of crack extension. A schematic of the procedure is shown in fig. 2.14.

Specimens and experimental apparatus for J testing were the same as those described for K testing in section 2.3.1. Crack front marking by fatigue before and after the J test proved to be effective in determining the positions of the crack front. These positions were sometimes difficult to establish in alloy MT because the fatigue micromechanism of crack extension is K_{max} controlled (Edverds, 1981) and thus similar in appearance to the monotonic micromechanism. However, all other alloys showed a clear change in appearance (see fig. 2.16), making accurate measurement of a_0 and Δa straightforward.

Some data points used to determine the linear equation of J versus Δa fell outside the minimum or maximum allowable crack extension according to Clarke and Landes (1979). With respect to minimum extension, it was felt that any test with a measurable amount of monotonic crack extension on the fracture surface should be included. The maximum allowable extension seems somewhat arbitrary since it effectively limits Δa to less than about 1.5mm. To reduce the number of tests required to obtain a J - Δa line, this requirement was relaxed to $\Delta a=2.5\text{mm}$ in this study. The intention that the procedure should not be used to characterize the resistance curve for large amounts of crack extension was still satisfied.

2.4 Plastic Zone Size Measurement

Various possible methods of crack tip plastic zone size measurement were discussed in section 1.5.3. Due to its applicability to plane strain zone measurement and its sensitivity, the electron channelling pattern method was used in this study.

2.4.1 Electron Channelling Patterns (ECP)

Electron channelling patterns can be obtained under special conditions using a scanning electron microscope (SEM). The requisite contrast arises from an anomalous absorption effect, in which the electron intensity of the primary beam as a function of depth into the crystal varies with crystallographic orientation (Hirsch, Bovis and Whelan, 1962; Booker et al., 1967). This mechanism can thus produce suitable contrast whenever there is a change in crystallographic orientation relative to the beam. These changes in crystallographic orientation can be obtained by rocking the electron beam about a point on the specimen surface. In a two scan coil SEM, the rocking condition is obtained by switching off the lower set of scan coils located at point B in the ray diagram of fig. 2.15. Thus single deflection of the beam is caused by the scan coil at point A. The strength of the second condenser lens is adjusted so that it focuses the electron beam on the front focal plane of the objective lens (B in fig. 2.15). The objective lens focal length is set so that the image of the object located at the rocking coil is focused on the specimen. Consequently, by varying the rocking coil current, the parallel electron beam can be made to rock about a given point on the specimen surface. In fact, the

point has a finite area because the inherent spherical aberration of the objective lens (Newbury, 1972) causes rays that are at different distances from the optic axis to focus at different points along the axis. This phenomenon creates a disc of least confusion on the specimen surface of radius Δr (shown in fig. 2.15 (Longhurst, 1967, p.347)) given by (Thornton, 1968, pg.36) as

$$\Delta r = C_s \theta^2 \quad (2.8)$$

where C_s is the spherical aberration coefficient of the lens and θ is the angle that a ray makes with the optic axis. Since C_s increases with increasing distance from the objective lens, the size of the spot on the specimen surface is a function of the working distance and the angle of scan. The volume of material which produces the channelling pattern depends on the spot size, the accelerating voltage of the electron beam and the atomic number of the material. Since the quality of the resulting ECP depends on the perfection of the crystal lattice, the ECP offers a non-destructive method of obtaining information about the defect density of a crystal (Davidson, 1981). Unfortunately, the specimen-electron interaction and the way this interaction varies with beam voltage and defect characteristics are not yet fully understood. The concept of a model relating changes in ECP to defect type and density has recently been reviewed by Davidson (1981). However, despite the theoretical difficulties in treating the effect of individual defects on ECPs, channelling patterns have been shown to provide significant information on the average number of defects in the volume of material sampled by the beam. As a result, deterioration of ECPs can be shown experimentally to depend on dislocation density, a fact which enables ECPs to be used to map plastic zones at crack

tips. Davidson (1974) used a tapered tensile specimen to obtain a series of calibration ECPs for known values of strain. He then compared experimental ECPs from a crack tip region to the calibration ECPs and plotted strain contours around the crack tip.

Prince (1977) similarly classified material at specific locations around the crack tip as deformed or undeformed; this technique required constant switching of the microscope conditions. However, the resulting locus of points considered to be comprised of deformed material allowed him to construct the line representing the elastic-plastic interface. The objective of the use of ECPs in the present work was to determine the elastic-plastic interface around the crack tip (and thus the plastic zone size) by a method that was accurate, repeatable and reasonably rapid.

2.4.2 Experimental Technique

The microscope used to map plastic zones was a JEOL 100C electron microscope with an EM-ASID-4D scanning attachment operating at 100kV accelerating voltage. Compact tension specimens (CTS) were tested as described in section 2.3.1. However, the specimens were loaded to a predetermined value of K which was calculated to be less than that which would cause crack extension. Following the test, the crack tip region and surrounding material were cut from the CT specimen by spark erosion. Special care was taken throughout the preparation for plastic zone measurement to preclude additional loading in the plane perpendicular to the crack. The bulk specimen holder on the JEOL 100C limits the specimen dimensions to approximately 2mm x 5mm x 15mm. This specimen size was obtained by first spark eroding to slightly larger

dimensions and then grinding to final size on wet abrasive paper.

Since good electron channelling pattern quality depends on having a flat, polished surface, the short transverse plane that corresponded to the midplane of the compact tension specimen was mechanically polished and electropolished using the method described in section 2.5.

Values of applied K and J for these plastic zone size specimens were calculated using equations (2.5) and (2.6). Crack length measurement was not as accurate as for fracture toughness specimens because the nine point crack profile method using the SEM on the fracture surface could not be used. Instead, the electropolished mid-plane crack length was measured with a travelling microscope and the result averaged with the surface crack length. Although not as precise a method, the functions of a/W in equations (2.5) and (2.6) do not strongly depend on crack length.

The plastic zone specimens were then held in a special jig built to fit in the JEOL 100C bulk specimen holder and inserted into the microscope. A normal secondary electron image was obtained at 1000X magnification. The precise location of the crack tip was determined by digital volt meters (DVM) attached to the specimen translation gears and calibrated using a 10 μm copper mesh. Although the DVMs gave a readout of position accurate to the nearest micron, backlash in the specimen translation system limited the accuracy to about $\pm 5\mu\text{m}$. The position of the elastic-plastic interface in relation to the crack tip was determined as follows: At a distance several millimeters ahead of the crack tip, a collimated beam in rocking mode was obtained by adjusting the objective lens current so that a piece of dust or a pore was at the largest obtainable magnification. Then moving away from the

dust or pore, an ECP characteristic of undeformed material was optimized using the differentiated back-scattered electron signal with 10° angle of rock and SLOW scan speed. Since an ECP has inherently low contrast, an improved pattern could often be obtained by using the manual lens control on condenser lenses C1 and C2. Up to a point, decreasing the strength of C1 gave a larger signal in the ECP while increasing the strength of C2 brought the ECP back into focus. The improved signal to noise ratio of this manual lens control technique gave a good quality ECP, frequently with fourth order lines visible. An example is shown in fig. 2.17. If an acceptable quality ECP could not be obtained on undeformed material, the specimen was removed and repolished. While remaining in channelling mode, the specimen translation knobs were adjusted so that the crack tip was under the beam according to the previously recorded crack tip position on the DVMs.

Arrival at the crack tip could be confirmed by the distorted image on the viewing screen. Then, using the crack tip as the origin of a coordinate system based upon the DVM readouts, the specimen was traversed, moving the crack tip away from the beam until the ECP returned to the quality characteristic of undeformed material. The beam was then scanned several times across the transition region until the position of the elastic-plastic interface was established. DVM readings of this position were recorded and the procedure repeated at another position along the plastic zone boundary. Eventually the profile of the crack tip could be constructed as shown in fig. 2.18.

2.4.3 Sensitivity, Reproducibility and Accuracy

Three major concerns about the ECP technique for plastic zone measurements were sensitivity to plastic strain, reproducibility of measurements and accuracy of plastic zone dimensions. Since the location of the plastic zone boundary depended upon a subjective decision based on visible deterioration in ECP quality, it was felt that a method of quantifying the minimum plastic strain detectable was needed. Therefore, a series of three Hounsfield tensile specimens of alloy MH were pulled to 10%, 1.0% and 0.2% plastic strain, respectively. Specimens were prepared from these so that ECP conditions could be established on the deformation free shoulder of the specimen and the specimen then traversed until the gauge length was under the beam. The ECP on the 10% plastic strain specimen was almost completely lost upon moving to the gauge length. For the 1.0% plastic strain specimen, traversing to the gauge length caused detectable loss of channelling pattern quality. However, there was no well defined change in ECP quality for the 0.2% plastic strain specimen. On the basis of these results, it was determined that the method for plastic zone measurements was capable of detecting plastic strains of at least 1.0%. The plastic zone maps thus experimentally measured are more correctly 1.0% plastic strain contours than profiles of the true elastic-plastic interface. This method relies on the ability of the human eye to assess overall ECP quality, to include loss of higher order lines and broadening of lower order lines on a continuous basis. With considerable practice, this method became quicker and more reliable than other methods of quantifying changes in ECP quality, such as the width of lower order lines or the indexing of

the highest order lines visible (Prince, 1977; Davidson, 1979).

The second major concern about the technique was reproducibility. Did this subjective method of identifying plastically deformed material give the same result for repeat measurements? One way of checking this during a single microscope session was to return to a previously measured section of plastic zone boundary and to repeat the measurement. Although the readings on the DVMs were not usually exactly the same, the results were consistent to within about $\pm 25\mu\text{m}$. This same reproducibility was verified by remeasuring a plastic zone after several days. Another method used was to repolish a plastic zone specimen. This in effect removed a surface layer of several hundred microns and revealed a slightly different plastic zone. Although the details of the remeasured zone were not exactly the same as before, its overall shape and dimensions were reproducible. Thus the repeatability of measurements was good, both on a particular plastic zone and after repolishing.

Accuracy of the ECP method for measurement of plastic zone dimensions depends, in part, on the size of the spot the beam makes as it rocks on the specimen surface. The JEOL 100C is an extremely good microscope in this regard because of the short working distance and small spherical aberration coefficient of its objective lens (see equation (2.8)). Prince (1977), using a Cambridge 34-10 Stereoscan, measured his spot size by micrometer monitored specimen displacement required for the channelling pattern to completely cross a grain boundary; the resulting spot size was $29\mu\text{m}$. In the present work, this method gave a spot size of approximately ten micron diameter. Additionally, a through focus series channelling condition was set up on a copper mesh having $10\mu\text{m} \times 10\mu\text{m}$ grid openings. In the optimum

focus condition at a rocking angle of 10° , one grid opening filled the screen from edge to edge. It was concluded that the ECPs in the present work lay within an area on the specimen surface of approximately ten microns diameter, an area adequately small since the alloys examined had a grain size of 70 microns or larger. Because of the small spot size, the limiting factor on plastic zone size dimensions was the error involved in the judgement of the quality of an ECP as free deformed or undeformed material. Based on the considerations of reproducibility discussed in the preceding paragraph, the plastic zone size dimensions were considered to be accurate to $\pm 25\mu\text{m}$.

2.5 Metallography

Specimens for optical metallography and plastic zone size measurement were prepared by wet grinding on silicon carbide abrasive paper to 800 grit followed by polishing with Brasso, 6 μm diamond paste and, finally, 3 μm diamond paste. The specimens were then electropolished in a solution of 64% ethanol, 18% perchloric acid and 18% glycerol (Pashley et al., 1966). Electropolishing occurred in about 30 seconds using a voltage of $\sim 20\text{V}$ (half wave rectified) and a large aluminium cathode. The solution was maintained at 0°C by pouring liquid nitrogen into the beaker; current density was about 0.1amp/cm^2 .

Specimens for grain size determination were subsequently anodized so that the grain structure was revealed through crossed polarizers in the optical microscope (Edwards, 1981). The anodizing solution contained 2% fluoroboric acid (HBF_4) in distilled water with small

amounts of dissolved aluminium to increase conductivity. Again, a half wave rectified power source supplied ~ 38 volts at room temperature using a large aluminium cathode. The solution was constantly agitated by a magnetic stirrer. Under these conditions, anodizing was completed in about 80 seconds. Optical examination, photography and grain size measurements were performed using a Zeiss Ultraphot IV microscope.

2.6 Fractography

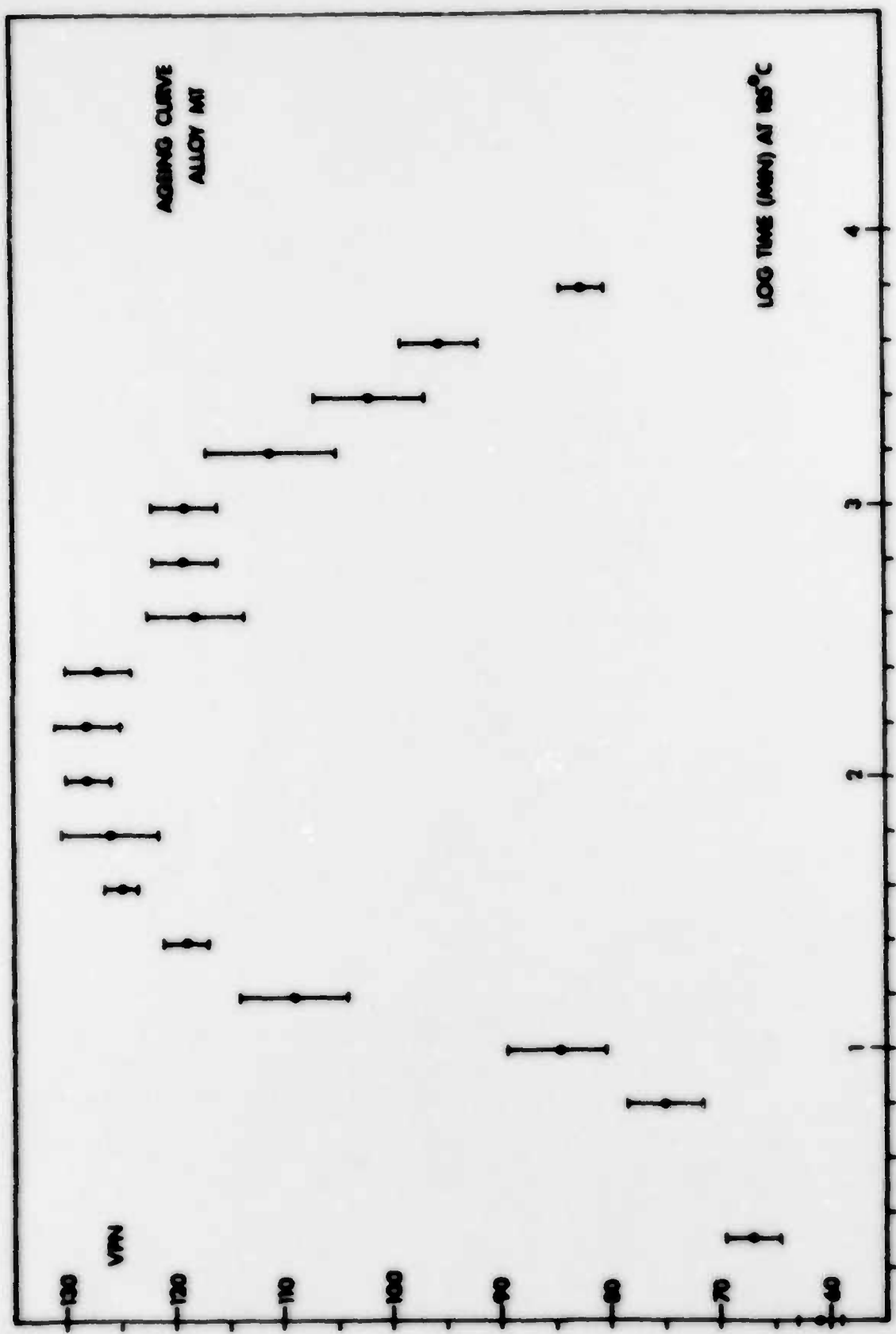
Fracture surfaces were examined using JEOL JSM 35X and EOL 100C scanning electron microscopes in secondary electron image mode. Crack length a and crack extension Δa of fractured compact tension specimens were measured in the JSM 35X using the micrometer controlled specimen translation system. Fracture surfaces were mounted on a 39mm working distance stub so that the actual working distance was approximately 30mm. Magnifications of photographs at non-standard working distances were calculated from a calibration photograph of the 3mm spark machine notch.

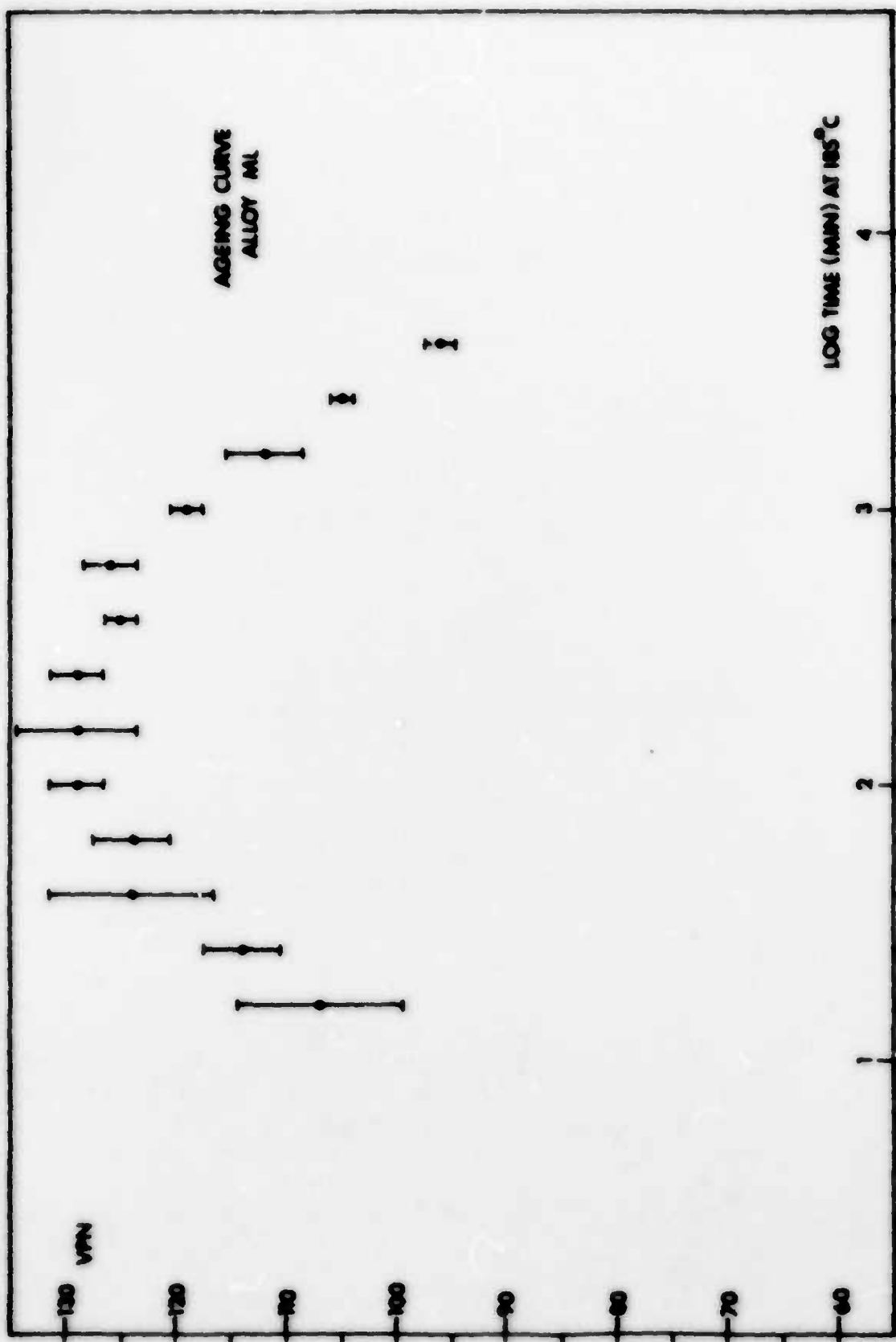
The JSM 35X was also used to estimate the area fraction of a fracture surface covered by intergranular and transgranular fracture modes. This quantitative fractography was performed by a point counting method whereby a 42 point grid was placed on the viewing screen at a screen magnification of ~ 200X. Since the intergranular fracture mode predominated, the points on the grid which covered the larger dimples characteristic of transgranular ductile rupture were counted, and the remaining points attributed to intergranular fracture. The results thus represent a percentage area covered by each fracture mode. Several fields of view were counted on each type of

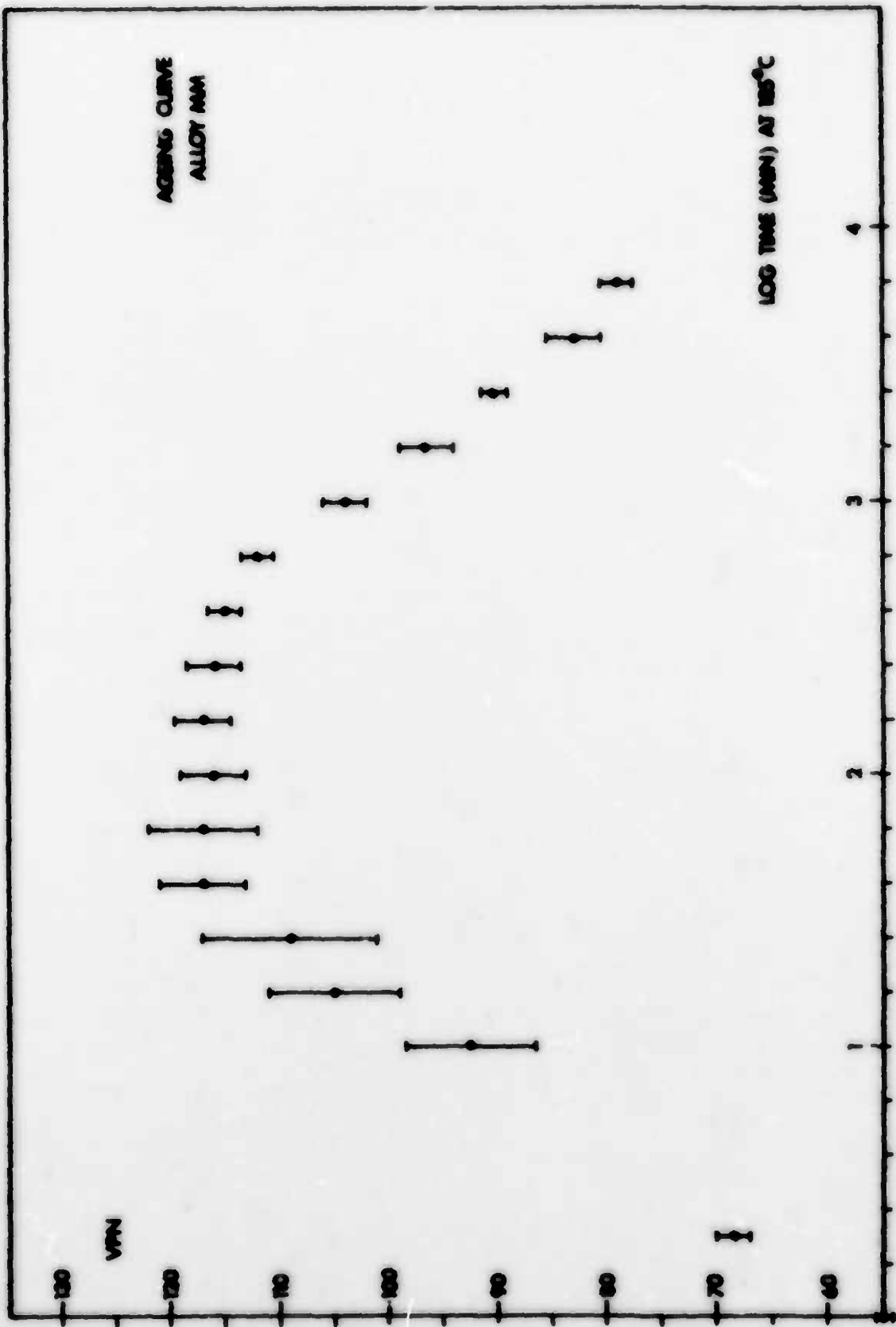
alloy, and the results for that alloy averaged. Although these counts may not provide an authoritative statistical significance, the quantitative fractography did provide an adequate comparison between alloys of the relative amounts of ductile rupture fracture mode.

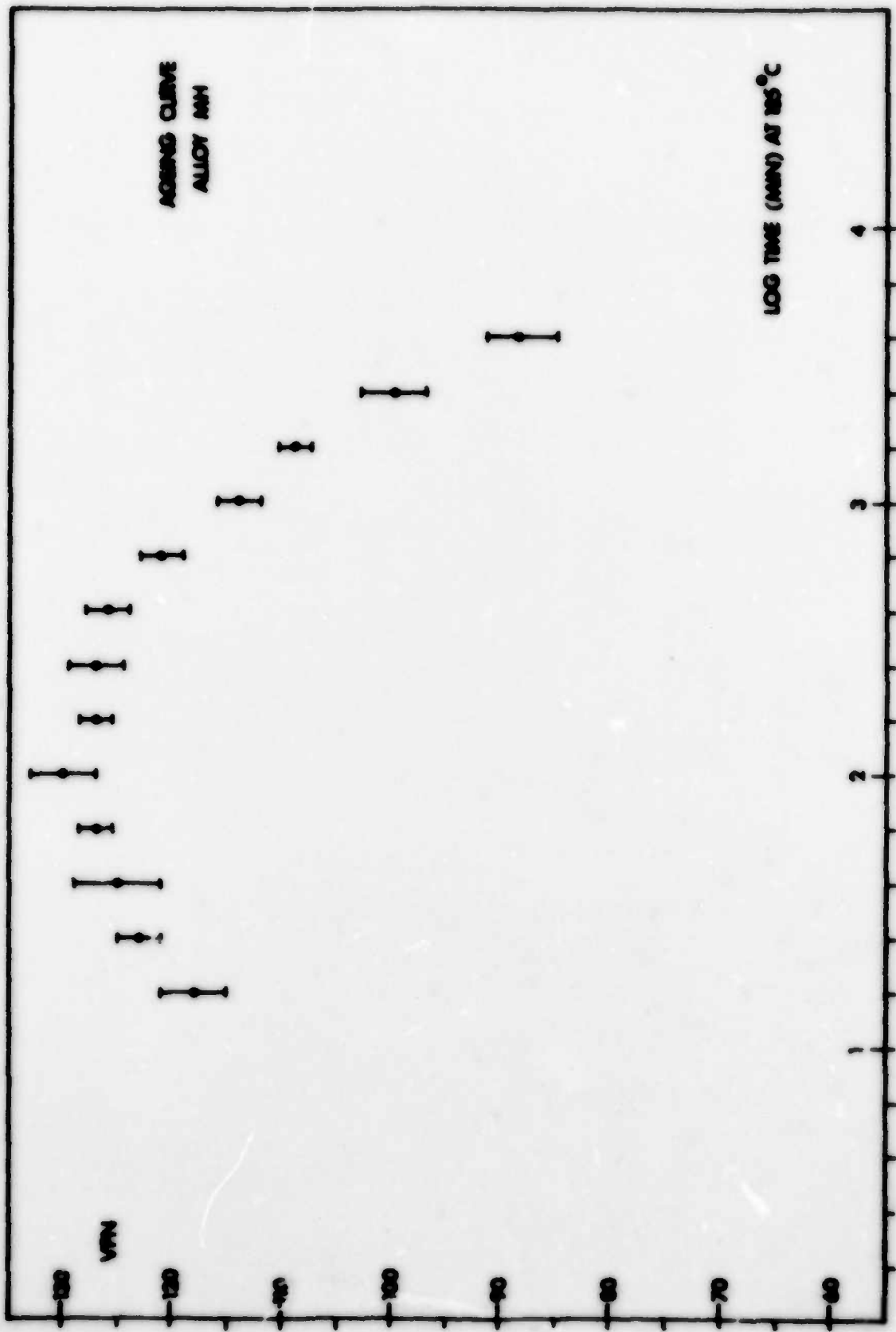
Figures 2.1 to 2.5

Ageing curves for alloys MT, ML, MM, MH and MC, respectively. Error bars represent the standard deviation for at least five hardness readings.









AGING CURVE
ALLOY MC

LOG TIME (min) AT 150°C

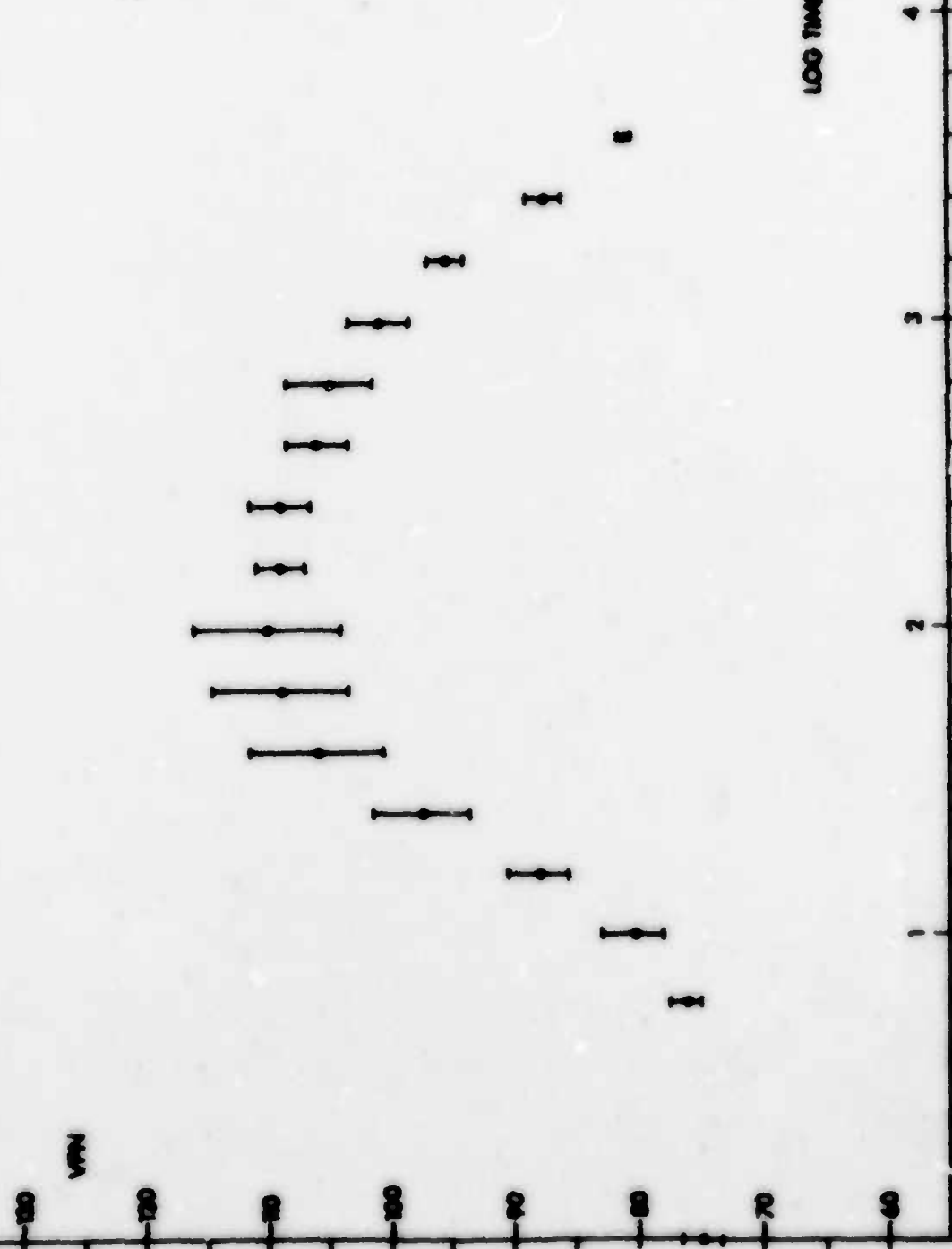


Figure 2.6

- (a) Modified strain gauge extensometer for measuring diametral displacement of tensile test specimens.
- (b) Clip gauge for measuring load line displacement of compact tension specimens.



O

O

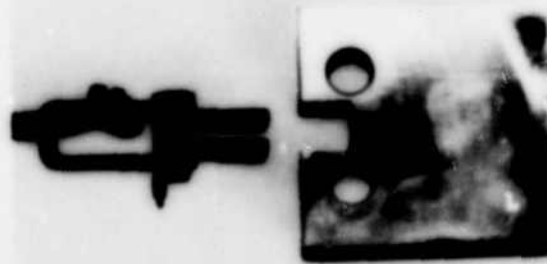


Figure 2.7

Calibration results for strain gauge extensometer.

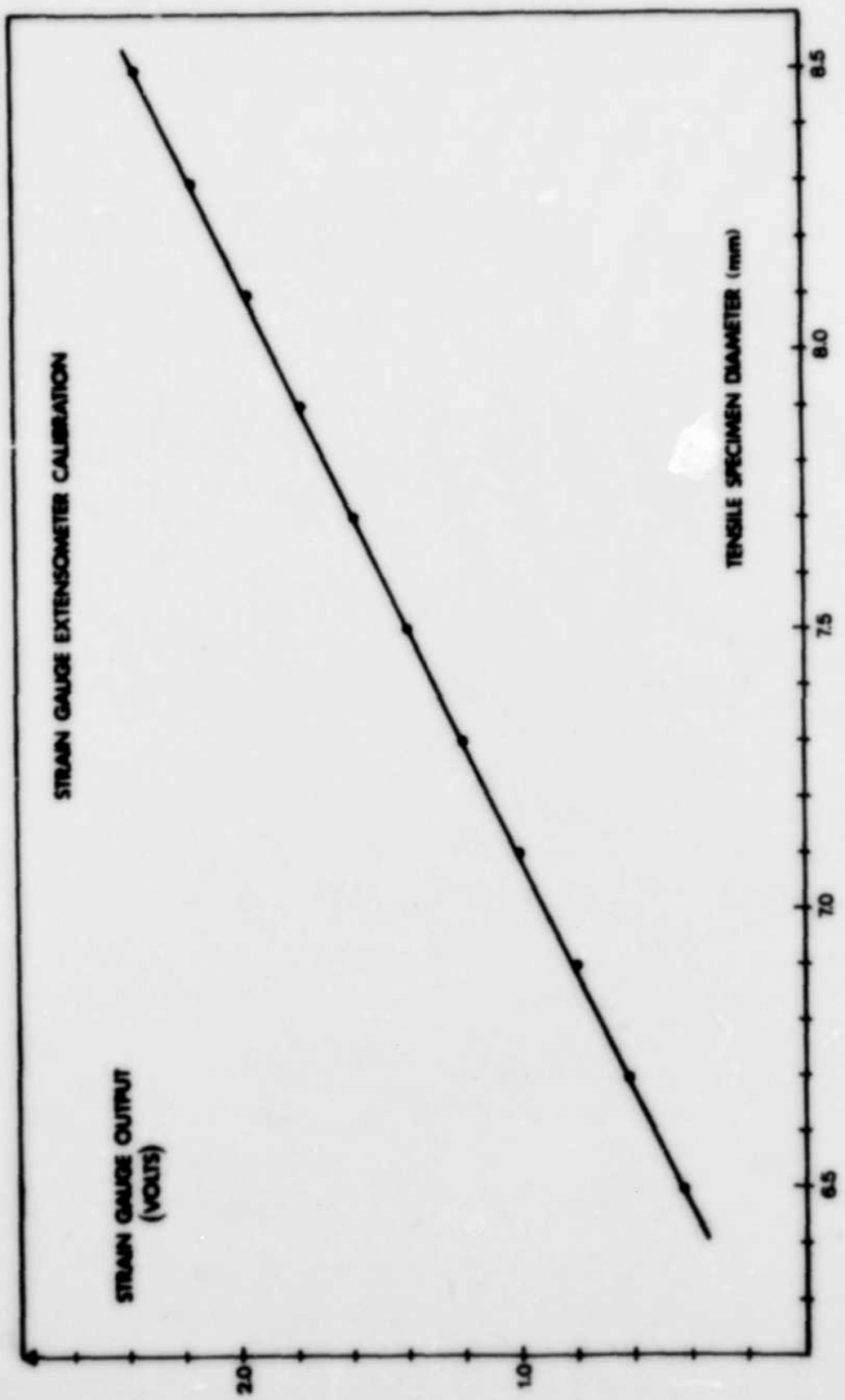
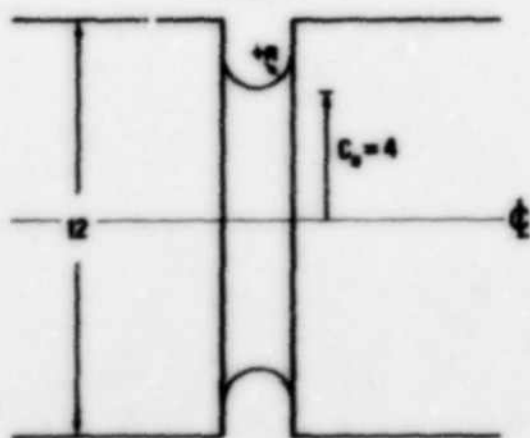
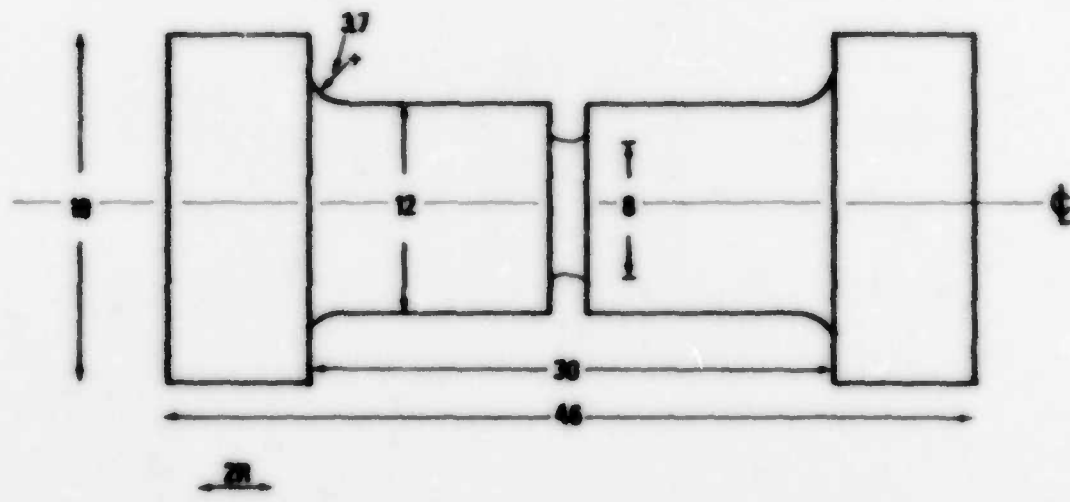
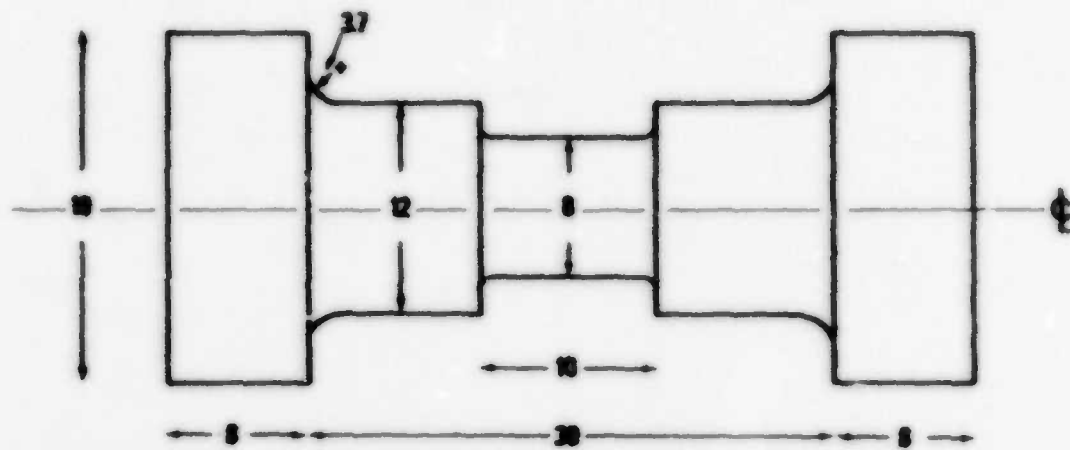


Figure 2.8

Unnotched tensile test specimen. Dimensions are in mm.

Figure 2.9

Notched tensile specimen. Dimensions are in mm. Values of
notch root diameter ($2R$) are also shown.



SPECIMEN	$2h$ (mm)
①	1.96
②	2.37
③	2.17

Figure 2.10

Bridgman analysis for stress and strain distributions in the minimum cross-section of a notched tensile specimen.

Figure 2.11

Compact tension specimen. Dimensions are in mm.

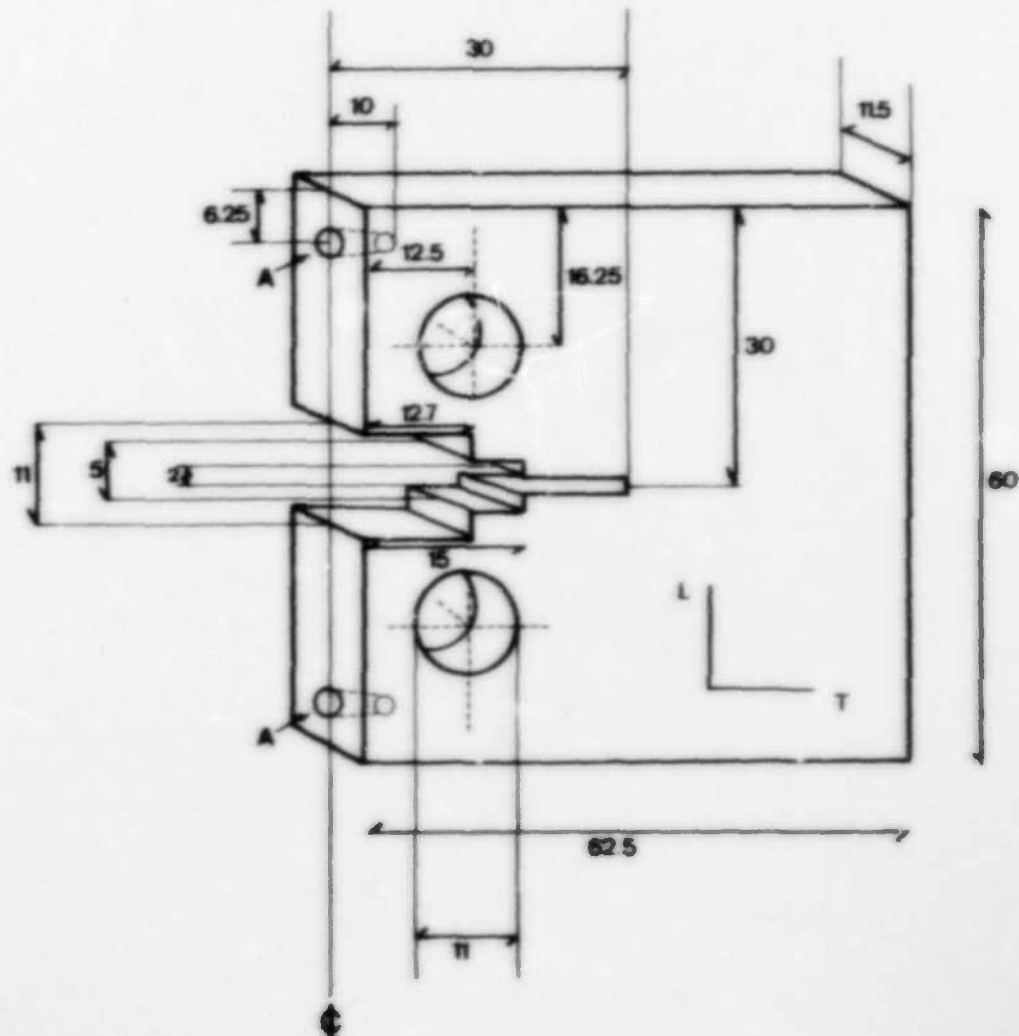
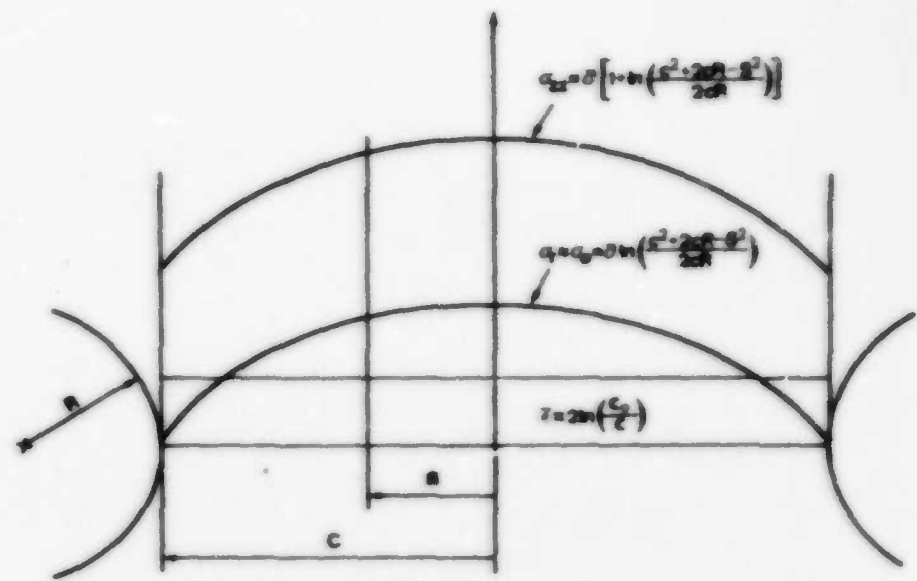


Figure 2.12

Calibration curve for clip gauge used to measure load line
displacement of compact tension specimens.

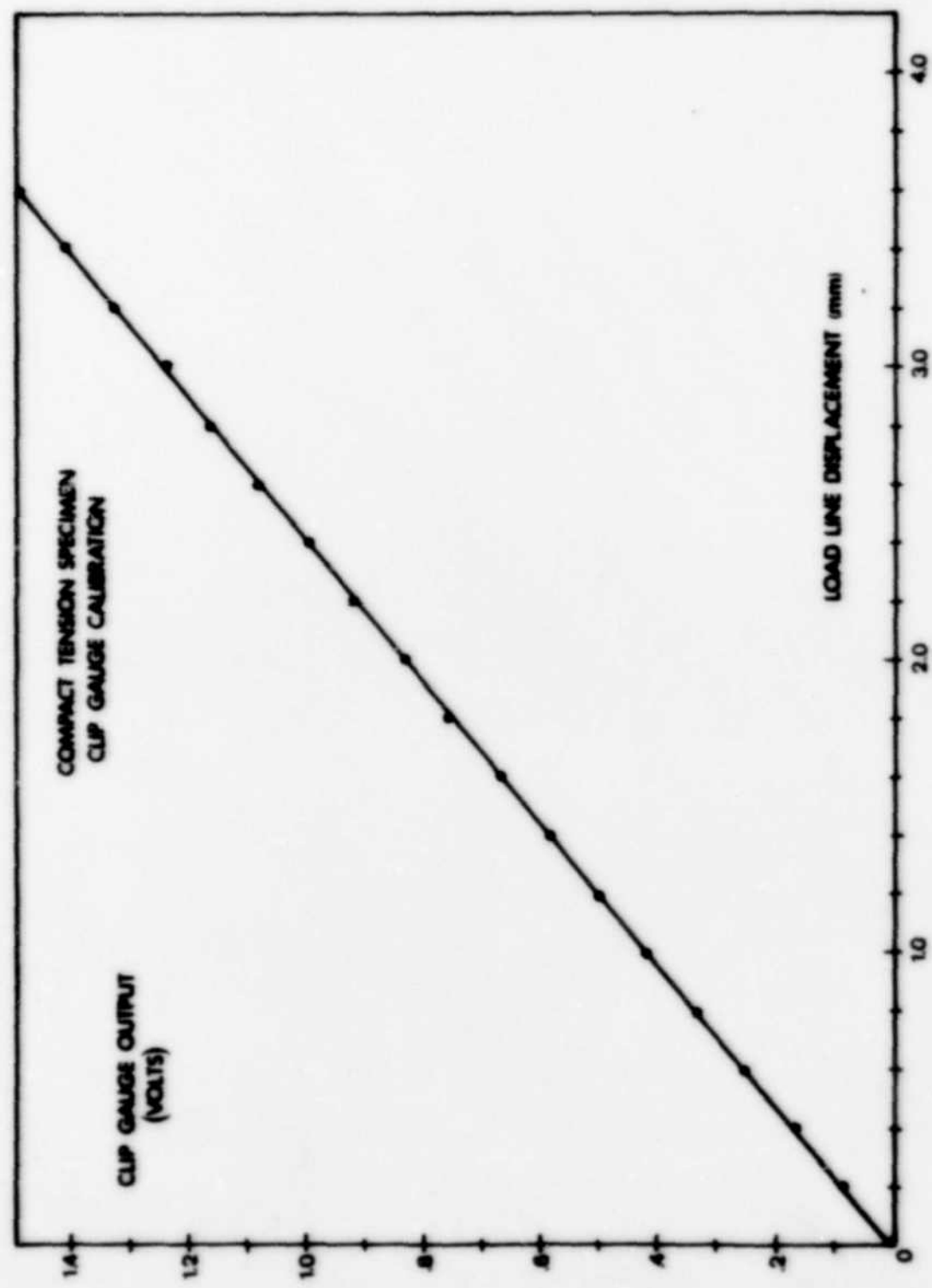


Figure 2.13

Typical test record of load versus load line displacement
for a compact tension specimen.

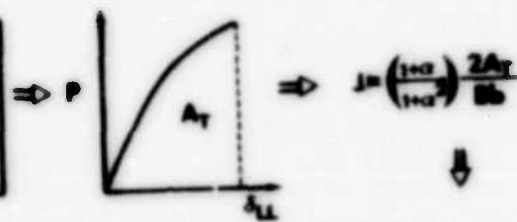
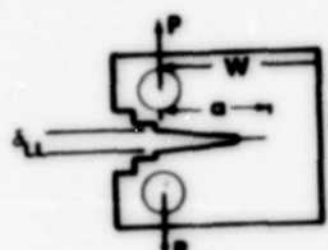


Figure 2.14

Schematic of procedure for I_{lc} determination.

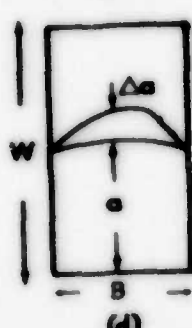
Figure 2.15

SEM ray diagram for electron channelling pattern conditions.

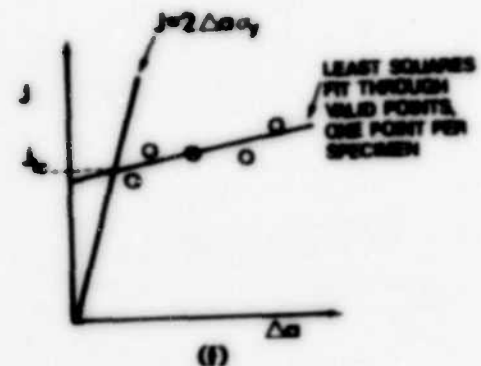


$$\Rightarrow A_U = \left(\frac{1}{16\pi} \right) \frac{2w^2}{h} r^2$$

(a)



(d)



(e)



Figure 2.16

Fracture surface of compact tension specimen from alloy MN
showing crack front shape before and after crack extension.
Direction of crack propagation is from bottom to top.

Figure 2.17

Electron channelling pattern typical of those from
undeformed material. Alloy ML. Backscattered electron
signal. Differentiated. $\theta=10^\circ$



1mm



Figure 2.18

Typical map of crack tip plastic zone obtained by electron
channelling pattern technique.

ALLOY MM
CTS #58
PLASTIC ZONE
ON MID-PLANE
 $K = 39.3 \text{ MPa}\sqrt{\text{m}}$

100 μm

FATIGUE CRACK

$r_p = 430 \mu\text{m}$

Chapter 3

EXPERIMENTAL RESULTS

3.1 Tensile Tests

3.1.1 Unnotched Tensile Tests

The conventional stress-strain characteristics of the alloys were determined from the load versus diametral displacement plots of the Hounsfield type tensile specimens described in Section 2.2.1. An experimental trace from one of these tests on alloy ML is shown in fig. 3.1. The general shape of the curve was the same for all the alloys in that, after yield the curve was very flat, rising only slightly to maximum load before decreasing gradually to final fracture. From these traces, engineering stress-strain curves were derived; typical plots for all alloys are shown in fig. 3.2. Values for 0.2% yield stress σ_y and ultimate stress σ_u determined from the engineering stress-strain curves are listed in Table 3.1. Multiple tests were performed for each alloy.

Comparing values of yield strength from Table 3.1, the ternary alloy MT yielded at 279MPa, somewhat lower than the other alloys. The dispersoid containing alloys ML, MM and MC have effectively the same yield strength within an experimental error of 15MPa. Alloy MM is slightly higher at 323MPa. Values for σ_u follow the same trend, i.e. 313MPa for MT; 350MPa for ML, MM and MC; and 380MPa for ML.

Table 3.1

Summary of Results - Unnotched Tensile Tests

Alloy	σ_y (MPa)	σ_u (MPa)	N	k (MPa)	ϵ_u	ϵ_f	σ_f (MPa)
MT	279	313	0.050	379	0.06	0.08	332
ML	318	350	0.051	419	0.12	0.24	417
MM	310	347	0.054	420	0.11	0.29	419
MH	323	380	0.062	471	0.10	0.26	463
MC	309	354	0.062	438	0.12	0.40	452

True stress-strain curves were also obtained from the load versus diametral displacement traces, with typical plots shown in fig. 3.3. From these curves, values shown in Table 3.1 for true strain at fracture ϵ_f , true stress at fracture σ_f and uniform strain ϵ_u (i.e. true strain at ultimate stress σ_u) were obtained. The ductility of alloy MT given by the true strain at fracture is quite low ($\epsilon_f=0.08$). Alloys ML, MM and MH have roughly the same fracture strain ($\epsilon_f=0.27$) while alloy MC exhibits the greatest ductility ($\epsilon_f=0.40$). Results for the uniform strain ϵ_u are much higher in the dispersoid containing alloys than the ternary MT. However, no discernible trend is evident within the dispersoid containing alloys, perhaps due to the difficulty in distinguishing strain at the ultimate stress for such flat stress-strain curves. The true stresses at fracture σ_f show the same variation as the yield stresses discussed above, with the exception of alloy MC which falls between MM and MH.

The true stress - true strain curves between yield and specimen necking were found to fit the general flow curve expression of

$$\sigma_t = kc^N \quad (3.1)$$

where k is a constant and N is the strain hardening exponent. To determine the values of these constants for each alloy, plots of $\log \sigma_t$ versus $\log c$ for the portion of the curve just past yield were constructed as shown in fig. 3.4. Values of N from the slope of these plots and k from the intercept at $\log c=0$ are given in Table 3.1. Results for k follow the same pattern as for σ_u and reflect the capacity of each alloy for strain hardening. Table 3.1 shows that values for N do not vary widely, ranging from 0.050 for MT to 0.062 for alloys MH and MC. Although the variation is slight, N does increase with increasing amounts of dispersoid, a trend that emerges when the lines are plotted from a common origin as in fig. 3.5.

3.1.2 Notched Tensile Tests

The procedure for determining the variation in alloy fracture strain in response to changes in the stress state of notched tensile specimens was discussed in Section 2.2.2. The stress state in the specimen gauge length was varied by using different notch root radii R as shown in fig. 2.10. Fig. 3.6 shows the response of the load versus diametral displacement trace to changes in R for alloy MH. As expected, when R decreases, the fracture strain decreases and the strain hardening rate increases due to increased constraint. Multiple tests were performed for each material and value of notch severity, and results are presented in terms of the effective plastic strain to fracture $\bar{\epsilon}_f$ versus stress triaxiality $\sigma_u/\bar{\sigma}$ from eq. (2.4). These results, displayed in fig. 3.7 and Table 3.2, show that alloy MT has a

very low fracture strain at all stress triaxialities tested. The fracture strains of alloys ML and MM, though progressively higher, are not strong functions of σ_u/σ . Alloys MH and MC both show a more pronounced decrease in $\bar{\epsilon}_f$ at high stress triaxialities; alloy MC actually becomes slightly less ductile than alloy MH under these conditions.

Table 3.2

Summary of Notched Tensile Test Results

Alloy	Stress Trixiality (σ_u/σ)	Mean Fracture Strain $\bar{\epsilon}_f$
MT	1.16	0.014
	1.32	0.012
	1.61	0.011
ML	1.16	0.114
	1.32	0.108
	1.61	0.068
MM	1.16	0.139
	1.32	0.122
	1.61	0.097
MH	1.16	0.209
	1.32	0.200
	1.61	0.138
MC	1.16	0.227
	1.32	0.224
	1.61	0.130

3.2 Fracture Toughness Tests

Section 2.3 has outlined the method for measurement of the critical fracture parameters K and J for the onset of crack extension using compact tension specimens. Although it was originally intended to test all CT specimens at precisely the same value of a/W , this aim was found to be experimentally impractical due to uncertainties caused by curvature of the fatigue crack front, the optical method of crack length measurement and the load shedding technique for growing the crack. Therefore, even though the desired value of a/W of 0.53 was not always achieved, the crack length for most specimens fell within the ASTM E399 standard range for a/W of 0.45 to 0.55. Typical load versus load line displacement traces for all the alloys at approximately the same value of a/W are shown in fig. 3.8. Due to the geometry of the specimens and the method of testing, it was possible to measure K_Q according to the ASTM E399 standard and J_{Ic} according to the method of Clarke and Landes (1979) for each specimen, using the same load versus load line displacement trace.

3.2.1 Plane Strain Fracture Toughness (K_{Ic})

K_Q for each compact tension specimen was calculated using the load P_Q given by the 95% slope secant line construction of ASTM E399 standard. These values of K_Q did not qualify as valid values of K_{Ic} due to the excessive plasticity at the crack tip; both validity criteria of $P_{max}/P_Q < 1.10$ and $\delta > 2.5 (K_Q/\sigma_y)^2$ were violated. The specimen strength ratio given in the ASTM standard as a measure of relative toughness for non-valid K_{Ic} specimens was not used for

several reasons: in many cases, specimens were not tested until maximum load so that a true ν_{max} was not always available. Also, when Prince (1977) calculated the specimen strength ratio for similar alloys he found that the results did not give a realistic comparison of toughness. Because the specimen strength ratio is mainly a function of the maximum load sustained and the specimen geometry, results reflect a quantity measured after considerable crack extension may already have occurred. Since the aim of the present study is to focus on parameters for the onset of crack extension, it was felt that K_Q provided the best available comparative toughness parameter arising from the plane strain fracture toughness tests.

The resulting K_Q for each alloy is shown in Table 3.3. Since K_Q can vary with crack length, values of Table 3.3 represent an average of at least four tests of specimens in the a/W range 0.55 to 0.60. Error figures represent the standard error. The trend is clearly one of increasing K_Q as the amount of added manganese increases, with the commercial purity alloy (MC) slightly less than MR.

Table 3.3
Summary of K_Q Values

Alloy	K_Q (MPa $\sqrt{\text{m}}$)	
MT	28.2	±0.4
ML	35.9	±0.3
MM	39.6	±0.3
MR	43.6	±0.6
MC	41.2	±1.0

3.2.2 Ductile Fracture Toughness (J_{Ic})

Although K_Q from the plane strain fracture toughness tests provides a toughness ranking of the alloys, its failure to meet the valid K_{Ic} requirements makes it questionable as a quantifiable fracture criterion. The ductile fracture toughness given by the J -integral at incipient crack growth was thus measured using the procedure developed by the ASTM Task Group E24.01.09 on elastic-plastic fracture (Clarke et al., 1979).

Typical load P versus load line displacement δ_{LL} traces for compact tension specimens of all the alloys are shown in fig. 3.8. For each test, the area A_p was determined by counting the squares under the curve, and J was calculated from equation (2.6), described in Section 2.3.2. This enabled J to be plotted against the amount of crack extension Δa for each specimen; these results are shown in fig. 3.9. The resistance to crack extension line was then calculated by the linear regression analysis of these data points. J_{Ic} was determined from the intersection of the resistance line and the blunting line, and the tearing modulus T was calculated from equation (1.43) using the slope of the resistance line dJ/da . The resulting values of J_{Ic}

and T are given in Table 3.4.

Table 3.4

Summary of ductile fracture toughness results.

Alloy	J_{lc} (N/mm)	$dJ/d\alpha$ (N/mm ²)	T
MT	11.2	3.33	2.7
ML	19.3	1.96	1.9
MM	25.2	9.96	6.4
MR	30.2	29.11	16.4
MC	28.8	11.52	7.3

These results for J_{lc} reflect the same basic trend as K_Q and σ_c at high triaxiality stress states, i.e. MT < ML < MM < MR. The trends in $dJ/d\alpha$ and T are similar except that alloy MT is slightly larger than alloy ML. This is probably a consequence of the lack of data points for J in alloy MT at Δa less than 1mm. This difficulty in obtaining small values of crack extension in alloy MT is indicated by the typical $P-\delta_{LL}$ trace of this material in fig. 3.8. At maximum load, sudden crack extension occurred so quickly along the entire crack front that it proved impossible to unload the specimen rapidly enough to obtain a crack extension less than about 1mm.

With the other alloys initial crack extension occurred on the mid-plane, giving a thumb-nail appearance. The shape of the crack front before and after crack extension could be obtained from SEM measurements of a and Δa at multiple points through the thickness of the specimen. Although the details of the fracture surface appearance will be described in Section 3.5, the crack front shape will be

considered here. For comparison, fig. 3.10 shows the crack front profiles for CT specimens of MT, ML and MH. Although locally jagged and discontinuous, the extended crack front for alloy MT (fig. 3.10(a)) is roughly constant across the width of the specimen. However, the crack fronts for alloys ML and MH (fig. 3.10(b) and (c), respectively) show an increasing tendency for greater extension in the plane-strain region of the mid-plane and less extension in the plane-stress region near the surfaces. These results suggest that increasing the manganese content of the alloys causes an increase in the constraint required for the crack to extend. This finding is also consistent with the relatively high value of T in Table 3.4 for alloy MH where T represents the resistance to unstable crack growth.

3.3 Plastic Zone Size Measurement

The mapping of crack tip plastic zones based on electron channelling patterns was performed as described in Section 2.4.2. Figure 3.11 is an example of the resulting plot of plastic zones for specimens of alloy ML at several values of K . A line drawn through these points then describes the profile in the ST plane of the crack tip plastic zone.

One advantage of the ECP method is that the plastic zone at any desired location through the thickness of the specimen can be mapped. Thus, by sectioning a specimen at approximately 2.5mm intervals and plotting the plastic zone of those sections, a graphical representation of the three dimensional plastic zone can be obtained. This procedure was used on a specimen of alloy ML, with the resulting plastic zones at points through the thickness shown in fig. 3.12. This

particular specimen was loaded to produce a K of 34.5 MPa \sqrt{m} . The lines up to the plastic zone represent the crack length at each interval through the thickness. The plane of the paper represents the crack plane, and the plastic zones are shown rotated through 90° with respect to the plane in which they were actually measured. PZ3 is closest to the mid-plane and is the smallest, as would be expected from the theoretical dog-bone shape of the plastic zone (see fig. 1.8). The size of the plastic zone increases as the distance from the mid-plane increases. However, its shape changes from an almost circular arc in PZ3 to a profile with more pronounced lobes at an angle to the crack plane in PZs 2, 4 and 5. This profile is not consistent with the predicted change in shape of fig. 1.7, which indicates more pronounced lobes in plane strain. Also, the distance from the crack tip to the elastic-plastic interface perpendicular to the crack plane, r_y , shows a larger increase than does the distance directly ahead of the crack tip, r_x .

Figure 3.13 shows an interesting aspect of the crack tip region; microcracks that have opened up ahead of the main crack tip when the specimen was loaded to a K just less than that required for crack extension. These microcracks, frequently observed on plastic zone size specimens, followed grain boundaries in the plastic zone (fig. 3.13(a)). In fig. 3.13(b), the dimples characteristic of the intergranular ductile rupture micromechanisms are evident.

To evaluate the manner in which plastic zone size varies with applied stress intensity, CT specimens of each material were loaded to obtain different values of K . This procedure raised the question of what dimension of the plastic zone should be used for comparison. The main possibilities, shown in fig. 3.14, were: area of the plastic zone

forward of the crack tip; an average of the two distances r_y measured perpendicular to the crack plane to the elastic-plastic boundaries above and below the crack tip; the distance r_g measured at some predetermined angle θ to the crack tip; the maximum extent of the plastic zone size r_{\max} ; or the distance r_x measured directly in front of the crack tip ($\theta=0$). Since the mapped plastic zones were often asymmetric with respect to the crack plane, additional ambiguity would have been introduced by using r_y , r_g or the plastic zone area. In addition, the majority of the estimates of crack tip plastic zone size given in Section 1.2.2 were for a distance directly ahead of the crack tip. Therefore, r_x was chosen as the plastic zone dimension to be used for comparison and will be referred to as r_p .

In general, the equations for estimating r_p from Chapter 1 can be written in the form

$$r_p = a \frac{K^2}{\sigma_y^2} \quad (3.2)$$

where a is the variously derived constant of proportionality. For example, $a=0.007$ from equation (1.23) (Rice and Rosengren, 1968) for a material with a strain hardening exponent $N=0.05$. Results for plastic zone size measurement on individual specimens are tabulated in Table 3.5 along with other information, such as applied K and J . These results are also presented graphically in fig. 3.15 on a plot of r_p versus $(K/\sigma_y)^2$. For reference, the line shown represents $a=0.032$, predicted from the analysis of Rice and Johnson (1970). Several comments can be made regarding fig. 3.15: First, although there is considerable spread in the data, especially at higher K , the results are reasonably consistent with those of Rice and Johnson (1970).

However, the values for r_p seem to fall into two separate groupings. For r_p less than 100 μm the values are tightly grouped. Above 100 μm , values for r_p show some distinction between alloys. These groupings suggest a transition in the plastic zone size response to K at $r_p = 100\mu\text{m}$. Table 2.2 indicates that the grain size of the dispersoid containing alloys is slightly smaller than 100 μm . Thus the apparent divergence in zone size may well correspond to the elastic-plastic boundary no longer being contained by the statistically averaged first grain along the crack front.

Table 3.5

Results of Plastic Zone Size Measurements

Alloy	Specimen Number	Applied K (MPa $\sqrt{\text{m}}$)	Applied J (N/mm)	σ_y (MPa)	$(\frac{K}{\sigma_y})^2$ (mm)	r_p (μm)
MT	2	12.1	-	279	1.88	18
	1	18.2	-		4.26	50
	44	25.5	6.5		8.35	98
ML	23	12.1	-	318	1.45	25
	22	18.4	-		3.35	53
	13	25.8	7.3		6.38	97
	14	31.0	10.8		9.30	320
	21	34.5	10.5		11.8	395
MH	61	18.7	3.6	310	3.64	80
	62	30.9	9.7		9.94	235
	58	39.3	20.3		16.1	430
MH	26	12.5	-	323	1.50	57
	25	18.0	-		3.11	43
	28	29.8	9.0		8.51	125
	29	35.6	15.3		12.1	265
	27	42.2	27.6		17.1	500
MC	69	32.4	14.8	309	11.0	185
	71	36.3	17.5		13.8	190
	70	42.4	23.0		18.8	405

To investigate the relative plastic zone size between the alloys at $r_p > 100\mu\text{m}$, the best fit line for r_p versus $(K/\sigma_y)^2$ passing through the origin for each alloy is shown in fig. 3.16. (Alloy MT is not shown because its low toughness meant that crack extension occurred before a large enough K to give $r_p > 100\mu\text{m}$ could be applied.) The slope of each line in fig. 3.16 gives the value of α from equation (3.2) for each material. For the high purity, Mn containing alloys ML, MM and MH, values for α are 0.034, 0.025 and 0.023. It seems significant that α steadily decreases with increase in manganese content, i.e. 0.2wt% for ML, 0.4wt% for MM and 0.6wt% for MH. Therefore, a given applied stress intensity K creates a smaller crack tip plastic zone as the Mn-bearing dispersoid content of the alloy is increased.

3.4 Metallurgy

Optical micrographs revealing the grain structures of the alloys are shown in fig. 3.17. These photographs were taken using polarized light after the specimens had been anodized (see Section 2.5). In fig. 3.17(a), alloy MT is seen to have an equiaxed grain structure and fairly straight grain boundaries. Alloys ML, MM, MH and MC also have roughly equiaxed grain structures. However, their grain shapes are more distorted, with many of the grain boundaries curved and irregular.

Another notable feature of the optical micrographs is the presence of coarse constituent particles, as seen in fig. 3.18 for alloys ML, MM, MH and MC. Alloy MT is not shown because it contains very few coarse particles. However, the other alloys show an increasing volume fraction of coarse particles, $\text{M}_{23}\text{C}_6\text{Mn}_{23}\text{C}_6\text{C}$. Edwards

(1981) used a point counting technique on optical micrographs to estimate the volume fractions of coarse constituent particles in alloys ML, MM and MC as 0.78%, 2.03% and 6.40%, respectively. In alloys ML, MM and MR, the majority of the coarse particles are α -AlMnSi intermetallic phase which formed during casting. However, alloy MC had a much higher iron content and, therefore a greater volume fraction of coarse particles due to FeAl₃ and α -AlFeSi. As fig. 3.18 shows, the coarse particles tend to lie in transgranular strings oriented in the rolling direction. According to Edwards (1981), this orientation occurs because the coarse particles form during casting and impede grain growth during hot working. After hot working, these coarse particles generally lie along the grain boundaries. On subsequent cold working and recrystallisation, new grains nucleate on the coarse particles. Thus, at the end of recrystallization and grain growth, the coarse particles lie within the new grains.

3.5 Fractography

3.5.1 Alloy MT

Typical fracture surfaces of alloy MT are shown in fig. 3.19. At the low magnification in fig. 3.19(a), it is apparent from the fairly flat, faceted grains that the crack path is almost completely intergranular. Fig. 3.19(b) and (c) are progressively higher magnifications of the central region of fig. 3.19(a). Some small regions of transgranular fracture can be seen in fig. 3.19(b); however, these appear to be merely an accommodation process near the junction of grains. One begins to see features on the grain facets in

fig. 3.19(b), features that are much more evident in fig. 3.19(c) where grain faces have a rough, fibrous appearance. This rough appearance is due to a network of tiny dimples covering the intergranular fracture surfaces. These dimples are shown in fig. 3.20 for two intersecting grains. Also apparent is a secondary grain boundary crack. More such branchings from the main crack are evident in several pieces in fig. 3.19(a). These secondary cracks are consistent with the bifurcated crack front often observed in this alloy in the electropolished plastic zone specimens.

In fig. 3.21, the fine dimpled intergranular surface structure is more apparent. The dimples, irregular in shape but generally in the range 0.5-1.0μm diameter, also appear to be extremely shallow and flat with a membrane-like wall forming the sides of the cusp. Of particular note are the 0.1 to 0.2μm particles present in the centre of most of the dimples and which almost certainly serve as the void nucleation sites. Thus, the seemingly brittle intergranular fracture of alloy MT is seen on a microscopic scale to be a small scale ductile rupture process. These voids grow out from the particles along the plane of the PFZ and coalesce by the final rupture of a thin remaining ligament.

3.5.2 Alloy ML

Alloy ML also fractures in a predominantly intergranular manner as seen in fig. 3.22(a), although the grains are smaller than for alloy MT. In fig. 3.22(b) and (c), the large void from the centre of fig. 3.22(a) is shown at higher magnification. The surrounding intergranular surfaces have the rough appearance caused by small scale

dimples along the PFZ. The inclusions which formed the large void in fig. 3.22(c) are readily apparent. Fig. 3.23 shows several different dimple sizes in the same region. The particles in the central part of the figure are approximately one micron in diameter. The small intergranular dimples are shown again in fig. 3.24. Although not as clear as for alloy MT, most of the dimples include particles of similar size to those in MT. Many of the dimples are parabolic with particles near one end, indicating that this particular region probably separated by either shearing or tearing movement of the grains (Broek, 1978). However, except for the slightly larger amount of large voids on the fracture surface, the micromechanism of fracture for alloy MM is the same as alloy MT, i.e. ductile rupture along the intergranular PFZ.

3.5.3 Alloy MM

A low magnification view of an alloy MM fracture surface is shown in fig. 3.25(a). Its tortuous topography compared to alloy ML is due to its larger proportion of transgranular ductile rupture around coarse particles and a more distorted grain structure. At slightly higher magnification (fig. 3.25(b)) it can be seen that the majority of the fracture surface is still intergranular ductile rupture along the irregular grain boundaries. In fig. 3.25(c), several large dimples containing inclusions are surrounded by regions of small dimples. The intergranular ductile rupture regions are not shown separately for alloy MM as they are essentially the same as for alloy ML.

3.5.4 Alloy MH

Major features on the fracture surfaces of alloy MH are basically the same as for alloy MM. These are illustrated in figs. 3.26 to 3.29. At the low magnification in fig. 3.26(a), the MH fracture surface seems to be composed of patches of large dimpled ductile rupture separated by intergranular fracture regions. Figs. 3.26(b) and (c) show the large inclusion related dimples and the small intergranular ductile rupture, respectively; some intermediate size dimples can also be seen in fig. 3.26(b). Particles are evident in the high magnification view of the MH intergranular fracture surface, fig. 3.27. Two types of inclusion initiated voids were observed. In fig. 3.28, the large central inclusion created a void which grew with a large amount of associated local plasticity forming a large cusp. Alternatively, the inclusion in fig. 3.29 has apparently separated from the matrix along its interface, but there has been little void growth before final fracture. In fact, this dimple appears to be just a larger case of the small dimples of the PFZ type that surround it. It is concluded that this inclusion lay in or very near to a grain boundary PFZ and contributed to the PFZ ductile rupture in the same manner as the small particles in fig. 3.27. However, the majority of inclusion related dimples were of the type shown in fig. 3.28.

3.5.5 Alloy MC

Typical features of alloy MC fracture surfaces are shown in figs. 3.30 and 3.31. As can be seen from fig. 3.30(a), alloy MC displays a larger amount of transgranular ductile rupture than the other alloys.

Three general ranges of dimple size appear in fig. 3.30(b). Several inclusions can be seen in the larger dimples, and regions of fine intergranular dimples are also present. Often these two types are joined by small regions of intermediate size dimples. These variations in dimple size are also evident at the slightly higher magnification in fig. 3.30(c). Finally, the fine intergranular structure of alloy MC in fig. 3.31 clearly contains fine ($\sim 0.1\mu\text{m}$) particles lying in shallow dimples of the 1-5 μm diameter.

3.5.6 Summary of Fractography

Evidence gained from the fractographic analysis of regions of crack extension on compact tension specimens indicates that altering the composition of the ternary Al-0.6wt%Mg-1.0wt%Si alloy affects the micromechanisms of crack advance. The two major mechanisms which operate are intergranular ductile rupture and transgranular ductile rupture. Although a macroscopically brittle process, the intergranular fracture occurs by the ductile rupture sequence of: void nucleation at sub-micron size particles in the PFZ; void growth along the PFZ; and, ultimately, void coalescence. This process follows a low energy ductile rupture path because the size of the PFZ limits the volume of material subjected to large plastic deformation. In general, the transgranular ductile rupture begins by void nucleation at large ($>5-10\mu\text{m}$) inclusions. Because of the tendency for inclusions to congregate, it is difficult to state whether the voids form due to cracking of single inclusions or to debonding at the inclusion-matrix interface. As the alloy composition is changed by adding Mn and (in the case of MC) Fe, the degree of transgranular ductile rupture

increases accordingly. The area fractions were estimated using a point count technique described in Section 2.6. The results are shown in Table 3.6.

Table 3.6

Estimated area fraction of transgranular ductile rupture mode on compact tension fracture surfaces.

Alloy	χ Transgranular Ductile Rupture
HT	0
HL	11
HM	17
HR	22
HC	40

Figure 3.1

Typical test record of load versus diametral displacement
for an unnotched tensile specimen of alloy ML.

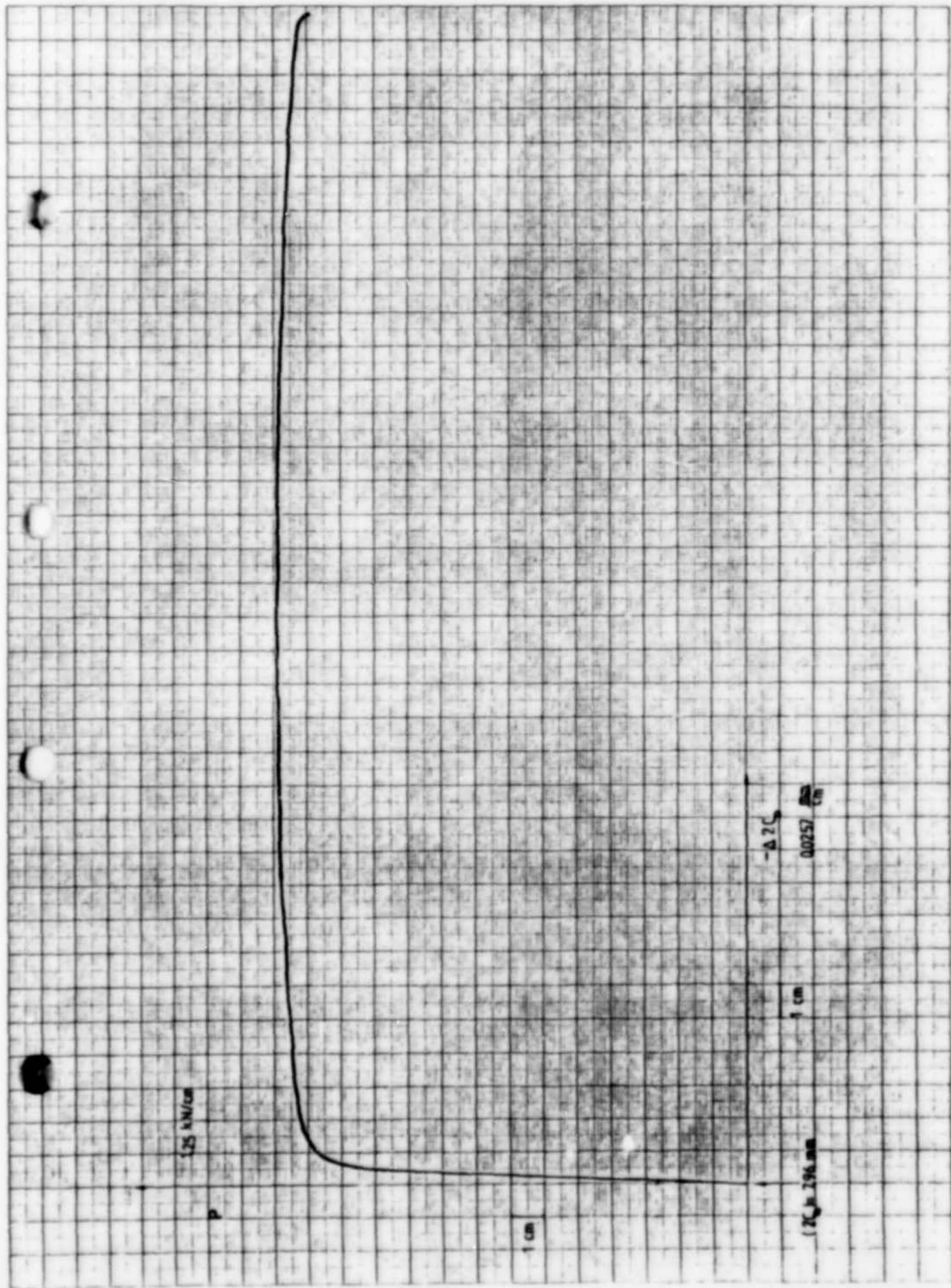
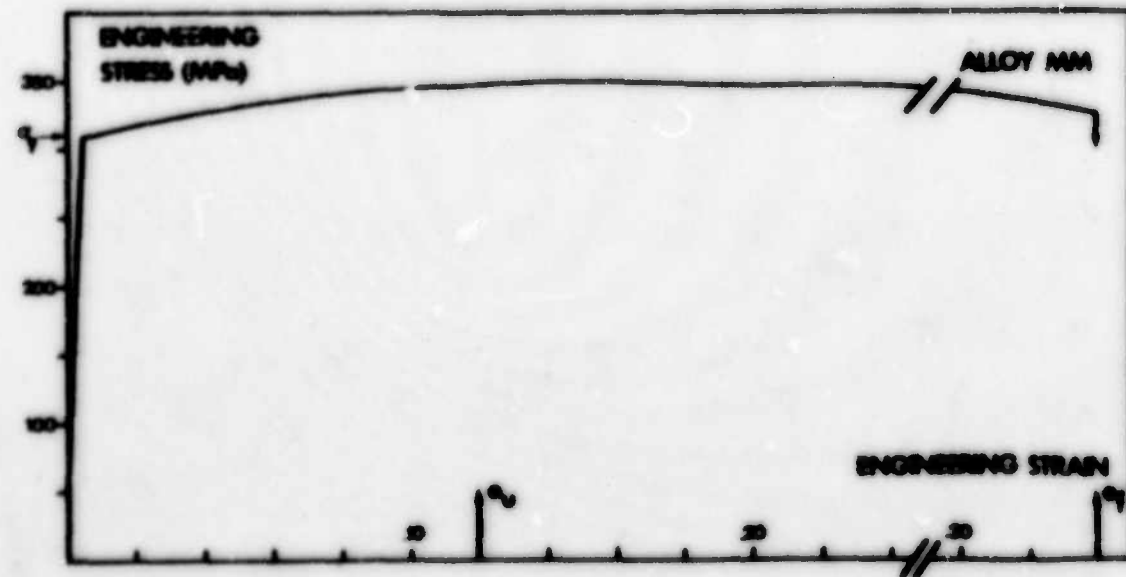
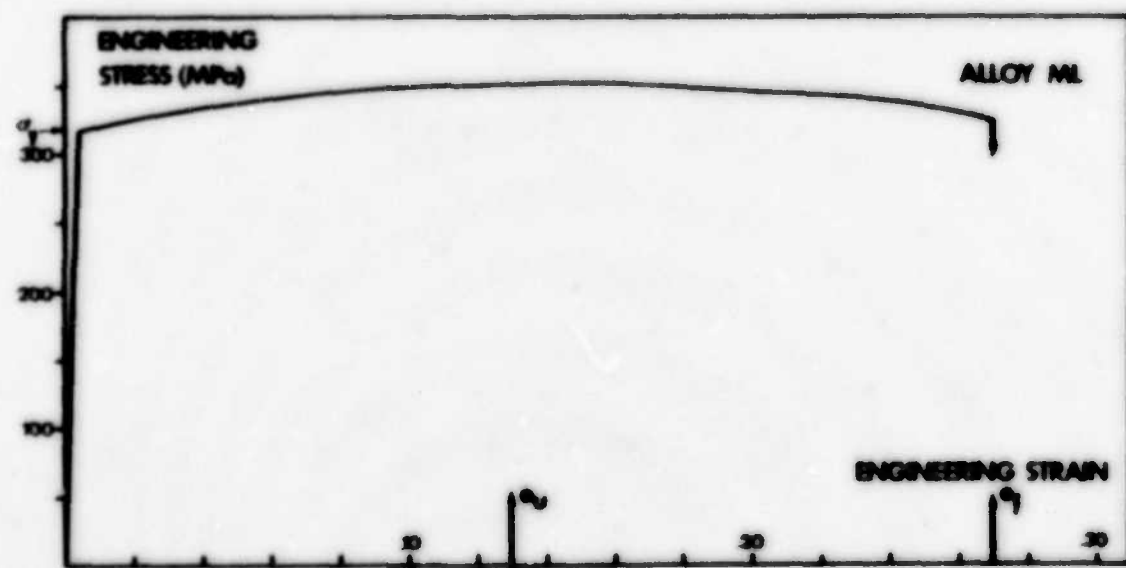
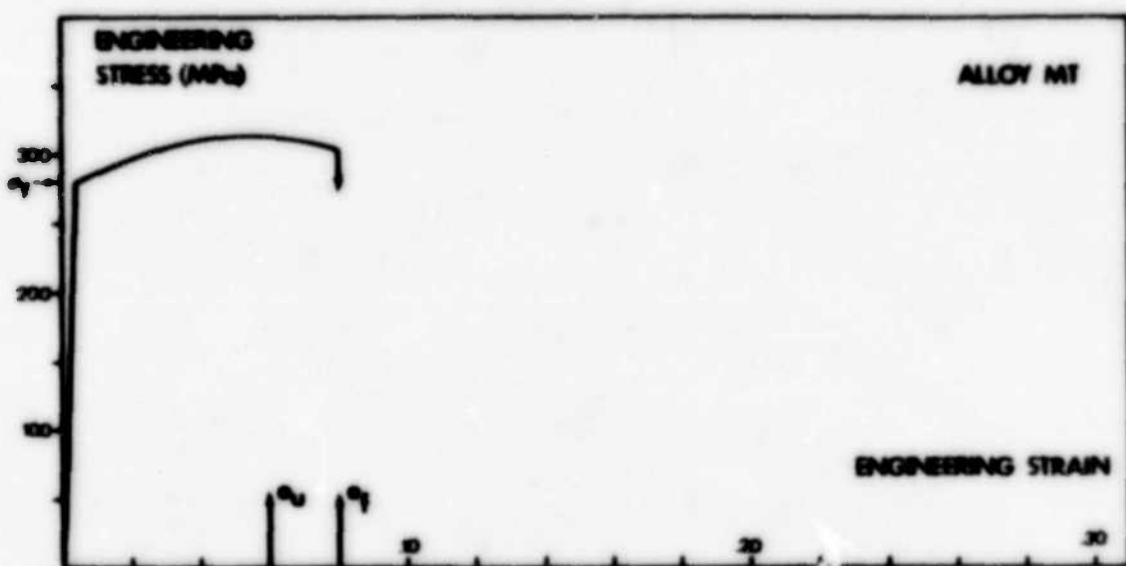


Figure 3.2

Engineering stress versus engineering strain.

- (a) Alloy MT
- (b) Alloy ML
- (c) Alloy MM
- (d) Alloy MR
- (e) Alloy MC



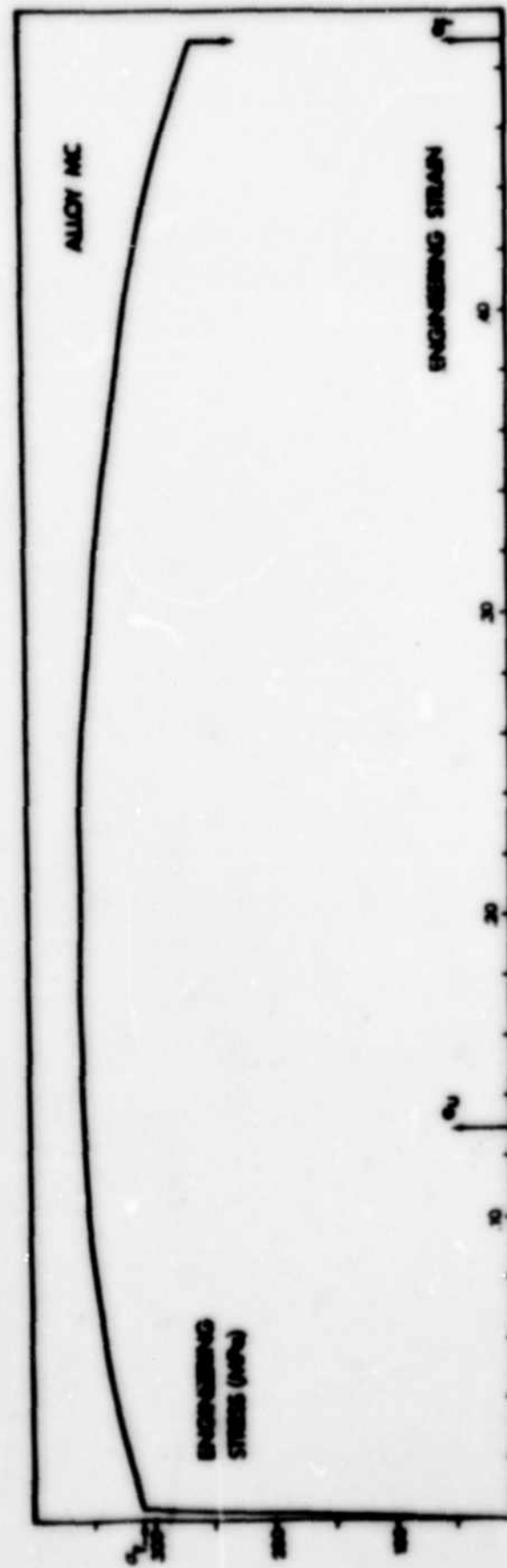
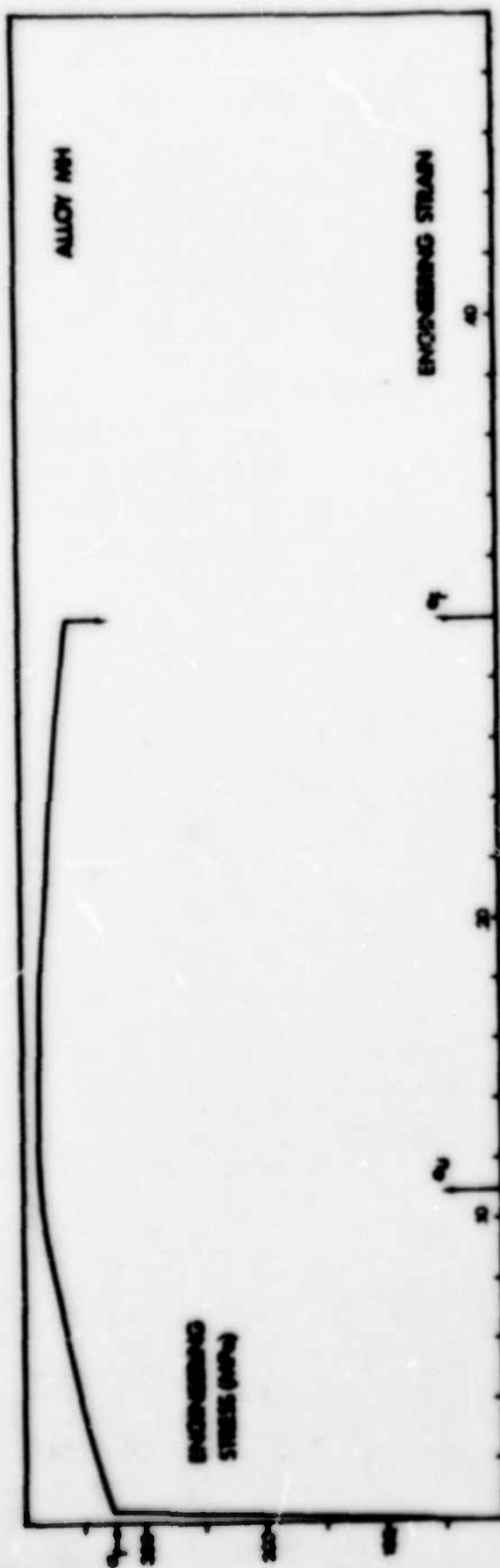
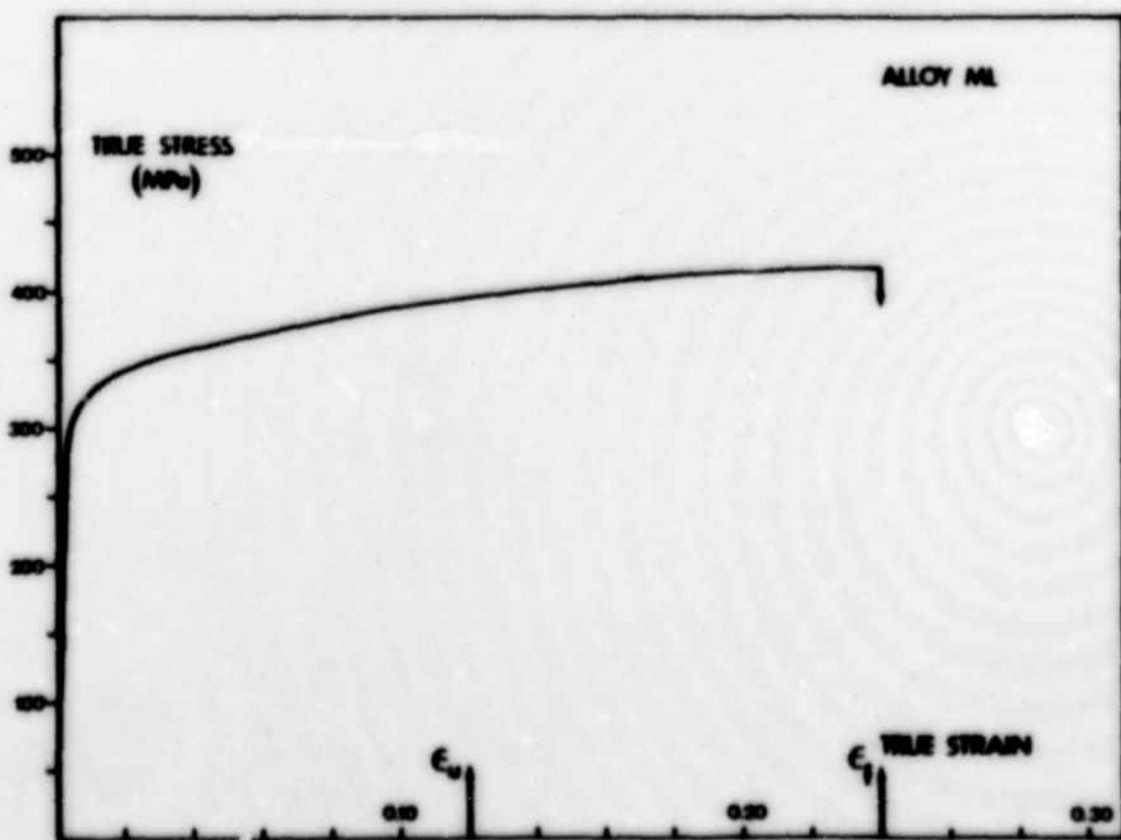
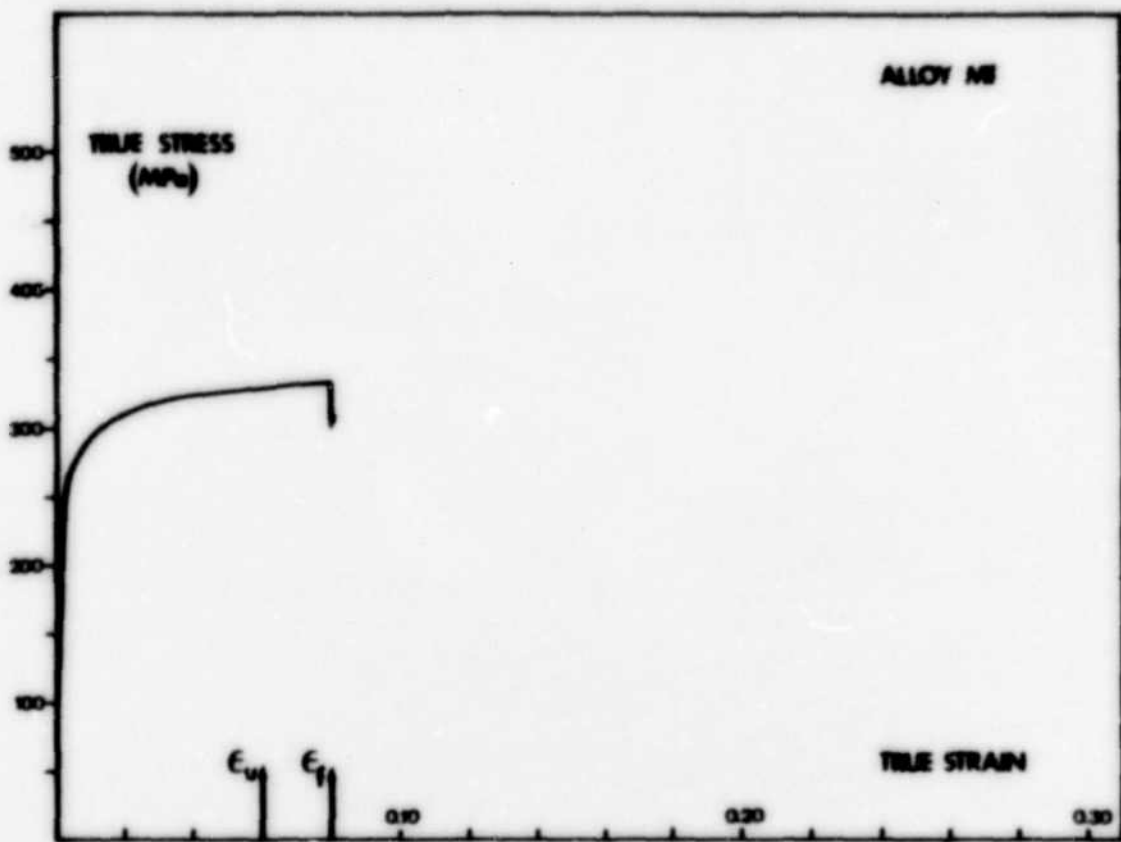
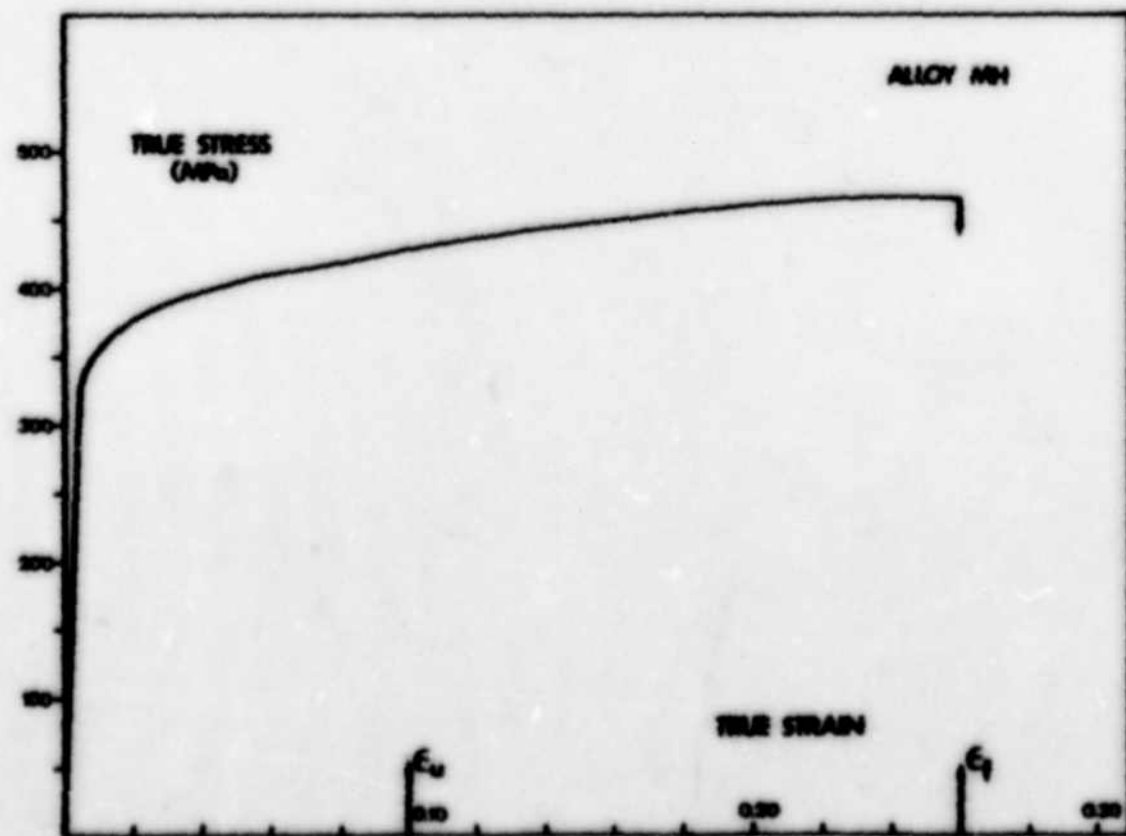
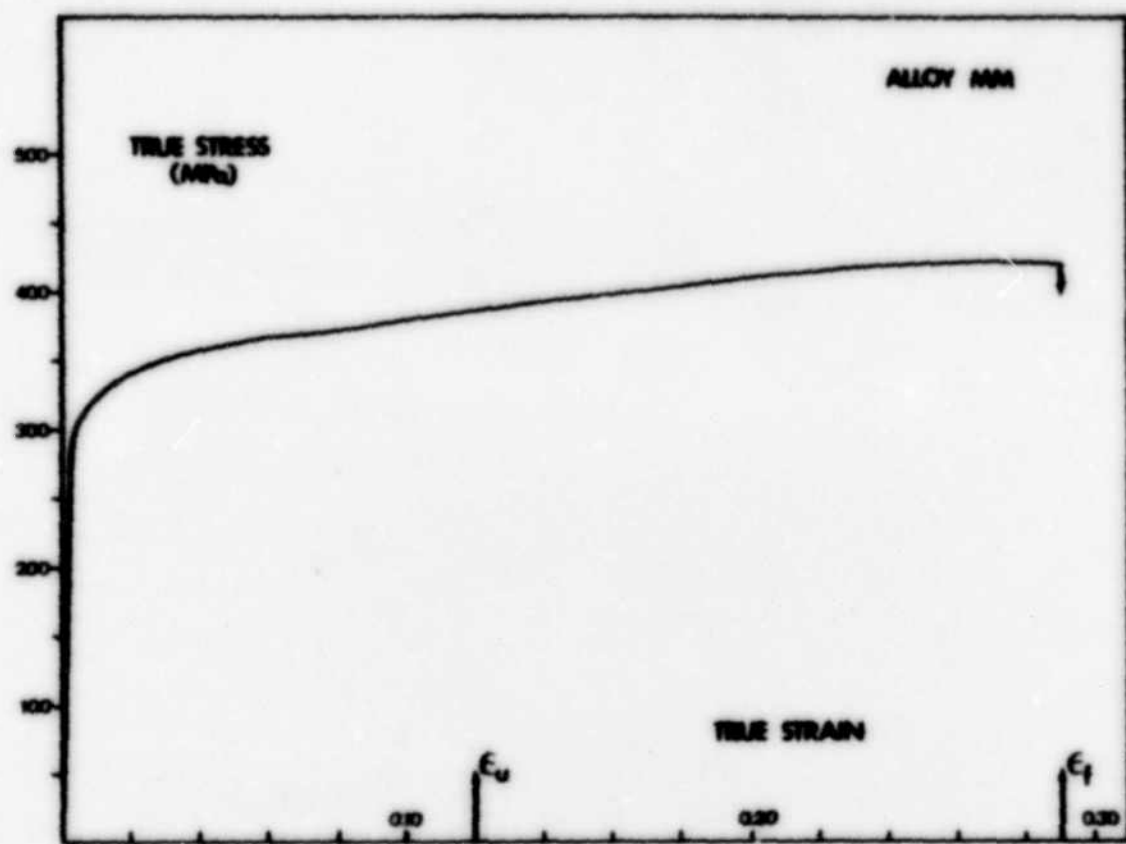


Figure 3.3

True stress versus true strain.

- (a) Alloy MT
- (b) Alloy ML
- (c) Alloy MM
- (d) Alloy MN
- (e) Alloy MC





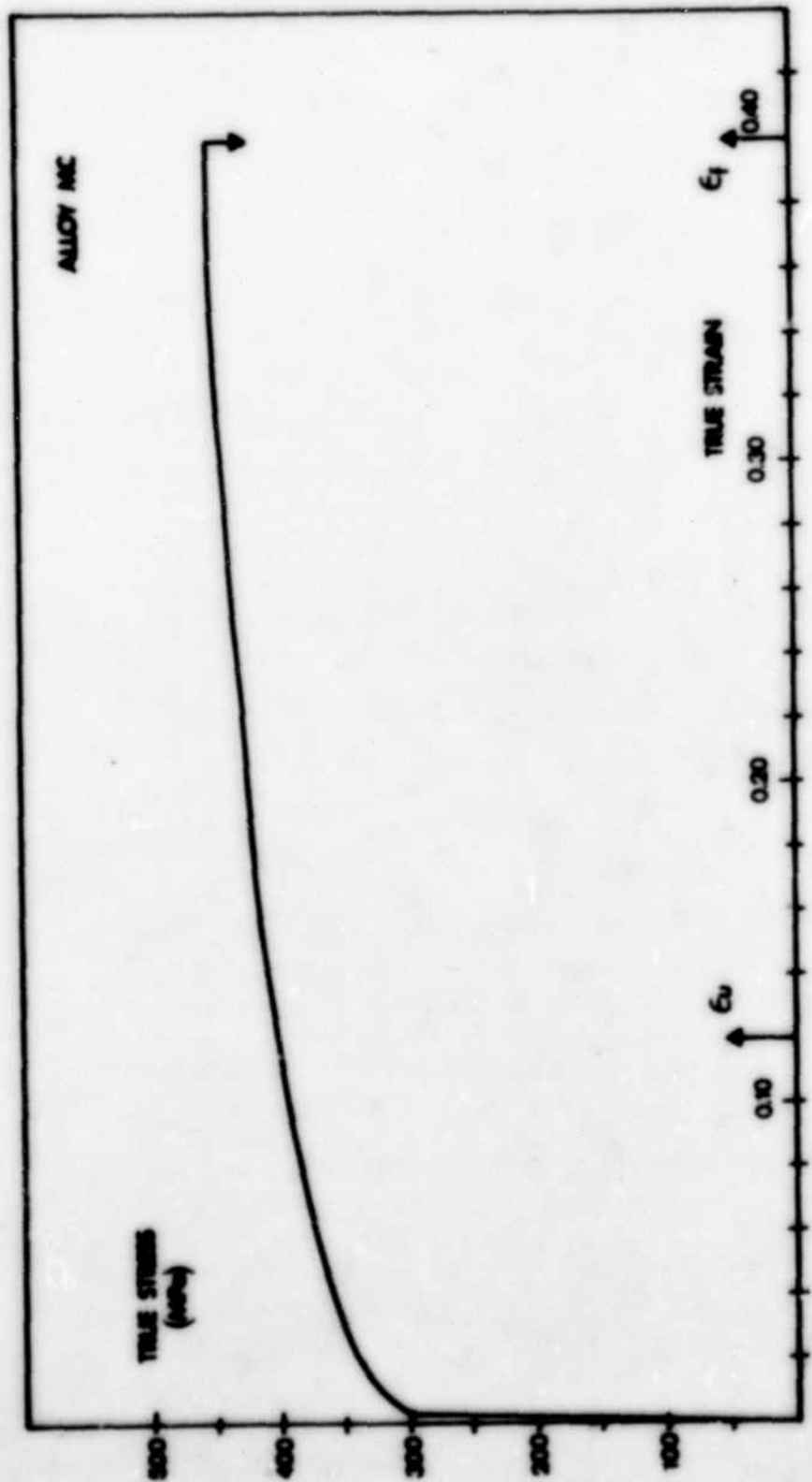


Figure 3.4

Log true stress versus log true strain.

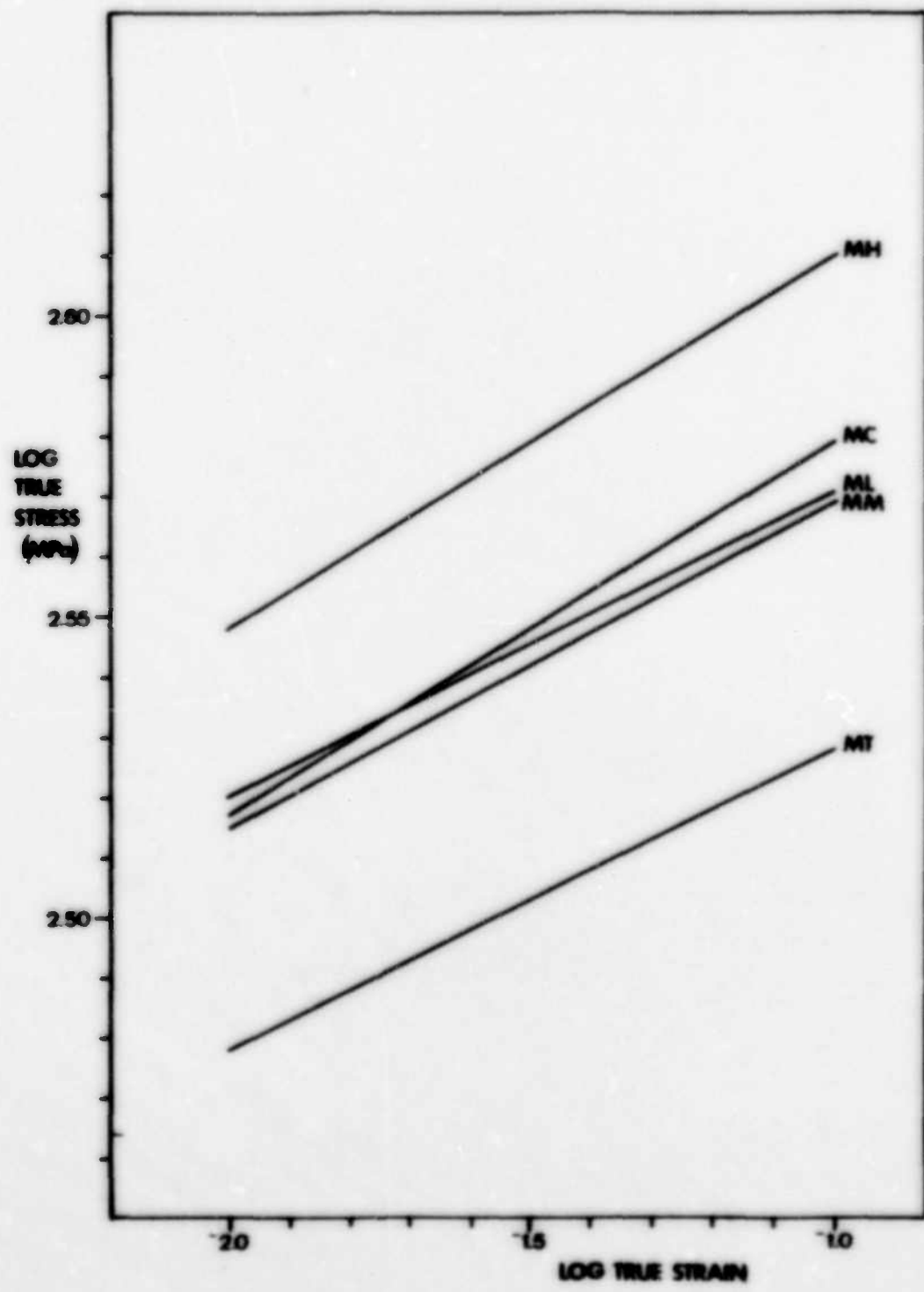


Figure 3.5

Log true stress versus log true strain for the alloys of the present study plotted from a common origin.

LOG
TRUE
STRESS
(MPa)

ALLOY	<i>N</i>
MT	0.050
ML	0.051
MM	0.054
MH	0.062
MC	0.062

10⁻¹

10⁻⁴

LOG TRUE STRAIN

MC+MH

MM

ML

MT

Figure 3.6

Variation in notched tensile test record of load versus diametral displacement for several values of R . The examples shown are for alloy M. Values of R are given in fig. 2.9.

Specimen	Initial Diameter (mm)
1	8.30
2	8.08
3	8.12

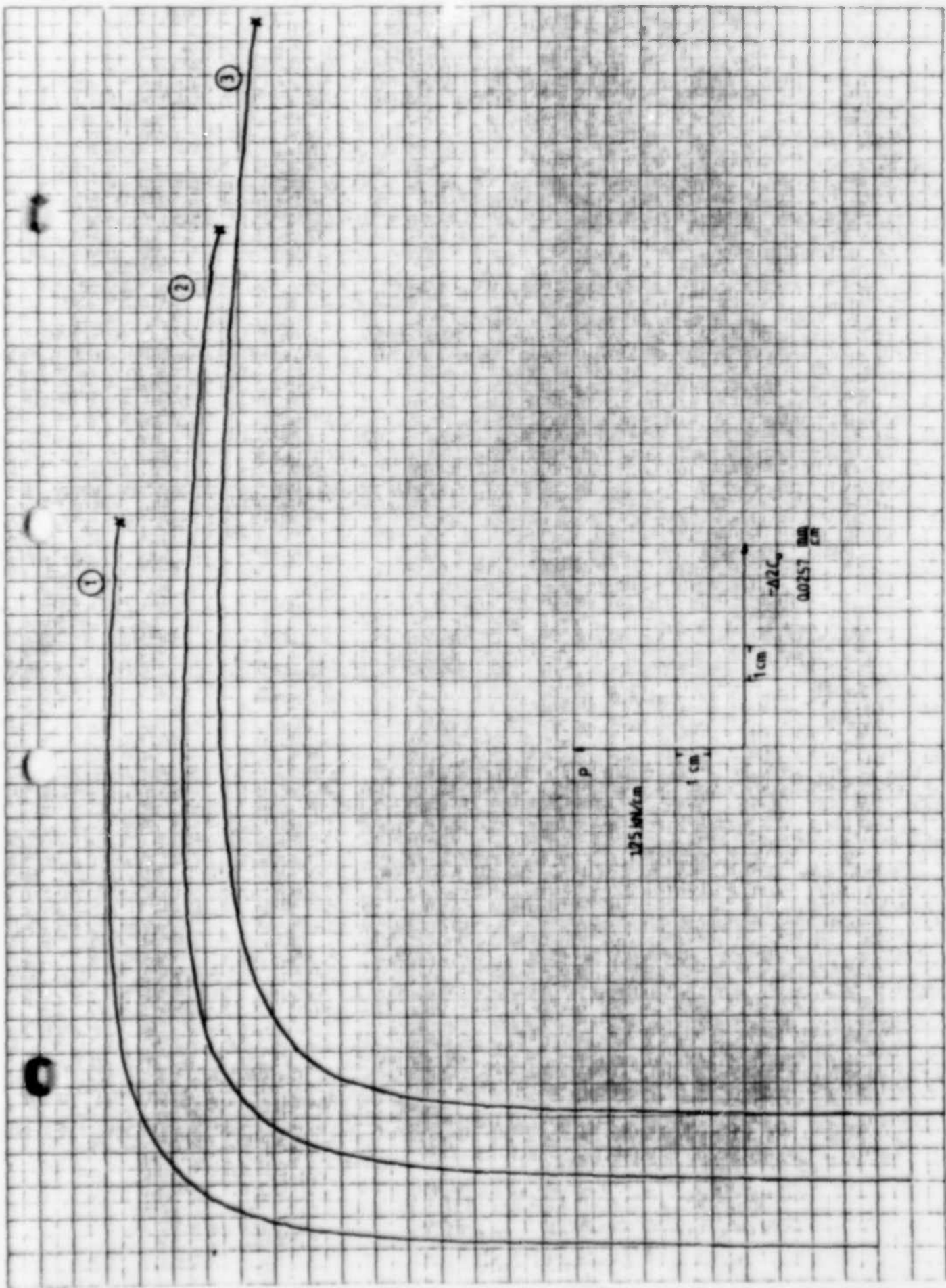
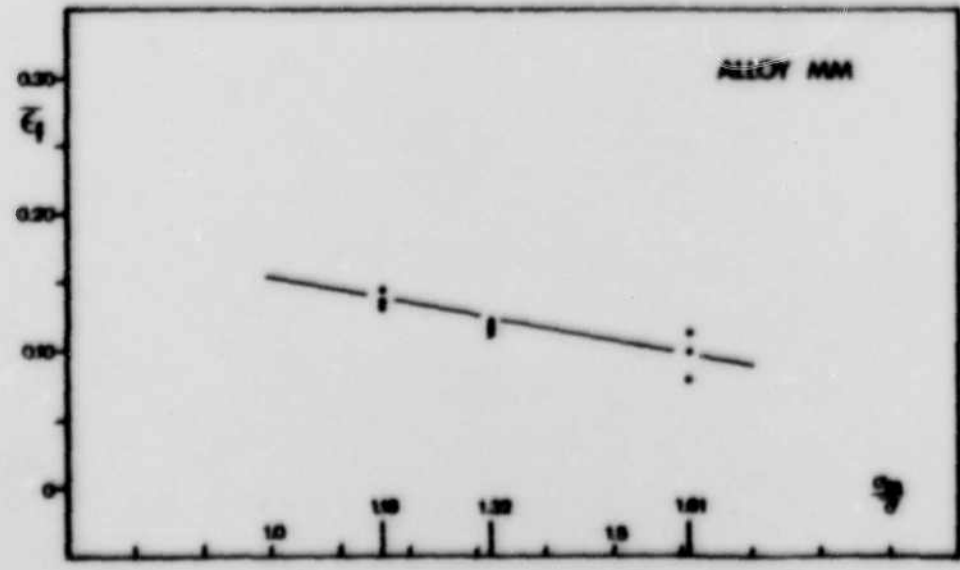
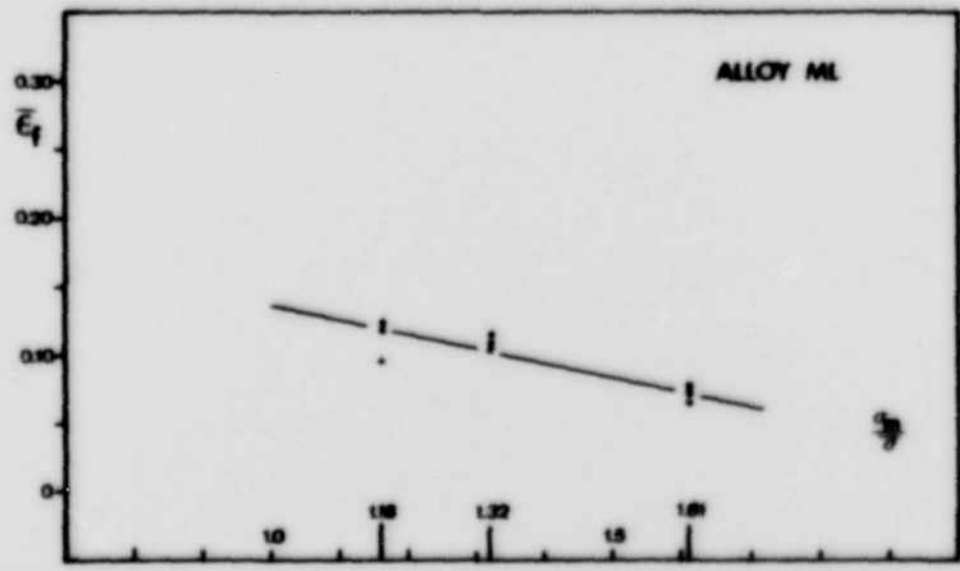
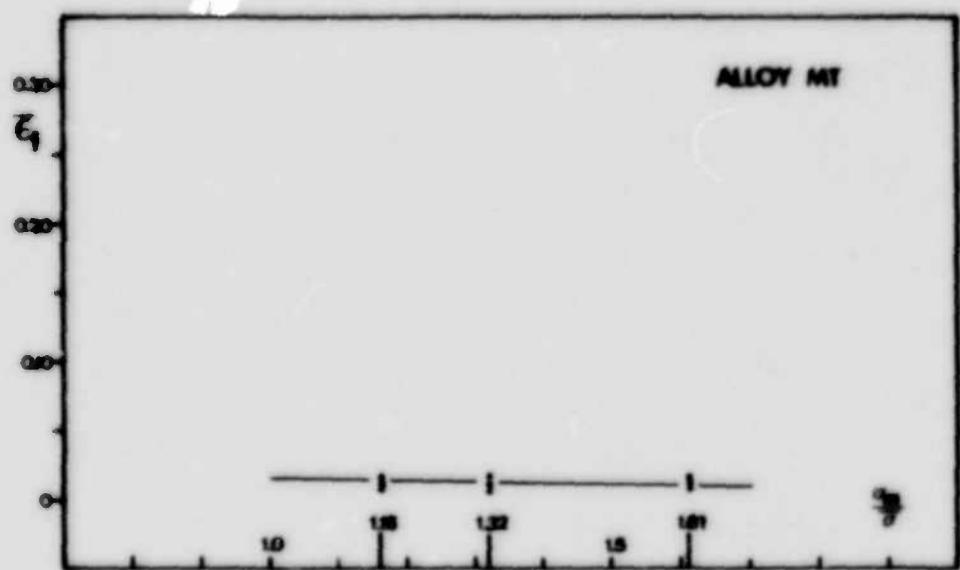


Figure 3.7

Effective plastic strain to fracture versus stress triaxiality. Individual test results are shown.

- (a) Alloy MT
- (b) Alloy ML
- (c) Alloy MM
- (d) Alloy MH
- (e) Alloy MC



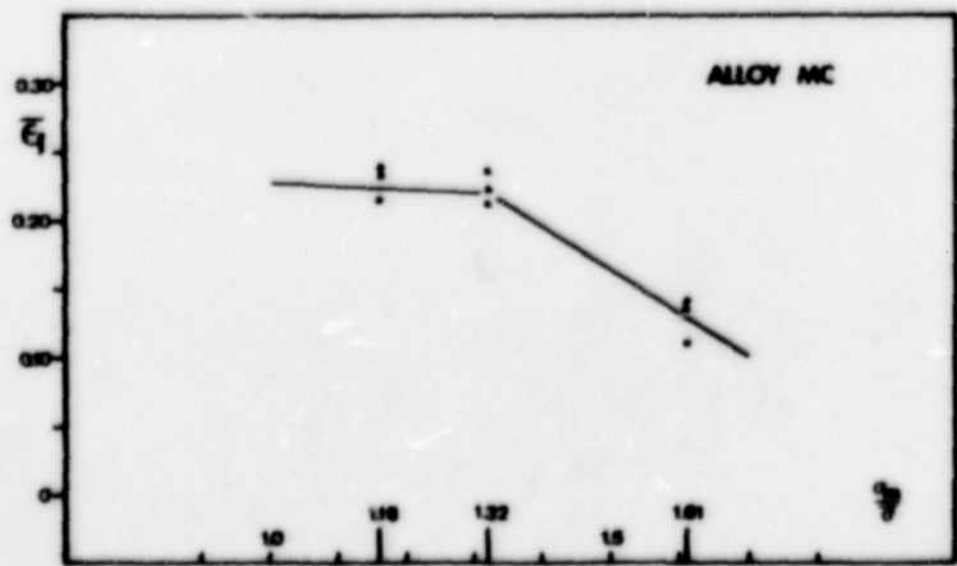
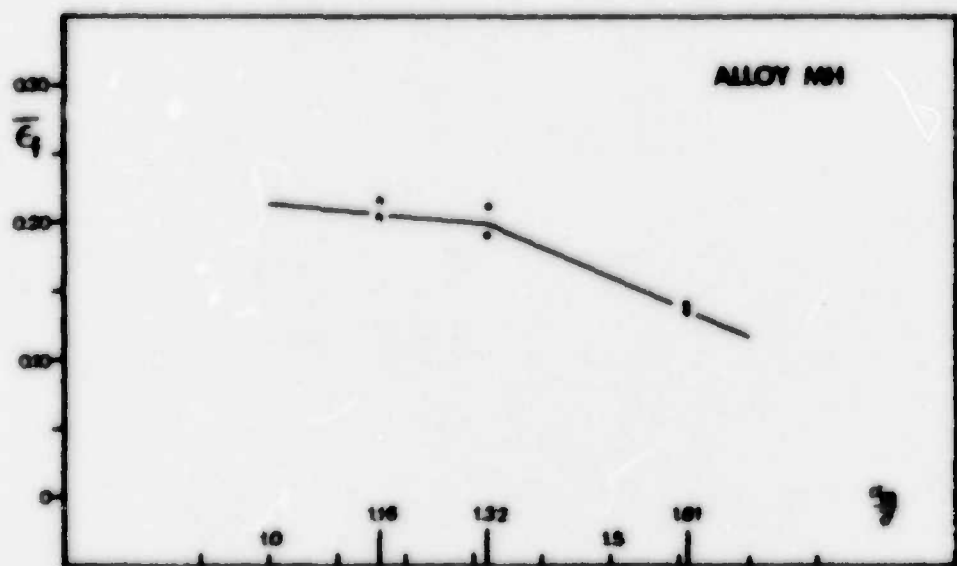


Figure 3.8

Typical test records of load versus load line displacement
for compact tension specimens at similar values of a/W .

(a) Alloy MT	$a/W = 0.5266$	$\Delta a = 2.15\text{mm}$
(b) Alloy ML	$a/W = 0.5166$	$\Delta a = 0.79\text{mm}$
(c) Alloy MH	$a/W = 0.5404$	$\Delta a = 0.72\text{mm}$
(d) Alloy MH	$a/W = 0.5190$	$\Delta a = 0.47\text{mm}$
(e) Alloy MC	$a/W = 0.5143$	$\Delta a = 0.58\text{mm}$

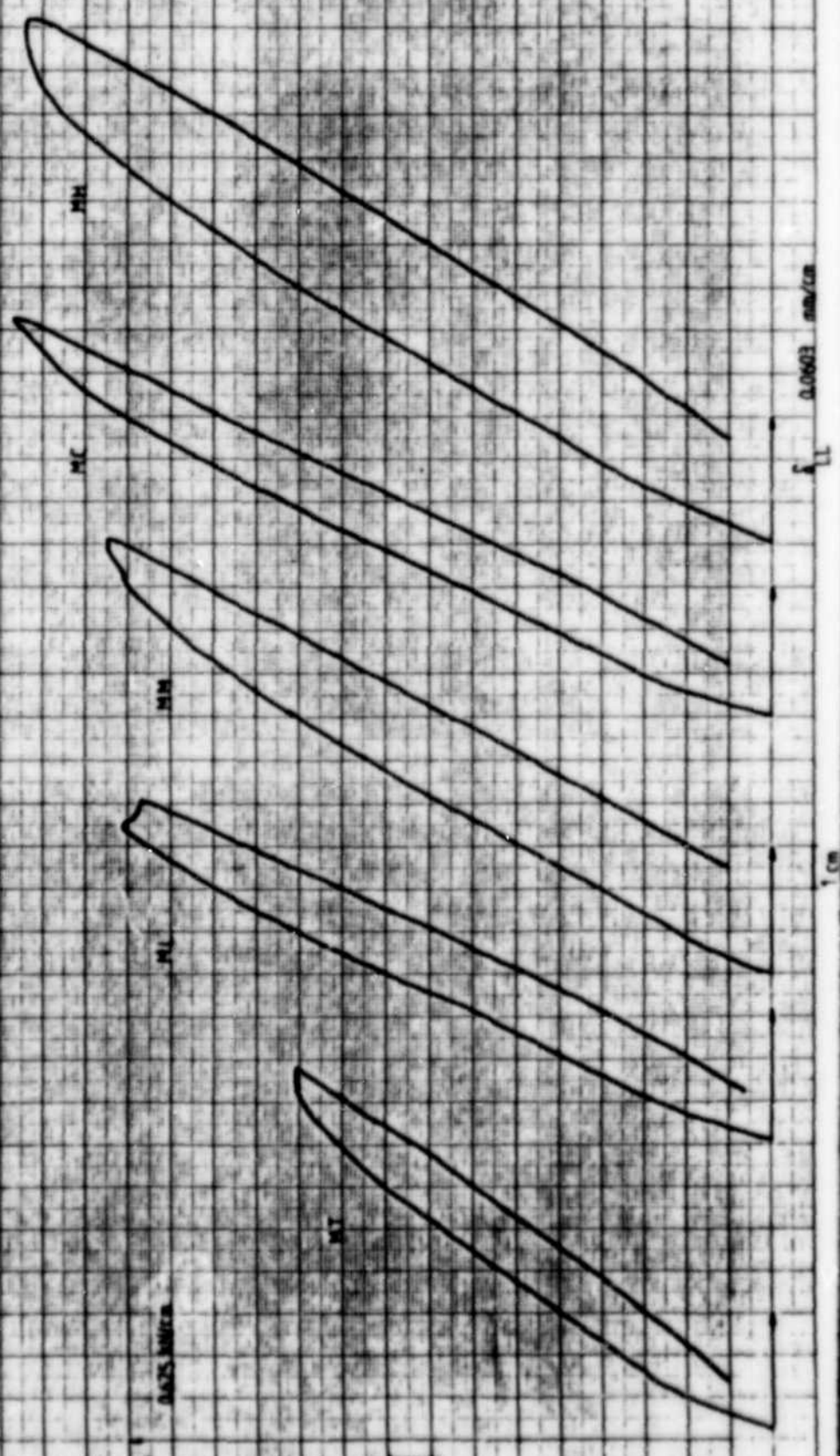
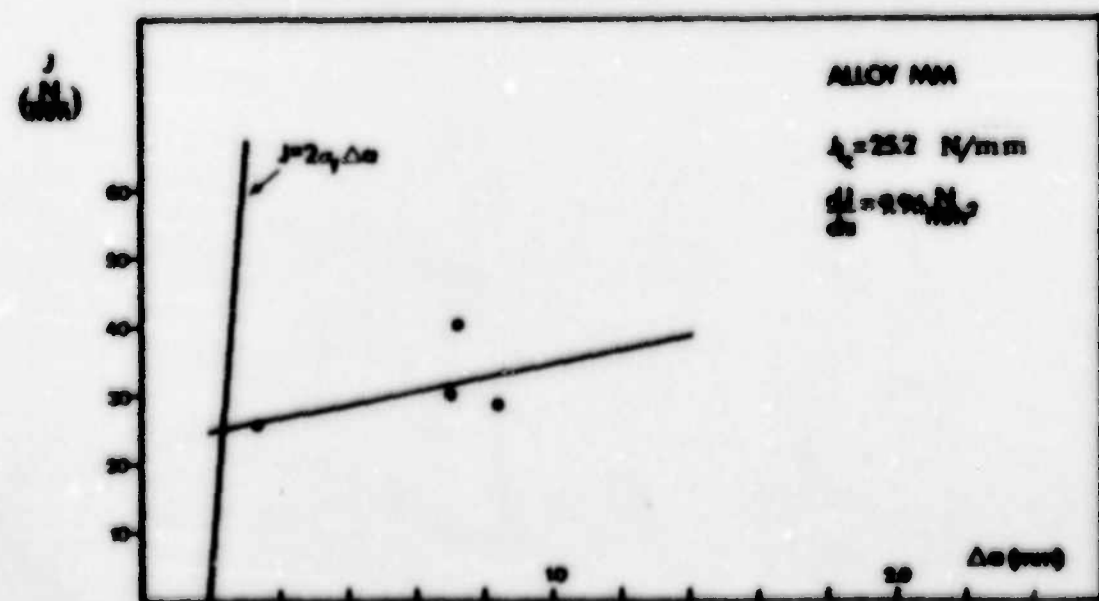
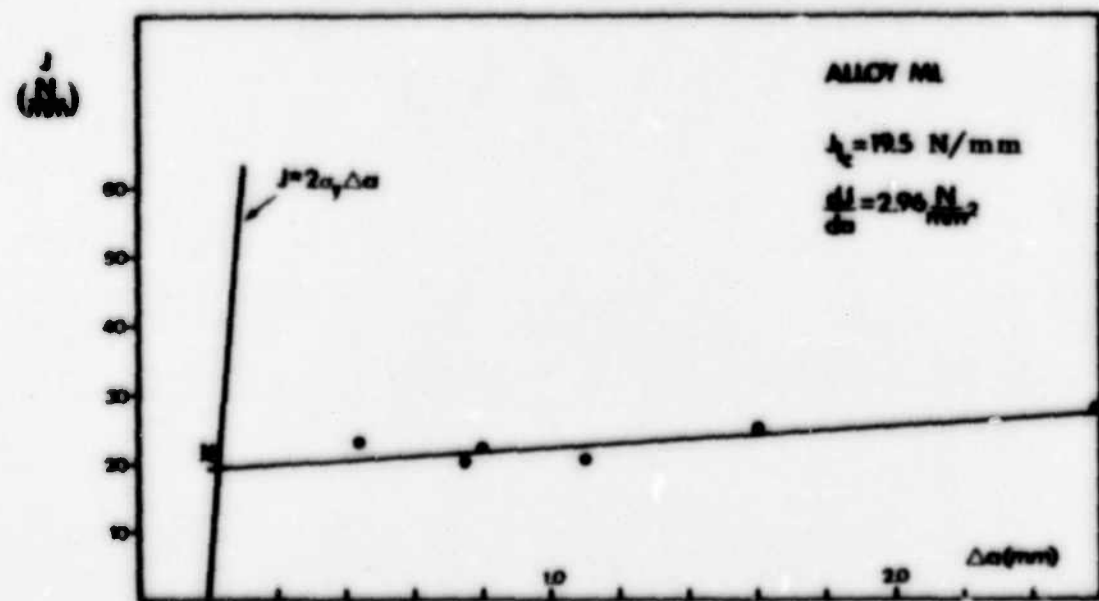
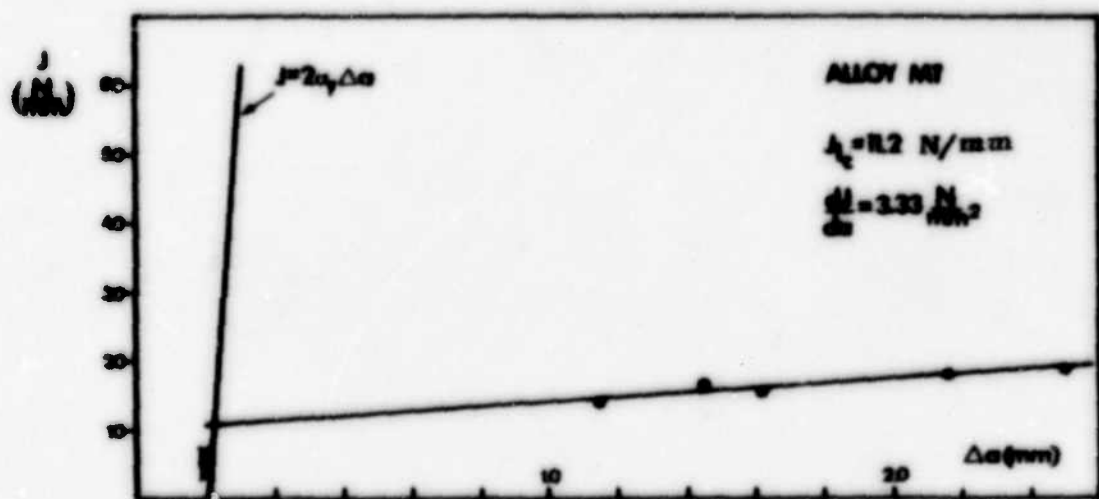


Figure 3.9

Experimentally determined J-integral versus amount of crack extension resistance lines.

- (a) Alloy MT
- (b) Alloy ML
- (c) Alloy MM
- (d) Alloy MH
- (e) Alloy MC



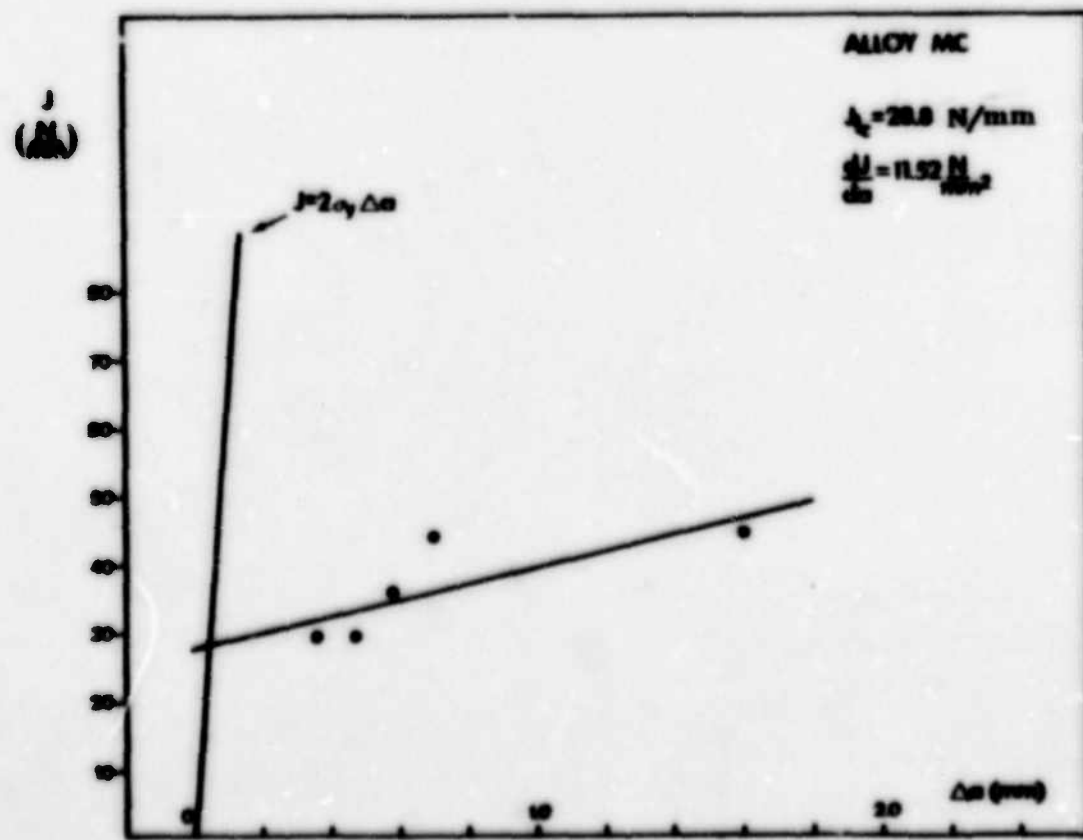
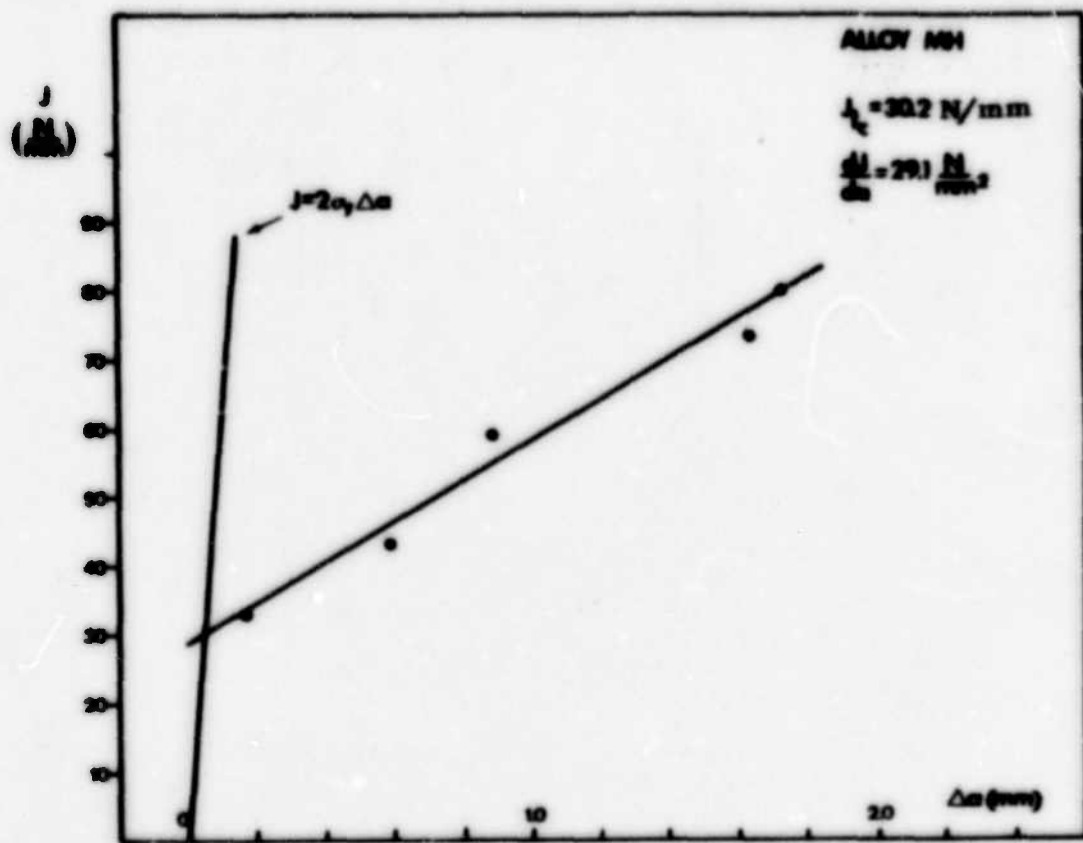


Figure 3.10

Crack front profiles before and after crack extension for selected specimens.

- (a) Alloy MT
- (b) Alloy ML
- (c) Alloy MH

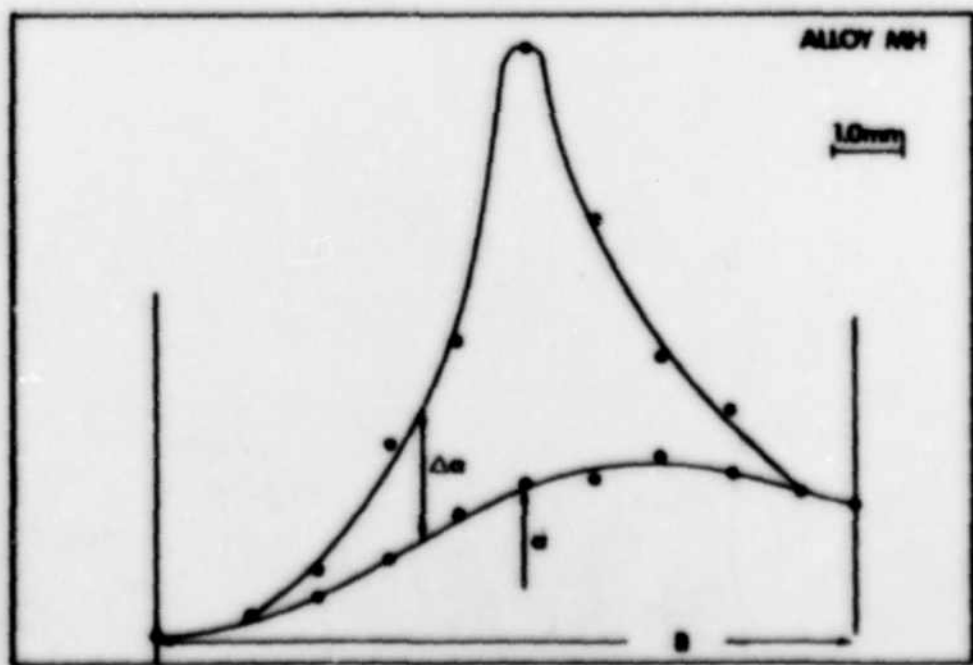
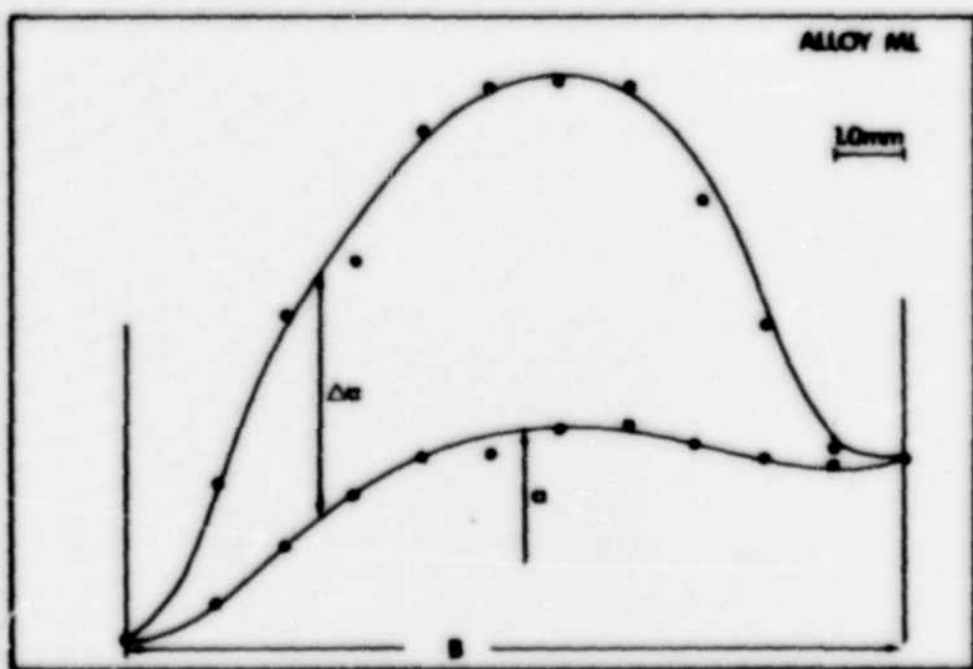


Figure 3.11

Superimposed crack tip plastic zone from specimens loaded to different values of K .

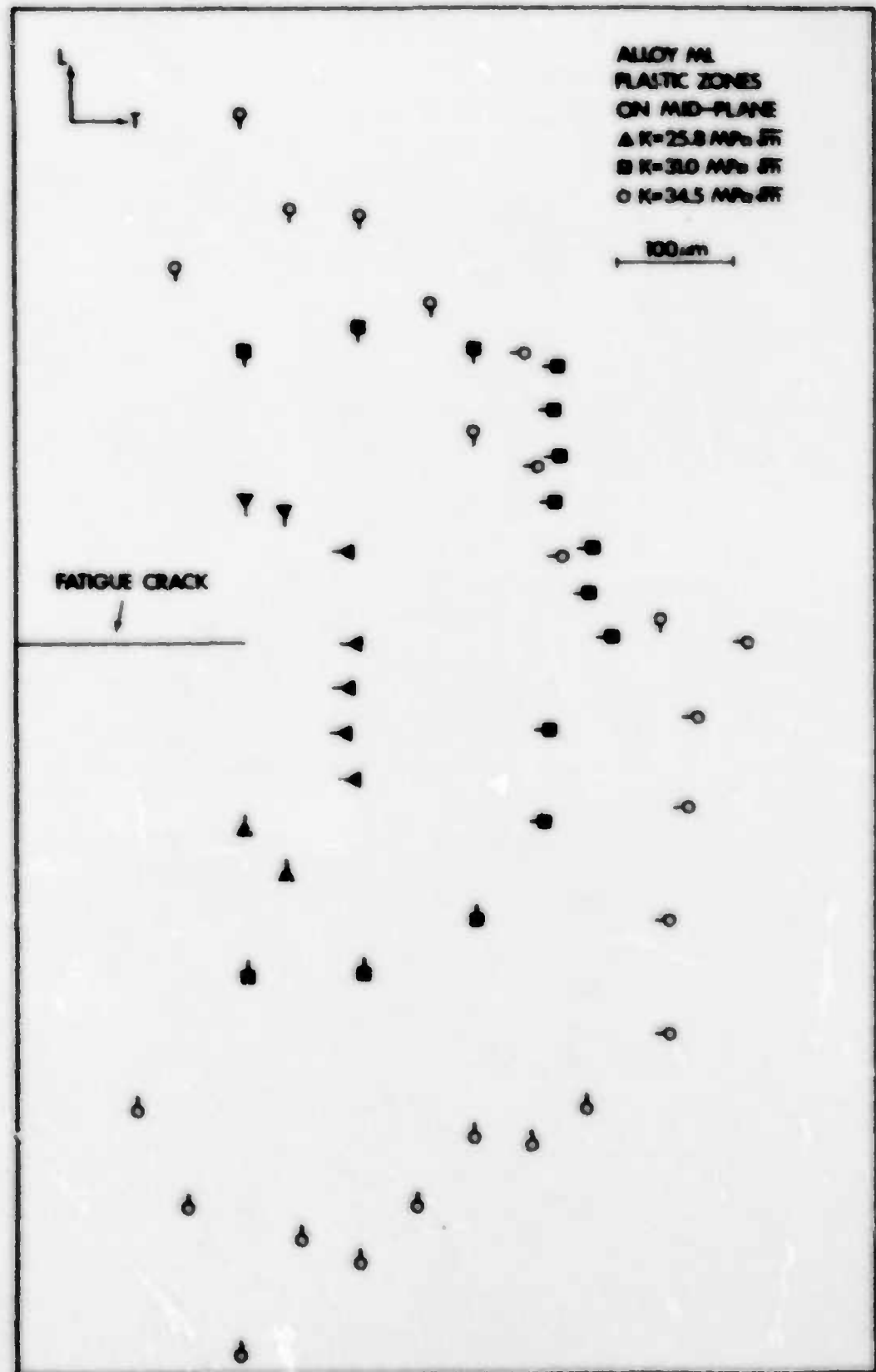


Figure 3.12

Variation of crack tip plastic zone through the thickness.
Alloy ML. $K=34.5 \text{ MPa}\sqrt{\text{m}}$. Plastic zones are shown rotated 90°
from the plane in which they were measured.

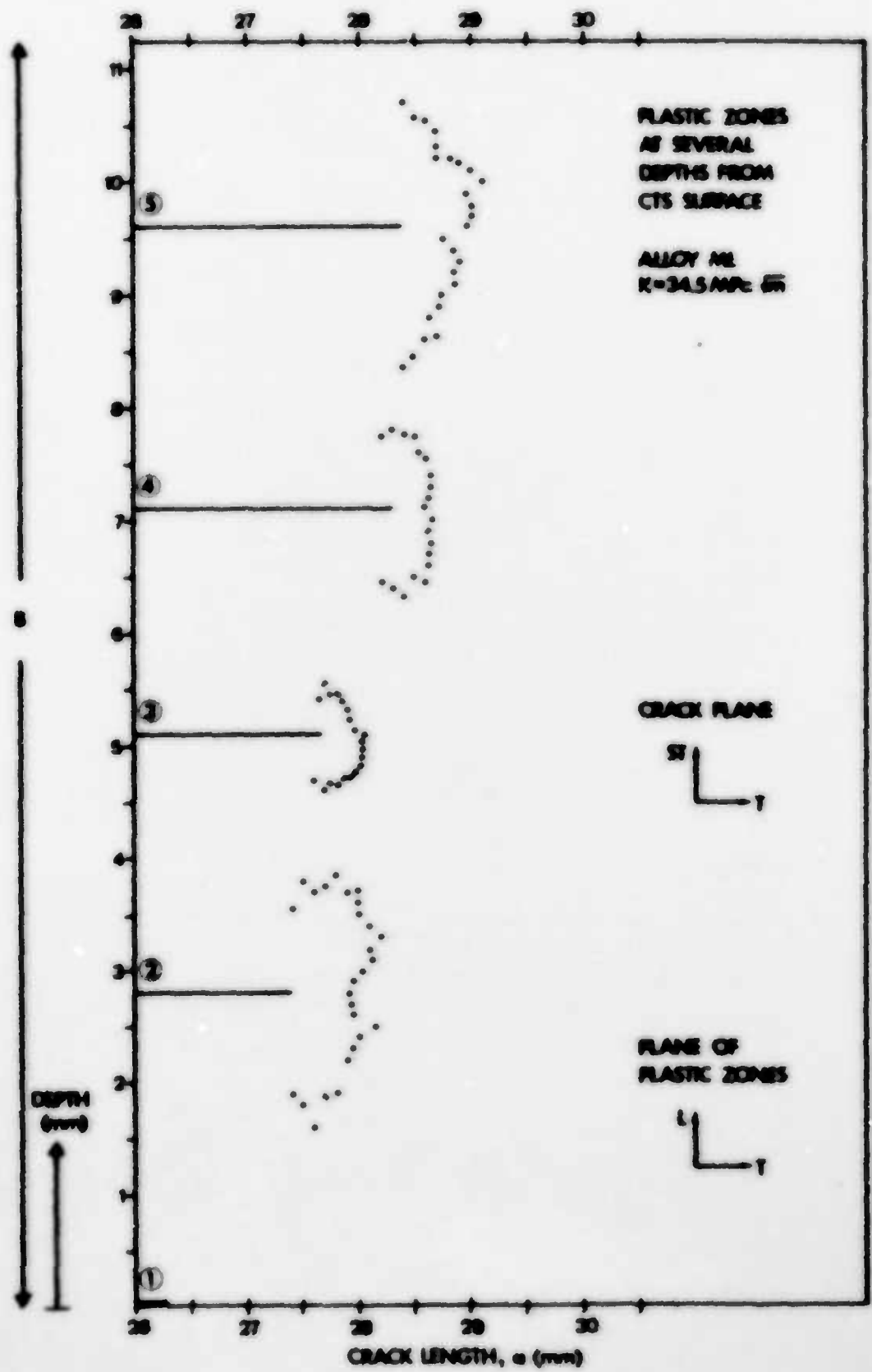


Figure 3.13

Examples of grain boundary separation (microcracks) in front of the macroscopic crack tip.

- (a) Low magnification view of mechanically polished crack tip region of alloy ML. $K = 34.5 \text{ MPa}\sqrt{\text{m}}$. Crack propagation direction from bottom to top. Grain boundaries have opened up in the region in front of the crack tip.
- (b) Detail of a grain boundary that has opened up in front of the main crack. Note the dimples that are distinguishable on the grain boundary fracture surface.



10 μ m



10 μ m

Figure 3.14

Possible parameters for plastic zone size comparison.

- (a) Area of the plastic zone in front of the crack tip.
- (b) Average of the two r_y distances measured perpendicular to the crack plane.
- (c) Distance r_y measured at some predetermined angle θ to the crack tip.
- (d) Distance r_{\max} measured from the tip to the maximum extent of the plastic zone.
- (e) Distance r_x measured directly in front of the crack tip, i.e. r_y for θ not equal to 0°.

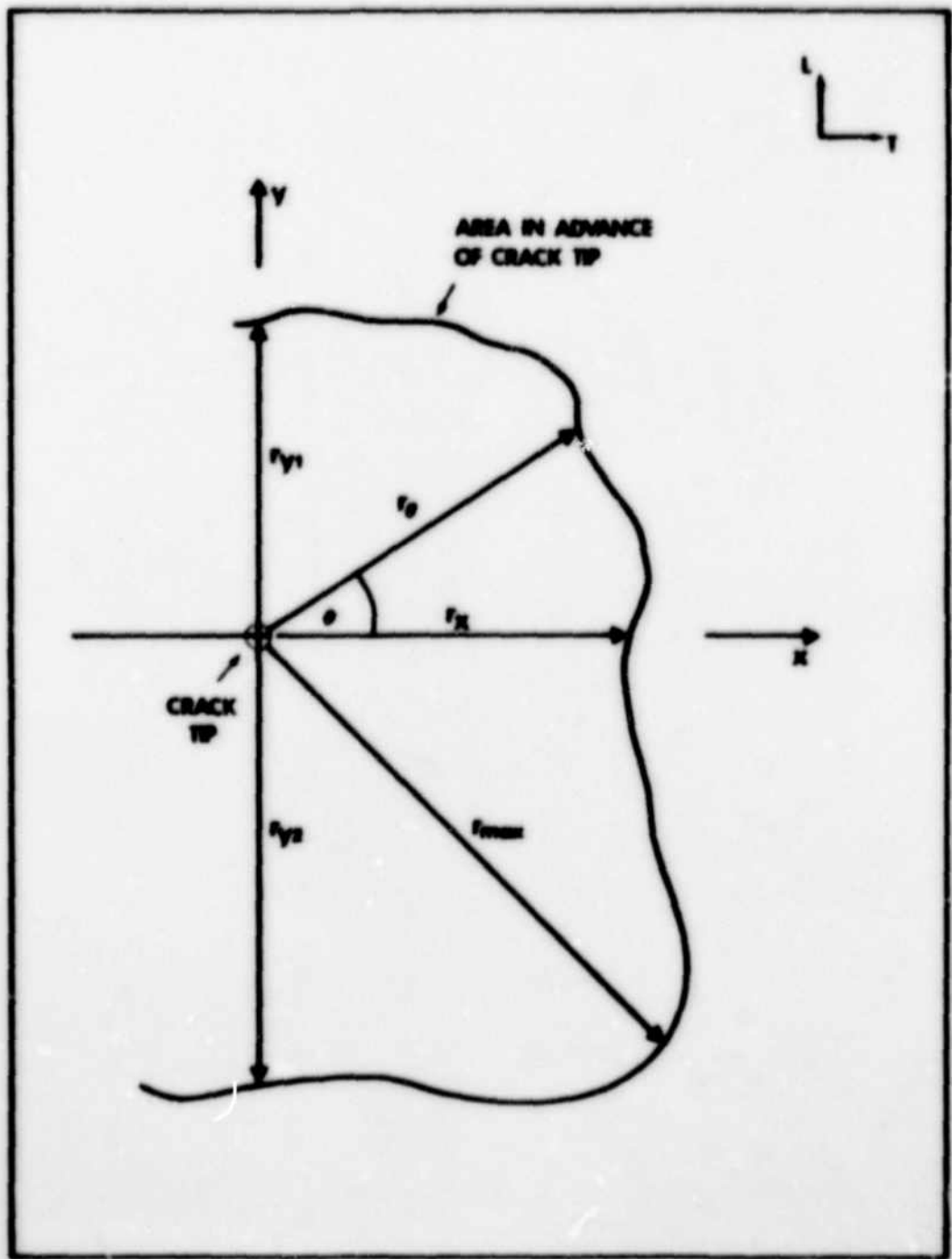


Figure 3.15

Correlation between experimentally measured plastic zone size and applied stress intensity factor. σ_y is the yield strength. The line represents the prediction for plane strain plastic zone size ($\theta=0^\circ$) from Rice and Johnson (1970).

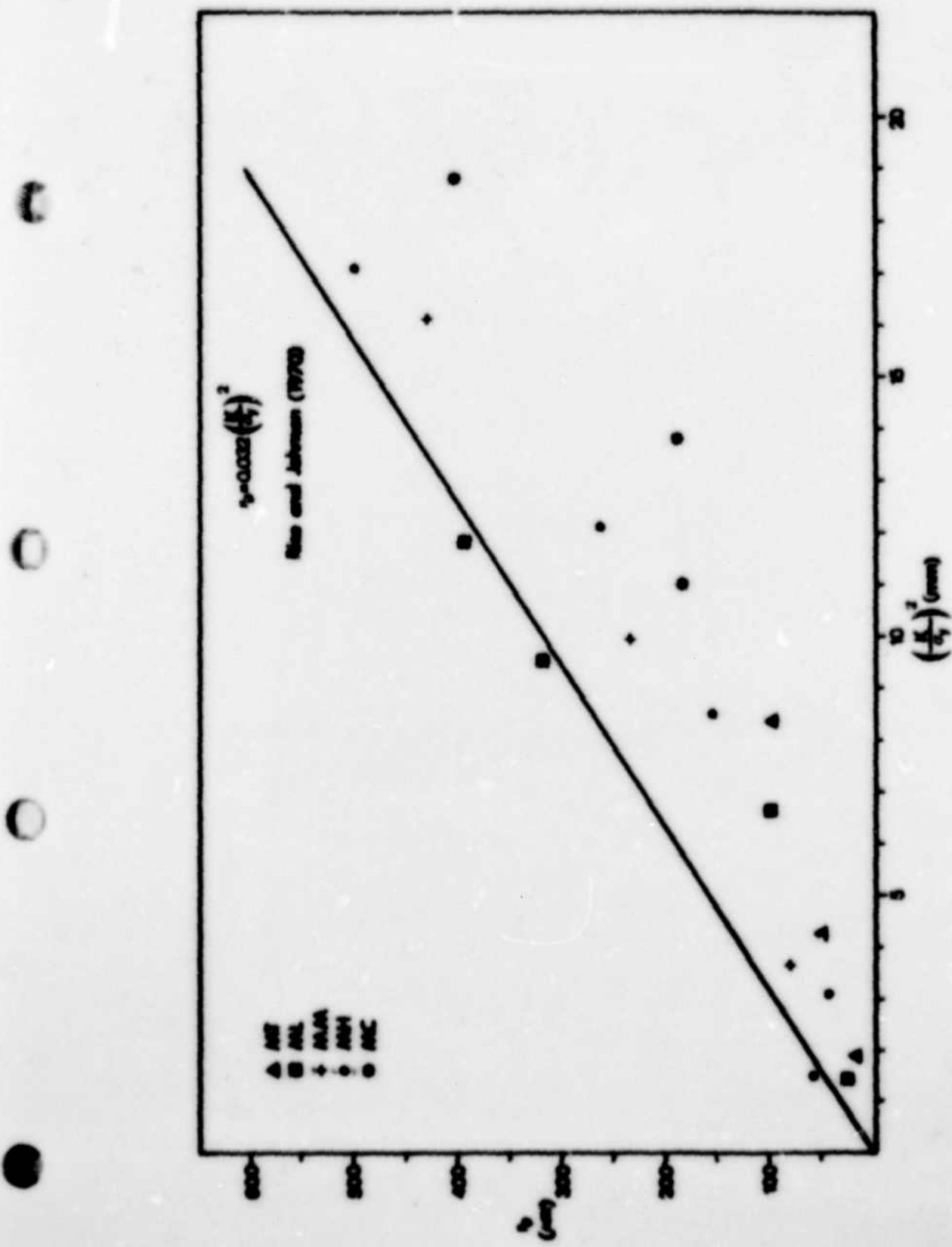


Figure 3.16

Best fit lines for each alloy correlating r_p with K and σ_y
using the average slope of all data having $r_p > 100\mu\text{m}$.

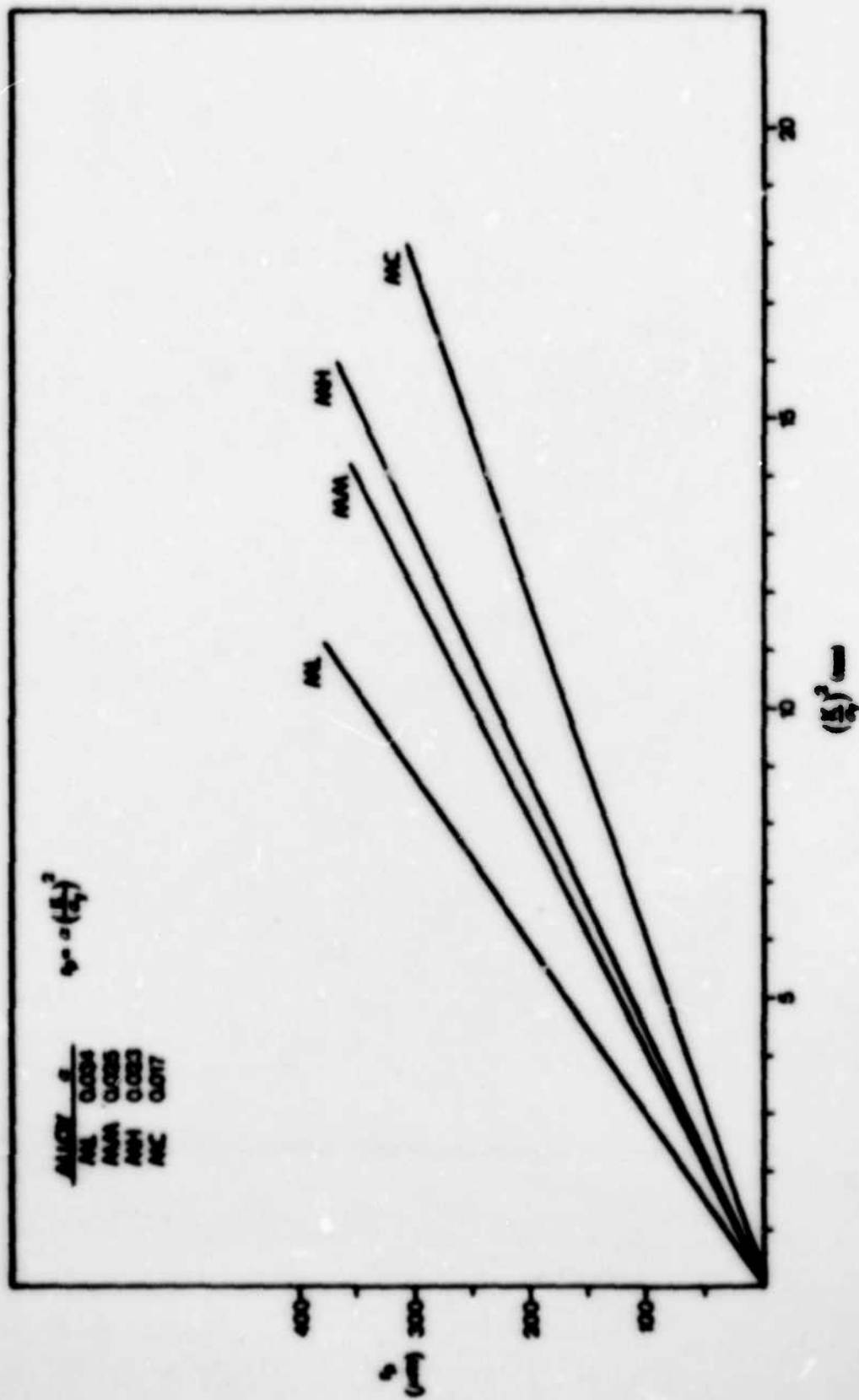


Figure 3.17

Optical micrographs, partially polarized light, showing
alloy grain structure.

- (a) Alloy MT
- (b) Alloy ML
- (c) Alloy MM



100 μ m



100 μ m



100 μ m

Figure 3.17 (cont.)

(d) Alloy MH

(e) Alloy MC



100 μm



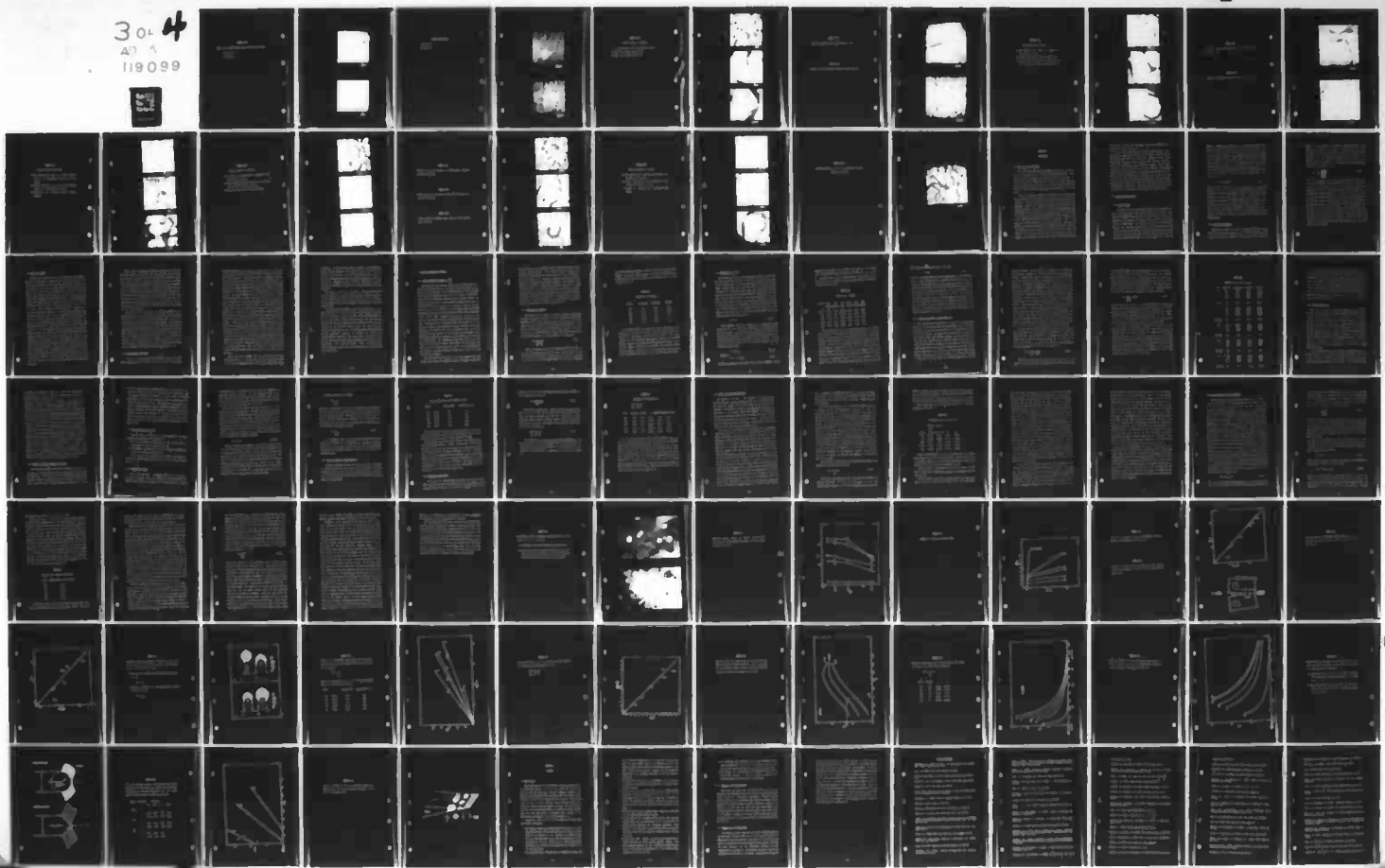
100 μm

AD-A119 099 AIR FORCE INST OF TECH WRIGHT-PATTERSON AFB OH
MICROMECHANISMS OF CRACK EXTENSION IN ALLOYS. (U)
1982 J A BLIND
UNCLASSIFIED AFIT/CI/NR/82-250

F/G 11/6

NL

304 4
AD-A
119099



3 OF 4

AD A

119099

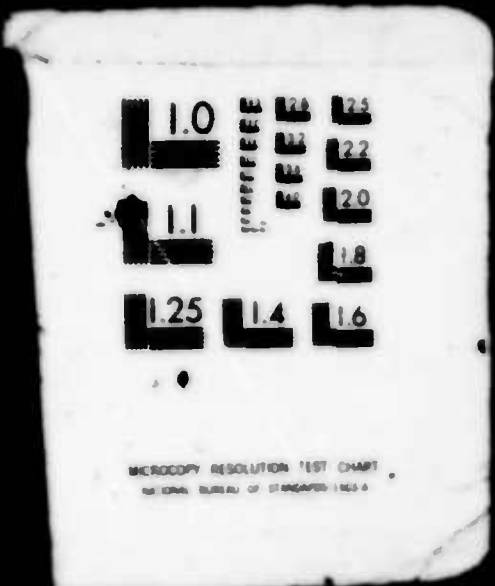


Figure 3.18

Optical micrographs showing coarse constituent particles.

(a) Alloy ML

(b) Alloy MM



100 μm

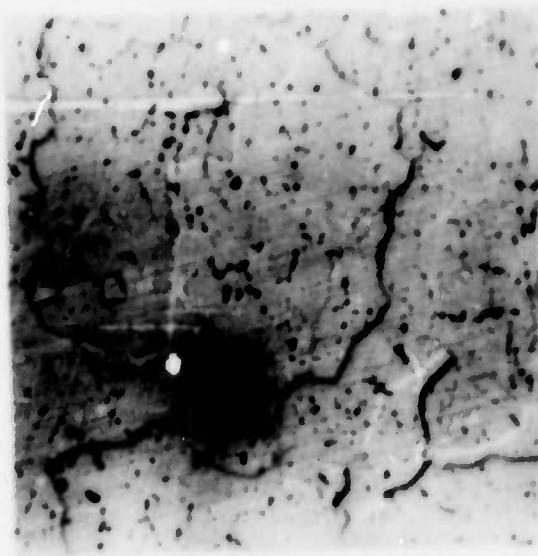


100 μm

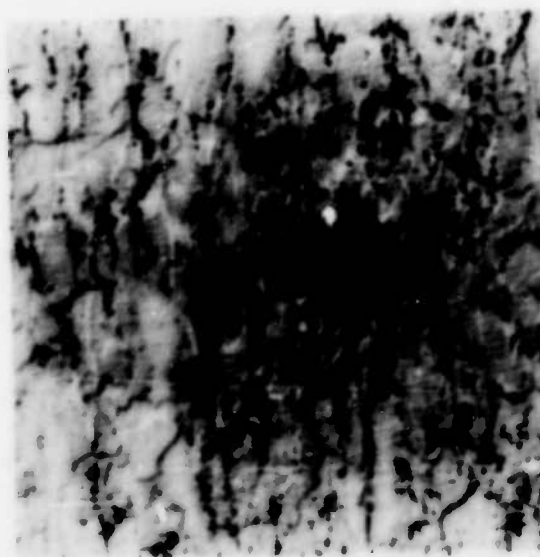
Figure 3.18 (cont.)

(c) Alloy MH

(d) Alloy MC



100 μ m



100 μ m

Figure 3.19

Fracture surface of alloy MT.

- (a) Low magnification view of intergranular fracture.
- (b) Same as (a). Higher magnification.
- (c) Same as (b). Higher magnification.



Figure 3.20

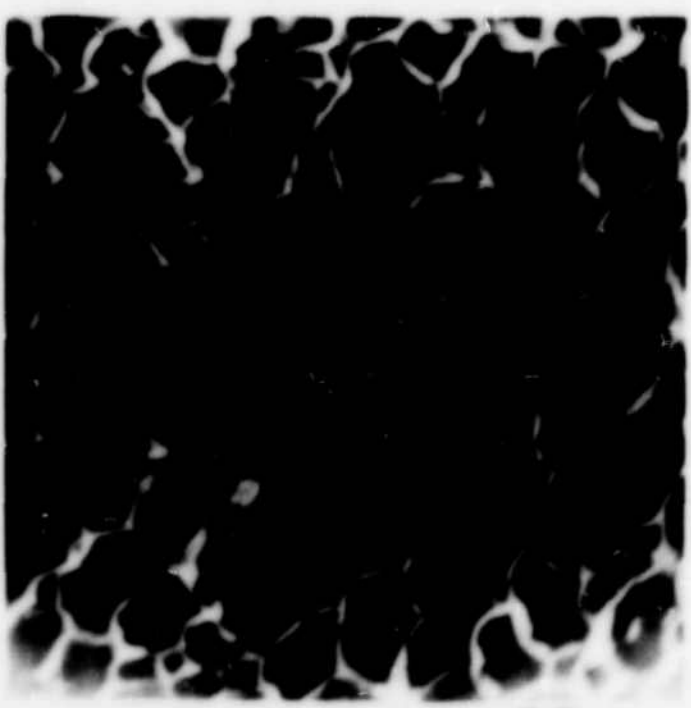
Dimples on intergranular fracture surface. Alloy MT

Figure 3.21

Dimples on the intergranular fracture surface. Alloy MT.



5 μm



0.5 μm

Figure 3.22

Fracture surface of alloy ML.

- (a) Low magnification view of predominantly intergranular failure.
- (b) Higher magnification of central region of (a).
- (c) Large particle and associated dimple from (b).
Fine intergranular dimples are also evident.

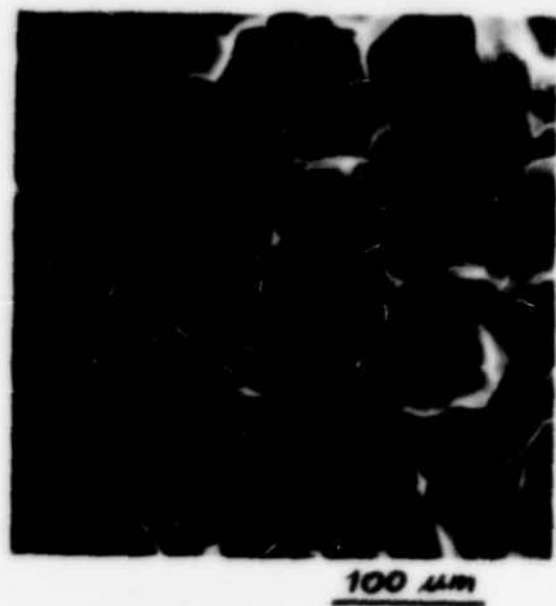
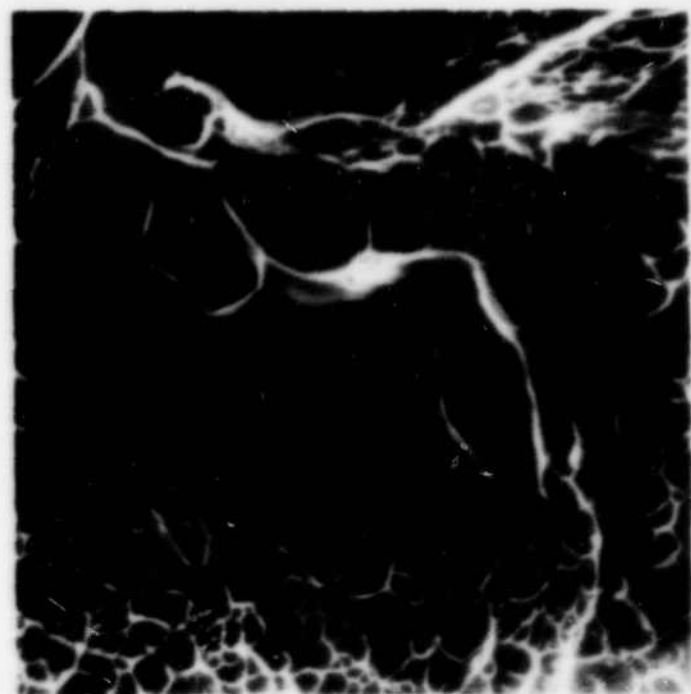


Figure 3.23

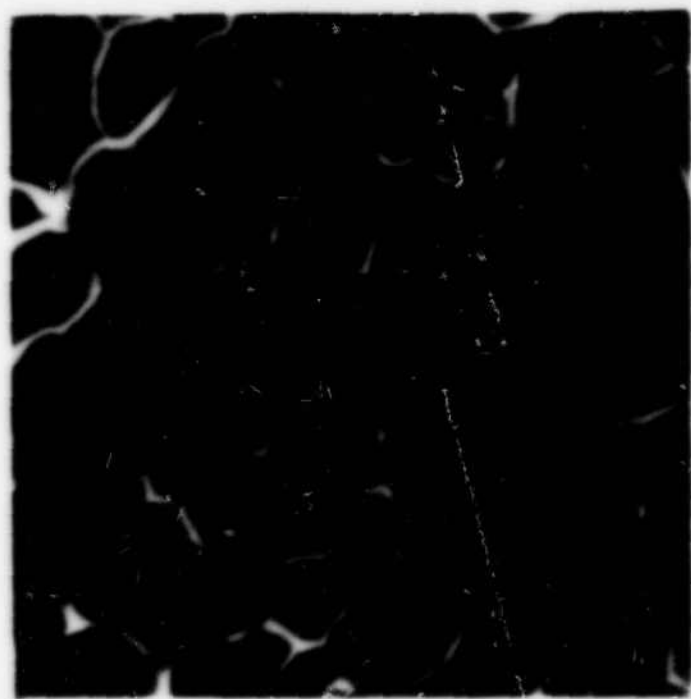
Fracture surface of alloy ML with several different dimple sizes visible.

Figure 3.24

Dimples on intergranular fracture surface of alloy ML.



2 mm



1 mm

Figure 3.25

Fracture surface of alloy 316.

- (a) Low magnification view of fracture surface showing both intergranular and ductile rupture regions.
- (b) Higher magnification with fine scale features apparent on the intergranular surfaces.
- (c) Inclusions and associated ductile rupture dimples.

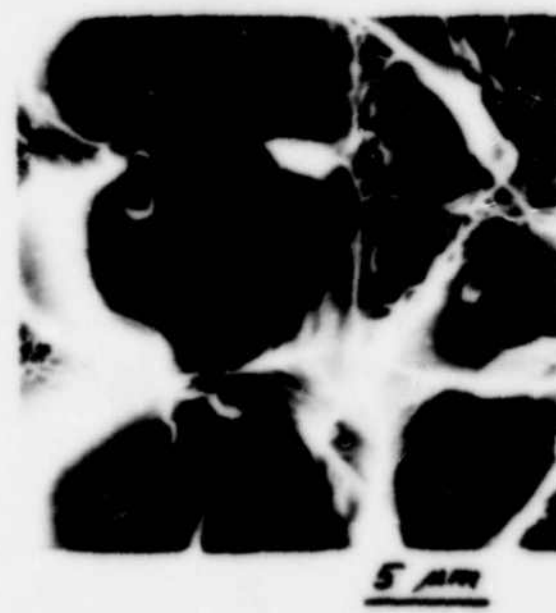


Figure 3.26

Fracture surface of alloy 101.

- (a) Low magnification showing both intergranular and ductile rupture regions.
- (b) Higher magnification showing fine scale features on intergranular fracture surfaces.
- (c) Dimples on intergranular fracture surface.

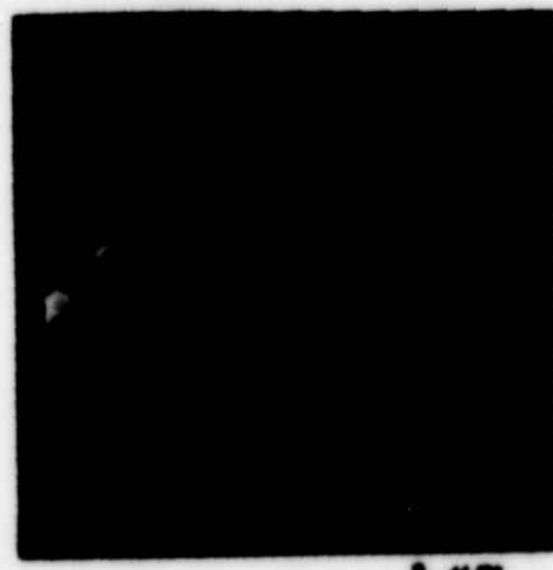
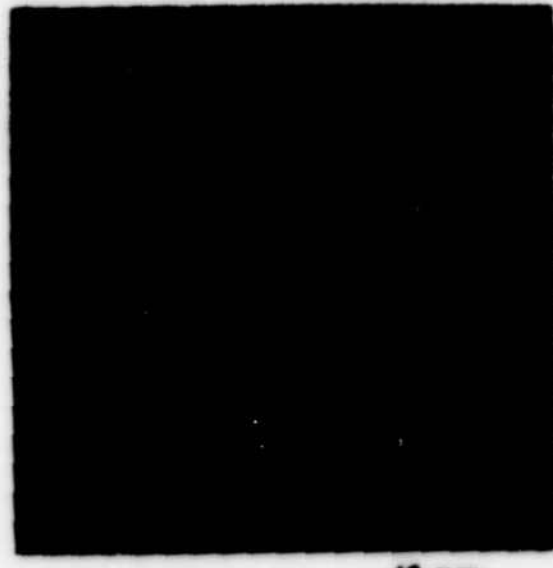


Figure 3.27

Dimples containing particles on intergranular fracture surface of alloy MH.

Figure 3.28

Dimple formed by large amount of local plasticity around an inclusion. Alloy MH.

Figure 3.29

Void at inclusion showing a small amount of local plastic flow. Alloy MH.



Figure 3.30

Fracture surface of alloy MC.

- (a) Low magnification showing intergranular and ductile rupture regions.
- (b) Higher magnification showing features on the intergranular fracture surface.
- (c) Cluster of inclusions and associated large dimple.



50 μm



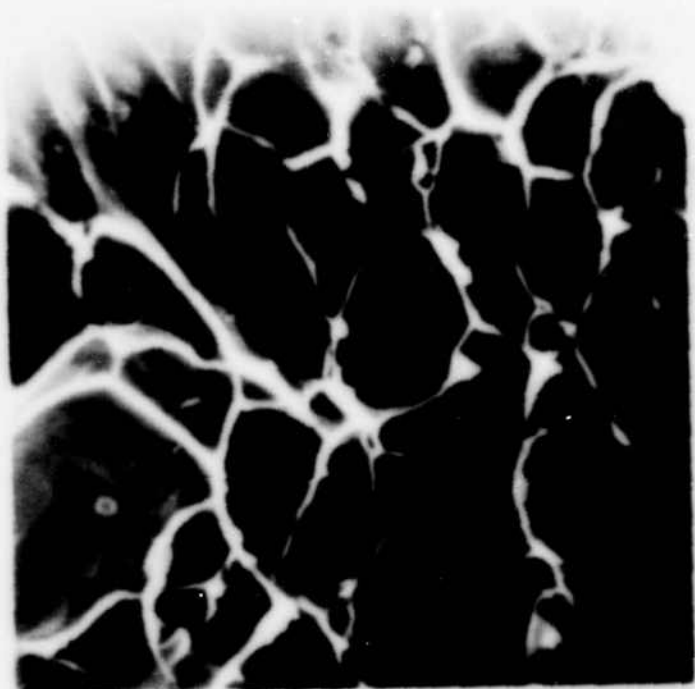
10 μm



5 μm

Figure 3.31

Dimples containing particles on intergranular fracture
surface of alloy MC.



1 mm

Chapter 4

DISCUSSION

4.1 Microstructural Features

Since later discussion explains changes in macroscopic parameters and crack extension mechanisms in terms of microstructure, it is appropriate now to summarize the salient microstructural features of the alloys studied. These features include grain size, particle analysis (precipitates, dispersoids and inclusions) and grain boundary structure (grain boundary precipitates and precipitate free zones PFZ).

Alloy MT, essentially dispersoid and inclusion free, has equiaxed grains of approximately 200 μm diameter with essentially straight grain boundaries. Alloys ML, MH and MR contain increasing amounts of manganese, which forms incoherent intermetallic particles of the $\alpha(\text{Al}_{12}\text{Mn}_3\text{Si})$ phase. The majority of the rod shaped dispersoids are approximately 0.1 μm in diameter, although some coarser 5 μm particles of the same phase have been observed (Dowling, 1975); the grain sizes of the dispersoid containing alloys are similar (70 - 100 μm). The grains are slightly elongated in the rolling direction, and the grain boundaries are more distorted than in the ternary alloy MT. Alloy MC, the commercial purity equivalent of alloy MH, has a higher iron content which results in the formation of particles of FeAl_3 and $\alpha\text{-AlFeSi}$. The majority of the iron induced particles are coarse

inclusions (5 - 10 μm), but the volume fraction of dispersoid size particles will also be increased.

All the alloys were tested in the peak aged condition, i.e., containing a fine ageing precipitate of Mg_2Si , grain boundary precipitates and precipitate free zones adjacent to the grain boundaries. In similar alloys, Dowling (1975) found the PFZ to be 0.1 μm wide and constant with dispersoid content. Prince (1977) detected two types of particles in the grain boundary and concluded that these were dispersoids and grain boundary precipitates. Fig. 4.1 shows two TEM micrographs taken by Prince of his alloy 4 (MH) that illustrate the typical structure of the dispersoid containing alloys. Dowling (1975) proposed that the 0.1 μm dispersoid particles control the deformation mechanism of these alloys through homogenization of slip. The results of Chapter 3 will be discussed in that context.

4.2 Unnotched Tensile Tests

4.2.1 Yield Strength

An initial objective of the present work was to investigate the effect of dispersoids on crack extension mechanisms in alloys of the same yield strength. This similarity of yield strength was essentially achieved for the dispersoid containing alloys, in which σ_y varies from 309MPa to 323MPa (Table 3.1). However, alloy MT yields at 279MPa. Although the individual microstructural contributions to the yield stress are difficult to quantify, the primary contributors are the age hardening precipitate and the grain size. Alloy compositions were chosen to produce similar volume fractions of Mg_2Si in the peak aged

condition. Although the post-cold work recrystallization/solution treatment time was much briefer for MT than for the other alloys (see Ch. 2), the Mg was held in solid solution by the one hour solution treatment before cold work. Since Edwards (1981) obtained a yield stress of 30MPa for alloy MT having a grain size of 125 μ m, the lower yield strength of alloy MT in the present study, as compared to dispersoid containing alloys, would appear to be mainly due to the grain size being larger by approximately 120 μ m. The magnitude of this effect can be estimated using the Hall-Petch relation (Hall, 1951; Petch, 1953)

$$\sigma_y = \sigma_0 + k_f d^{-1/2} \quad (4.1)$$

where σ_0 is the resistance to flow in the grain, d is the grain diameter and k_f is a constant associated with the propagation of deformation across the grain boundary. Evensen, Ryum and Embury (1975) estimated k_f in peak aged Al-Mg-Si alloys to be 0.7MN/m^{3/2}. Thus, increasing the grain size of MT from 80 μ m to 200 μ m would theoretically decrease its yield stress by 29MPa and adequately account for the observed value lower than the dispersoid containing alloys. Due to their size and small volume fraction, the 0.1 μ m incoherent dispersoids should only slightly increase the alloy yield strength and work hardening rate.

4.2.2 Work Hardening Rates

Referring to fig. 3.5, the work hardening exponent N does increase with dispersoid content, i.e. $N=0.051$ for alloy ML increasing to 0.062 for alloy MH. While this increase is not large in absolute

terms, it does represent an increase of approximately 22%. These results are consistent with those of Dowling (1975) and reflect contributions to the work hardening rate due to the grain size and the dispersoid size and distribution. The grain size effect can be estimated using the approach of Ashby (1970). The ratio of the observed work hardening rate at a constant strain for materials of different grain sizes is given by

$$\frac{d\sigma}{d\epsilon_1} : \frac{d\sigma}{d\epsilon_2} = \left[\frac{d_2}{d_1} \right]^{1/2} \quad (4.2)$$

where d_1 and d_2 are the grain sizes of the two materials. This ratio for alloys ML ($d=99\mu\text{m}$) and MH ($d=79\mu\text{m}$) is 1.12. Thus, the grain size accounts for approximately half of the observed increase in the work hardening rate. The additional increment in alloy MH is then due to the manganese bearing dispersoids. In the presence of coherent Mg_2Si precipitates alone, dislocations cut through the precipitates and produce local softening of the slip plane by reducing the effective cross-sectional area of the precipitates (Cleiter and Hornbogen, 1967; Hornbogen and Zum Gahr, 1975). However, the incoherent dispersoid particles are not sheared and dislocation debris forms around the particles. Thus, the slip bands work harden and alternative dislocation sources operate. As Dowling (1975) points out, the influence of the dispersoids on the work hardening rate is a subtle effect in these alloys.

4.2.3 Fracture Strains

Dowling (1975) contains an extensive discussion of the tensile ductility and deformation structure of her alloys BD3, BD6 and BD8 (essentially equivalent to MT, ML and MH, respectively). Her results are consistent with those of the present study in that alloy MT fractures at quite low strains (0.08 for MT, see Table 3.1) while alloys ML and MH show similar strains to fracture ($\epsilon_f=0.24$ and 0.26, respectively). Dowling proposed a model based on the interdependent effects of dispersoids and inclusions on the ductile rupture mechanisms of void initiation, growth and coalescence. According to this model, voids initiate at coarse particles ($\sim 5\mu\text{m}$) at lower strains in BD8 than in BD6 due to its containing a greater volume fraction of these particles. However, $0.1\mu\text{m}$ dispersoids do not void until a very late stage in the deformation, and they inhibit the growth of voids initiated at the coarse particles. Consequently, the higher volume fraction of dispersoids in BD8 accounts for its slightly larger fracture strain over BD6. While this appears to be a realistic model, it does not account for the significantly larger fracture strains of alloy MC in the present study ($\epsilon_f=0.40$). Alloy MC, the commercial purity equivalent of alloy MH, contains 0.27wt% Fe which significantly increases the number of coarse constituent particles. Also, the volume fraction and composition of the dispersoids are altered (Edwards, 1981). According to the Dowling model, the major effect of the added iron would be to decrease the fracture strain by increasing the number of voids initiated at low strains. Since this was not observed in the present study, additional factors may be involved.

Broek (1972) investigated fracture processes in thirteen aluminium alloys. He observed that large particles could initiate voids at small strains of the order of a few percent. However, since final fracture occurred at strains of the order of 25%, he concluded that large inclusions would decrease ductility but were not essential to the fracture process. However, it seems significant that the large particle voiding referred to by Broek was due to fractured inclusions. Void formation by the decohesion of the particle-matrix interface was observed at a few isolated particles in a few specimens only. As inclusions have not been observed to fracture in the present alloys, the strength of the particle-matrix interface must be the controlling factor in void nucleation.

Decohesion of the inclusion-matrix interface depends on the maximum stress normal to the interface and would therefore be expected to be sensitive to the local stress triaxiality which occurs in the necked region of the tensile test specimens. However, the dimensions of the unnotched tensile specimens (see fig. 2.8) were too small to allow development of large hydrostatic stress components in the notch. Thus it appears that the lack of constraint in the tensile tests of alloy MC prevented the deleterious effect of void nucleation at inclusions from overshadowing the beneficial effect of the larger volume fraction of dispersoid size particles. Corroborating evidence for this suggestion was obtained from the notched tensile tests.

4.3 Notched Tensile Specimens

Results for notched tensile tests are given in fig. 3.7 and Table 3.2. Variations of the fracture strain ϵ_f as a function of the stress

triaxiality σ_3/σ for all the alloys are shown in fig. 4.2. For the range of stress triaxialities tested, fracture strains for alloys MT, ML, MM and MH reflect increasing ductility with dispersoid content. This definite separation between the alloys is in marked contrast to the similar fracture strains of alloys ML, MM and MH in the unnotched tensile tests. Considering the Dowling model and the effect of stress triaxiality on void nucleation at inclusions discussed in the previous section, one would predict that the larger inclusion content (MH>MM>ML) would have a stronger influence on fracture strain as the stress triaxiality is increased. This concept appears to be reinforced by the greater rates of decrease in fig. 4.2 with coarse particle content, but does not satisfactorily account for the considerably higher fracture strains with dispersoid content. Dowling based her model on the ductile rupture mechanisms of void nucleation, growth and coalescence as the dominant fracture mechanism in alloys BD6 and BD8. However, Prince and Martin (1979) concluded that these alloys fractured in a predominantly intergranular manner. Results for the percentage of ductile rupture on fracture surfaces from the present study (see Table 3.3) tend to reinforce the view of Prince and Martin. They propose that fracture occurs because slip bands impinge on grain boundaries causing local strain concentrations which, at some critical value, nucleate voids. High magnification fractographs of the alloys in the present study (e.g. fig. 3.31) confirm that the intergranular failure mechanism begins with void nucleation at grain boundary particles.

Prince and Martin suggest that the dispersoids inhibit this intergranular ductile rupture mechanism both by reducing the grain size and also by homogenizing slip. As with ductile rupture at coarse

inclusions, a triaxial stress state influences the intergranular ductile rupture mechanism. The notched tensile results are thus consistent with this view. That is, in the triaxial stress field of the notch, dispersoids increase the requisite macroscopic strain to fracture by homogenizing slip and thus reducing the stress concentrations at the points where the slip bands impinge on the grain boundaries.

The tensile test results therefore suggest that the dominant fracture mechanism of grain boundary ductile rupture requires a critical combination of local stresses and strains for void nucleation at grain boundary particles and subsequent void growth and coalescence along the PFZ.

Considering now the response of alloy MC to stress state, it is clear from fig. 4.2 that this alloy shows a sharp decrease in fracture strain at the highest stress triaxiality. This is understandable in view of the greater coarse particle content and the increased proportion of transgranular ductile rupture mechanism in this alloy. In contrast to the unnotched tensile results for alloy MC, where constraint in the neck was low, the sharply notched tensile specimens provide sufficient constraint to elevate the stresses at inclusion-matrix interfaces, and cause voids to initiate at lower strains. Void growth is also strongly dependent on hydrostatic tension (McClintock, 1971; Rice and Tracey, 1969), accentuating the deleterious effect of the coarse constituent particles in the notched tensile specimens.

4.4 Fracture Toughness Parameters

4.4.1 Ductile Fracture Toughness - J_{Ic}

The resistance lines obtained from the experimental values of J and Δa are plotted in fig. 4.3. The ductile fracture toughness J_{Ic} , as given by the intersection of the blunting line with the resistance line, increases significantly with dispersoid content (MH>MD>ML>MT). (Alloy MC will be considered separately later.) In this instance J_{Ic} cannot be interpreted as a critical potential energy release rate in the same way as G_{Ic} for a purely elastic material; J can be regarded as a measure of the intensity of the stress and strain fields surrounding the crack tip within the elastic-plastic region (Kobayashi et al., 1979b). Thus, J_{Ic} does reflect the work, both elastic and plastic, required for the onset of crack extension. It therefore seems that for the alloys in the present study, the increase in ductile fracture toughness with dispersoid content reflects an increasing dissipation of work in the crack tip plastic zone. As will be discussed in the section on plastic zone size measurements, this additional work does not necessarily go toward increasing the size of the plastic zone. By homogenizing the slip distribution the dispersoids effectively spread a given number of dislocations more evenly over a unit volume of material. Thus, a larger deformation of that volume of material is required before local criteria for crack extension are satisfied.

The ductile fracture toughness of alloy MC is slightly lower than for MT, even though the dispersoid content is higher, because the

micro-mechanism of crack extension involves significantly more coarse particle ductile rupture. In a compact tension specimen, the decohesion enclave slightly in front of the crack tip, described by Boyd (see Sect. 1.5.1), contains a highly triaxial stress field similar to the sharply notched tensile specimens. The response of the ductility of alloy MC to the stress triaxiality indicates that voids initiate earlier at the coarse inclusions in the decohesion enclave. The local stress triaxiality also favours void growth and coalescence. Therefore, the additional contribution of ductile rupture at coarse particles to the micro-mechanism of ductile rupture along the PTZ causes crack extension to occur at lower values of J .

4.4.2 Comparison of J with K

An objective of J_{lc} testing is to obtain a toughness measurement on small laboratory specimens that can be applied to large scale components. However, K_{lc} represents a lower bound toughness and can be used directly for materials selection through the calculation of the stress intensity factor for the design geometry, which is not yet the case for J . One method available to convert experimental J_{lc} values to corresponding K_J values is to use the LEFM eq. (1.41) giving

$$K_J = \left[\frac{J_{lc} \pi}{(1-v^2)} \right]^{1/2} \quad (4.3)$$

Some investigators have found good agreement between K_J based on J_{lc} and an experimentally measured K_{lc} (e.g. Logsdon, 1976). For the alloys in the present study, a valid K_{lc} was not obtained. K_Q values were found to vary with crack length and so are not geometry

independent material parameters. However, when taken at similar crack lengths, K_Q provides a useful ranking for the alloys studied and an overestimation of K_{Ic} . The comparison of K_J to K_Q for all the alloys is made in Table 4.1.

Table 4.1

Comparison of K_Q and K_J

Alloy	K_Q (MPa $\sqrt{\text{m}}$)	K_J (MPa $\sqrt{\text{m}}$)	K_J/K_Q
MT	28.2	29.7	1.05
ML	35.9	39.1	1.09
MM	39.6	44.5	1.12
MR	43.6	48.7	1.12
MC	41.2	47.6	1.16

It is apparent that K_J is consistently greater than K_Q which can be assumed to be greater than K_{Ic} . Also, the relative difference increases as the toughness goes up, as indicated by K_J/K_Q . These results are not surprising. They simply illustrate that the LEFM equation cannot be relied upon when LEFM assumptions no longer apply. In these alloys, calculation of a critical stress intensity factor from J_{Ic} yields a non-conservative value because J_{Ic} represents both elastic and plastic work terms, as will be seen in the next section.

4.4.3 Comparison of J with G

For totally elastic situations, J equals G , where G is the crack extension force discussed in Ch. 1. However, it is less clear what relation these have in the elastic-plastic case. Louat and Griffiths (1982) consider this point from the view that a real crack is a combination of a perfectly elastic crack and a plastically relaxed crack that is surrounded by elastic material. They propose that the crack is held in equilibrium by a point force G applied to the crack itself and by a force F arising from resistance to dislocation motion in the plastic zone. Using the result of Eshelby (1951 and 1975) that the J -integral measures the component in the direction of crack advance of the total force on all elastic singularities, Louat and Griffiths derive the general relation

$$J = G + F \quad (4.4)$$

This J measures the rate of change of system energy with crack advance and does not include the climb forces on edge dislocations which are assumed to do no work in the deformation involved in the experimental determination of J . The term F is the scalar sum of all dislocation glide forces in the direction of crack advance. For the particular model of a single ended crack in mode I loading, Louat and Griffiths determine that

$$F = 0.2\sigma_y b \quad (4.5)$$

Therefore,

$$G = J - 0.2\sigma_y b \quad (4.6)$$

Although the numerical coefficient in eq. (4.5) is dependent on the

assumptions of the model, the validity of eq. (4.6) can be checked using the experimental results in the present study, i.e. J_{Ic} , σ_y and δ_0 , the CTOD at the onset of crack extension. The method used to determine δ_0 will be discussed in the next section. Table 4.2 contains the results of eq. (4.6).

Table 4.2

$$G_{crit} = J_{Ic} - 0.2\sigma_y\delta_0$$

Alloy	J_{Ic} (N/mm)	σ_y (N/mm ²)	δ_0 (mm)	G_{crit} (N/mm)	K_G (MPa \sqrt{m})	K_Q (MPa \sqrt{m})
MT	11.2	279	0.060	7.85	24.6	28.2
ML	19.5	318	0.070	15.0	34.0	35.9
MM	25.2	310	0.075	20.6	39.8	39.6
MR	30.2	323	0.092	24.2	43.2	43.6
MC	26.6	309	0.081	21.6	40.8	41.2

Thus, according to the Louriet and Griffith analysis, the G in eq. (4.6) and Table 4.2 represents the elastic force acting on the crack itself, and they propose that the fracture criterion for a particular material is the attainment of a critical value of G . Since a crack has no mass, it is difficult to interpret the physical significance of G when defined as a crack driving force. It is tempting to return to Irwin's original definition of G as the elastic energy released per unit area of new crack surface. In either case, it is clear that G_{crit} increases with dispersoid content in the present alloys in the same manner as J_{Ic} . It is interesting to note that G_{crit} is of the order of

$0.8J_{Ic}$ which is to be expected from eq. (4.6) and

$$J = \frac{G}{E\delta_y} \quad (4.7)$$

for $\delta_y = 1$, as in the Dugdale-BCS crack. Again using the LEFM equation (1.41), G can be converted to a stress intensity factor, K_G , and compared to the experimental K_Q . These values are also shown in Table 4.2 and plotted in fig. 4.4. The excellent agreement between K_G and K_Q for all the alloys may be due primarily to the fortuitous choice of the numerical coefficient in eq. (4.5). However, the G fracture criterion proposed by Louat and Griffiths makes the essential point that the experimental J reflects both the elastic energy release rate and the energy expended to dislocation motion. The fact that K_J , discussed in the previous section, is consistently larger than K_Q is further confirmation of this point.

4.4.4 Detecting the Onset of Crack Extension

The interpretation of experimental J and K values as determined from a plot of load against load line displacement is more meaningful as fracture criteria if the precise point of crack extension is known. For brittle materials, this point may be indicated by a sharp drop in the load as the crack extends. However, the smooth change in compliance for elastic-plastic materials makes the point of crack extension more difficult to define. In other than very thin specimens, surface observations are unreliable because the crack front usually moves forward first at the middle of the section. Another method which has been used successfully for crack length measurement is the change in electrical potential caused by crack extension when a constant

current is applied across the remaining ligament. Such a method is described for a constant D.C. power supply in British Standard DD19 (1972). A simultaneous record of load versus electrical potential across the ligament is predicted to change slope at the onset of crack extension. This method was attempted in the present study but was unsuccessful. Although there appeared to be a change in slope at about the point of expected crack extension, excessive noise in the voltage signal made it impossible to determine accurately the load at which the change in slope occurred. The noise was caused by temperature fluctuations at the potential measuring probes on the specimen surface. Since the electrical potential signal is inherently small in aluminium alloys, a 50 amp current provided sufficient signal after 1000X amplification, but, not surprisingly, raised the temperature of the specimen above 45°C. Difficulties in maintaining a constant specimen temperature caused this direct method of determining the onset of crack extension to be abandoned. Druse (1981) also found the potential drop method to be unreliable in his tests on C-Mn steel.

Lacking a direct method for detecting the point on the load-displacement trace corresponding to crack extension, an indirect method was used. Once the value of the J integral at incipient crack growth was determined for a particular alloy, eq. (2.6) was used to calculate the area A_0 under a particular load-displacement trace corresponding to the onset of crack growth, i.e.

$$A_0 = \frac{1+t_a^2}{1+t_a} \frac{J_{Ic}Bb}{2} \quad (4.8)$$

The point on the trace that gave this area was defined as the point of crack extension onset and values for the load at onset P_0 and

load line displacement δ_{LL0} thus determined. P_0 was converted to a stress intensity factor at onset K_0 via eq. (2.5). The crack tip opening displacement at onset δ_0 was calculated from δ_{LL0} based on the simple geometric construction shown schematically in fig. 4.5. This construction assumes that, as the crack opens, a CT specimen rotates about a hinge point which is some fraction of the remaining ligament in front of the crack tip. Accordingly, by similar triangles,

$$\delta_0 = \frac{Hb}{a+Hb} \cdot (\delta_{LL0}) \quad (4.9)$$

where H is the hinge rotation factor. A major difficulty in using this method is determining the correct value of H . Ponton and Lee (1980), using crack opening displacement to measure crack length in compact tension specimens, investigated four values of H , i.e. $H=0$, 0.195, 0.33 and 0.5, and found that $H=0.195$ gave the best correlation of results. Therefore, H was taken as 0.195 in the present work.

To illustrate the consistency between specimens of the indirect method of determining crack extension onset, values of K_0 and δ_0 for specific tests are given in Table 4.3 along with the previously discussed K_Q values. It is interesting to compare K_0 with K_Q . Although individual comparability may vary, the general similarity of K_0 and K_Q enhances their credibility as toughness parameters in these alloys. Also, the technique used here to calculate K_0 from δ_{LL0} using equivalent areas under load-load line displacement plots seems preferable to the LEFM equation method (K_J).

Table 4.3

Summary of K_Q , K_o and δ_o results.

Alloy	Specimen	K_Q (MPa \sqrt{m})	K_o (MPa \sqrt{m})	δ_o (μm)
MT	4	28.5	28.0	69.3
	5	26.5	24.5	68.3
	41	27.1	26.9	57.9
	42	31.2	29.3	47.6
	45	27.7	28.4	54.0
AVG FOR	MT	28.2	27.4	59.5
ML	17	37.3	37.4	83.3
	19	34.3	36.5	66.6
	20	36.7	37.1	69.5
	11	34.4	35.3	54.0
	12	36.9	37.7	68.8
AVG FOR	ML	35.9	36.8	68.4
MH	55	40.2	40.7	71.5
	57	40.7	42.6	68.9
	52	38.5	40.8	78.8
	53	38.8	40.5	79.4
AVG FOR	MH	39.6	41.2	74.7
MR	35	45.8	43.1	98.5
	36	45.0	45.0	93.8
	37	40.6	42.9	90.4
	38	42.9	42.9	87.1
AVG FOR	MR	43.6	43.5	92.5
MC	64	40.8	43.5	85.4
	65	46.7	47.2	86.8
	66	36.9	44.0	78.4
	67	40.3	44.3	71.7
AVG FOR	MC	41.2	44.8	80.6

Excessive confidence should not be placed on the absolute values of the critical crack tip opening displacements δ_0 in Table 4.3. Although they are the correct order of magnitude and vary in the same way as the toughness, there is uncertainty in the value of H in eq. (4.9). The variation of δ_0 with toughness is predicted from eq. (4.7). In fact, the correlation between J_{IC} and $\sigma_0\delta_0$ is good when $n=1$ in eq. (4.7) as can be seen in fig. 4.6. This agreement would be more significant had δ_0 been measured independently rather than calculated from a load line displacement.

4.4.5 Tearing Modulus - T

The fracture toughness parameters discussed so far have been related to the onset of crack extension. While it is this onset that is the specific interest of the present work, the tendency for unstable crack extension was also measured. Paris et al. (1979) discuss the theory of instability of elastic-plastic crack growth, defining the conditions for unstable behaviour in terms of the J-integral resistance curve (J vs. Δa). Formulating a non-dimensional material parameter, the tearing modulus T , (see sec. 1.3.4.) which is simply the normalized slope of the J resistance line (eq. 1.43), the Paris et al. concept may, in some cases, be of greater practical significance than the fracture toughness (e.g. the leak before break design philosophy).

The tearing moduli for the alloys in the present study, as determined from eq. (1.43) and the J-integral resistance lines, are given in Table 3.4. Results for alloys MT and ML are similar, reflecting extremely low values of dJ/da . The tearing modulus

increases with dispersoid content for alloys MM and MH, but T decreases then for alloy MC. Thus the tearing modulus exhibits the same qualitative variation for these alloys as does J_{Ic} , but the proportional change in values is much greater; a fact which may be explained in terms of the geometry dependence of dJ/ds . Gudas et al. (1979), varying s/W and the amount of face grooving on CT specimens of HY-130 steel, showed that J_{Ic} was independent of specimen geometry in the range tested but the tearing modulus increased with crack length, being higher in non-face grooved specimens where crack tunnelling occurred. Bruce (1981) also found that increasing the out-of-plane constraint by increasing the thickness or degree of side grooving had a marked effect in reducing dJ/ds . Therefore, T values for the present alloys cannot be considered geometry independent. However, since the geometry was basically the same between alloys, the higher values of T represent a greater tendency for crack tunnelling. This conclusion is supported by the extended crack front shapes in fig. 3.10 where the severity of the tunnelling increases with dispersoid amount. This behaviour is a manifestation of the influence of dispersoids on the constraint required for crack extension, as discussed previously in relation to the fracture strains of notched tensile specimens.

4.4.6 Summary of Fracture Toughness Parameters

For the alloys studied, the fracture toughness parameters J_{Ic} , K_Q , K_0 , δ_0 , K_C and T provide a convincingly consistent ordering of HTCHLOMOMCOMH. This sequence can be qualitatively rationalized through the effect of dispersoid particles on slip distribution and hence on the local stress and strain combination required to activate

the grain boundary ductile rupture mechanism of crack extension. For alloy MC, which has the greater volume fraction of dispersoids, the contributing mechanism of ductile rupture at coarse constituent particles reduces the toughness compared to that of alloy MH which has a lower coarse inclusion content. The parameters J_{IC} and K_Q appear to give equivalent rankings of material toughness although they are not related according to the LEFM equation. The increase in material toughness due to the influence of dispersoid particles on slip distribution and grain size is thus established. The manner in which these items relate to crack tip plasticity will be considered in the next section.

4.5 Crack Tip Plastic Zone Size

In the context of relating dispersoid parameters to alloy toughness, two questions of interest are:

- a) For the same stress intensity factor, what is the effect of dispersoids on crack tip plastic zone size?
- b) Is toughness determined by a critical crack tip plastic zone size at the onset of crack extension?

To investigate these questions, the plastic zone size as a function of applied stress intensity factor was measured, as discussed in Section 3.3.

4.5.1 Correlation with K

Fig. 3.16 shows the midplane plastic zone size r_p as a function of $(K/c_y)^2$. Since the dispersoid containing alloys have essentially the same yield strength, the decreasing value of a in eq.

(3.2) means that, for the same K , the plastic zone size is smaller for increasing dispersoid content. At first inspection this is a surprising result because one would expect the tougher, more ductile alloy to have a larger plastic zone. This disparity can be explained in terms of the blunting geometry at the crack tip.

Most solutions for the plastic zone size at the tip of a crack assume that the crack is sharp i.e. the crack tip radius of curvature r approaches zero. Kim, Fine and Mura (1979) consider the effect of a finite r on the two-dimensional plastic domain at the tip of a blunt crack tip. Using the work of Rice (1967) and Neuber (1961), Kim et al. (1979) show that the actual plastic zone size r_p at the tip of a blunted crack tip is given by the plastic zone of an imaginary sharp crack r_K , subjected to an applied stress intensity factor K , minus the geometric effect of the blunting. Therefore,

$$r_p = r_K - r_p \quad (4.10)$$

Figure 4.7 schematically displays the variation in plastic zone size with applied stress intensity factor and crack tip geometry. Two situations are illustrated: In fig. 4.7(a), the crack tips have the same geometry but different applied stress intensity factors. The plastic zone size as given by AC increases with the applied K since r_K increases even though r_p is constant in eq. (4.10). In fig. 4.7(b), the crack tips have different radii of curvature but the same length and applied K . At constant K , r_p decreases with increasing tip bluntness since r_p increases while r_K remains constant.

According to the Kim et al. model,

$$r_p = \frac{1}{\frac{N}{N+1}}^2 \quad (4.11)$$

Therefore, a material with a high work hardening rate can be expected to have a smaller plastic zone size than a more ductile material with a lower work hardening rate. Although this is the case in the present alloys, the small difference in N accounts for a difference in r_p between ML and MH of only about 2%. The major effect of microstructure is on the crack tip bluntness, because

$$r_p = \frac{p}{\frac{N}{N+1}} \quad (4.12)$$

It is suggested that increasing the alloy dispersoid content effectively increases p , and therefore r_p , causing the observed decrease in r_p for the same stress intensity factor. The mechanism responsible for the local increase in crack tip bluntness will be considered later.

4.5.2 Values at Onset of Crack Extension

In order to estimate the crack tip plastic zone size at the onset of crack extension for each alloy, the lines of fig. 3.16 were extended to the onset value of stress intensity factor K_o (see Sect. 4.4.4). This construction is shown in fig. 4.8. The values of r_{po} thus obtained are given below.

Table 4.4

Plastic zone size at crack extension onset.

Alloy	α	$(K_0/\sigma_y)^2$ (mm)	$r_{po} = \alpha(K_0/\sigma_y)^2$ (μm)
MT	0.012	9.6	115
ML	0.034	13.5	460
MM	0.025	17.7	440
MH	0.023	16.1	420
MC	0.017	20.7	350

The values of both α and r_{po} are low for alloy MT. As a result of an easy grain boundary fracture path, crack extension occurs before the crack tip plasticity extends beyond approximately 100 μm .

The dispersoid containing alloys exhibit a decreasing r_{po} with increasing dispersoid content. However, for alloys ML, MM and MH the differences in r_{po} are small. For alloy MC, r_{po} is approximately 100 μm less than for alloy ML. It appears, therefore, that the crack tip plastic zone size at the onset of crack extension is not constant with dispersoid volume fraction. It is concluded that dispersoids alter the crack tip plastic zone size and, therefore, the stress and strain distributions in front of the crack tip. These stress and strain distributions will be considered in Sect. 4.5.4.

4.5.3 Correlation with dW/dA

At the onset of crack extension the crack driving force G is equal to dW/dA where dW is the work absorbed by the specimen as an incremental area of new crack surface dA is created. Davidson and

Lankford (1980) used this relationship and the fact that G is equal to K^2/E , to rewrite eq. (3.2) as

$$r_p = \frac{\alpha (dW/dA)E}{\sigma_y^2} \quad (4.13)$$

Calculating r_p assuming that α equals $1/\pi$ and integrating dW/dA over the plastic zone, their experimentally measured plastic zone sizes correlated reasonably well with the calculated r_p . These experiments were performed on 2024-T4, 6061-T6 and 7075-T6 aluminum. Results from the present study permit a straightforward verification of eq. (4.13), rewritten as

$$\frac{dW}{dA} = \frac{r_{po}}{\alpha} \frac{\sigma_y^2}{E} \quad (4.14)$$

The values of r_{po} , σ_y and α were determined experimentally, and the elastic modulus is known ($E=70$ GPa). Thus, the work expended in creating new crack surface area dW/dA can be calculated directly and compared to the experimental J_{Ic} . These results are tabulated in Table 4.5.

Table 4.5

Comparison of dW/dA and J_{lc}

$$\frac{dW}{dA} = \frac{r_{po}}{a} \frac{\sigma_y^2}{2}$$

Alloy	r_{po} (mm)	σ_y (MPa)	a	(dW/dA) (N/mm)	J_{lc} (N/mm)
MT	.115	279	0.012	10.7	11.2
ML	.460	318	0.034	19.5	19.5
MM	.440	310	0.025	24.2	25.2
MR	.420	323	0.023	27.2	30.2
MC	.350	309	0.017	28.1	26.6

As can be seen from Table 4.5 and the plot of dW/dA and J_{lc} in fig. 4.9, the agreement between these two quantities is remarkably close. This correlation adds physical significance to J_{lc} ; it is a measure of the work done in the formation of a unit area of new crack surface. Considering eq. (4.14), the ratio r_{po}/a strongly affects the dW/dA calculation. Since the dispersoid volume fraction does not greatly alter the plastic zone size at the onset of crack extension (r_{po} is approximately equal for ML, MM and MR), the dominant effect of adding dispersoids is to decrease a , indicating a modification of the strain distribution within the plastic zone.

4.5.4 Stress and Strain Distributions

As referred to in Ch. 1, the validity of J_{lc} as a ductile fracture toughness criterion depends on its ability to characterize the crack tip plastic stress-strain field at the onset of crack extension. The pronounced increase in J_{lc} with dispersoid content for the alloys in the present study thus suggests that dispersoids increase the necessary stresses and/or strains at the crack tip for the predominant fracture micromechanism to operate. The nature of the change in stress and strain distribution of the plastic zone can be inferred from the work of Rice and Johnson (1970).

Rice and Johnson considered the role of large crack tip geometry changes in plane strain fracture and related crack blunting to the stress and strain distributions in front of the crack tip. Their graphical solutions present these distributions as a function of X/δ where X is the position of a point in front of the initially sharp crack and δ is the CTOD. Considering first the stress distribution, Rice and Johnson (1970) fig. 10 shows approximate modified stress distributions (σ_{yy}/σ_y) as dependent on initial yield strain σ_y/E and hardening exponent N . These curves are shown in fig. 4.10 (where σ_y/E was taken as 0.005) for N equal to 0 and 0.10. Since N is approximately 0.05 for the present alloys, this curve was interpolated from the Rice and Johnson result. Because of their low work hardening rates, the present alloys are subjected to a maximum achievable stress that is just over three times the yield stress and occurs at about 2.5 crack opening displacements in front of the tip. Since the values of N are similar, the larger δ_0 (see Table 4.2) with increased dispersoid content means that the maximum stress occurs further in front of the

crack tip. However, the maximum absolute value of σ_{yy} would not change significantly. This indicates that the predominant fracture mechanism is not simply stress controlled since, if it were, a larger δ_0 would not be required.

Rice and Johnson (1970) also plot the effective plastic strain as a function of x/δ . The distribution is shown in fig. 1.21. The approximate equation for this strain distribution was given by Schwalbe (1977) as eq. (1.57), although Schwalbe's equation appears to correspond to the fully plastic curve. The small scale yielding curve of fig. 1.21 predicts zero plastic strain at approximately two crack opening displacements in front of the crack tip. This is clearly not accurate for the present alloys where the plastic zone size at onset was up to six times larger than the crack opening displacement. Also, the notched tensile test results showed that dispersoids increase the effective plastic strain at fracture for the same stress triaxiality. It therefore seems reasonable to assume that the strain distribution in front of the crack tip changes from alloy to alloy and that this change is controlled by the dispersoid content. The following summarizes an attempt to describe the magnitude of the strain distribution change.

Taking the form of the plastic strain distribution from Rice and Johnson, one obtains the general form:

$$\bar{\epsilon}_p = A \frac{\delta}{x} + B \quad (4.15)$$

Solving for the constants A and B for each alloy requires two boundary conditions. The first sets $\bar{\epsilon}_p$ equal to 0 at the elastic-plastic interface, i.e. at $(\delta/x) = (\delta_0/r_{po})$. The second boundary

condition invokes the fracture strain of the most highly triaxial notch tensile specimen geometry. The most severe notch corresponds to σ_{yy}/σ_y of 2.28. From fig. 4.10, this stress state occurs at x/δ equal to 1.09. Therefore the second boundary condition is $\bar{\epsilon}_p = \bar{\epsilon}_f$ at $x/\delta = 1.09$.

These conditions and the resulting values for A and B are tabulated in Table 4.6.

Table 4.6

Constants A and B for eq. (4.15)

Alloy	δ_0/τ_{p0}	$\bar{\epsilon}_f$ for for				
			$\bar{\epsilon}_p = 0$	$x/\delta = 1.09$	A	B
HT	0.522	0.011		0.028		-.0145
ML	0.152	0.068		0.089		-.0135
MM	0.170	0.097		0.130		-.0221
MH	0.233	0.138		0.202		-.0470
MC	0.231	0.130		0.190		-.0438

Due to the assumptions involved, the values of A and B given above cannot be taken with absolute confidence. However, they provide a reasonable comparison of the strain distribution in front of a blunting crack tip as a function of dispersoid content.

These results will be discussed in two contexts: first, at the critical moment when δ equals δ_0 ; and second, in the general case of δ less than δ_0 .

When δ_0 is used in eq. (4.15), the strain profiles in the plastic zone at onset can be compared, as is done in fig. 4.11. The plastic

zone size at onset r_{po} is shown for each alloy on the abscissa. When presented in this way, several points become clear. At the onset of crack extension, alloy MT sustains high strains over only a very short distance. Due to the intense slip bands that form, strain concentrations (and therefore stress concentrations) are created at the grain boundaries. Conditions for void nucleation at grain boundary particles are satisfied quickly and low energy ductile rupture occurs along the PFZ. For the dispersoid containing alloys, the plastic zone sizes at onset are similar, but the strain profiles reflect the increase in strain required for rupture as dispersoids homogenize the slip. As a fracture criterion, this is equivalent to saying that the critical strain must be achieved over a larger critical distance. Thus, in this series of alloys, the critical microstructural distance increases with slip homogenization. The results for alloy MC show that this is true only as long as the fracture mechanism does not change. The lower strain profile at crack extension onset for alloy MC reflects the decrease in the critical distance caused by the presence of coarse inclusions. These coarse inclusions serve as void nucleation sites for the transgranular ductile rupture mechanism which is superimposed on the grain boundary ductile rupture mechanism, giving fracture at lower strains.

A second way to consider the results for A and B in Table 4.6 is to compare the strain profiles plotted against x/δ_0 for δ less than δ_0 . These are shown in fig. 4.12. For a given position x and crack opening displacement δ , the strains are higher as the amount of dispersoid increases. This can be explained by the effect of dispersoids on the crack tip geometry referred to in sec. 4.3.1. However, the model proposed by Kim, Fine and Mura (1970) must be

modified slightly. Their model ignores the material microstructure and assumes a smooth, semi-circular crack tip. Thus, for the same applied stress, the plastic zone size is smaller when the crack tip opening displacement is larger, i.e. greater blunting. This aspect of the model contradicts the elastic and elastic-plastic analyses which predict the same crack tip opening displacement for alloys of the same yield strength loaded to a given stress intensity factor. As an alternative, it is suggested that the crack tip opening displacements are indeed the same, but the smoothness and shape of the blunting notch root depend on the microstructure. This idea is represented schematically in fig. 4.13 for extreme situations of homogeneous and heterogeneous slip. For the homogeneous slip case (fig. 4.13(a)), slip occurs on many planes and as the crack tip opens to a given displacement the crack tip profile can blunt in a smooth arc. This blunting relaxes the local stress intensity at the crack tip by plastic flow which produces higher strains in front of the tip.

When slip is heterogeneous as in fig. 4.13(b) the crack tip cannot blunt smoothly because slip is occurring on a few coarse slip bands. Thus, for the same δ , the crack tip is sharper and the local stress intensity higher than for homogeneous slip. The plastic zone extends further due to the higher local K at the tip, but the strain in the plastic zone is smaller because of the smaller displacements of the opening tip faces. This model can be used to explain both the change in plastic zone size and the change in plastic strain distributions within the plastic zone in terms of the microstructural effect on crack tip geometry.

4.6 Micromechanisms of Crack Extension

The model proposed in the previous section does not specifically consider the microstructural mechanisms involved in crack extension. To do so, the three dimensional crack tip plastic zone must be considered. Fractographic analysis of the present study has shown that the predominant fracture mechanism in these alloys is ductile rupture along the PFZ. As the coarse inclusion content increases, transgranular ductile rupture also becomes an important contributing mechanism but, for the moment, only the PFZ path will be considered. The appearance of fine dimples containing particles on the intergranular fracture surfaces confirm that the mechanism occurs by void initiation at grain boundary particles followed by void growth and coalescence. Goods and Brown (1979) review the literature concerning nucleation of cavities by plastic deformation. One of their conclusions is that, for materials which exhibit coarse slip, plastic relaxation is not favoured and cavities nucleate at low plastic strains. This situation can be illustrated by assuming that void nucleation occurs when the interfacial strength σ_I of a grain boundary particle is exceeded by the local stress σ_l near the particle. The local stress will be greatest at the points where slip bands impinge on the grain boundaries (Stroh, 1954 and 1955). Assuming that a slip band impinges on a particle, the local stress near the particle is given by (Brown and Stobbs, 1976)

$$\sigma_l = \alpha' \nu b(\rho_1)^{1/2} \quad (4.16)$$

where ρ_1 is the local dislocation density and $\alpha' = 1/7$. Dowling (1975) has shown that the effect of dispersoids on the slip distribution of

the present alloys is to increase both the number of slip bands and the width of each band. In the context of eq. (4.16), the broadening of a slip band by dispersoids will reduce the local dislocation density and, in turn, the local stress at the head of the slip band. In terms of the local strain, eq. (4.16) becomes

$$\epsilon_1 > \left[\frac{\sigma_I}{\sigma'_{UB}} \right]^2 \quad (4.17)$$

for the nucleation of a void at a grain boundary particle. Although eq. (4.17) is derived on the basis of a critical stress at the particle interface, the stress is produced by the local dislocation density which is a function of the plastic strain in the material. Therefore, the failure criterion refers fundamentally to strain (Goods and Brown, 1979).

Several studies (Argon et al., 1975; French and Weinrich, 1974) have shown that the critical stress to nucleate cavities is dependent on hydrostatic stress. Thus, the condition for void nucleation at grain boundary particles becomes

$$\sigma_I + \sigma_H > \sigma'_I \quad (4.18)$$

where σ_H is the hydrostatic tension. By analogy to the development by Goods and Brown (1979), eq. (4.17) becomes

$$\epsilon_1^{1/2} > k_2(\sigma_I - \sigma_H) \quad (4.19)$$

where k_2 is a constant that is an inverse function of the volume fraction and size of grain boundary particles. The results of the present study for both tensile tests and fracture toughness tests can be explained qualitatively in terms of dispersoid effects on local

dislocation density and grain size using eq. (4.19).

Considering first the term k_2 , the theory predicts that the nucleation strain should decrease as the volume fraction of particles increases. Prince (1977) concluded that the grain boundary particles of the present alloys are of two types - dispersoids which happened to be intersected by a grain boundary and the usual grain boundary precipitate found in many age hardening systems. Thomas (1961) suggested that the latter could be silicon precipitates. Since alloy MT does not contain dispersoids yet does exhibit void initiation at the grain boundary particles it is reasonable to presume that particles of the second type are responsible for the grain boundary nucleation sites in all the alloys. However, calculation of the weight percent of excess silicon shows that there is little difference between alloys. The results of these calculations, assuming all of the Mg goes to form Mg_2Si , are given in Table 4.7.

Table 4.7

Excess silicon contents (calculated)

Alloy	Weight percent excess silicon
MT	0.63
ML	0.58
NM	0.58
MM	0.58
MC	0.53

It therefore appears that the excess silicon content should have little differentiating effect between the alloys. Rather, the grain

boundary precipitates are most likely enlarged Mg_2Si particles of approximately equal size and distribution for all the alloys. Accordingly, k_2 in eq. (4.19) would not vary significantly.

Considering next the hydrostatic tension term in eq. (4.19), as σ_y increases the nucleation strain will decrease. Results from notched tensile tests are consistent with this prediction. The fracture strains did decrease with increased triaxiality in the notch although the decrease was not excessive for the range of triaxialities tested. Cane (1981) has shown that a state of locally increased triaxiality is induced in the PFZ when there is a difference between the strength of the PFZ and the matrix. The magnitude of this local triaxiality increases with the strength differential. Since the separate stress-strain relations for the PFZ and matrix are not known for the present alloys, the severity of this effect cannot be determined directly. However, Prince (1977) found that the width of the PFZ did not vary with dispersoid content. If the properties of the PFZ can be assumed to be similar and the stress-strain relation of the bulk characteristic of the matrix, then the similar work hardening exponent of the present alloys would indicate that the effect of this PFZ induced triaxiality is approximately the same for each alloy.

Finally, dispersoids effectively reduce the local strain term γ_1 in eq. (4.19) by reducing the dislocation density in slip bands as they impinge on the grain boundaries. Although this effect is also difficult to quantify, Dowling measured the slip band spacing of alloys equivalent to HT, HE and MH as a function of compressive strain. A view of how this slip band spacing changes in front of a blunting crack tip can be obtained by combining Dowling's measured spacings with the strain distributions shown in fig. 4.11. Assuming

that her measurements as a function of compressive strain can be applied to the tensile strain in front of the crack tip. Fig. 4.14 shows the slip band spacing ρ plotted against distance ahead of the initially sharp crack x at the value of δ corresponding to crack extension onset for each alloy, δ_0 . For each alloy, the slip band spacing decreases as the strain increases near the crack tip. Also, for a given distance in front of the crack tip, the slip band spacing decreases with increasing dispersoid content. Since slip band width can be considered to be inversely proportional to slip band spacing (Dowling, 1975), the stress concentration ψ at the head of a slip band given by (Evensen et al., 1975)

$$\psi = \left[\frac{d}{W} \right]^{1/2} \quad (4.20)$$

decreases as dispersoid content increases. In eq. (4.20) d is the grain size and W is the slip band width. Thus, the criterion for activation of the grain boundary ductile rupture micromechanism can be considered, in the light of fig. 4.14, as occurring in a region in front of the crack tip where the combination of high principal tensile stress, high stress triaxiality and narrow, intense slip bands provide the necessary conditions. A useful model to describe this concept is the semi-cohesive zone suggested by Gerberich and Moody (1979) in which the crack tip region contains areas that have fractured separated by unfractured ligaments. Using this model Moody and Gerberich (1980) successfully predict the grain size effect on the fatigue threshold stress intensity in titanium alloys. Edwards (1981) extended the semi-cohesive zone concept as a model of the fatigue crack growth mechanism at all levels of stress intensity factor range

for the present alloys. The model is equally applicable to the monotonic loading crack extension mechanisms of the present study.

A schematic of the semi-cohesive zone model is shown in fig. 4.13. At the tip of the main crack lies a plastic zone that contains within it the semi-cohesive zone. As the load is increased, the plastic zone grows larger and certain grain boundaries that are favourably oriented to the maximum tensile stress will fracture by microvoid coalescence along the PFZ. Since dispersoids suppress this fracture mechanism, fewer of these grain boundaries open up ahead of the crack tip and more unfractured ligaments remain in the semi-cohesive zone. Macroscopic crack extension then corresponds to the fracture of the remaining ligaments and the joining of the microcracks to the main crack. This aspect of the model is consistent with observations made on plastic zone specimens loaded to stress intensities less than those required for onset. In many cases, short microcracks were observed in the plastic zone ahead of the main crack tip; examples of this grain boundary separation are shown in fig. 3.13. In alloy MT, the intergranular fracture mode occurs at low strains. As the volume fraction of dispersoids increases, slip becomes more homogeneous and the tendency for intergranular fracture is reduced; the size of the semi-cohesive zone is decreased and larger strains are required to fracture the remaining ligaments. Thus, larger crack tip opening displacements at crack extension onset and larger fracture toughnesses result. The semi-cohesive zone model also applies to alloy MC. However, due to its much larger number of coarse constituent particles, the opening up ahead of the crack tip will be due to both intergranular ductile rupture and coarse particle ductile rupture. Thus, even though alloy MC has more dispersoids and,

therefore, more homogeneous slip than alloy M1, the fracture toughness is decreased due to the coarse constituent particles.

The semi-cohesive zone' serves as a realistic and consistent model for the discussion of fracture processes in these Al-Mg-Si alloys. The model essentially predicts that continued crack extension will occur by discontinuous jumps as the microcracks ahead of the crack tip link up with the main crack. The present study has shown that the addition of manganese-bearing dispersoids to peak aged Al-Mg-Si alloys inhibits the microcrack formation ahead of the crack tip and, therefore, increases the resistance to crack extension. Thus, the macroscopic fracture toughness parameters in these alloys are controlled by the dispersoid influence on the micromechanisms of crack extension.

Figure 4.1

Transmission electron micrographs from Prince (1977) of his alloy 4 (equivalent to alloy MH).

- a) Dispersoids, PFZ and grain boundary precipitates (A).
- b) Lower magnification micrograph showing dispersoids at a grain boundary (B) and light area (C) where dispersoids have been preferentially etched out at the surface.

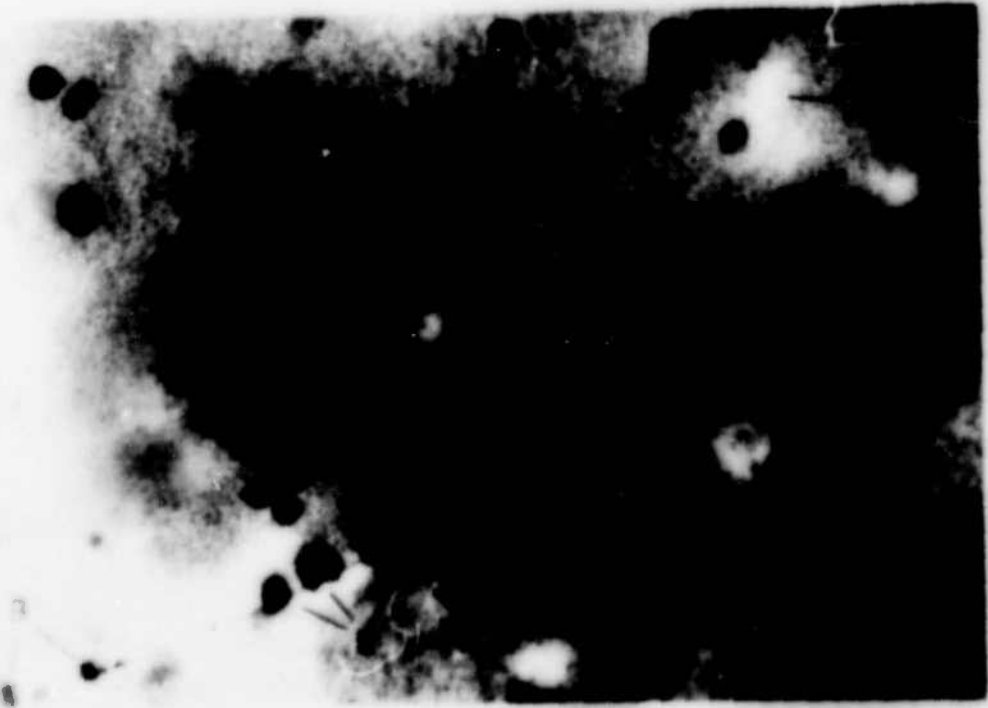
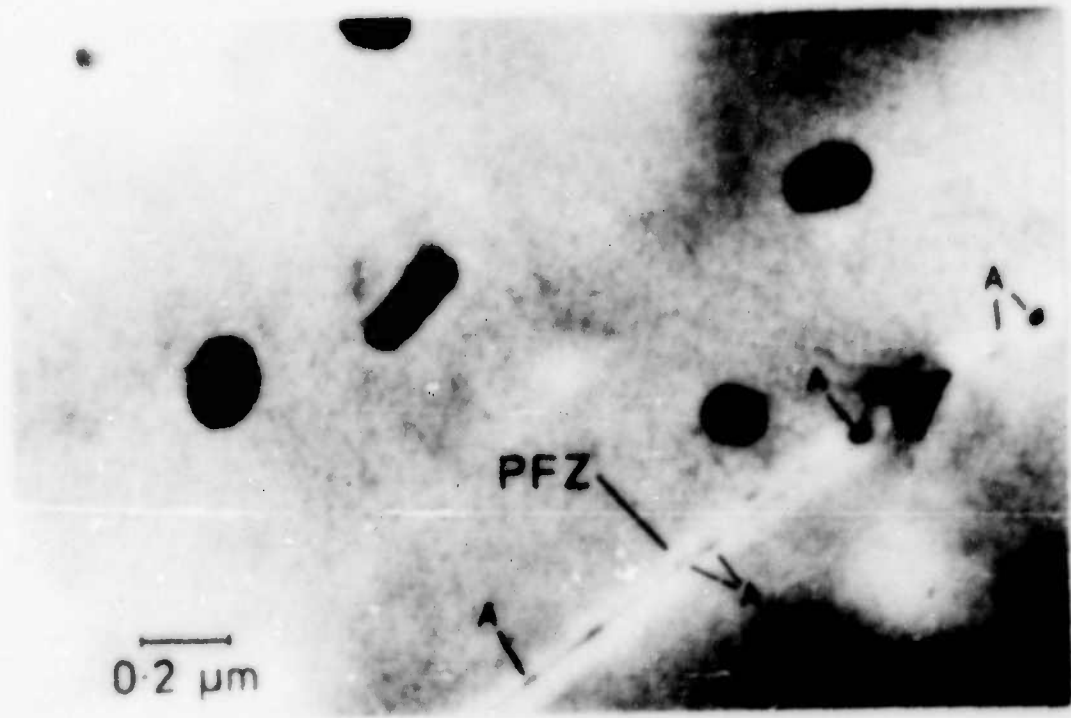


Figure 4.2

Effective plastic strain at failure versus stress triaxiality for notched tensile specimens. Error bars show full range of values.

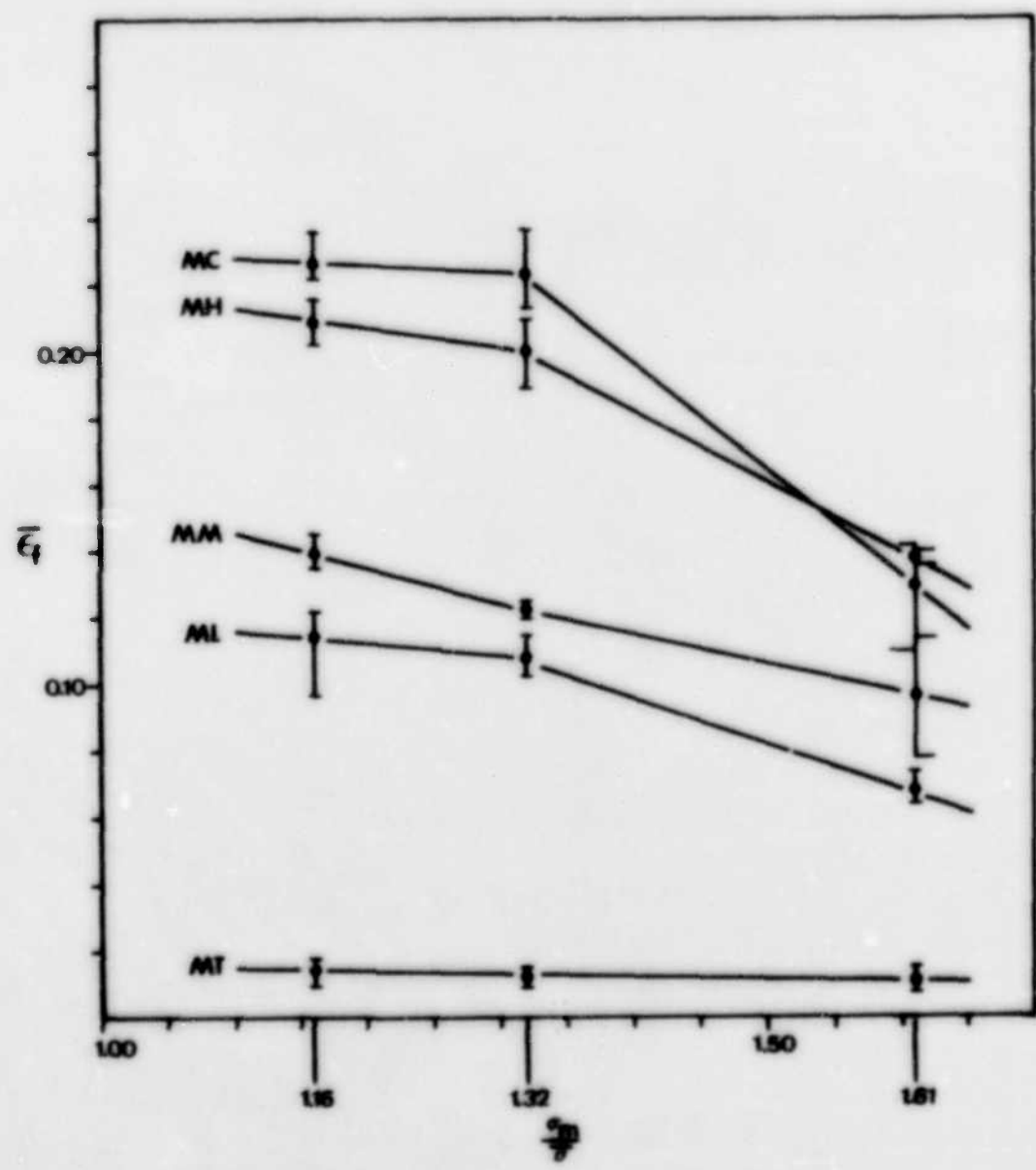


Figure 4.3

Summary of J-integral resistance lines.

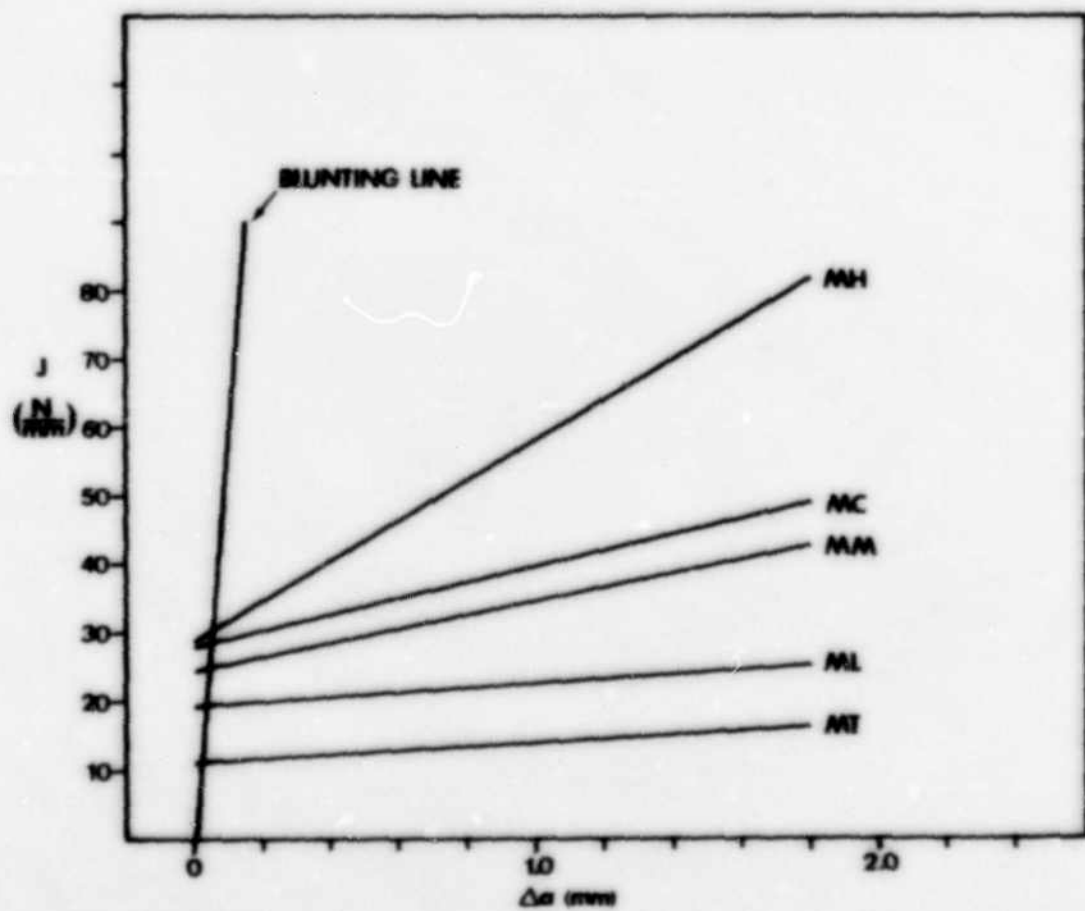


Figure 4.4

Plot of K_G , calculated from Lowat and Griffith's analysis, against the experimentally determined K_Q .

Figure 4.5

Schematic of compact tension specimen under load, showing location of the centre of rotation. R is the rotation factor and $b = R-a$.

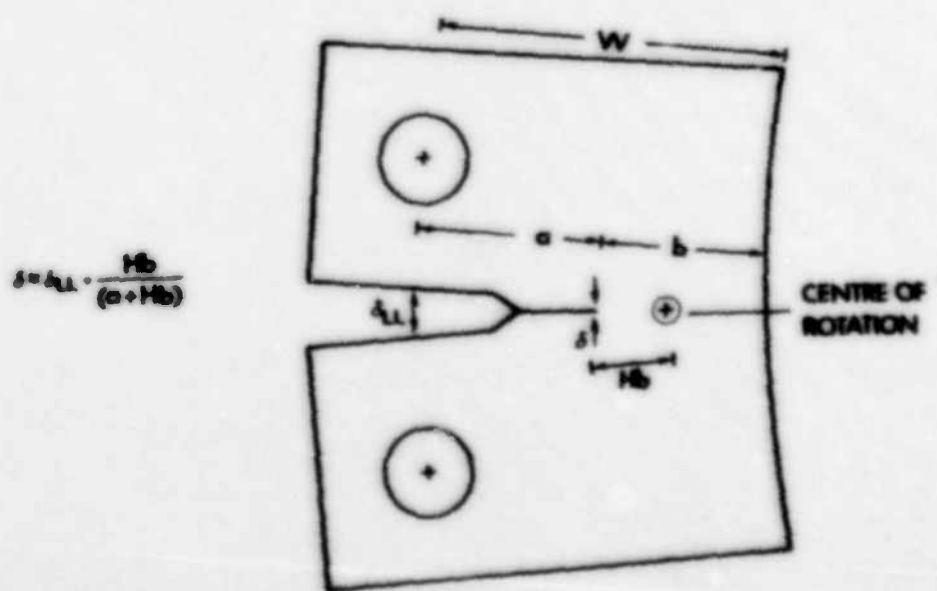
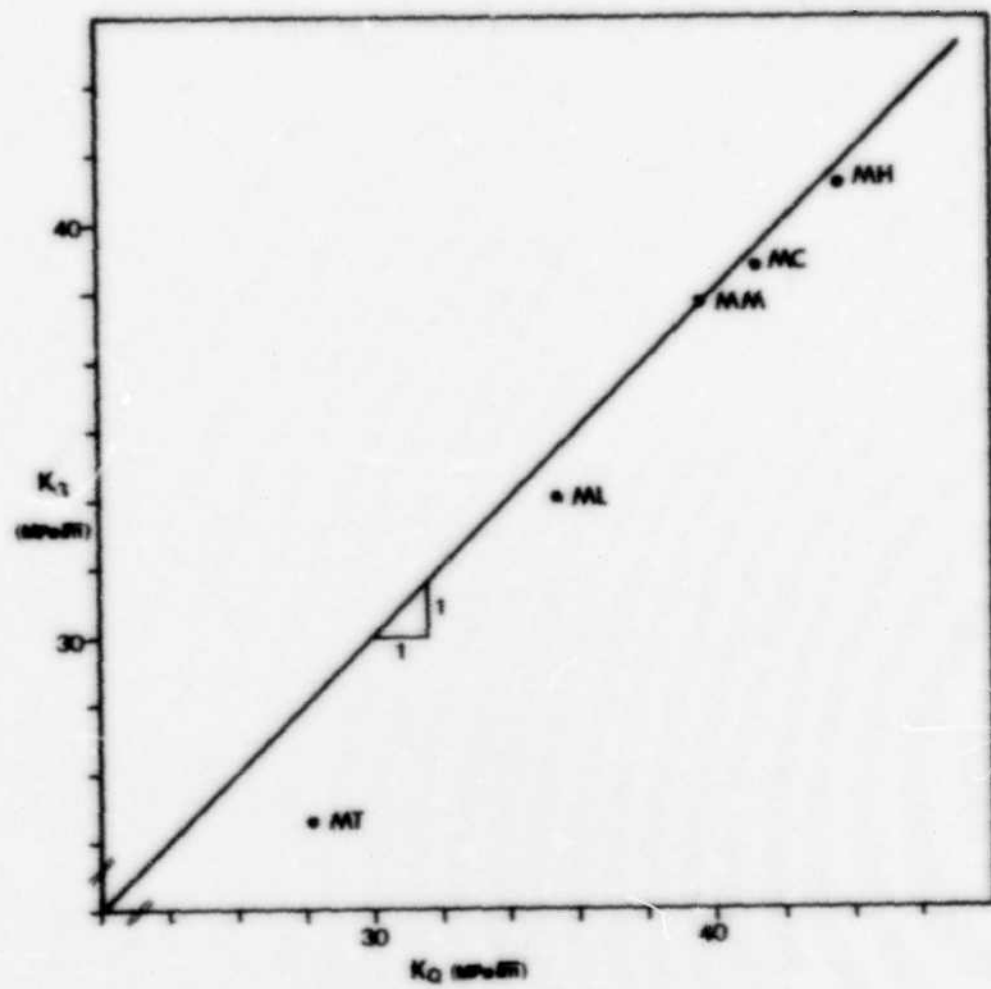


Figure 4.6

Correlation between experimentally determined J_{lc} and $\sigma_{y\delta}$.
Straight line is based on the formula $J = m\sigma_{y\delta}$ with m set
equal to one.

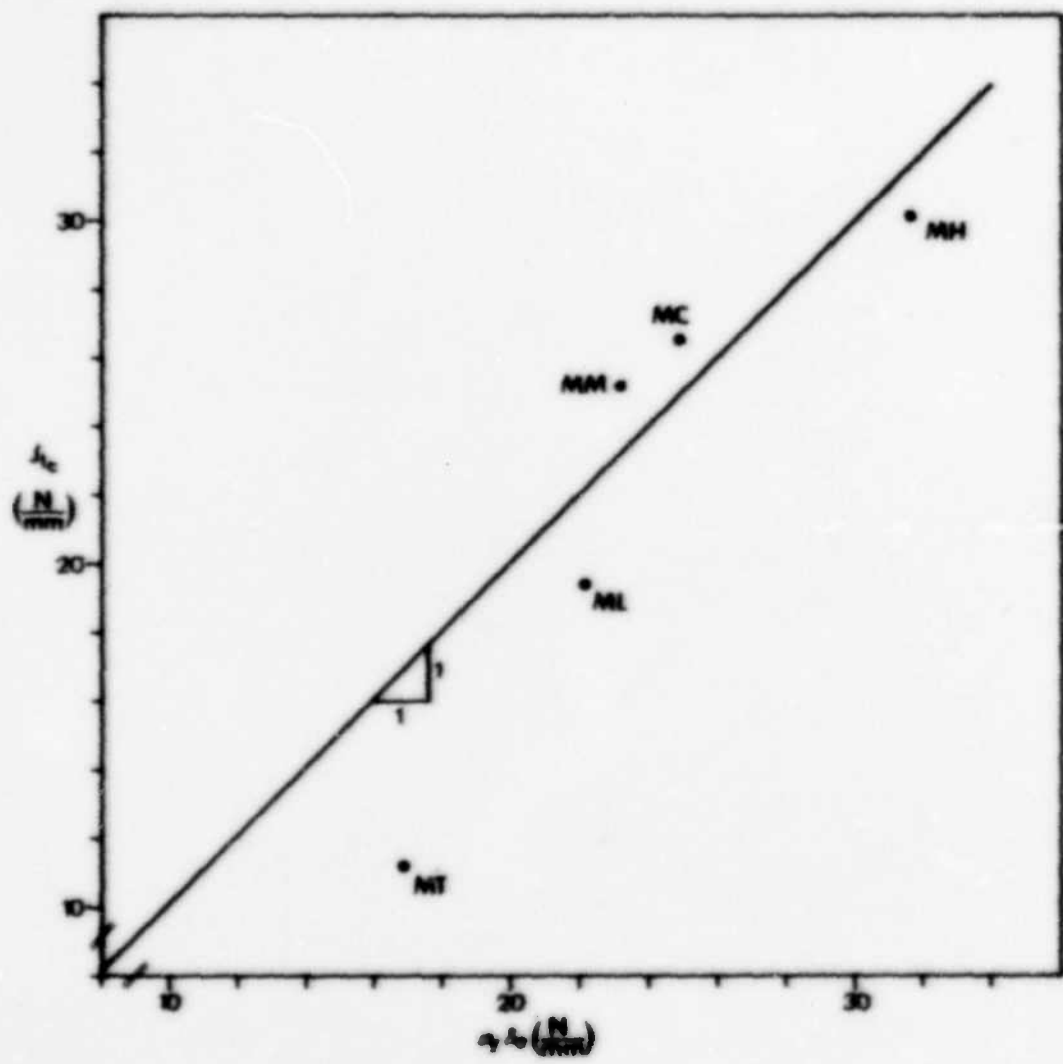


Figure 4.7

Schematic showing the dependence of plastic zone size upon the geometry of the notch and the applied stress intensity factor, K (after Kim et al., 1979).

a) Same geometry but different applied stress intensities,

$$K_2 > K_1.$$

$$r_{p_2} > r_{p_1}$$

b) Different geometries at the same applied stress intensity, $K_2 = K_1$.

$$r_{p_1} > r_{p_2}$$

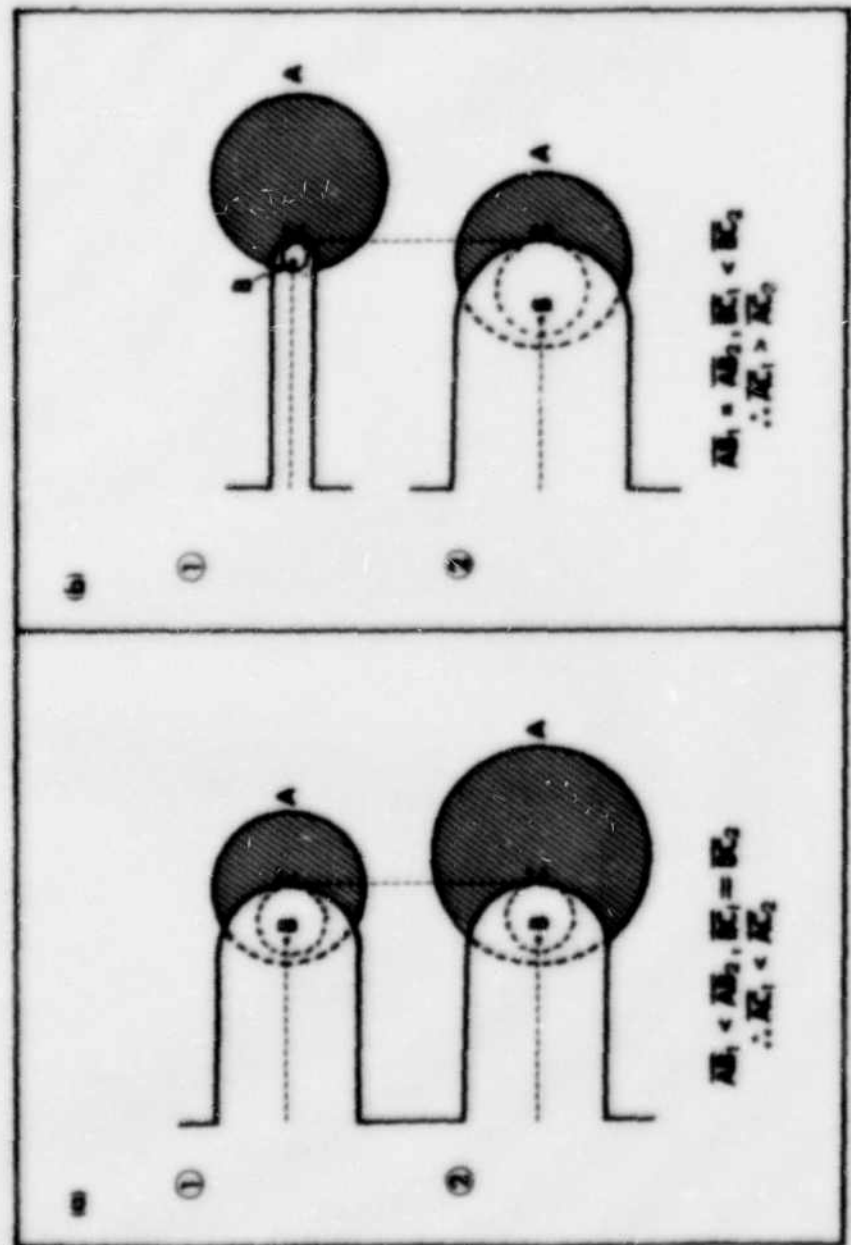


Figure 4.6

Variation of experimental plastic zone size with stress intensity factor and yield strength. Values of α are derived from the equation

$$r_p = \alpha \frac{K^2}{\sigma_y}$$

Lines are extrapolated to the value of stress intensity factor at crack extension onset, K_0 .

Alloy	α	$(K_0/\sigma_y)^2$ (mm 2)	$r_{p0} = \alpha (K_0/\sigma_y)^2$ (μm)
HT	0.012	9.6	115
HL	0.034	13.5	460
HH	0.025	17.7	440
HR	0.023	18.1	420
HC	0.017	20.7	350

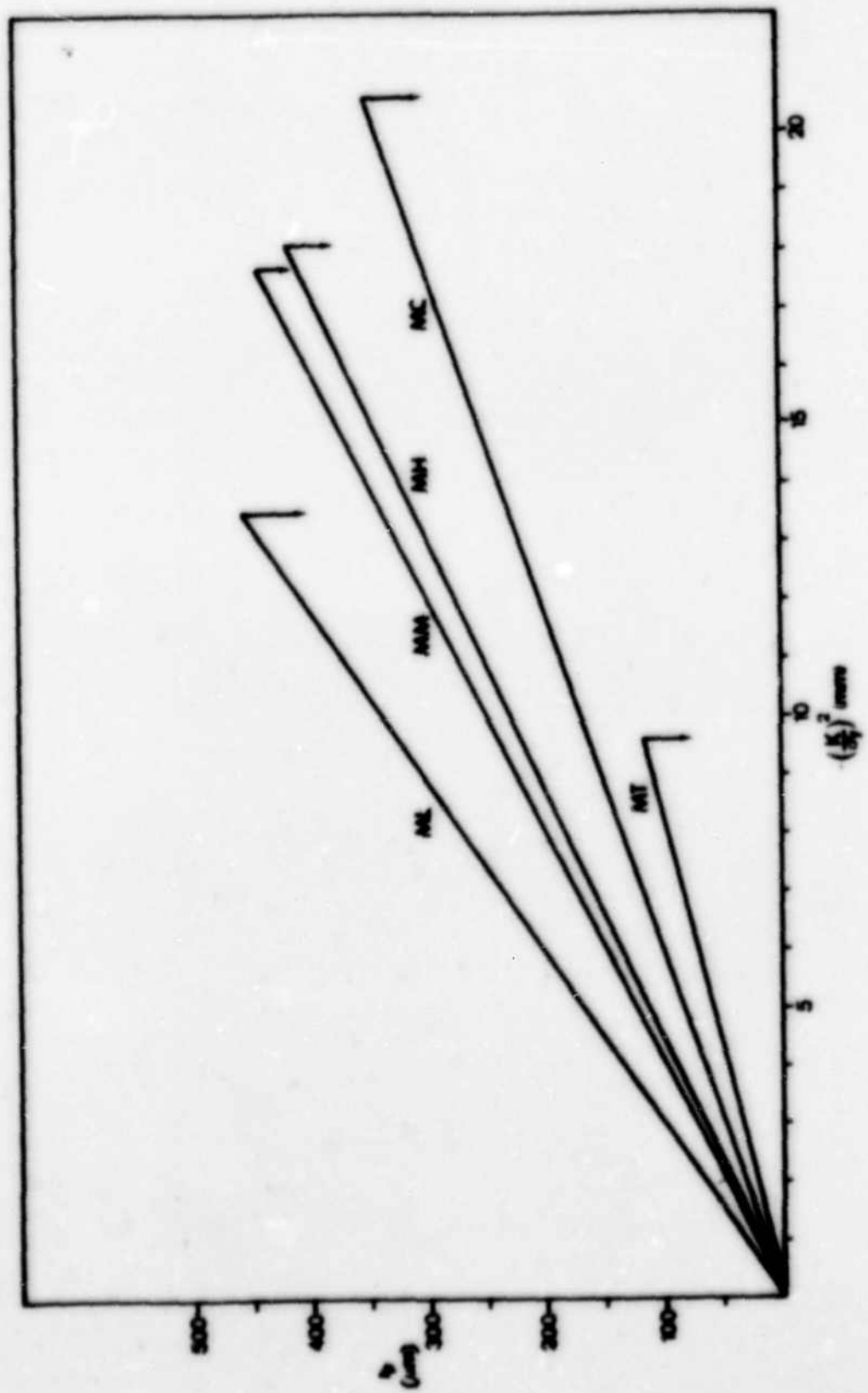


Figure 4.9

Correlation of work absorbed per unit area of crack surface
(as calculated below) with experimental J_{lc} .

$$\frac{dW}{da} = \frac{r_{po} \cdot \sigma_y^2}{a - E}$$

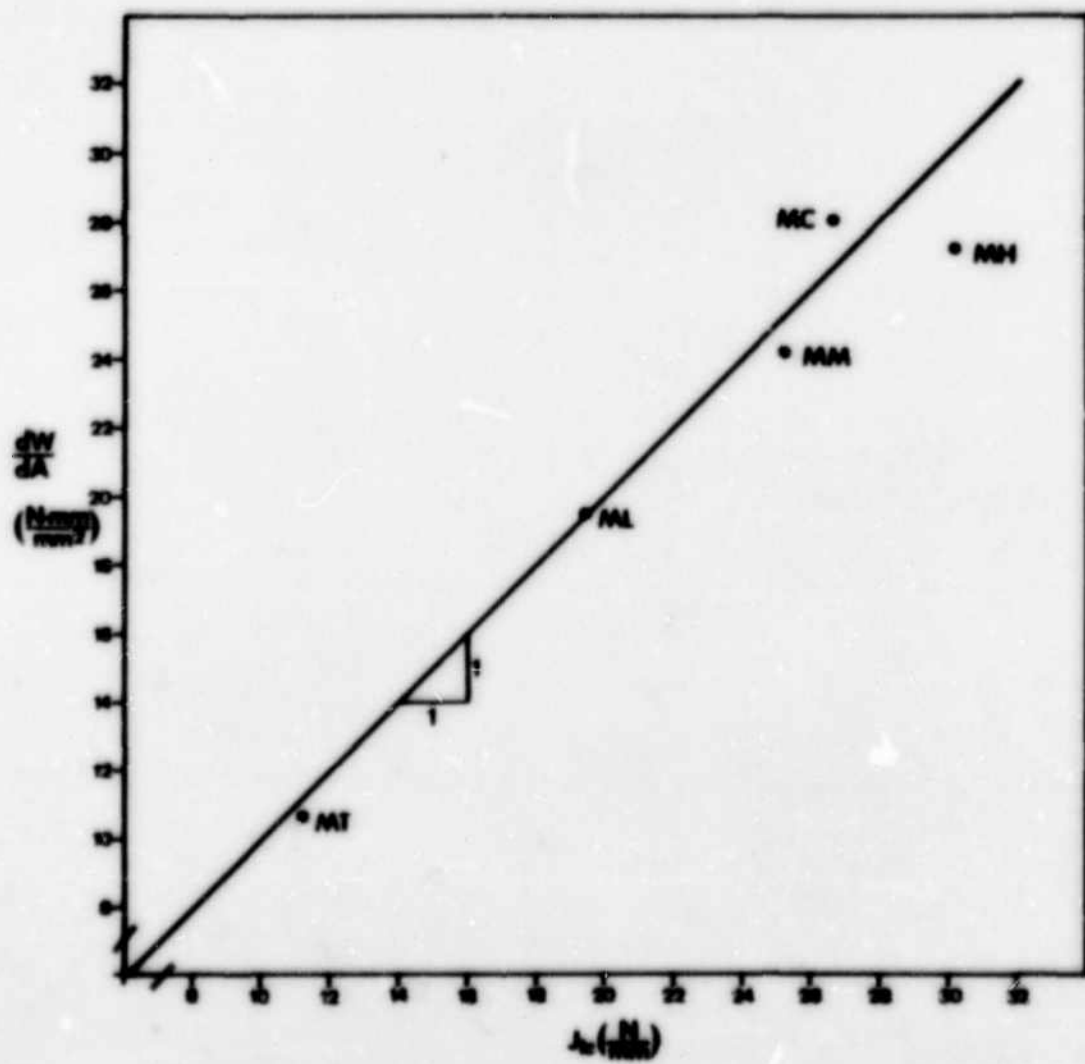


Figure 4.10

Modified stress distribution due to crack tip blunting.
Taken from Rice and Johnson (1970) fig. 10 for $\sigma_y/E=0.005$.
The most highly triaxial notched tensile specimen gives
 σ_{yy}/σ_y of 2.26 which corresponds to X/a of 1.09.

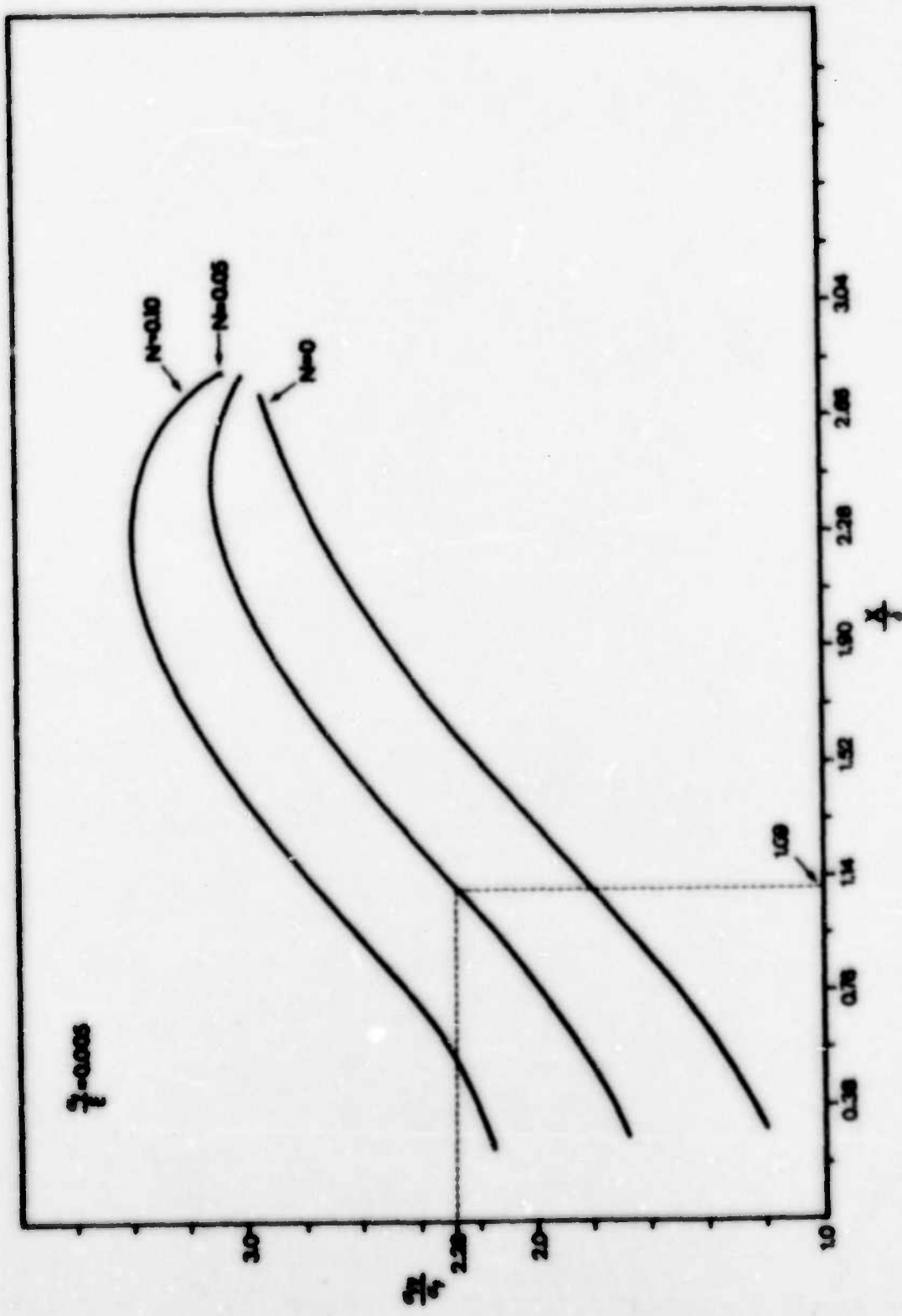


Figure 4.11

Effective plastic strain versus distance ahead of the crack tip, shown at the onset of crack extension.

$$\bar{\epsilon}_p = A \frac{\delta_0}{x} + B$$

Alloy	δ_0 (μm)	A	B
HT	60	0.0278	-0.0145
HL	70	0.0889	-0.0135
HM	75	0.1299	-0.0221
HH	92	0.202	-0.0470
HC	81	0.1895	-0.0438

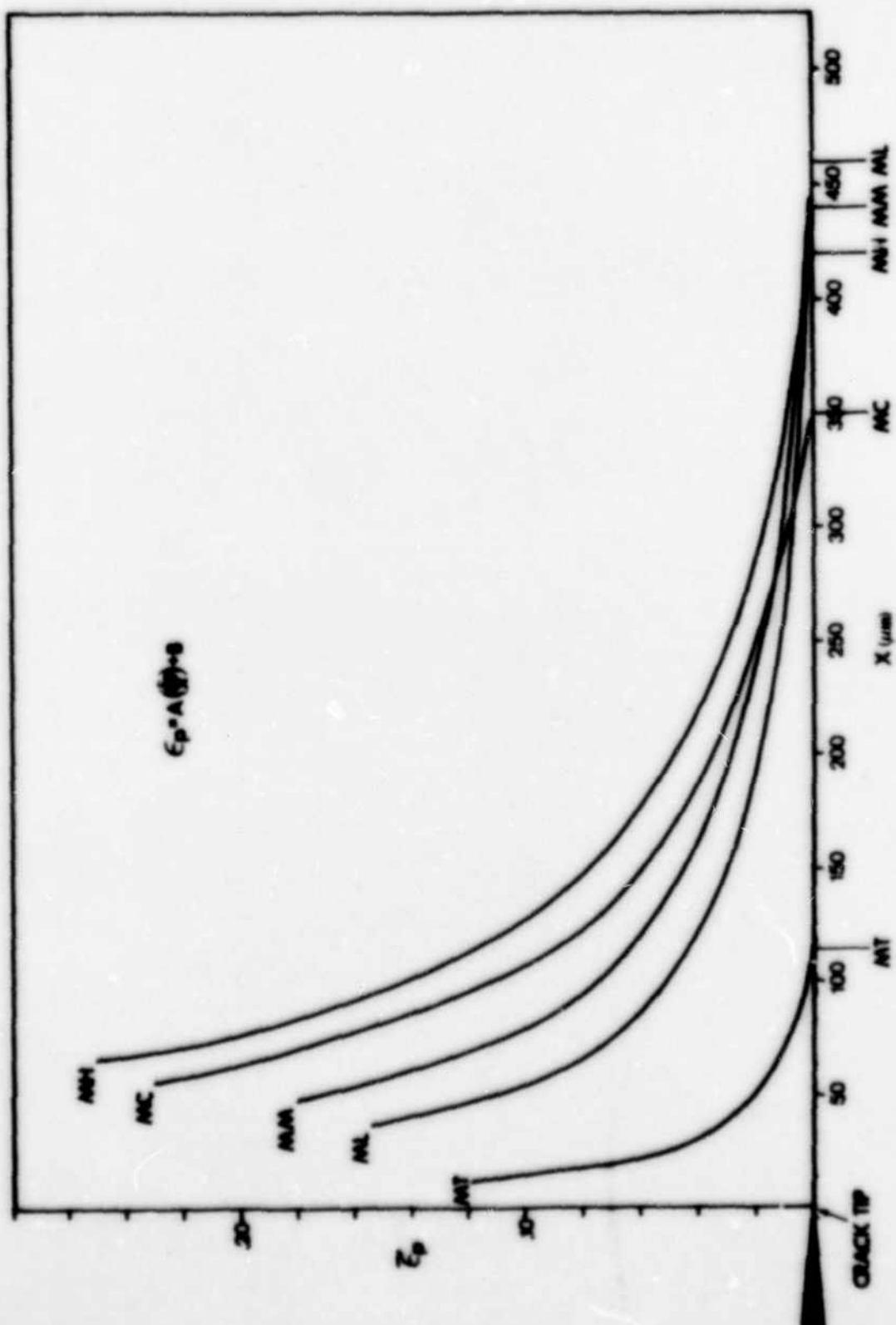


Figure 4.12

Effective plastic strain as a function of distance ahead of the crack tip and crack tip opening displacement. Values of A and B are shown in the caption for fig. 4.11.

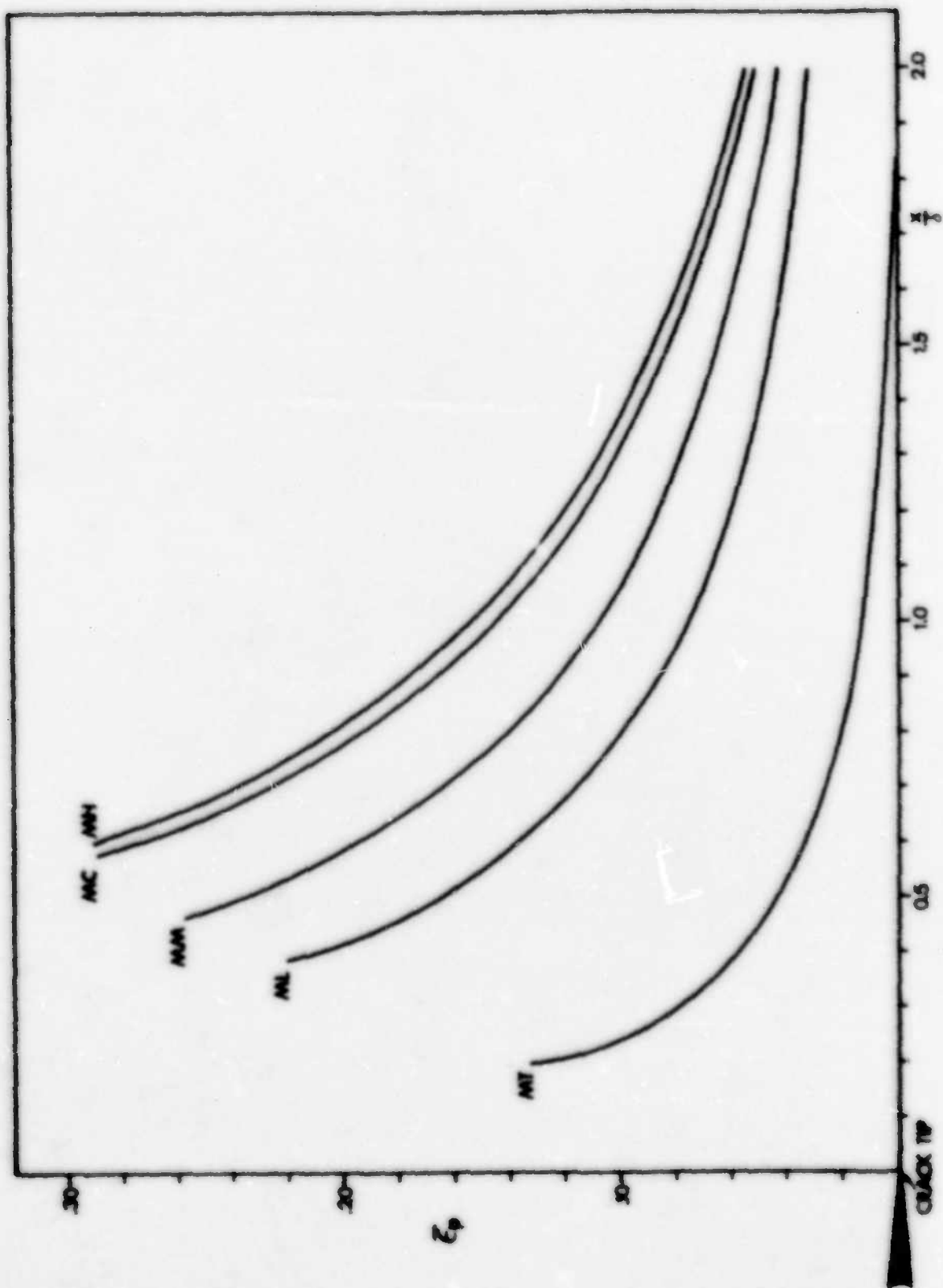
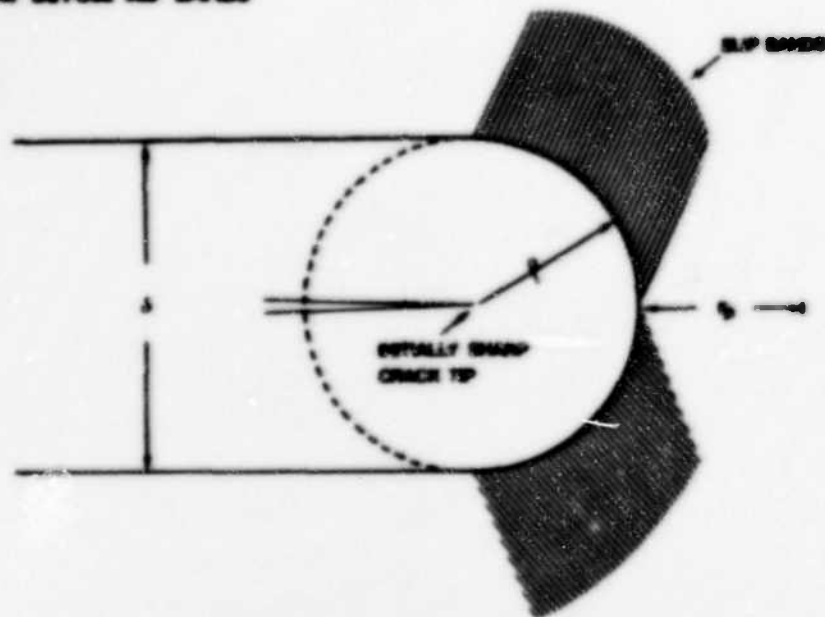


Figure 4.13

Schematic showing the effect of slip distribution on the crack tip radius of curvature, ρ . Both (a) and (b) are shown at the same applied K and the same δ .

- (a) Homogeneous slip distribution gives a smooth blunting notch, large radius of curvature and small plastic zone size.
- (b) More heterogeneous slip distribution gives an uneven notch root, smaller radius of curvature and larger plastic zone size.

A DIFFUSE SLIP BANDS



B INTENSE SLIP BANDS

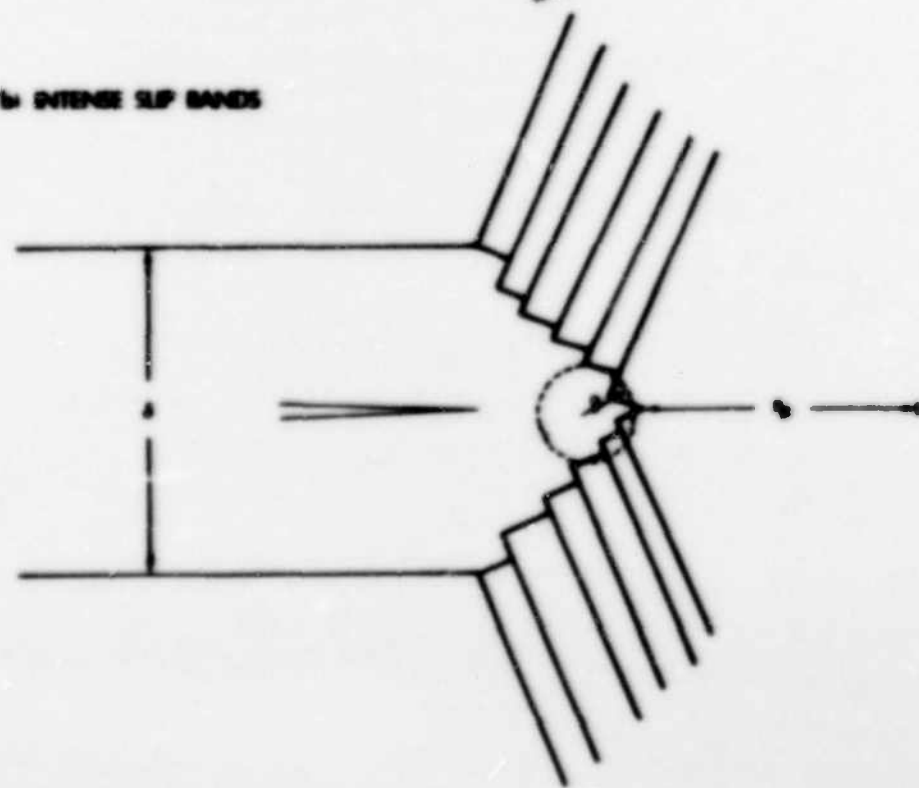


Figure 4.14

Slip bond spacing, p (taken from Dowling, 1975) versus distance ahead of the crack tip, shown at crack extension onset using the strain distributions of fig. 4.11. Lines show the linear regression analysis for each alloy.

Alloy	X or p (nm)	Z Strain			
		1.8	2.6	3.9	9.0
HT					
	X	52.5	42.5	30	18.5
	p	2.31	2.72	2.79	1.61
HL					
	X	200	160	120	62.5
	p	2.13	1.69	1.25	0.34
HM					
	X	295	260	222	-
	p	1.39	1.21	0.90	-

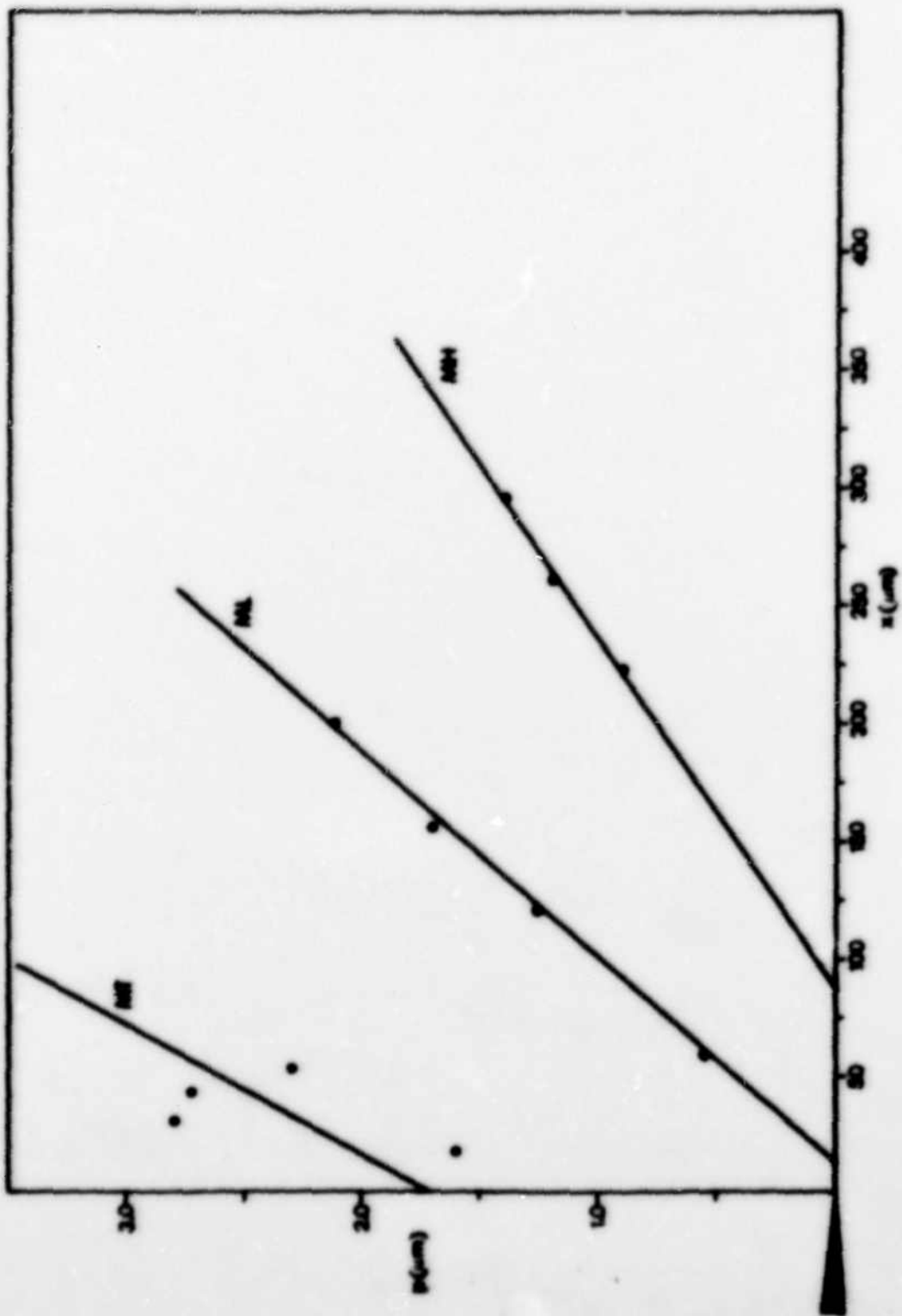
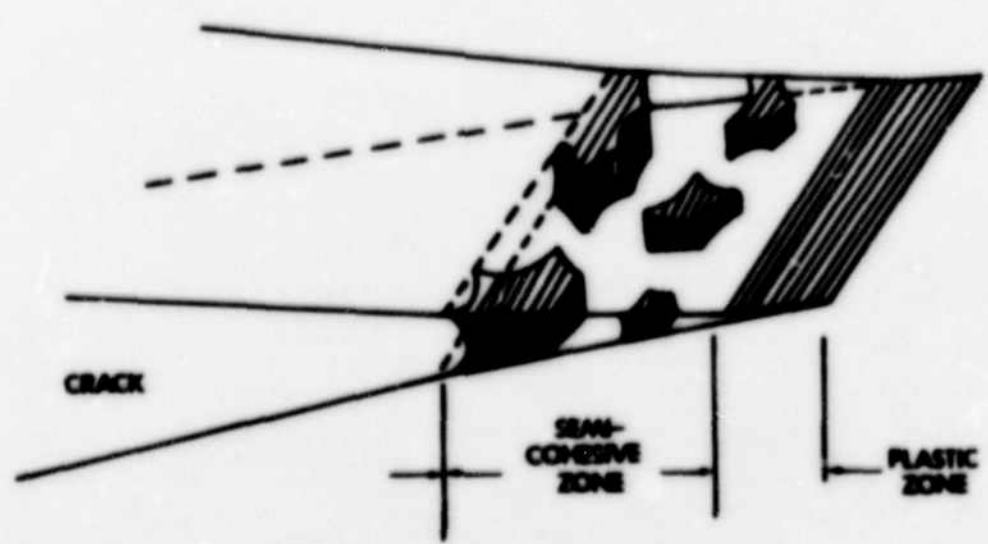


Figure 4.15

Schematic of crack tip, semi-cohesive zone and plastic zone.
Shaded areas represent unfractured ligaments. (after
Gerberich and Moody, 1979).



Chapter 3

CLOSURE

3.1 Conclusions

This investigation has established a direct link between the microstructural factors controlling the crack tip deformation processes and the macroscopic fracture toughness parameters. By promoting more homogeneous slip, dispersoids alter the geometry of the blunting crack tip to give a larger radius of curvature. This blunted crack tip has a smaller effective stress intensity factor and, therefore, a smaller associated plastic zone size. The work to form a unit area of new crack surface dW/dA , as calculated from the plastic zone size, has been shown to correspond quite closely to the experimentally determined ductile fracture toughness J_{lc} .

In addition, other specific conclusions which can be drawn from this work are as follows:

- 1 The addition of manganese-bearing dispersoid particles to a peak aged Al-Mg-Si alloy significantly improves the ductile fracture toughness as measured by the J -integral at incipient crack extension. The improvement brought about by dispersoids is due to suppression of the grain boundary ductile rupture mechanism by dispersoid effect on grain size and shape and the homogenisation of slip distribution.
- 2 The beneficial effect of dispersoids is optimised by using the

maximum amount of manganese that can be held in solid solution with the iron content kept to the minimum obtainable. The commercial purity alloy containing an appreciable amount of iron has a lower ductile fracture toughness than the optimum but higher than alloys containing less than the maximum amount of dispersoid.

- 3 The dispersoids also result in an improvement in alloy resistance to unstable crack extension as measured by the slope of the J resistance curves.
- 4 For the same induced triaxial stress state in notched tensile specimens, ductility increases with dispersoid content. For the most highly triaxial stress state notch geometry, the beneficial effect of dispersoids is somewhat negated by the deleterious effect of coarse constituent particles in the commercial purity alloy.
- 5 The alloy work hardening exponent shows a small but detectable increase with dispersoid volume fraction.
- 6 For the similar yield strengths in these alloys, the crack tip plastic zone size is proportional to K^2 and the constant of proportionality decreases with increasing dispersoid volume fraction. This effect can be rationalised in terms of dispersoid influence on the effective radius of curvature of the blunting crack tip.
- 7 For the iron free alloys, the predominant micromechanism of crack extension is grain boundary ductile rupture. This micromechanism operates by void initiation at grain boundary particles followed by void growth and coalescence along the grain boundary precipitate free zone.

- 8 The conditions for activation of the grain boundary ductile rupture mechanism are controlled not by the plastic zone size but by the strain and stress distributions within the plastic zone.
- 9 The concept of a semi-cohesive zone immediately ahead of the crack tip provides a realistic model to describe the micromechanisms of crack extension in these alloys.

3.2 Implications for Alloy Design

This study has shown that the current commercial practice of maximizing the Mn-bearing dispersoid content of peak-aged Al-Mg-Si alloys results in substantial improvements in ductile fracture toughness and resistance to unstable crack extension. Although further improvement in these parameters could be obtained by manufacturing commercial products from the same alloy but using a high purity aluminium base (MH as opposed to MC in the present study), the results of the current investigation indicate that the additional benefit gained would be far outweighed by the increased cost of aluminium base purification.

3.3 Suggestions for Further Work

The present study has shown that the ductile fracture toughness of peak aged Al-Mg-Si alloys is increased by the introduction of dispersoids to the microstructure. This effect has been explained in terms of a suppression of the grain boundary ductile rupture mechanism of crack extension via the dispersoid influence on slip homogenisation. Although the yield strength and grain sizes of the dispersoid containing alloys are smaller, increasing the dispersoid

content does bring about a slight reduction in grain size and increases the curvature of the grain boundaries. Since these effects will also influence the grain boundary micromechanisms, it would be desirable to alter the slip distribution independently of grain size effects. This could be done by varying the ageing treatment for one of the dispersoid containing alloys. Considering the ageing curves in figs. 2.1 to 2.5, it is possible to underage and overage the alloy to the same yield strength for a fixed grain size and shape. Thus, one could alter the slip distribution in the matrix independently of the dispersoid. Using the experimental techniques described in the study, the ductile fracture toughness and plastic zone size variations and the resulting micromechanisms of crack extension could be related to slip distribution in a single alloy.

LIST OF REFERENCES

Abou-Sayed, I.S., Brock, D., Porte, T.P. and Stonerifer, R.B. (1981). ICFS, Cannes, France, 4, 1707-1713.

Airy, G.B. (1862). Brit. Assoc. Advances Sci. Rept.

Allia, P. and Mercher, P. (1972). Metals and Materials, 6, 343-346.

Argon, A.S., Im, J. and Safoglu, R. (1975). Met. Trans., 6A, 825-837.

Ashby, M.F. (1970). Phil. Mag., 21, 399-424.

ASTM (1978). E399-78, Standard Method of Test for Plane-Strain Fracture Toughness of Metallic Materials.

Barenblatt, G.I. (1962). Advances in Applied Mechanics, 7, 55-129.

Bathias, C. (1977). ICP4, 2, 1307-1312.

Bathias, C. and Pelloix, R.H. (1973). Met. Trans., 4, 1265-1273.

Baxter, W.J. and Rouze, S.R. (1976). Met. Trans., 7A, 647-654.

Begley, J.A. and Landes, J.D. (1972). Fracture Toughness, Proceedings of the 1971 National Symposium on Fracture Mechanics, Part II, ASTM STP 514, 1-20.

Billby, B.A., Cottrell, A.H. and Swinden, K.H. (1963). Proc. Roy. Soc. A272, 304-310.

Billby, B.A. (1981). Phil. Trans. Roy. Soc., London, A299, 155-167.

Booker, G.R., Shaw, A.M.B., Whelan, M.J. and Hirsch, P.B. (1967). Phil. Mag., 16, 1183-1191.

Boyd, G.M. (1972). Engineering Fracture Mechanics, 4, 459-482.

Bridgman, P.W. (1952). Studies in Large Plastic and Fracture, McGraw-Hill, New York.

Broek, D. (1972). "Some Contributions of Electron Fractography to the Theory of Fracture", N.L.R. Report No. TR 72029U, National Aerospace Laboratory (NLR), The Netherlands.

Broek, D. (1978). Elementary Fracture Mechanics, Noordhoff International Publishing, The Netherlands.

Brown, L.M. and Stobbs, W.M. (1976). Phil. Mag., 34, 351-372.

Burdekin, P.M. and Stone, D.E.W. (1966). J. Strain Analysis, 1, 145-153.

Cane, B.J. (1981). Acta Met., 29, 1581-1591.

Chadwick, R., Muir, N.B. and Grainger, H.B. (1953). J. Inst. Metals, 82, 75-80.

Chenani, G.R. (1977). Int. J. of Fracture, 13, 394-399.

Clarke, G.A. et al. (1979). Journal of Testing and Evaluation, 7, 49-56.

Clarke, G.A. and Landes, J.D. (1979). Journal of Testing and Evaluation, 7, 264-269.

Clavel, H., Tournier, D. and Pineau, A. (1975). Met. Trans., 6A, 2305-2307.

Davidson, D.L. (1974). Scanning Electron Microscopy/1974, 927-934.

Davidson, D.L. (1979). Private Communication. Address: Southwest Research Institute, Post Office Drawer 28510, 6220 Culebra Road, San Antonio, Texas, 78284, USA.

Davidson, D.L. (1981). Assessment of Defect Density Magnitude by Change in Selected Area Electron Channelling Patterns, To be Published in SEM/1981.

Davidson, D.L. and Lankford, J. (1976). J. Engineering Materials and Technology, 98, 24-29.

Davidson, D.L. and Lankford, J. (1980). Fatigue of Eng. Mat. and

Structures, 3, 289-303.

Davidson, D.L. and Lyle, F.F. (1975). Corrosion, 31, 135-139.

Davidson, D.L., Lankford, J., Yokobori, T. and Sato, K. (1976). International Journal of Fracture, 12, 579-585.

Dixon, J.R. (1966). Inst. Phys. Soc. Conf. Ser. No. 1, Dec. 1966.

Dowling, J.M. (1975). D.Phil. Thesis, Oxford University.

Dowling, J.M. and Martin, J.W. (1973). ICSMA3, Cambridge, 1, 170-174.

Dowling, J.M. and Martin, J.W. (1976). Acta Met., 24, 1147-1153.

Dowling, J.M. and Martin, J.W. (1977). ICF4, Waterloo, Canada, 2, 87-95.

Dowling, N.E. and Begley, J.A. (1976). Mechanisms of Crack Growth, ASTM STP 590, 82-103.

Druse, S.G. (1981). ICF5, Cannes, France, 2, 843-854.

Dugdale, D.S. (1960). J. Mech. Phys. Sol., 8, 100-108.

Dunwoody, B.J., Moore, J.M. and Thomas, A.T. (1973). J. Inst. Met., 101, 172-175.

Edwards, L. (1981). D.Phil. Thesis, Oxford University.

Edwards, L. and Martin, J.W. (1981). ICF5, Cannes, France, 1, 323-328.

Eftis J. and Liebowitz, H. (1972). Int. J. Fracture Mech., 8, 383-392.

Ershelby, J.D. (1951). Phil. Trans. Roy. Soc., A244, 87.

Ershelby, J.D. (1975). J. Elasticity, 5, 321.

Evensen, J.D., Ryan, N. and Embury, J.D. (1975). Materials Science and

Engineering, 18, 221-229.

French, I.E. and Weinrich, P.F. (1974). Scripta Met., 8, 87-90.

Gerberich, W.W. (1964). Experimental Mechanics, 4, 335-344.

Gerberich, W.W. and Moody, N.R. (1979). ASTM STP 675, 292-341.

Gleiter, H. and Hornbogen, E. (1967). Materials Science and Engineering, 2, 285-302.

Goods, S.H. and Brown, L.M. (1979). Acta Met., 27, 1-15.

Griffith, A.A. (1920). Phil. Trans. Roy. Soc., A221, 163.

Gudas, J.P., Joyce, J.A. and Davis, D.A. (1979). ASTM STP 677, 474-485.

Rahn, G.T., Hoagland, R.G. and Rosenfield, A.R. (1972). Met. Trans., 3A, 1189-1202.

Rahn, G.T. and Rosenfield, A.R. (1973). Proceedings Third International Congress on Fracture, Munich, 1-20.

Rahn, G.T. and Rosenfield, A.R. (1975). Met. Trans., 6A, 653-668.

Hall, E.O. (1951). Proc. Phys. Soc. London, 64B, 747.

Hancock, J.W. and Mackenzie, A.C. (1976). J. Mech. Phys. Solids, 24, 147-169.

Harries, I.R. and Varley, P.C. (1953). J. Inst. Metals, 82, 379-393.

Hirsch, P.B., Bowie, A. and Whelan, M.J. (1962). Phil. Mag., 7, 2093-2100.

Honeycombe, R.W.K. (1968). The Plastic Deformation of Metals, Edward Arnold (Publishers) Ltd., London.

Hornbogen, E. (1971). Z. Metallkunde, 66, 511-513.

Hornbogen, E. and Zum Gahr, K.H. (1975). *Metallography*, 8, 181-202.

Hutchinson, J.W. (1968). *J. Mech. Phys. Solids*, 16, 13-31.

Iino, Y. (1976). *Metal Science*, 10, 159-164.

Irwin, G.R. (1948). *Fracturing of metals*, ASM publication, 147-166.

Irwin, G.R. (1958). *Encyclopedia of Physics*, Vol. VI, Springer, Heidelberg.

Irwin, G.R. (1960). *Proceedings, Seventh Sagamore Conference*, IV-63.

Izumi, Y. and Pine, M.Z. (1979). *Engineering Fracture Mechanics*, 11, 791-804.

Jacobs, M.H. (1972). *Phil. Mag.*, 26, 1-13.

Joy, D.C. and Newbury, D.E. (1972). *J. Materials Science*, 7, 714-716.

Kleouri, A.P. and Rice, J.R. (1977). *ICFM4*, Waterloo, Canada, 1, 43-59.

Kim, Y.H., Pine, M.Z. and Mura, T. (1979). *Engineering Fracture Mechanics*, 11, 653-660.

Kobayashi, R., Nakamura, R. and Nakazawa, R. (1979). *Recent Researches on Mechanical Behaviour of Solids*, R. Miyamoto, Ed., University of Tokyo Press, Tokyo.

Kobayashi, R., Nakamura, R. and Nakazawa, R. (1979b). *ICM3*, 3, Cambridge, England, 529-538.

Knott, J.F. (1973). *Fundamentals of Fracture Mechanics*, Butterworths, London.

Knott, S.I. and Pine, M.Z. (1980). *Scripta Met.*, 14, 155-158.

Lake, R.L. (1976). *Mechanics of Crack Growth*, ASTM STP 790, 200-214.

Lankford, J. and Davidson, D.L. (1976). *International Journal of*

AD-A119 099

AIR FORCE INST OF TECH WRIGHT-PATTERSON AFB OH
MICROMECHANISMS OF CRACK EXTENSION IN ALLOYS. (U)

1982 J A BLINO

UNCLASSIFIED AFIT/CI/NR/82-250

F/G 11/6

NL

40 4
AD-A119 099



END
DATE FILMED
10 82
DTIC

Fracture, 12, 775-776.

Lankford, J., Davidson, D.L. and Cook, T.S. (1977). Cyclic Stress-Strain and Plastic Deformation Aspects of Fatigue Crack Growth, ASTM STP 637, 36-55.

Latiers, H.J. (1976). Engineering Fracture Mechanics, 8, 691-700.

Lui, H.W. and Ino, N. (1969). Fracture 1969, Chapman and Hall, London 812-823.

Lugsdon, W.A. (1976). Mechanics of Crack Growth, ASTM STP 590, 43-60.

Lohne, O. and Naess, O.J. (1979). ICSMAS, Aachen, 2, 781-788.

Longhurst, R.S. (1967). Geometrical and Physical Optics, Longmans, Green and Co. Ltd., London.

Louat, N.P. and Griffiths, J.R. (1982). "A criterion for crack extension", submitted for publication.

Lutjering, G. (1976). Slip Distribution and Mechanical Properties of Metallic Materials, Report No. DLR-FB-74-70, DFLR, Forz-Wehn, West Germany.

Mackenzie, A.C., Hancock, J.W. and Brown, D.K. (1977). Engineering Fracture Mechanics, 9, 167-188.

Martin, J.W. (1980). Micromechanisms in particle-hardened alloys, Cambridge University Press, Cambridge.

Martin, J.W. and Edwards, L. (1980). Proc. of Symposium on the Plasticity and Fracture of Engineering Materials, Oxford University, April 1980, to be published by Pergamon Press.

McClintock, F.A. (1971). Fracture - An Advanced Treatise, Vol. III, ed. H. Liebowitz, Academic Press, New York, 47-225.

McClintock, F.A. and Irwin, G.R. (1965). ASTM STP 381, 84-113.

Moody, W.R. and Gerberich, W.W. (1980). Metal Science, 14, 95-100.

Neuber, H. (1961). *J. Appl. Mech.*, 28, 544-550.

Newbury, D.E. (1972). D.Phil. Thesis, Oxford University.

Paris, P.C., Tada, H., Zahoor, A. and Ernst, H. (1977). NUREG Report No. 0311, U.S. Nuclear Regulatory Commission.

Paris, P.C., Tada, H., Zahoor, A. and Ernst, H. (1979). ASTM STP 668, 5-36.

Parker, A.P. (1981). *The Mechanics of Fracture and Fatigue*, E. and F.N. Spon Ltd., London.

Pashley, D.W., Rhodes, J.W. and Sendorek, A. (1966). *Journal of the Institute of Metals*, 94, 41-49.

Patch, W.J. (1953). *J. Iron Steel Inst.*, 173, 25.

Petit, J., Bouchet, B., Gasc, C. and de Fouquet, J. (1977). ICP4, 2, 867-872.

Pettit, D.E. and Hoepner, D.W. (1973). *Engineering Fracture Mechanics*, 5, 923-934.

Pineau, A.G. and Pelloix, R.M. (1974). *Met. Trans.*, 5, 1103-1112.

Ponton, J.W. and Lee, G.M.C. (1980). *Journal of Strain Analysis*, 15, 31-35.

Pook, L.P. (1970). NEL Report No. 465, National Engineering Laboratory, Glasgow.

Prince, K.C. (1977). D.Phil. Thesis, Oxford University.

Prince, K.C. and Martin, J.W. (1977). *Metallography*, 10, 107-113.

Prince, K.C. and Martin, J.W. (1979). *Acta Met.*, 27, 1401-1408.

Purcell, A.H. and Woertman, J. (1974). *Met. Trans.*, 5, 1805-1809.

Rice, J.R. (1967). ASTM STP 415, 247-311.

Rice, J.R. (1968a). J. Appl. Mech., 35, 379-386.

Rice, J.R. (1968b). Fracture - An Advanced Treatise, Vol. II, Academic Press, New York, 191-311.

Rice, J.R. and Johnson, H.A. (1970). Inelastic Behaviour of Solids, H.P. Kanninen et al., Eds., McGraw-Hill, New York, 641-672.

Rice, J.R., Paris, P.C. and Merkle, J.C. (1973). ASTM STP 536, 231.

Rice, J.R. and Rosengren, G.P. (1968). J. Mech. Phys. Sol., 16, 1-12.

Rice, J.R. and Tracey, D.M. (1969). J. Mech. Phys. Sol., 17, 201-217.

Rice, J.R. and Tracey, D.M. (1973). Numerical and Computer Methods in Structural Mechanics, S.J. Perves et al., Eds., Academic Press, New York, 585-623.

Ritchie, R.O., Server, W.L. and Vellaert, R.A. (1979). Metallurgical Transactions A, 10A, 1557-1570.

Sexena, A. and Antolovich, S.D. (1975). Met. Trans., 6A, 1809-1828.

Schwalbe, K-H. (1977). Engineering Fracture Mechanics, 9, 795-832.

Schuelliger, P. (1980). Scripta Met., 14, 769-772.

Shoji, T. (1976). Metal Science J., 10, 165-169.

Sih, G.C. (1966). Int. J. Fracture Mech., 2, 628-631.

Spencer, J.P. (1974). D.Phil. Thesis, Oxford University.

Stickler, R. and Booker, G.R. (1971). Proc. of the Fifth International Materials Symposium, Berkeley, California, 301.

Stroh, A.N. (1954). Proc. Roy. Soc., A223, 404-414.

Stroh, A.N. (1955). Proc. Roy. Soc., A232, 549-560.

Stuwe, H.P. (1980). Engineering Fracture Mechanics, 13, 231-236.

Tateishi, A.S. and McEvily, A.J., Jr. (1967). Fracture of Structural Materials, John Wiley & Sons Inc., New York.

Thomas, G. (1961). J. Inst. Metals, 90, 57-63.

Thompson, D.S. and Zinkham, R.E. (1975). Engineering Fracture Mechanics, 7, 389-409.

Thornton, P.R. (1968). Scanning Electron Microscopy, Chapman and Hall Ltd., London.

Tracey, D.M. (1971). Engineering Fracture Mechanics, 3, 255-265.

Tracey, D.M. (1976). Journal of Materials Technology, 98, 146-151.

Tschegg, E., Faltin, C. and Stanzl, S. (1980). Journal of Materials Science, 15, 131-138.

Van De Kastele, J.C.W. and Broek, D. (1977). Engineering Fracture Mechanics, 9, 625-635.

Wahi, R.P. and Von Neimondahl, H. (1974). Phys. Stat. Sol. (A), 24, 607-612.

Wells, A.A. (1962). Proc. Conf. Crack Propagation, Cranfield, England, 1961, 210-230.

Westergaard, R.M. (1939). J. Appl. Mech., 61, A49-53.

Wilkins, M.A. and Smith, G.C. (1970). Acta Met., 18, 1035-1043.

Yokobori, T., Sato, K. and Taguchi, H. (1973). Reports of the Research Institute for Strength and Fracture of Materials, Tohoku University, Sendai, Japan, 9, 1-10.

DATE
ILMED
8